© Copyright 2021

Gabriel V. S. Seufitelli

Mechanisms and kinetics of ethylene oligomerization over nickel-based heterogeneous catalysts

Gabriel V. S. Seufitelli

A dissertation

submitted in partial fulfillment of the

requirements for the degree of

Doctor of Philosophy

University of Washington

2021

Reading Committee:

Rick Gustafson, Chair

Renata Bura

Anthony Dichiara

Program Authorized to Offer Degree:

Environmental and Forest Science

University of Washington

Abstract

Mechanisms and kinetics of ethylene oligomerization over nickel-based heterogeneous catalysts

Gabriel V. S. Seufitelli

Chair of the Supervisory Committee:
Professor of Environmental and Forest Sciences, Dr. Rick Gustafson
School of Environmental and Forest Sciences

The present research describes the kinetics and mechanisms of the ethylene oligomerization over nickel-based solid catalysts at subcritical and supercritical ethylene conditions. The Ni-H-Beta catalyst was used due to its high activity for the conversion of ethylene into higher alkenes.

Initially, the role of nickel and Brønsted sites on the ethylene oligomerization over Ni-H-Beta catalysts is investigated. According to the catalyst characterization results, nickel is present on the catalyst surface as Ni^{2+}, from the free NiO phase and highly dispersed Ni^{2+} interacting with the catalyst's lattice oxygen. Ethylene sorption results indicate that ethylene dissociates over two active sites upon adsorption over the Ni-H-Beta. Further characterization via pyridine sorption suggests that the presence of non-coordinated Ni^{2+} or Brønsted sites decreases the probability for the formation of the active sites on the catalyst surface. Then, the kinetics of

ethylene oligomerization over the Ni-H-Beta are discussed. A kinetic model was developed for temperatures varying between 50 and 100^{o}C and pressures varying between 5 and 28 atm. The results indicate the butene and hexene are formed via a series of ethylene coordination-insertion steps and the formation of octene follows the co-oligomerization of ethylene and desorbed butene. In the present study, we refer to the pathway involving co-oligomerization of butene and hexene as *"cascade co-oligomerization"*. A detailed reaction network is proposed and modeled based on the Langmuir-Hinshelwood-Hougen-Watson kinetics.

After studying the mechanisms and kinetics of the ethylene oligomerization under subcritical conditions, the solubility of coke in supercritical ethylene is discussed. The solubility of coke in ethylene was investigated at 30, 50, and 75^{o}C and pressures ranging from 1 to 68 bar; conditions previously screened by our research group for ethylene oligomerization. The approach uses *n*-decane as a model compound to simulate coke formed during the catalytic process. A detailed thermodynamic model is developed for the solubility of *n*-decane in subcritical and supercritical ethylene. Beyond the ethylene critical point (P = 50.3 bar and T = 9.4^{o}C) the solubility of *n*-decane in ethylene at 30^{o}C reaches a maximum value of 3.0%; close to the value observed at 50 and 75^{o}C, under the same pressure. Comparison of kinetic and solubility data show that the transport of products from the catalyst to the bulk of the supercritical fluid is a function of the reaction temperature. At low temperatures (30^{o}C), coke dissolution rates are higher than apparent coke production rates. However, at high temperatures (60 and 90^{o}C), coke dissolution rates are not able to outcompete the high rates of coke formation.

The last step of the study with the Ni-H-Beta catalyst involves a kinetic model under supercritical ethylene conditions. The kinetic data under supercritical conditions are modeled based on the Langmuir-Hinshelwood-Hougen-Watson kinetics. Three different reaction limiting

steps are compared: adsorption, chain-growth, and desorption. The model that assumes desorption of products as the reaction limiting step provides the best fitting of the kinetic data among the models proposed in the present work. Therefore, the slow desorption of products from the catalyst surface to the bulk of supercritical ethylene limits the reaction. This result is consistent with the result obtained in the solubility study.

Based on the previous solubility and kinetic studies, a novel catalyst is designed for the oligomerization of supercritical ethylene. This catalyst is composed of nickel supported on mesoporous SIRAL support. We report the production of liquid products at 50, 100, and 200^{o}C and 40 and 65 bar operating at both single and dual reactor configurations. The novel Ni-SIRAL catalyst is able to oligomerize ethylene at supercritical conditions without experiencing deactivation. The liquid product is composed of linear alkenes and a substantial fraction of cycloalkanes (8.5 wt. %). A high yield for liquid hydrocarbons of 60.8 wt. % is reported at 200^{o}C and 65 bar.

TABLE OF CONTENTS

List of Figures vii

List of Tables xi

Chapter 1. Background 1

1.1 Conversion path of renewable resources into chemicals 1

1.2 Why ethylene oligomerization? 2

1.3 Avoiding coking via supercritical ethylene 3

1.4 The current state of ethylene oligomerization over heterogeneous catalysts 4

1.5 Objective and hypothesis 5

Chapter 2. The role of Ni^{2+} and Brønsted sites during the ethylene oligomerization over Ni-H-Beta catalysts 8

2.1 Introduction 9

2.2 Experimental Method 13

2.2.1 Catalyst synthesis 13

2.2.2 Catalyst characterization 14

2.2.3 Ethylene adsorption experiments 15

2.2.4 Ethylene oligomerization experiments 16

2.3 Results and discussion 17

2.3.1 Ethylene adsorption study 17

2.3.2 Physicochemical properties of the Ni-H-Beta catalyst 21

2.3.3 Effect of nickel and Brønsted sites on the ethylene oligomerization 25

2.4 Conclusion 31

Chapter 3. Kinetics of ethylene oligomerization over Ni-H-Beta catalysts' 32

3.1 Introduction 33

3.2 Experimental Method 35

3.2.1 Catalyst synthesis 35

3.2.2 Ethylene oligomerization experiments 35

3.2.3 Kinetic model development 38

3.3 Results and discussion 40

3.3.1 Kinetic parameters assessment 40

3.3.2 Reaction network 51

3.3.3 Kinetic model analysis 55

3.3.4 Comparison between "cascade co-oligomerization" and "solely ethylene coordination-insertion steps" 61

3.3.5 Model performance 68

3.4 Conclusion 69

Chapter 4. Effect of coke solubility on the oligomerization of supercritical ethylene over heterogeneous catalysts' 71

4.1 Introduction 72

4.2 Thermodynamics 75

4.2.1 Solubility modeling 75

4.2.2 Equations of state (EOS) 76

4.3 Experimental section 78

4.3.1 Materials 78
4.3.2 Solubility system setup 78
4.3.3 Solubility experiments 79
4.3.4 Data treatment 80
4.3.5 Pyridine sorption 81
4.4 Results and discussion 81
4.4.1 Nitrogen – n-decane system 81
4.4.2 Ethylene – n-decane system 84
4.4.3 Effect of the n-decane solubility on the ethylene oligomerization process 86
4.5 Conclusion 93
Chapter 5. Kinetics of supercritical ethylene oligomerization over the Ni-H-Beta 95
5.1 Introduction 96
5.2 Experimental section 100
5.2.1 Catalyst synthesis 100
5.2.2 Ethylene oligomerization experiments 100
5.2.3 Kinetic metrics 101
5.2.4 Kinetic model development 102
5.2.5 Model treatment and statistics 103
5.3 Results and discussion 104
5.3.1 Effect of temperature and pressure 104
5.3.2 Schulz-Flory distribution of product selectivity 109
5.3.3 Kinetic model development 111
5.3.4 Kinetics under supercritical conditions 115

5.4 Guidelines 120

5.5 Conclusion 120

Chapter 6. A novel route for alkenes and cycloalkanes via ethylene oligomerization over Ni-SIRAL catalysts 122

6.1 Introduction 123

6.2 Experimental section 129

6.2.1 Materials 129

6.2.2 Catalyst synthesis 129

6.2.3 Catalysis characterization 129

6.2.4 Reaction system 130

6.2.5 Ethylene oligomerization experiments 132

6.3 Results and discussion 135

6.3.1 Catalyst characterization 135

6.3.2 Ethylene oligomerization over Ni-SIRAL40 137

6.3.3 Liquid characterization 144

6.3.4 Reaction pathway 147

6.4 Conclusion 149

Chapter 7. Tecno-economic assessment of poplar conversion into jet fuel via alcohol-to-jet technology 150

7.1 Process overview 150

7.2 Process design and cost estimating 153

7.2.1 Area 100: Pretreatment 154

7.2.2 Area 200: Enzymatic hydrolysis and overliming 155
7.2.3 Area 300: Fermentation 156
7.2.4 Area 400: Purification and product recovery 157
7.2.5 Area 500: Boiler and power plant 158
7.2.6 Area 600: Ethanol dehydration 159
7.2.7 Area 700: Ethylene oligomerization 160
7.2.8 Area 800: Alkene hydrogenation 161
7.2.9 Area 900: Wastewater treatment 162
7.3 Process economics 162
7.3.1 Cost-year indices 162
7.3.2 Equipment cost 163
7.3.3 Variable and fixed operating costs 165
7.3.4 Discounted cash flow analysis and minimum jet fuel selling price 166
7.4 Results and discussion 166
7.4.1 Base case: 2,000 dry metric tons of poplar per day 166
7.4.2 Economy of scale 169
7.4.3 Sensitivity analysis 170
7.4.4 Comparison with previous techno-economic studies 172
7.5 Conclusion 174
Chapter 8. Conclusion and future work 175
8.1 Conclusion 175
8.1 Future work 177

Reference 178

Appendix A 188

LIST OF FIGURES

Figure 1.1. Flow diagram of the activities performed in the present work. Arrows represent the sequence as the tasks were performed and how the results were compared. 7

Figure 2.1. Possible reaction mechanisms (adapted from Moussa et al., Brogaard and Olsbye et al., Henry et al., and Brückner et al.) for the ethylene oligomerization over the Ni-H-Beta and Ni-SSZ2-24 catalysts. The first two pathways (A and B) are based on the Cossee-Arlman mechanism. The last pathway is based on the metallacycle mechanism proposed by Andrei et al. for the ethylene oligomerization over Ni-SBA-15. Both Cossee-Arlman and metallacycle mechanisms are the most accepted mechanisms involved in the ethylene oligomerization over homogeneous catalysts. 10

Figure 2.2. (●) Experimental ethylene coverage over the Ni-H-Beta catalyst as a function of ethylene partial pressure at 198 and 258 K. Solid lines: Modeled ethylene coverage according to the models shown in Table 2.1 – (**—**) Dissociation over two sites, (**- -**) Dissociation over one site, and (**-··-**) Association over one site. 19

Figure 2.3. Infrared spectra in the pyridine region after pyridine adsorption over Ni-H-Beta catalysts at different nickel loading followed by evacuation at 250^{o}C. LAS = Lewis acid sites and BAS = Brønsted acid sites. 23

Figure 2.4. Ni $2p_{3/2}$ X-ray photoelectron spectra of Ni-H-Beta catalysts with nickel loadings of 1.5, 2.5, and 4.1 wt. %. 23

Figure 2.5. X-ray powder diffraction of the pristine H-Beta support and Ni-H-Beta catalysts at different Si/Al ratios and nickel loadings. 29

Figure 3.1. Process flow diagram of the fixed-bed reactor used in the kinetic study. 36

Figure 3.2. Ethylene conversion (%) as a function of the inverse of WHSV (g cat.h.g of ethylene^{-1}) at P = 28 atm and T = 100^{o}C. Solid line shows the linear fitting of ethylene conversion as a function of the $WHSV^{-1}$. 41

Figure 3.3. Product selectivity given in wt. % for products ranging from C_4 to C_{10} under different temperatures. 43

Figure 3.4. Arrhenius plot for the ethylene oligomerization over the Ni-H-Beta catalyst for temperatures ranging from 50 to 200°C at 28 atm (ethylene partial pressure) and WHSV of 48.4 g ethylene g cat.$^{-1}$ h^{-1}. 44

Figure 3.5. Log-log plots of ethylene consumption and butene, hexene, and octene formation rates versus partial pressures of (○) ethylene, (□) butenes, and (△) hexene. Data collected at 100°C and WHSV = 48.4 g ethylene g cat.$^{-1}$ h^{-1}. 50

Figure 3.6. *"Cascade co-oligomerization"* pathway proposed based on the results obtained in the present work. The pathways assume the formation of a Cossee-Arlman center in agreement with reports from the literature. 52

Figure 3.7. (■) Calculated rates of ethylene consumption and butene, hexene and octene formation using the *"cascade co-oligomerization"* model. Dotted lines show the rates upper and lower limits calculated based on the confidence interval of the parameters reported in Table 3.4. (●) Experimental rates with their respective standard deviations calculated from the replicates shown in Table S1. The sum of the squared difference is shown as a representation of the total error after regression. 60

Figure 3.8. (▲) Calculated rates of ethylene consumption and butene, hexene and octene formation using the *"solely ethylene coordination-insertion steps"* model. Dotted lines show the rates upper and lower limits calculated based on the confidence interval of the parameters reported in Table 3.6. (●) Experimental rates with their respective standard deviations calculated from the replicates shown in Table S1. The sum of the squared difference is shown as a representation of the total error after regression. 63

Figure 3.9. Square of the difference between experimental and calculated reaction orders of butene, hexene, and octene relative to ethylene for the (■) *"cascade co-oligomerization"* and (●) *"solely ethylene coordination-insertion steps"* models. Dotted lines (*"cascade co-oligomerization"* = ····· and *"solely ethylene coordination-insertion steps"* = - - -) show the errors upper and lower limits calculated based on the confidence interval of the parameters reported in Table 3.4 and Table 3.6. 65

Figure 3.10. Parity plot showing experimental rates of ethylene consumption and products formation against the calculated values according to the rate expressions shown in Table 3.5

and kinetic parameters shown in Table 3.4. (●) 28 atm and 50°C, (■) 28 atm and 75°C, (◆) 28 atm, 100°C, and WHSV = 36.5, and (▲) 28 atm, 100°C, and WHSV = 60.8.68
Figure 4.1. Schematic process flow diagram of the saturator system. 80
Figure 4.2. A – Effect of flow rate on the mole fraction of n-decane in nitrogen. Data collected under 75°C and 38.8 bar. B – Long term steady-state behavior of the solubility system. Data collected under 75°C and 27 bar. 82
Figure 4.3. A – Vapor-phase solubility of n-decane in nitrogen at (○) 30, (◇) 50, (△) 75, and (×) 100 °C. (□) experimental solubility data reported by Prausnitz et al. in [30] and [29]. Solid lines show the calculated solubilities from the fitting of the thermodynamic model described in Section 4.2.1. B – n-decane vapor-phase fugacity coefficients calculated using the virial EOS at (—) 30, (- -) 50, (-··-) 75, and (-··-) 100 °C. (□) Values reported by Prausnitz et al. at 75°C [29]. 83
Figure 4.4. A – Vapor-phase solubility of n-decane in ethylene at (○) 30, (◇) 50, and (△) 75°C. Solid lines show modeled solubility isotherms from the fitting of the thermodynamic model described in Section 4.2.1 using the Peng-Robinson EOS. B – n-Decane vapor-phase fugacity coefficients calculated using Peng-Robinson EOS at (—) 30, (- -) 50, and (-··-) 75°C..... 86
Figure 4.5. Simplified reaction pathway for the oligomerization of supercritical ethylene over the Ni-H-Beta. 88
Figure 4.6. Semi-log plot showing the rates of alkene production, average coke production, and coke dissolution as a function of temperature for the oligomerization of supercritical ethylene (ethylene total pressure = 52.5 bar). Data extracted from [25]. 90
Figure 4.7. Preferential pathways involved in the oligomerization of supercritical ethylene at low and high temperatures. Blue arrows: More selective pathways. Red arrows: Less selective pathways. 93
Figure 5.1. Selectivity (in mole %) for C_4-C_{16} alkenes at 30, 50 and 100°C and ethylene partial pressures of (●) 53, (■) 56, and (▲) 60 atm. Same data shown in Table 5.1. 106
Figure 5.2. Arrhenius plot at different pressures. 108
Figure 5.3. Selectivity (in mole %) for C_4-C_{16} alkenes at 30, 50 and 100°C and ethylene partial pressures of (●) 53, (■) 56, and (▲) 60 atm. Lines show modeled selectivities at ethylene

partial pressures of (—) 53, (--) 56, and (····) 60 atm based on a Schulz-Flory-type distribution according to Equations 5.10-5.12. 111
Figure 5.4. Simplified reaction pathway proposed in the present study to model the ethylene oligomerization over the Ni-H-Beta under supercritical conditions. 113
Figure 5.5. A – Calculated residues ($rexp. - rcalc.$) for the rates of C_4, C_6, and C_8 formation as a function of temperature for ***Model 3***. B – Selectivities (in mole %) for C_{10}-C_{16} alkenes at 30, 50, 75°C, and 100°C and ethylene partial pressures of (●) 53, (■) 56, and (▲) 60 atm. Lines show modeled selectivities at ethylene partial pressures of (—) 53, (--) 56, and (····) 60 atm based on calculated rates of formation from ***Model 3***. 119
Figure 6.1. Process flow diagram for the ethylene oligomerization system used in the present study. In Reactors #1 and #2, the shaded area represents the catalyst bed location.131
Figure 6.2. A – X-Ray Diffraction pattern of the fresh Ni-SIRAL catalyst (4.9 wt. % nickel) and the pristine SIRAL40-HPV support. B – Ni 2p X-Ray Photoelectron spectrum of the 4.9 wt. % nickel Ni-SIRAL catalyst. 135
Figure 6.3. Proposed reaction pathway for the ethylene oligomerization over the Ni-SIRAL catalyst. 148
Figure 7.1. Process flow diagram of the designed process for the production of jet fuel from poplar. Only main component streams are shown. 153
Figure 7.2. Variable operating cost breakdown per gallon of jet fuel. 169
Figure 7.3. Minimum jet fuel selling price as a function of biorefinery capacity and discount rate. 170
Figure 7.4. Change in minimum jet fuel selling price for biomass, process configuration, discount rate, and enzyme variation relative to the Base Case scenario. 172

LIST OF TABLES

Table 2.1. Adsorption models developed using the Langmuir formulation 18
Table 2.2. Statistical parameters used to compare the quality of fitting of the proposed adsorption models 20
Table 2.3. Physicochemical properties and ethylene conversion of the Ni-H-Beta catalyst as a function of nickel loading 24
Table 2.4. Physicochemical properties, ethylene conversion, and product selectivity of the Ni-H-Beta catalysts at different Si/Al ratios and nickel loadings 30
Table 3.1. Apparent activation energies for consumption of ethylene and formation of butene, hexene, and octene in the range of 50 to 100^{o}C (lines with highest slope in Figure 3.4 and Figure S4)..... 46
Table 3.2. Rate expressions developed using the LHHW kinetics based on the *"cascade co-oligomerization"* pathway presented in Figure 3.6..... 54
Table 3.3. Kinetic constant values calculated for the *"cascade co-oligomerization"* model via minimization of the objective function (Equation 3.6)..... 55
Table 3.4. Revised kinetic constant values calculated for the *"cascade co-oligomerization"* model via minimization of the objective function presented in Equation 3.6 58
Table 3.5. Revised rate expressions developed using the LHHW kinetics based on the *"cascade co-oligomerization"* model presented in Figure 6 58
Table 3.6. Revised kinetic constant values calculated for the *"solely ethylene coordination-insertion steps"* model via minimization of the objective function presented in Equation 6 62
Table 3.7. Revised rate expressions developed using the LHHW kinetics based on the *"solely ethylene coordination-insertion steps"* model presented in Figure S7..... 62
Table 3.8. Reaction order for the production of butene, hexene, and octene as a function of the ethylene partial pressure..... 67
Table 4.1. Second virial cross coefficients calculated from the solubility data shown in the present work compared with the values reported by Prausnitz et al. in [29] 84

Table 4.2. Measured and calculated solubilities assuming ideal gas at 30, 50, and 75°C and 1 atm 85
Table 5.1. Overview of ethylene conversion and product selectivity as a function of temperature and pressure 105
Table 5.2. Activation energies as a function of ethylene partial pressure. Values calculated from the data shown in Figure 5.2. Upper-end and lower-end values calculated with a confidence level of 95% 108
Table 5.3. Reaction rate expressions developed using the Langmuir-Hinshelwood-Watson-Hougen kinetics, assuming different RLS (Adsorption, chain-growth, and desorption) 114
Table 5.4. Initial fitting of kinetic data based on the minimization of the objective functions given in Equation 5.6 115
Table 5.5. Kinetic parameters calculated from the fitting of the models shown in Table 5.3 117
Table 6.1. Summary of experimental results reported in the present work 137
Table 6.2. Relative content of the fractions (wt. % of total quantified liquid) 140
Table 6.3. Yield of the fractions in the liquid (in grams) 142
Table 6.4. Most abundant molecules in the liquid (T=200°C, P=65 bar, double reactor configuration) identified via GC-MS and their respective yields 145
Table 7.1. Conditions used for pretreatment 154
Table 7.2. Dilute acid pretreatment hydrolysis reactions and conversions 154
Table 7.3. Overliming reactions and conversions 155
Table 7.4. Seed fermenters reactions and conversions 156
Table 7.5. Main fermenters reactions and conversions 156
Table 7.6. Boiler reactions 158
Table 7.7. Parameters designed for the distillation columns used for the recovery of cycloalkanes 161
Table 7.8. Installation factors and exponents used for installation and scaling cost estimations 164
Table 7.9. Costs for raw materials, waste disposal, and by-products 165

Table 7.10. Fixed operating cost assumptions 165
Table 7.11. Project cost worksheet 167
Table 7.12. Summary of yields, rates, and conversion costs 168
Table 7.13. Comparison of capital investment between the Base Case scenario and the scenario where the cycloalkanes are recovered and sold separately 171
Table 7.14. Summary of yields, rates, and conversion costs for the scenario where the cycloalkanes are recovered and sold separately 171
Table 7.15. Overview of techno-economic studies on biomass conversion into hydrocarbon fuel 173

ACKNOWLEDGEMENTS

This work would not have been possible without the help and support of many colleagues, friends, and family.

First and foremost, I would like to thank my advisor Rick Gustafson for assisting and guiding me through the last two years of this project. His help to make me understand the implications of my work and set a more defined direction for my Ph.D. project was crucial for my development as a researcher. He is the most knowledgeable person that I had the chance to work with, and I feel lucky to have him as the advisor of my Ph.D.

Second, I would like to thank Fernando Resende for giving me the opportunity to work with him, first during my master's project and then during the Ph.D. Fernando always demonstrated interest in my work and my growth as a researcher. I enjoyed the conversations we had while he was a professor at the University of Washington and the opportunity to discuss new ideas.

Under the supervision of Rick and Fernando, I was able to cover a wide range of areas within the Ethylene Oligomerization project, from chemical reaction engineering to process economics, and this was a unique opportunity that enriched my experience during the Ph.D. program.

I also want to thank the members of my committee Renata Bura, Anthony Dichiara, and Eric Stuve. Their help and support during my Ph.D. study were of ultimate importance to improve the quality of my work, in special the feedbacks that they have to me during the committee meeting and Exams. I also want to thank Renata Bura for every advice that she gave me during crucial moments of my Ph.D.

During this project, I had the chance to work with several undergraduate students: Nathan Parcel, Sam, Nhu Tran, and Jason. I would not be able to do so many experiments if it were not for their help in the lab.

I also want to thank all the students that I taught during my Ph.D. study. In the last 2 years of my Ph.D., I taught 3 courses in the Bioresource and Engineering program at the University of Washington. The feedback that I received from the undergraduate students every quarter helped me improve my teaching skills and make me a better instructor. I will really miss all of them and I hope I was able to teach the same amount that they taught me during these last 2 years.

When I first got to Seattle, I made very good friends. In special, James, Miguel, Rodrigo, Daniel, Samantha, and Cata who, without knowing me, let me live with them for good 3 years. I thank them for giving me a roof, and Mauricio and Pedro for helping in this process.

I also thank Devin Chandler, with whom I shared very good moments and laughs. He also tried to teach me baseball, but still, I fail to understand the rules. This work is also dedicated to all my colleagues in the Bioresource Science and Engineering program, Heather Wise, Sheila Goodman, and Kurt Haunreiter, who are also getting their Doctoral degrees.

This work is also dedicated to all my friends in Rio de Janeiro and Danielle's family who were all present with me the day before my move to the U.S. in 2016, and are always with me when I visit Brazil.

Last, this work is dedicated to the three most important people in my life: Danielle Uchimura Pascoli, Mariland Viana Sueth, and Jandir Seufitelli, who at times had to stand the burden of the distance, but gave me all the support and love I needed to conclude this work.

DEDICATION

To my beloved wife Danielle

and my parents Mariland Viana Sueth and Jandir Seufitelli

whose support and love I can always rely on.

Chapter 1. BACKGROUND

1.1 CONVERSION PATH OF RENEWABLE RESOURCES INTO CHEMICALS

The high fluctuation prices of crude oil and the environmental implications of using fossil fuel resources are driving the development of sustainable technologies for the production of biofuels and biochemicals products from renewable feedstocks (*i.e.*, biomass and waste products). The main technologies for the conversion of renewable feedstocks into fuels and chemicals involve biochemical or thermochemical conversions. In biochemical conversion, enzymes and microorganisms are used to convert the feedstock into chemicals. Thermochemical conversion involves the use of heat combined with catalysts to promote chemical reactions that transform the feedstock into useful molecules. In some cases, biochemical and thermochemical conversions are integrated to transform the feedstock into high-value products. The biochemical conversion is used to fractionate the feedstock into intermediate molecules, which are upgraded into final products via thermochemical conversion. Alcohol-to-jet (ATJ) is a common process where biochemical and thermochemical conversion paths are integrated to produce biofuels from biomass. In this path, the biomass is fractionated into sugars and converted into ethanol via biochemical conversion. Then, ethanol is dehydrated into ethylene, which is converted into alkenes via oligomerization. The alkenes can be easily hydrogenated to produce liquid alkanes, commonly used in liquid fuels (*i.e.*, gasoline and jet fuel). The last steps of the ATJ process, dehydration, oligomerization, and hydrogenation, where ethanol is converted into alkanes, involve primarily thermochemical conversion steps. In the present research, the use of thermochemical conversion is investigated to upgrade intermediates from bioconversion processes (*i.e.*, ethanol) into useful fuels and chemicals. More specifically, the present work focuses on the oligomerization of ethylene into alkenes.

1.2 WHY ETHYLENE OLIGOMERIZATION?

Oligomerization consists of the conversion of small building block molecules into larger molecules via some extent of polymerization reactions. Ethylene is the smallest alkene and one of the most versatile commodity chemicals. Most of the ethylene production comes from petrochemical resources, such as crude oil and shale gas. However, ethylene can also be produced from renewable resources via ethanol dehydration. Ethylene oligomerization has the potential to transform ethylene from renewable resources into high-value products (*i.e.*, jet fuel and gasoline).

The main commercial processes for the oligomerization of ethylene are performed over organometallic homogeneous catalysts[1], [2]. Examples of commercial homogenous oligomerization processes are the Dimersol and Shell Higher Olefin Process (SHOP), which use nickel-based homogenous catalysts to convert propene and butene into hexene and heptene, and ethylene into alkenes in the C_4-C_{20} range, respectively[1]–[3]. Chevron Phillips developed a one-step process to convert ethylene into higher alkenes using a Ziegler-Natta catalyst at 200^{o}C and 250 bar[3], [4]. INEOS developed a two-steps ethylene oligomerization process also using a Ziegler-Natta homogeneous catalyst[3], [4]. In some of these processes, ethylene undergoes oligomerization at relatively mild conditions. However, pressures as high as 100 bar are still required.

There has been a lot of interest in replacing the homogenous catalyst used in the ethylene oligomerization with a more sustainable and environmentally friendly heterogeneous catalyst. Heterogeneous catalysts exist in a different phase than reactants and products, thus not requiring the use of solvents during the reaction. Also, heterogeneous catalysts are solids that can be easily separated from the products – usually in the gas or liquid phases – reducing operating costs[2], [5]. A heterogeneous catalyst consists of a metal supported in a solid structure. The solid structure can

serve simply as support or it can also be catalytic active. Different publications proposed nickel-based heterogeneous catalysts for the ethylene oligomerization process[6]–[11]. The idea is to "mimic" the catalyst used in the homogeneous ethylene oligomerization process[12]. Different solid supports have been reported for the ethylene oligomerization, HZSM-5, MCM-41, SBA-15, Y-zeolite, and H-beta[6]–[11]. Some of these supports contain acidic sites, which are active in the ethylene oligomerization process[3].

However, acidic catalysts suffer from severe deactivation due to the build-up of long carbon chains on the catalyst surface – a phenomenon defined as coking[1]. Introducing nickel into inorganic solid structure has been shown to reduce catalyst deactivation and prolong catalyst lifetime. Another important parameter that defines the catalyst activity and coking resistance is the pore structure and pore size. By introducing mesoporosity on solid catalysts it is possible to minimize coke production and increase catalyst selectivity towards higher alkenes. Nickel exchanged H-beta is a catalyst that includes both properties, active nickel sites and mesoporous structures. This catalyst has been shown to have a prolonged lifetime relative to other metal exchanged catalysts and a high selectivity towards liquid alkenes. There are reports in the literature of ethylene conversion as high as 87% using the Ni-H-beta catalyst at milder conditions relative to homogeneous technologies[7]. Still coking is an inevitable process in heterogeneous catalysis.

1.3 AVOIDING COKING VIA SUPERCRITICAL ETHYLENE

A supercritical fluid is any fluid above its critical temperature and pressure. Supercritical fluids are known for their high solvation power, due to the high intramolecular forces under supercritical conditions. Ethylene becomes a supercritical fluid above 9.4^{o}C and 50.3 bar, relatively mild conditions for ethylene oligomerization. The high solvation power of supercritical ethylene can assist the removal of coke from heterogeneous catalysts during the oligomerization

of ethylene. In our previous publication, we show visual evidence that supercritical ethylene can remove coke from heterogeneous catalysts[13]. However, the high pressures under supercritical conditions will also promote an increase in chain-growth reactions, increasing the extent of coke production on the catalyst. Therefore, further investigation is necessary to understand the effect of supercritical ethylene on the kinetics of the ethylene oligomerization over nickel-based solid catalysts.

1.4 THE CURRENT STATE OF ETHYLENE OLIGOMERIZATION OVER HETEROGENEOUS CATALYSTS

Although the oligomerization of ethylene over heterogeneous catalysts is a topic of interest in academia and industry, this technology lacks a more fundamental understanding of the reaction mechanism and kinetics associated with the conversion of ethylene into higher alkenes. Recently, great attention has been dedicated to unveil the nature of the active site involved in the ethylene oligomerization over nickel-based solid catalysts including the Ni-H-Beta[6], [10], [14]–[18]. It is believed that ethylene oligomerizes over heterogeneous catalysts follows the Cossee-Arlman mechanism, which is the same mechanism involved in the homogeneous ethylene oligomerization process (Shell Higher Olefin Process – SHOP). However, the number of ethylene molecules and the nature of the active site involved in the initial step of the catalytic process is still a topic of debate.

Although publications dating from the 80's and 90's[19]–[22] described kinetic models for the ethylene oligomerization over nickel-based solid catalysts, only a few publications developed kinetic models for the ethylene oligomerization over recently developed catalysts, such as the Ni-H-Beta. A recent study described the kinetics of the ethylene oligomerization over the Ni-H-Beta under conditions where the production of propylene and *n*-butene is maximized via Single-Event

MicroKinetic (SEMK)[23]. Further investigation is necessary to understand the kinetics of the ethylene oligomerization under conditions where the production of higher alkenes is maximized.

1.5 OBJECTIVE AND HYPOTHESIS

The overall goal of the present research is to investigate the ***mechanisms and kinetics of the ethylene oligomerization over heterogeneous catalysts under subcritical and supercritical conditions and the effect of coke dissolution by supercritical ethylene on the reaction kinetics.*** For this project we chose the Ni-H-Beta catalyst, which has been shown to be an outstanding catalyst for the conversion of ethylene into higher alkenes, with high selectivity to liquid hydrocarbons[7], [13], [23]–[26].

The first step of this research ***(Task 1)*** involves the investigation of the nature of the active site involved in the ethylene oligomerization over the Ni-H-Beta (Results discussed in Chapter 2). Then, the second step ***(Task 2)*** involves a kinetic study aiming to develop a comprehensive reaction pathway that can be used to further elucidate the production of higher alkenes during the ethylene oligomerization over the Ni-H-Beta under subcritical conditions (Results discussed in Chapter 3).

In order to understand the effects of supercritical ethylene during the catalytic process, an investigation is presented to unveil the interaction of ethylene with coke molecules. The coke produced during the ethylene oligomerization over the Ni-H-Beta under subcritical and supercritical conditions was previously characterized as aliphatic alkanes[10], [11], [13], [16]. Even though several studies reported the solubility of alkanes in ethane, very little information is known about the solubility of alkanes in ethylene. Important solubility studies reported in the literature addressing the solubility of solids and liquids in compressed gases include the works performed by Diepen, Scheffer, Prausnitz, Avila, and Benson[27]–[30]. The solubility of aliphatic

alkanes in supercritical ethylene is described in ***Task 3*** (Results discussed in Chapter 4). Based on the coke characteristics reported in previous studies, *n*-decane was used as a coke model compound to simulate coke molecules formed during the catalytic process.

After studying the solubility of *n*-decane in ethylene, a kinetic model under supercritical ethylene conditions is developed ***(Task 4)*** by combining kinetic and solubility data to understand the effects of coke solubility on ethylene conversion and product selectivity (Results discussed in Chapter 5). Then, the mechanism and kinetics of the ethylene oligomerization over the Ni-H-Beta under subcritical and supercritical conditions are compared to underline the advantages and disadvantages of using supercritical ethylene during the ethylene oligomerization over the Ni-H-Beta. The last step of the project ***(Task 5)*** involves the design of a novel catalyst, according to specific guidelines obtained in the previous tasks (Results discussed in Chapter 6). The Chapters are presented in the form of publications, each addressing the Tasks underlined in this section.

The Tasks are subdivided as follow:

Task 1: Mechanism of the ethylene oligomerization under subcritical conditions (Chapter 2).

Task 2: Kinetics of the ethylene oligomerization under subcritical conditions (Chapter 3).

Task 3: Solubility of n-decane in subcritical and supercritical ethylene (Chapter 4).

Task 4: Kinetics of the ethylene oligomerization under supercritical conditions (Chapter 5).

Task 5: Design of a new catalyst (Chapter 6).

As a Complementary Task, a techno-economic analysis of an ATJ process is presented. The model was developed in Aspen using the data presented in this research to model the ethylene oligomerization step of the ATJ process. The results of the techno-economic analysis are presented in Chapter 7. Figure 1.1 shows the flow diagram of the activities performed in this work. The

arrows in Figure 1.1 represent the sequence as the tasks were performed and how the results were compared.

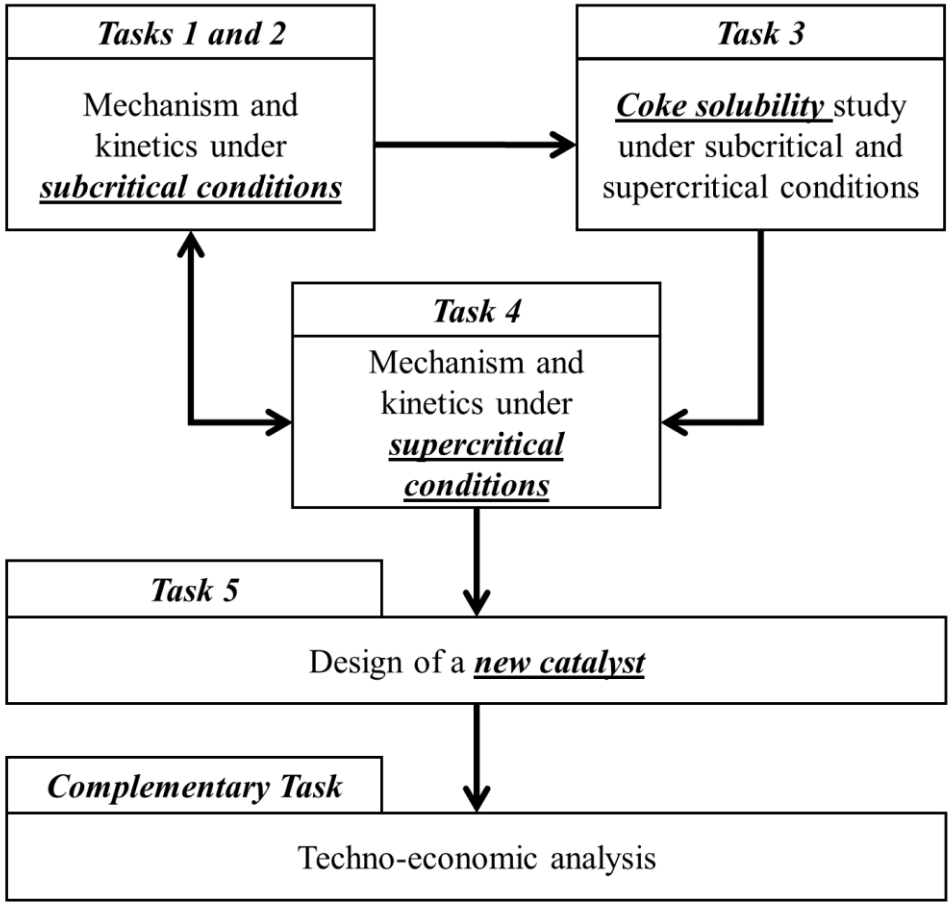

Figure 1.1. Flow diagram of the activities performed in the present work. Arrows represent the sequence as the tasks were performed and how the results were compared.

Chapter 2. THE ROLE OF NI^{2+} AND BRØNSTED SITES DURING THE ETHYLENE OLIGOMERIZATION OVER NI-H-BETA CATALYSTS[1,2]

Abstract

We investigated the role of nickel and Brønsted sites on the ethylene oligomerization over Ni-H-Beta catalysts with different nickel loadings (1.0, 1.5, 2.5, 4.1, and 6.0 wt. %) and silicon-to-aluminum ratios (12.5, 19, 63, 73, 108, and 150). The catalysts were characterized via X-ray powder diffraction (XRD), X-ray photoelectron spectroscopy (XPS), and pyridine sorption. Catalyst characterization results show that nickel is present on the catalyst surface as Ni^{2+}, originating from the free NiO phase and highly dispersed Ni^{2+} interacting with the catalyst's lattice oxygen. Ethylene sorption over the Ni-H-Beta catalyst with nickel loading of 4.1 wt. % and silicon-to-aluminum ratio equal to 12.5 indicate that ethylene dissociates over two active sites upon adsorption over the Ni-H-Beta. Pyridine sorption suggests a correlation between catalyst activity and the concentration of Ni^{2+} and Brønsted sites on the catalyst. We found that the presence of non-coordinated Ni^{2+} or Brønsted sites hinders the conversion of ethylene over the Ni-H-Beta. Based on these results, the active sites are most likely in isolated positions on the catalyst surface. We propose that the ethylene oligomerization over the Ni-H-Beta proceeds via the dissociation of ethylene over isolated $[Ni\text{-}H]^{+}$ sites following a Cossee-Arlman mechanism. We also found evidence that ethylene conversion varies with the silicon-to-aluminum ratio; directly related to the

[1] To be submitted to Applied Catalysis A: General, Gabriel V. S. Seufitelli, Jason J. W. Park, Phuong N. Tran, Anthony Dichiara, Fernando L. P. Resende, Rick Gustafson.

[2] Work presented at the American Institute of Chemical Engineers (AIChE) Annual Meeting in 2018.

concentration of Brønsted sites on the catalyst. This evidence supports the involvement of Brønsted sites in the conversion of ethylene into higher alkenes.

Keywords: Ethylene Oligomerization; Brønsted acid sites; Dissociative adsorption; Adsorption study; Langmuir isotherms; Cossee-Arlman mechanism.

2.1 INTRODUCTION

Ethylene oligomerization is a chemical process of foremost importance in the production of higher alkenes, which are feedstocks for the production of fuels and chemicals. Currently, ethylene is produced from the cracking of naphtha, and the total annual worldwide capacity is estimated to be around 140 million tons[2], [10], [18]. An alternative route for the production of ethylene is via ethane from shale gas, which has contributed to increasing production of ethylene relative to other alkenes, such as propene and butene[16], [31]. Currently, the oligomerization of ethylene is performed commercially over homogeneous catalysts[2], [10], [12], [32]. Even though these catalysts are effective, they require the use of co-catalysts, such as methyl aluminoxane (MAO) or $AlEtCl_2$ in excess[2], [12], [16], [18], [33]. Additionally, these catalysts require disposal of non-environmental friendly solvents, such as toluene, and the process requires the use of expensive equipment to separate the catalyst from the products in the reactor effluent[1], [2], [23], [34]. Because of that, there has been a significant effort to develop heterogeneous catalysts capable of oligomerizing ethylene at high conversions since these catalysts do not require the use of solvents, can be easily recovered and regenerated, and are more environmentally friendly[1], [2], [7].

Several studies proposed heterogeneous catalysts for the ethylene oligomerization[7], [9]–[11], [18], [35]–[44]. Most of those reports focused on the introduction of metals, such as nickel on acidic inorganic structures, to simulate the catalytic system employed in homogeneous

oligomerization processes. Among the heterogeneous catalysts proposed, the Ni-H-Beta is an outstanding option for the production of alkenes under mild conditions[7], [10], [11], [13], [23]–[26]. Martinez et al. were the first to report the production of liquid products using Ni-H-Beta catalysts, achieving conversions as high as 87%[7]. In recent publications from our research group, we reported the collection of liquid products during the ethylene oligomerization over the Ni-H-Beta under a wide range of conditions[13], [24]–[26].

The mechanism of ethylene oligomerization over nickel-exchanged catalysts has been the focus of several publications [10], [15], [16], [34], [45]–[47]. These reports agree that the ethylene oligomerization over heterogeneous catalysts follows mechanisms similar to the ones observed in homogeneous systems. The most accepted mechanisms for the ethylene oligomerization on heterogeneous catalysis are shown in Figure 2.1.

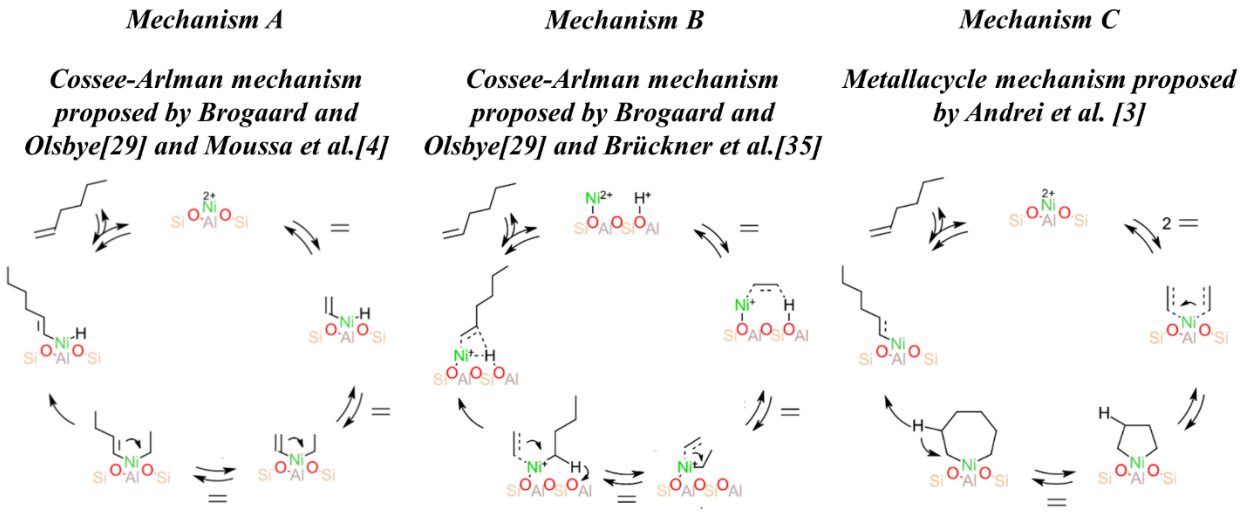

Figure 2.1. Possible reaction mechanisms (adapted from Moussa et al., Brogaard and Olsbye et al., Henry et al., and Brückner et al.) for the ethylene oligomerization over the Ni-H-Beta and Ni-SSZ2-24 catalysts. The first two pathways (A and B) are based on the Cossee-Arlman mechanism. The last pathway is based on the metallacycle mechanism proposed by Andrei et al. for the ethylene oligomerization over Ni-SBA-15. Both Cossee-Arlman and metallacycle mechanisms are the most accepted mechanisms involved in the ethylene oligomerization over homogeneous catalysts.

Mechanisms A and ***B*** (Figure 2.1), denoted Cossee-Arlman[48], [49], involves the coordination-migratory insertion of chain-growth and is the accepted mechanism for the Shell Higher Olefin Process (SHOP)[12]. The initial step for the formation of the Cossee-Arlman active center in ***Mechanism A*** involves the dissociation of ethylene over Ni^{2+} ions, producing an ethyl group that acts as a co-catalyst. This mechanism was recently proposed by Moussa et al.[16]. The initial step for the formation of the Cossee-Arlman active center in ***Mechanism B*** involves the adsorption of a single molecule on a nickel ion coordinated with a Brønsted site. The participation of Brønsted sites in the formation of the active site was proposed by Brückner et al. for the dimerization of butene over nickel-exchange acidic catalysts based on spectroscopy studies[17]. Brückner et al. proposed that Ni^{+} or Ni^{2+} are formed upon the interaction of Ni^{0} with Brønsted sites. Ng et al. proposed a similar mechanism involving the combination of Ni^{+} and H^{+} to produce a Ni^{+}-H^{+} site for the dimerization of ethylene over Ni-Y catalysts[6]. ***Mechanism C***, denoted metallacycle, involves the coupling of two ethylene molecules over a cationic center, which forms a metallacyclepentane species. Further insertion of ethylene leads to the increase in carbon number of the metallacycle species, which eventually desorbs as an alkene. Andrei et al. proposed that a metallacycle mechanism was involved in the ethylene oligomerization over Ni-AlSBA-15. The authors postulated this mechanism based on the absence of a co-catalyst in the reaction system, which is required for the oligomerization following the Cossee-Arlman mechanism[18].

The mechanisms shown in Figure 2.1 were investigated via DFT calculations by Brogaard and Olsbye, and according to the authors, the formation of a Cossee-Arlman active center from the adsorption of ethylene over isolated Ni^{2+} (Figure 2.1 – ***Mechanism A***) or Ni^{+}-H (Figure 2.1 – ***Mechanism B***) is the most plausible mechanism for the ethylene oligomerization over Ni-SSZ-22 catalysts[15]. More recently, Brogaard et al.[14] proposed via DFT calculations that Ni^{2+} in

exchanging positions acts as a mobile active center, in which the reversible mobilization of those centers is triggered by the coordination of ethylene molecules. Additional publications postulated Ni^{+} ions as the active site involved in the ethylene oligomerization over nickel-exchanged solid catalysts[36], [44], [50]–[52].

Based on the main investigations reported in the literature, Ni^{+}, Ni^{2+}, and $[Ni\text{-}H]^{+}$ sites have been proposed as active sites in the conversion of ethylene into alkenes over nickel-exchanged acidic catalysts. The main mechanisms listed in the literature are summarized in Figure 2.1. The active sites proposed by Brückner et al. (Figure 2.1 – ***Mechanism B***) and Ng et al.[6] are the only ones that involve the participation of Brønsted sites during the initiation step of the catalytic process. There is an agreement that a high energetic barrier is involved in the coordination of ethylene over Brønsted sites. Nonetheless, one cannot disregard a synergistic effect between nickel and Brønsted sites, perhaps forming a $[Ni\text{-}H]^{+}$ active center as proposed by Brückner et al.[17] and Ng et al.[6]. This synergistic effect could explain the formation of Cossee-Arlman active centers, with Brønsted sites acting as a *"co-catalyst"*[18].

Therefore, in the present study, we aim to investigate the role of Ni^{2+} and Brønsted sites on the ethylene oligomerization over nickel-exchanged aluminum silicate catalysts. We used Ni-H-Beta because of its high activity in the conversion of ethylene to oligomers and the extensive reports available in the literature for this catalyst. We analyzed the data collected in the present work based on the three main mechanisms proposed in the literature (Figure 2.1) with respect to the number of ethylene molecules and active sites involved in the initial step of the ethylene oligomerization reaction. We performed extensive characterization of the Ni-H-Beta catalysts with varying nickel loading via X-Ray Photoelectron Spectroscopy (XPS) and pyridine adsorption. Additionally, we report an ethylene adsorption study aiming to elucidate the number of ethylene

molecules and actives sites involved in the initial step of the catalytic process. Even though previous reports investigated the ethylene adsorption over the Ni-H-Beta by means of spectroscopy studies[10], [16], this is the first work to report ethylene adsorption isotherms over the Ni-H-Beta.

2.2 EXPERIMENTAL METHOD

2.2.1 *Catalyst synthesis*

Ammonium exchanged Beta zeolites with silica-to-alumina ratios (SiO_2/Al_2O_3) of 25 (part number = CP814E) and 39 (part number = CP814C) and the protonated form of the Beta zeolite with a SiO_2/Al_2O_3 of 300 (CP811-300) were purchased from Zeolyst International. Five nickel-exchanged H-Beta catalysts, denoted Ni-H-Beta, were produced by impregnation of the ammonium form of the Beta zeolite (SiO_2/Al_2O_3 = 25) with 0.065, 0.127, 0.254, 0.512, and 1.025 M solutions of $Ni(NO_3)_2$ purchased from Sigma-Aldrich (Purity: 99.999%). This process produced Ni-H-Beta catalysts with nickel loadings of 1.0, 1.5, 2.5, 4.1, and 6.0 wt. %. Nickel exchanged catalysts (nickel loading = 2.5 wt. %) with different silicon-to-aluminum ratios (Si/Al) were produced by impregnation of ammonium (SiO_2/Al_2O_3 = 39) and protonated (SiO_2/Al_2O_3 = 300) forms of the Beta zeolite with a 0.512 M solution of $Ni(NO_3)_2$. The procedure used for the production of nickel catalysts is described in previous publications from our group[13], [24]–[26]. Briefly, the $Ni(NO_3)_2$ solution was dropped onto 20 grams of zeolite powder for 1 hour, producing a slurry which was stirred for 5 hours using a Teflon stir bar. Then, the slurry was filtered under vacuum, followed by washing with deionized water. After the filtration, the solids were dried at 100^{o}C overnight. After drying, a material resembling clay was obtained, which was ground using a mortar/pestle. Finally, the powder was calcined at 550^{o}C for 5 hours to activate the catalyst.

Three additional H-Beta catalysts with Si/Al ratios of 63, 73, and 108 were produced by acidic treatment of the pristine H-Beta support (Si/Al = 19) with 0.2, 0.4, and 0.6 M solutions of

HNO_3, respectively. The solution was mixed with the pristine support at 80°C for 5 hours under agitation. Then, the solution was vacuum filtered, and the recovered solids were washed several times with deionized water to reduce the pH to neutral. The filtered solids were dried overnight at 100°C and calcined at 550°C for 5 hours to obtain the H-Beta catalysts with different Si/Al ratios. After acidic treatment, the Ni-H-Beta catalysts were produced via impregnation, according to the procedure described previously.

2.2.2 *Catalyst characterization*

ICP-AES was used to measure the nickel loading of the catalysts according to EPA protocol 200.7, in which the catalyst samples were digested with nitric acid and hydrochloric acid.

Pyridine was purchased from TCI. Adsorption experiments were conducted in a Harrick Sci. diffuse reflectance chamber mounted with ZnSe windows. Spectra were collected in a Shimadzu Prestige-21 Infrared Spectrophotometer equipped with a DLaTGS detector. The catalyst samples (5 mg – diluted in KBr with a 5% dilution) were pretreated at 300°C under vacuum (10^{-3} bar) for 30 min before sorption. After pretreatment, the temperature was reduced to 30°C and 20 µL of pyridine was admitted into the chamber under vacuum. The chamber was evacuated for 30 min to remove physisorbed pyridine species from the catalyst surface and the reactor chamber temperature was ramped to 250°C. Spectra of the catalyst surface were collected with a resolution of 8 cm^{-1}. Peaks located at 1450 and 1545 cm^{-1} were used to estimate the concentration of Lewis and Brønsted acid sites using the extinction coefficients reported by Emeis[53].

X-ray photoelectron spectra were collected in a Surface Science Instrumental S-Probe spectrometer (Service Physics, Bend OR) with a monochromatized Al X-Ray source and a spot size of 800 x 800 µm. The sample powders were pressed onto a piece of double Scotch tape. The samples were set as insulators, and a charge neutralizer was used during the measurements. For

the high-resolution spectra, all binding energies were referenced to the C 1s C-C bonds at 285.0 eV.

X-ray powder diffractions were obtained in a Bruker D8 Discover Microfocus diffractometer mounted with an IμS 2.0 microfocus X-ray source (Incoatec) using Cu K-α radiation and a Pilatus 3R 100K-A 2D detector. The samples were pressed flat onto a silicon wafer substrate.

2.2.3 *Ethylene adsorption experiments*

A packed-bed reactor was used to study the adsorption of ethylene over the Ni-H-Beta catalyst with a nickel loading of 4.1 wt. %. To avoid oligomerization reactions during the adsorption study, the experiments were conducted at cryogenic temperatures of 198 and 253 K by cooling the adsorption system in a dry-ice bath and a bath consisting of a mixture of ice and salt, respectively. The temperature of the packed-bed was kept approximately constant during each experiment with a variation of ±0.5^{o}C. Before ethylene adsorption, 50 mg of fresh catalyst was loaded inside the packed-bed. Next, the catalyst was pretreated for 3 hours at 300^{o}C under a nitrogen (Praxair, grade: 5.0, purity: 99.998%) flow of 100 ml/min to remove impurities and adsorbed water from the catalyst surface. Then, the adsorption system was cooled to the set-point temperature and ethylene (Praxair, grade: 2.5, purity: 99.5%) was admitted into the packed-bed. Several experiments were performed at varying ethylene concentrations from 76 to 2100 ppm, and for each experiment, the ethylene concentration was kept constant. Gases downstream of the packed-bed were analyzed using a GC-2014 (Shimadzu) equipped with a capillary column (Agilent 19091-QO4 - ID=0.32 mm, L=30 m, and film=20 μm) and coupled with FID and TCD detectors. To minimize the gap between analyses, we ran the GC using an isothermal temperature of 40 ^{o}C for 5 minutes. After adsorption equilibrium was reached (determined from the uptake

curves - not shown), we analyzed the gases downstream of the reactor using a different temperature profile (isothermal at 40 ^{o}C for 4 min, followed by ramping to 130 ^{o}C at a rate of 30 ^{o}C/min and holding for 5 min, followed by a ramping to 260 at a rate of 10 ^{o}C/min and holding for 10 min) to verify if any products were generated during the adsorption. Also, the catalysts were characterized after adsorption via FTIR (Shimadzu Prestige 21) coupled with a DLaTGS detector to verify the presence of products on their surface. FTIR spectra did not show peaks for C-H species on the catalysts after adsorption.

2.2.4 *Ethylene oligomerization experiments*

Ethylene oligomerization was carried out in a fixed-bed reactor loaded with 0.25 g of catalyst. We placed a thermocouple in the center of the catalyst bed to control the temperature of the reactor. Another thermocouple placed on top of the catalyst bed was used to measure the temperature gradient across the bed. The temperature gradient remained within ±5 ^{o}C for all experiments. The catalyst bed used in the experiments had a diameter of 1 mm and a height of 0.7 mm. A back-pressure regulator (ZF1 series, Equilibar) was used to control the pressure of the reactor and the outlet stream of the reactor was mixed with nitrogen (Praxair, grade: 5.0, purity: 99.998%) for mass balance quantification. The gas mixture was fed to a GC-2014 (Shimadzu) equipped with a capillary column (Agilent 19091-QO4 - ID=0.32 mm, L=30 m and film=20 µm) and coupled with FID and TCD detectors.

Before ethylene oligomerization, the fresh catalyst was pretreated overnight (300 ^{o}C for 15 hours), under a nitrogen flow rate of 100 ml/min. After the pre-treatment, the temperature was reduced to the reaction temperature and the reactor was pressurized to the reaction pressure with pure ethylene (Praxair, grade: 2.5, purity: 99.5%) at a flow rate of 700 ml/min to minimize the extent of reaction at this point. After the reactor reached the reaction conditions, we reduced the

ethylene flow rate from 700 ml/min to 160 ml/min and started the GC acquisition. Each experiment was done for at least 4 hours until the system reached steady-state conditions. Mass balance closure for the experiments presented in this study remained within ±7%. Ethylene conversion was calculated according to Equation 2.1:

$$X = \frac{F_{products}}{F_{a0}} \tag{2.1}$$

Where X is the ethylene conversion, F_{a0} is the ethylene mass fed rate ($g.min^{-1}$) and $F_{products}$ is the mass flow rate of all products downstream the reactor ($g.min^{-1}$). Product selectivity was calculated according to Equation 2.2:

$$S_i\ (wt.\%) = \frac{r_i(grams\ of\ i.g\ cat^{-1}.h^{-1})}{r_{total}(total\ grams.g\ cat^{-1}.h^{-1})} \tag{2.2}$$

Where $S_i\ (wt.\%)$ is the selectivity for species i in wt. %, r_i and r_{total} are the rates of formation of species i ($C_4 – C_{12}$) and total products, respectively.

2.3 RESULTS AND DISCUSSION

2.3.1 *Ethylene adsorption study*

Sorption equilibrium can be obtained from sorption measurements of reactants or products (i.e., adsorbates) on the catalyst surface (i.e., adsorbent). These measurements involve the adsorption under several adsorbate concentrations at a fixed temperature, producing adsorption isotherms. A number of models, such as Langmuir, Freundlich, Dubinin-Polanyi, and Dubinin-Astakhov can be used to model adsorption isotherms based on experimental adsorption data[54], [55]. The Langmuir adsorption model is one of the most widely used and assumes the monolayer adsorption of molecules on a plain surface in which all sites have the same energy[56]. Based on the mechanisms presented in Figure 2.1, we developed Langmuir adsorption expressions for the ethylene coverage (fraction of sites occupied by ethylene molecules) over the Ni-H-Beta as a

function of the number of sites and molecules involved in the adsorption process. Table 2.1 lists the models compared in the present work with their corresponding assumptions.

Table 2.1. Adsorption models developed using the Langmuir formulation

Model description	Mechanism[1]	Number of adsorbate molecules	Number of active sites	Adsorption expression[2]	Langmuir expression[3]
Dissociation over one site	A	1	1	$A + * \rightarrow A' * A''$	$\frac{q}{q_0} = \frac{KP_A}{1 + KP_A}$
Dissociation over two sites	B	1	2	$A + 2 * \rightarrow A' * + A'' *$	$\frac{q}{q_0} = \frac{\sqrt{KP_A}}{1 + \sqrt{KP_A}}$
Association over one site	C	2	1	$2A + * \rightarrow A_2 *$	$\frac{q}{q_0} = \frac{KP_A^2}{1 + KP_A^2}$

[1] Mechanism shown in Figure 2.1.
[2] A represents the adsorbate molecule (ethylene), * represents the active site involved in the adsorption process (nickel or acid), and *A'* and *A''* represent dissociated species, for example, $-C_2H_3$ and $-H$.
[3] $\theta = \frac{q}{q_0}$ represents the fraction of active sites that are occupied by molecule *A*, therefore, θ ranges between 0 and 1. q express the moles of adsorbate molecules adsorbed (moles/mg of catalyst) and q_0 represents the total adsorption capacity (in moles/mg of catalyst).

Figure 2.2 shows experimental ethylene adsorption isotherms at 198 and 258 K and the fitting of the experimental data according to the expression shown in Table 2.1. Preliminary observation of the fitted models at 198K and 258K, indicates that the model that assumes the dissociation of ethylene over two sites fits the experimental adsorption data with more accuracy than the other two models.

The Akaike information criterion was used to compare the quality of the fitted models relative to the experimental adsorption data. The Akaike information criterion, AIC, is calculated according to the following equation[57]:

$$AIC = 2k - \ln(L) \tag{2.3}$$

Where k is the number of estimated parameters – equals unity for all models – and L is the maximum value of the likelihood function of the model – taken as the square of the standard error (SSE) for the fitted models.

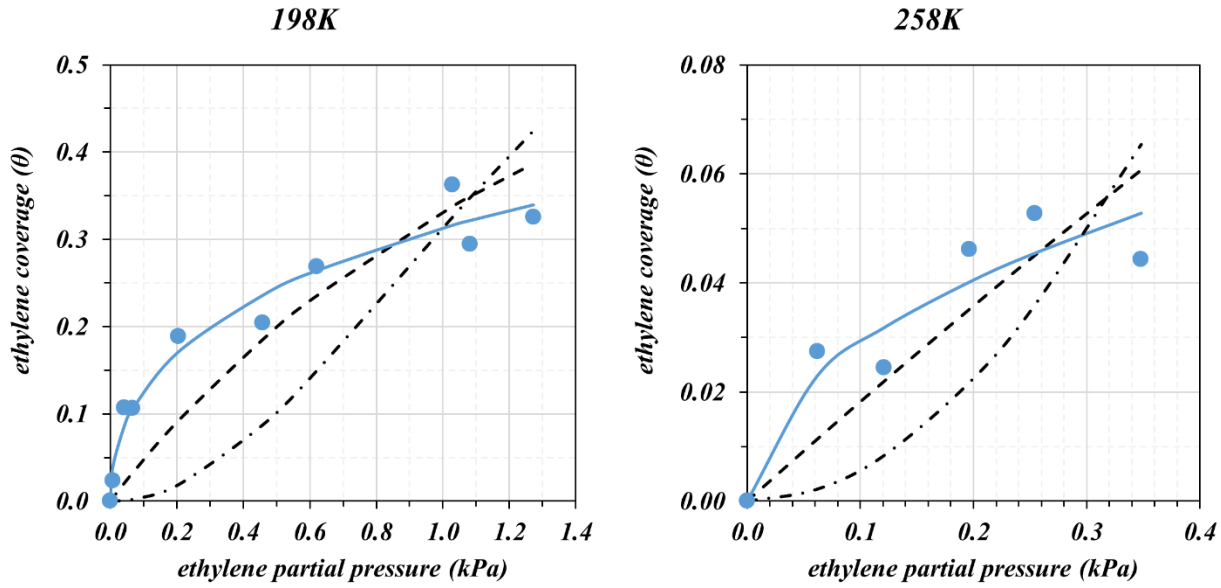

Figure 2.2. (●) Experimental ethylene coverage over the Ni-H-Beta catalyst as a function of ethylene partial pressure at 198 and 258 K. Solid lines: Modeled ethylene coverage according to the models shown in Table 2.1 – (—) Dissociation over two sites, (- - -) Dissociation over one site, and (-·-) Association over one site.

For small samples sizes[57]:

$$AIC_c = AIC + \frac{2k^2+2k}{n-k-1} \tag{2.4}$$

Where *AICc* is the Akaike information criterion for small sample sizes and n denotes the number of experimental data points. Equation 2.4 was used to compare the relative quality of the fitted models for the experimental data given in Figure 2.2. According to the criterion, for a given set of models, the model with the lowest *AICc* value has the highest probability to predict a set of experimental data points. Based on the AICc values, probabilities can be calculated according to the following equation[57]:

$$w_i = \frac{\exp(-0.5\Delta_i)}{\sum_{r=1}^{R}\exp(-0.5\Delta_r)} \quad (2.5)$$

Where w_i is the probability that model i is more likely to predict the experimental data than the other models, and Δ_i and Δ_r are the Akaike differences defined as[57]:

$$\Delta_i = AICc_i - AICc_{minimum} \quad (2.6)$$

$$\Delta_r = AICc_r - AICc_{minimum} \quad (2.7)$$

Where $AICc_i$ and $AICc_r$ are the Akaike information criterion for models i and r, respectively, and $AICc_{minimum}$ is the minimum Akaike information criterion value for the set of models. Table 2.2 shows the calculated *AIC*, *AICc*, and probabilities according to Equations 2.3, 2.4, and 2.5, respectively. According to the criterion, the model that assumes ethylene dissociation over two active sites is more likely to predict the experimental adsorption data than the other two models. Comparison of the probabilities in Table 2.2 shows that the model assuming dissociation over two active sites is 100.0% more likely to predict the experimental data relative to the models assuming dissociation over one site (probability = 0.0%) and association over one site (probability = 0.0%).

Table 2.2. Statistical parameters used to compare the quality of fitting of the proposed adsorption models

	Dissociation over one site	Dissociation over two sites	Association over one site
SSE	0.032	0.005	0.096
AIC	-95	-124	-78
AICc	-94	-123	-77
Δ	29	0	46
		Probabilities	
	Dissociation over one site	Dissociation over two sites	Association over one site
weight (w)	0.0%	100.0%	0.0%

In a recent publication, Moussa et al. provided indications that ethylene dissociates over Ni^{2+} ions forming a [ethyl-nickel-hydrogen] complex during the initial stage of the oligomerization over the Ni-H-Beta[16]. This evidence was based on the presence of molecular hydrogen identified

upon the initial contact of ethylene with the Ni-H-Beta catalyst via real-time GC-MS. The results obtained in the present study are consistent with this observation and support the hypothesis that ethylene dissociates upon adsorption on the catalyst surface. However, our results point to the involvement of two active sites during the adsorption process. Due to the bifunctional nature of the catalyst, which possesses both nickel and Brønsted sites, it is reasonable to assume that ethylene dissociates over a $[Ni\text{-}H]^+$ site instead of two nickel or two Brønsted sites. Therefore, based on the adsorption experiments, we propose that ethylene dissociates over $[Ni\text{-}H]^+$ sites. This result is in agreement with ***Mechanism B*** (Figure 2.1) proposed by Brückner et al.[17] for the butene oligomerization over a nickel-exchanged acidic catalyst and Ng et al.[6] for the ethylene dimerization over nickel-exchanged Y-zeolite. To further investigate our hypothesis, we conducted an extensive study on the effects of nickel and Brønsted sites on the ethylene oligomerization over the Ni-H-Beta.

2.3.2 *Physicochemical properties of the Ni-H-Beta catalyst*

Previous publications from our group used the same Ni-H-Beta catalysts presented in this work (samples from the same batch)[13], [24]–[26]. Therefore, extensive characterization is available including BET, FTIR, XRD, SEM, and TEM. In the present work, we conducted further characterization via pyridine adsorption and X-ray photoelectron (XP) spectroscopy.

Figure 2.3 shows infrared spectra in the pyridine region after pyridine adsorption over Ni-H-Beta catalysts loaded with different concentrations of nickel. Peaks at 1450 and 1545 cm^{-1} are assigned to pyridine coordinated with Lewis (LAS) and Brønsted (BAS) acid sites, respectively[7], [10], [16], [58]. The introduction of nickel on the H-Beta support causes a reduction in the area of the peak assigned to BAS. The decrease in Brønsted acidity with nickel loading is corroborated by a decrease in intensity of the peak located at 1632 cm^{-1} – assigned to pyridinium ions (conjugated

acid of pyridine). There is also a redshift of the peak located at 1450 cm^{-1} with increasing nickel loading, which suggests a change in the original Lewis acidity of the H-Beta support – assigned to highly dispersed extra framework aluminum[7]. These results are consistent with the replacement of some of the Brønsted sites present on the H-Beta support with cationic nickel species, which are characterized as Lewis acids[7]. Another feature of the H-Beta support is the peak centered between 1609 and 1622 cm^{-1} – characteristic of pyridine coordinated with extra framework Al^{3+}. For the series of nickel-exchanged catalysts, this peak is centered at a lower wavenumber, 1609 cm^{-1}. The peak at 1609 cm^{-1} with a prolonged shoulder at higher wavenumber[17], [59] (more visible at high nickel loadings) is assigned to pyridine coordinated with Ni^{2+} ions, thus indicating the presence of Ni^{2+} on the Ni-H-Beta catalysts. Similar trends have been reported in [7], [10]. Therefore, the decrease in the concentration of Brønsted sites and the redshift of the peak assigned to LAS is due to the formation of Ni^{2+} ions in cationic exchanging positions after the impregnation of the H-Beta support with the nickel nitrate solution.

Figure 2.4 shows X-ray photoelectron (XP) spectra of the Ni $2p_{3/2}$ region of Ni-H-Beta catalysts with nickel loadings of 1.5, 2.5, and 4.1 wt. %. All samples have characteristic peaks at 858.3 and 854.7 eV, assigned to highly dispersed Ni^{2+} in cationic exchanging positions and Ni^{2+} of the NiO phase, respectively[16], [60]. The absence of components at 852 eV – assigned to Ni^{0} – indicates that nickel is present on the catalyst only as ionic or oxide forms[61]. This results rules out the formation of cationic nickel (Ni^{+} or Ni^{2+}) via oxidation of Ni^{0} by Brønsted sites as previously postulated by Brückner et al.[17]. Also, no components at 855.5 eV were present in the XP spectra of the fresh catalysts, suggesting the absence of Ni^{+}[16], [61].

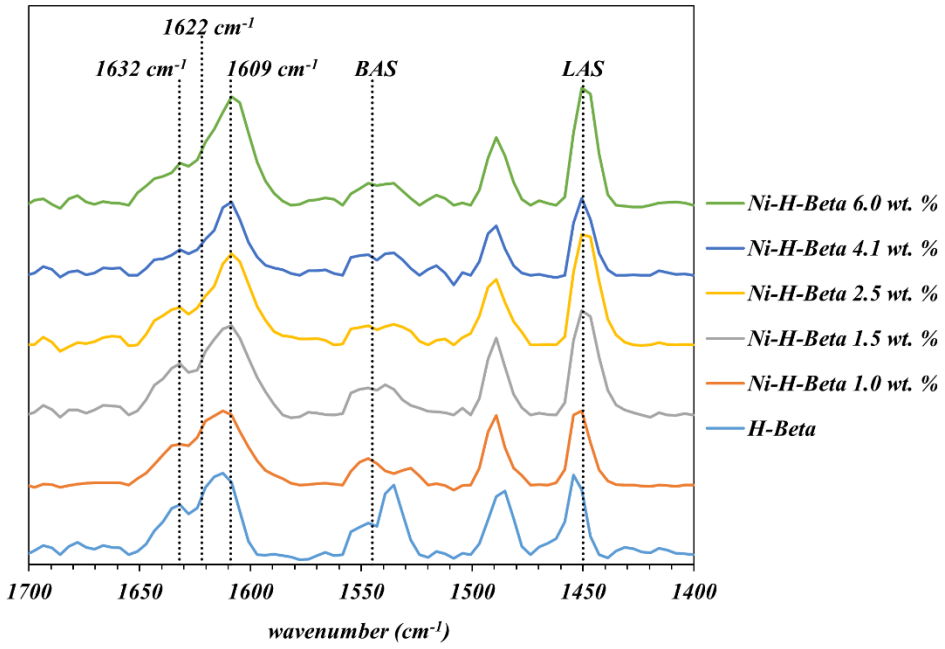

Figure 2.3. Infrared spectra in the pyridine region after pyridine adsorption over Ni-H-Beta catalysts at different nickel loading followed by evacuation at 250°C. LAS = Lewis acid sites and BAS = Brønsted acid sites.

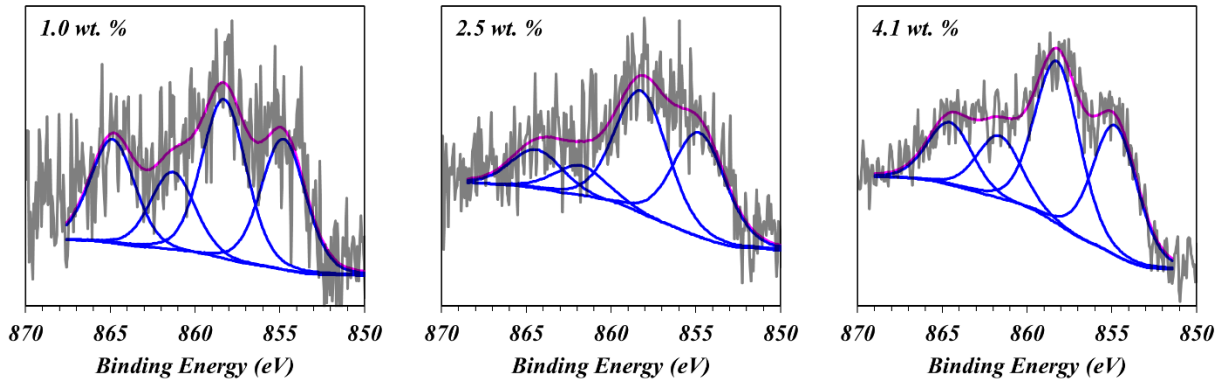

Figure 2.4. Ni $2p_{3/2}$ X-ray photoelectron spectra of Ni-H-Beta catalysts with nickel loadings of 1.5, 2.5, and 4.1 wt. %.

In our previous publication[13], we identified the presence of (111), (200), and (220) planes of fcc-NiO phases on Ni-H-Beta catalysts with nickel loadings greater than 1.0 wt. % via X-ray powder diffraction (XRD). It is believed that NiO forms at nickel loadings greater than 2.0 wt. %[2]. However, the results shown in Figure 2.4 indicate the presence of NiO phase even for

the Ni-H-Beta catalyst with nickel loading of 1.5 wt. %; lower than the minimum concentration of 2.0 wt. % previously reported in the literature for the formation of NiO. It is important to emphasize that the peak at 854.7 eV was also present on the XPS of the Ni-H-Beta catalyst with a nickel loading of 1.0 wt. % (not shown). Thus, NiO can form even at lower nickel concentrations during the impregnation of the H-Beta support with nickel nitrate followed by calcination at high temperatures. Note that the NiO crystals present on the catalyst with nickel loading of 1.0 wt. % (or lower) are small, given the absence of NiO reflections in the XRD pattern of this catalyst, according to the analysis reported in our previous publication[13]. While the NiO crystals are much lesser active than highly dispersed Ni^{2+} ions, they may contain nickel ions on their surface that promote a small extent of oligomerization reactions[7]. Also, the presence of NiO crystals may help to keep the catalyst surface clean, preventing the build-up of coke on the catalyst[13].

Table 2.3. Physicochemical properties and ethylene conversion of the Ni-H-Beta catalyst as a function of nickel loading

Nickel loading (wt. %)	$\frac{A_{858.3}}{A_{854.3}}$ (Ni^{2+}/NiO)	LAS (μmol/g)	ΔLAS (μmol/g) (Ni^{2+})	BAS (μmol/g) (H^{+})	|ΔLAS-BAS| (μmol/g)	BET (m^2/g)[1]	X (%)[2]
0.0	-	150	0	150	150	-	-
1.0	1.2	207	57	121	64	631	2.0
1.5	1.2	253	103	70	33	619	2.4
2.5	1.4	249	99	84	15	575	4.7
4.1	1.3	213	63	54	9	543	8.1
6.0	1.1	208	58	71	13	552	5.5
s.d.[3]	-	-	-	-	-	-	0.2

[1] Data obtained from[13]
[2] Experiments were performed at 100°C and 28 bar.
[3] Standard deviation for a triplicate at 100°C and 28 bar.

Table 2.3 shows the physicochemical properties of five Ni-H-Beta catalysts with different nickel loadings. We report the Ni^{2+}-to-NiO ratio (Ni^{2+}/NiO) measured using the peak areas obtained from the Ni $2p_{3/2}$ region of the XP spectra (Figure 2.4), the concentrations of LAS and

BAS measured via pyridine adsorption (Figure 2.3), the surface areas reported in our previous publication[13], and the ethylene conversion as a function of nickel loading at 100^{o}C and 28 bar.

Table 2.3 shows that the Ni^{2+}/NiO ratio for all catalysts varies between 1.1 and 1.4, with the maximum ratio observed at a nickel loading of 2.5 wt. %. This variation is small relative to the range of nickel loadings analyzed in this study and indicates that the impregnation process leads to similar distributions of cationic Ni^{2+} and NiO on the catalyst; independent of the nickel loading. In Table 2.3, the column denoted ΔLAS shows the difference in the concentration of LAS between the series of nickel-exchanged catalysts and the pristine support (nickel loading = 0.0 wt. %). The pyridine adsorption data shows that the concentration of ΔLAS increases with increasing nickel loading reaching a maximum of 103 μmol/g at a nickel loading of 1.5 wt. % (Table 2.3 – ΔLAS column). As previously discussed, the additional amount of LAS observed after nickel impregnation originates from cationic Ni^{2+} species in exchanging positions. A similar trend was reported by Martinez et al. with the maximum concentration of LAS (185 μmol/g) observed at a nickel loading of 3.8 wt. % for a series of nickel impregnated catalysts[7]. The trend shown in Table 2.3 for LAS, ΔLAS, and BAS supports the hypothesis that nickel exchanges Brønsted sites on the H-beta support and produces additional LAS with increasing nickel loading. As a result, Ni^{2+} in exchanging positions are identified as LAS, replacing acidic sites during impregnation.

2.3.3 *Effect of nickel and Brønsted sites on the ethylene oligomerization*

Table 2.3 shows the effects of nickel on ethylene conversion. The ethylene conversion first increases with nickel loading reaching a maximum value of 8.1% at 4.1 wt. % nickel, then it decreases to 5.5% at 6.0 wt. % nickel. The catalysts with nickel loadings of 4.1 and 6.0 wt. % have similar physicochemical properties, as shown in Table 2.3. At this point, it is important to note that the ethylene conversion is inversely proportional to the difference between the concentration of

LAS originated from Ni^{2+} species and the concentration of Brønsted acid sites (Table 2.3 – $|\Delta LAS - BAS|$ column). The Ni-H-Beta catalyst with nickel loading of 4.1 wt. %, which has the lowest concentration of $|\Delta\text{LAS} - \text{BAS}|$, displayed the maximum ethylene conversion among the catalysts tested in this work. Therefore, the decrease in ethylene conversion with increasing loading from 4.1 to 6.0 wt. % may be ascribed to an increase in $|\Delta\text{LAS} - \text{BAS}|$.

Based on the ethylene adsorption study, ethylene dissociates over two distinct sites over the Ni-H-Beta. The formation of a $[\text{Ni-H}]^+$ active site can be expressed by the following equation:

$$Ni^{2+} + H^+ + 2e^- \rightarrow [Ni - H]^+ \qquad (2.8)$$

In Equation 2.8, for each mole of Ni^{2+} (ΔLAS) present on the catalyst, one mole of H^+ (BAS) is consumed for the formation of the $[\text{Ni-H}]^+$ active center. The formation of the active center involves the association of a pair of electrons (Equation 2.8 – $2e^-$), which originates from the π-bond in the ethylene molecule. Therefore, we hypothesize that the formation of the active center requires coordination of an ethylene molecule over the pair Ni^{2+} and H^+. Thus, the difference between the concentrations of nickel and Brønsted sites – defined in this work by the variable $|\Delta\text{LAS} - \text{BAS}|$ – expresses the amount of either nickel or Brønsted sites *not involved* in the formation of the $[\text{Ni-H}]^+$ active center; these are inactive sites since they are not involved in the formation of the active center.

The increase in ethylene conversion with increasing nickel loading has been reported in the literature[2], including the Ni-H-Beta catalyst [7], and it is associated with the state of the nickel species on the catalyst. It is believed that isolated Ni^{2+} species (solely) in exchanging positions are the active sites for the conversion of ethylene into oligomers over nickel-exchanged acidic catalysts[11], [15], [16]. However, according to the data presented in the present work, one cannot establish a clear relationship between ΔLAS, which expresses the concentration of Ni^{2+} species,

and ethylene conversion. For instance, the concentration of ΔLAS almost doubles with increasing nickel loading from 1.0 to 1.5 wt. %. However, the ethylene conversion obtained over the two catalysts remains almost constant at approximately 2.0 %. With further increase in nickel loading from 1.5 to 2.5 wt. %, the concentration of ΔLAS remains almost constant while the ethylene conversion doubles, from 2.4 to 4.7 %.

On the other hand, the inversely proportional relationship between the ethylene conversion and $|\Delta LAS - BAS|$ suggests that the density of non-coordinated sites – Ni^{2+} or Brønsted sites not involved in the formation of $[Ni\text{-}H]^+$ active centers – reduces the conversion of ethylene over the Ni-H-Beta. Based on these results, we hypothesize that a great density of non-coordinated Ni^{2+} or H^+ sites decreases the probability of the formation of the $[Ni\text{-}H]^+$ active center. As a result, the formation of $[Ni\text{-}H]^+$ sites is favored when nickel and Brønsted species are well dispersed on the catalyst. This hypothesis is consistent with the idea that the active sites are isolated as previously postulated in the literature[11], [16], [44], [50], [51].

It is important to emphasize that the formation of $[Ni\text{-}H]^+$ centers still requires some degree of proximity between Ni^{2+} and H^+ sites. Previous studies investigated the contribution of acidity to ethylene oligomerization over nickel-exchanged inorganic catalysts. According to these studies, ethylene consumption is proportional to the density of acid sites on the catalyst[6], [22]. However, other research groups claim that catalyst acidity is detrimental to the conversion of ethylene over nickel-exchanged acidic catalysts[9], [38], [39]. They attribute the negative effect of acid sites to the build-up of strongly adsorbed hydrocarbon chains over Brønsted sites, which leads to catalyst deactivation. While the claim that acid sites can promote catalyst deactivation via coke deposition over Brønsted sites is true, Brønsted can participate in oligomerization reactions, forming an active site with nickel, as described in this work and previous studies in the literature[6], [17]. It is

important to emphasize that the catalysts tested in the present work did not suffer loss of activity after long reaction periods.

To better understand the contribution of Brønsted acidity on the formation of $[Ni\text{-}H]^+$ active centers, we investigated the effect of the Si/Al ratio on the conversion of ethylene over the Ni-H-Beta. As explained in the Experimental Section, H-Beta catalysts with Si/Al ratios of 19 and 150 were obtained from a supplier. Three additional H-Beta catalysts with Si/Al ratios of 63, 73, and 108 were produced by acid treatment of the pristine H-Beta (Si/Al = 19), as described in the Experimental Section. Note that the Si/Al ratio is an important parameter in the characterization of the catalyst acidity – directly impacting the formation of $[Ni\text{-}H]^+$ active centers and the density of inactive sites on the catalyst.

Figure 2.5 shows the X-ray powder diffraction (XRD) of the pristine H-Beta support with Si/Al ratios of 19 and 150 and Ni-H-Beta catalysts with Si/Al ratios of 19, 63, 73, 108, and 150 and nickel loadings of 1.0 and 2.5 wt. %. Comparison of the XRD patterns of the Ni-H-Beta catalysts and the H-Beta supports used in their preparation indicate no obvious changes in the intensity and position of the diffractions. This analysis suggests that the acid treatment and nickel impregnation did not cause significant changes to the crystallographic structure of the catalysts.

Table 2.4 shows the concentration of LAS, ΔLAS, BAS, and |ΔLAS-BAS| of the Ni-H-Beta catalysts with Si/Al ratios of 19, 63, 73, 108, and 150 and nickel loadings of 1.0 and 2.5 wt. % as well as the ethylene conversion and selectivity for butene (denoted as C_4), hexene (denoted as C_6), octene (denoted as C_8) over these catalysts at 100°C and 28 bar.

The trend shown in Table 2.4 indicates that the ethylene conversion decreases with increasing Si/Al ratio, in agreement with the results reported in[6], [22]. The highest ethylene conversions at both loadings were obtained with the Ni-H-Beta catalysts containing the lowest

concentration of non-coordinated sites, |ΔLAS-BAS|. Note that this result is consistent with our previous hypothesis that the presence of non-coordinated sites reduces the conversion of ethylene into higher alkenes. The results shown in Table 2.4 also suggest that the concentration of non-coordinated sites is not the only parameter that contributes to the conversion of ethylene over the Ni-H-Beta catalyst. At high Si/Al ratios, the concentration of Ni^{2+} – expressed by ΔLAS – is too small to promote the oligomerization of ethylene. This is evidenced by the lower conversions of the Ni-H-Beta catalysts with Si/Al ratios of 108 (nickel loading = 1.0 wt. %) and 150 (nickel loading = 2.5 wt. %) relative to the other Ni-H-Beta catalysts in their respective series.

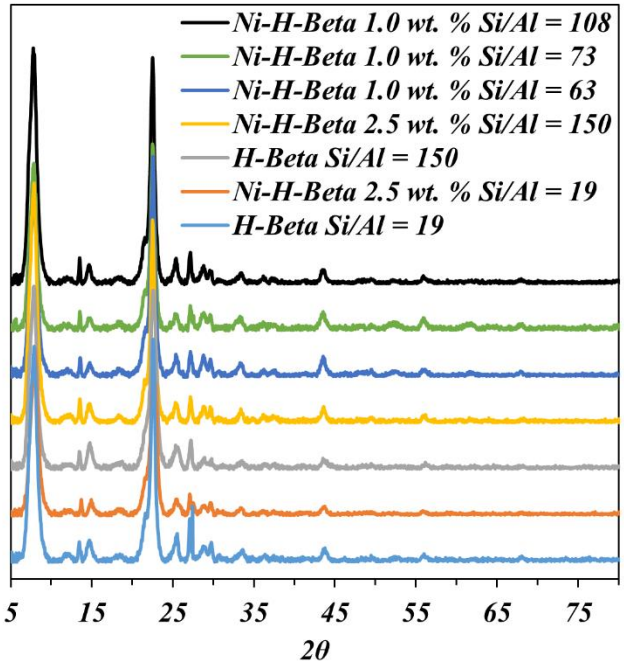

Figure 2.5. X-ray powder diffraction of the pristine H-Beta support and Ni-H-Beta catalysts at different Si/Al ratios and nickel loadings.

Table 2.4. Physicochemical properties, ethylene conversion, and product selectivity of the Ni-H-Beta catalysts at different Si/Al ratios and nickel loadings

Si/Al	Nickel loading (wt. %)	LAS (μmol/g)	ΔLAS (μmol/g)	BAS (μmol/g)	|ΔLAS-BAS| (μmol/g)	X (%)[1]	Selectivity (wt. %) C_4	C_6	C_8
63	1.0	82	63	56	7	1.1	46.2	7.1	10.2
73	1.0	100	90	68	23	0.7	41.9	7.7	11.6
108	1.0	59	41	47	5	0.5	40.7	7.1	9.4
12.5	2.5	249	100	84	16	3.8	39.9	28.9	17.8
19	2.5	210	158	96	62	2.7	42.5	28.3	19.3
150	2.5	58	29	58	29	0.5	45.2	21.8	19.8
s.d.[2]	-	-	-	-	-	0.2	6.3	3.9	0.3

[1] Experiments were performed at 100°C and 28 bar.
[2] Standard deviation for a triplicate at 100°C and 28 bar.

The product selectivity for C_4, C_6, and C_8 remained approximately unchanged with increasing Si/Al ratio for both series of nickel-exchanged catalysts, indicating that the change in the density of non-coordinated sites exclusively affects ethylene conversion, but not the overall reaction pathway and mechanism. Therefore, the effect of Brønsted site density on the reaction is associated with the number of active centers available for reaction, rather than the nature of the coordination between ethylene, Ni^{2+}, and Brønsted sites. Therefore, despite the varied Si/Al ratio, the nature of active sites present in the series of nickel-exchanged catalysts prepared in the present work is the same.

Based on the results, both Ni^{2+} and Brønsted sites are required for the conversion of ethylene during the ethylene oligomerization over Ni-H-Beta catalysts. However, low densities of Ni^{2+} sites and high densities of Brønsted sites decrease the probability for the formation of $[Ni\text{-}H]^+$ centers. The finds of this work are consistent with ***Mechanism B*** (Figure 2.1), in which ethylene dissociates over two sites formed by the combination of H^+ and Ni^{2+} species. As shown in Equation 2.7, we hypothesize that ethylene donates a pair of electrons to stabilize the excess of

positive charges present in both ions (H^+ and Ni^{2+}) to forming the $[Ni\text{-}H]^+$ active center. Once the adsorbed species desorb as high alkenes, the ions restore their original form to H^+ and Ni^{2+}.

2.4 CONCLUSION

The present study employs a series of catalyst characterization technics combined with kinetic data to investigate the role of nickel and Brønsted sites on ethylene oligomerization over Ni-H-Beta catalysts. The ethylene sorption study suggests that ethylene dissociates over two distinct active sites on the Ni-H-Beta. Pyridine sorption results show that Ni^{2+} species are identified as LAS and nickel exchanges Brønsted sites on the catalyst as previously reported in the literature[7]. Analysis of the ethylene conversion over a series of nickel-exchanged H-Beta catalysts indicates that the ethylene conversion is inversely proportional to the concentration of non-coordinated sites – defined in the present work by the difference between the concentration of Ni^{2+} and Brønsted sites. Non-coordinated sites are either solely Ni^{2+} or H^+ species. The presence of non-coordinated Ni^{2+} or Brønsted sites decreases the probability for the formation of $[Ni\text{-}H]^+$ active centers. Based on the experimental evidence, we hypothesize that $[Ni\text{-}H]^+$ sites have to be in isolated positions on the catalyst surface. Investigation of the effect of Si/Al ratio on catalyst activity suggests that Brønsted sites are required for the formation of $[Ni\text{-}H]^+$ active centers in agreement with literature reports. Finally, the product selectivity remained approximately constant with Si/Al ratio, suggesting that the presence of non-coordinated sites does not affect the mechanism or pathway involved in the conversion of ethylene into higher alkenes.

Chapter 3. KINETICS OF ETHYLENE OLIGOMERIZATION OVER NI-H-BETA CATALYSTS[3,4]

Abstract

We report the kinetics of ethylene oligomerization over the Ni-H-Beta for temperatures ranging between 50 and 100°C and pressures ranging between 5 and 28 atm. According to our results, the apparent activation energies involved in the formation of butene, hexene, and octene are 44, 78, and 60 kJ.mol^{-1}, respectively. The lower activation energy for butene formation relative to hexene and octene is due to the participation of butene in chain-growth reactions. Analysis of the reaction order indicates that participation of butene in chain-growth reactions takes place via desorption followed by re-adsorption of butene on the catalyst. The results also indicate that hexene undergoes a similar process. In the present study, we refer to the pathway involving co-oligomerization of butene and hexene as *"cascade co-oligomerization"*. Based on these findings, we proposed a reaction network and modeled reaction rate expressions for ethylene consumption and butene, hexene, and octene formation based on the Langmuir-Hinshelwood-Hougen-Watson kinetics. We calculated the kinetic parameters involved in the reaction network proposed and found evidence that the formation of octene proceeds mainly via the *"cascade co-oligomerization"* of re-adsorbed butene with ethylene.

Keywords: Ethylene Oligomerization; Langmuir-Hinshelwood-Hougen-Watson kinetics; Ni-H-Beta; Butene; Co-oligomerization; Cascade reactions.

[3] Manuscript under review at Journal of Catalysis, Gabriel V. S. Seufitelli, Jason J. W. Park, Phuong N. Tran, Anthony Dichiara, Fernando L. P. Resende, Rick Gustafson.

[4] Work presented at the American Institute of Chemical Engineers (AIChE) Annual Meeting in 2018.

3.1 INTRODUCTION

The industrial production of alkenes, which serve as important building blocks for commonly used chemicals, is normally achieved by steam cracking of naphtha. However, this scenario has been affected by the continuous discovery of large reserves of shale gas in the U.S. in the last 10 years[15], [31], [62]. Shale gas contains ethane, which can also undergo steam reforming to alkenes, leading to competition between ethane and naphtha for the production of these chemicals[15], [31]. While ethane from shale gas is a cheaper feedstock for steam reforming than naphtha, its C_{4+} yields are substantially lower than those obtained from cracking of naphtha[31]. Because ethylene can be readily produced via steam reforming of ethane[16], alternative routes have been considered to convert ethylene into C_{4+} building blocks. Among these processes, ethylene oligomerization shows promise for the conversion of abundant ethylene into C_{4+} alkenes with yields that justify the implementation of this process at large scale. Shell developed one of the most prominent ethylene oligomerization processes, denominated Shell Higher Olefin Process (SHOP)[32]. The process employs a nickel-ligand homogeneous catalyst capable of achieving high yields and selectivities to higher alkenes[32], [63]. Other companies such as Union Carbide and Phillips Petroleum sought similar routes employing other metal-ligand homogeneous catalysts to convert ethylene into higher alkenes[64].

However, the aforementioned processes use homogeneous catalysts mixed with organic solvents, such as toluene, which are toxic and associated with environmental implications. Homogeneous catalysts require expensive downstream processing to purify the final product. Thus there is a need for more environmentally-friendly catalysts, which can be easily recovered from the process effluent[65]. In this context, solid catalysts have been proposed and successfully employed to convert ethylene into alkenes. Very recently, LanzaTech in collaboration with the

Pacific Northwest National Laboratory (PNNL) designed an ethylene oligomerization process using Ni-H-Beta as a catalyst[66]. The Ni-H-Beta was initially proposed for the ethylene oligomerization by Martinez et al. in 2013 and the authors reported high yields to liquid alkenes under mild conditions[7]. A central discussion surrounding the Ni-H-Beta involves the nature of its active center, with several reports addressing this topic[10], [14]–[16], [18].

Even though previous publications have focused on the nature of the active center involved in the ethylene oligomerization over the Ni-H-Beta, only a few studies focused on kinetic models for the ethylene oligomerization over nickel-based solid catalysts. In the 80's and 90's, a few publications addressed the kinetics of ethylene oligomerization over Ni-Y, Ni-sulfated alumina, and Ni-exchange amorphous silica-alumina catalysts[19], [22], [52], [67]. However, with the development of new catalysts, such as Ni-MCM-41, Ni-AlSBA-15, and Ni-H-Beta[7], [18], [40], which are less susceptible to deactivation and able to oligomerize ethylene to higher alkenes under mild conditions, further kinetic modeling is required. In 2015, Toch et al. used a Single-Event MicroKinetic (SEMK) model to study the ethylene oligomerization over Ni-SiO_2-Al_2O_3[34]. Recently, Toch used the same technique to model the ethylene oligomerization over the Ni-H-Beta[23]. The authors proposed to maximize gasoline and propene yields by operating at temperatures higher than 170^{o}C and ethylene inlet pressures up to 4 atm. Under these conditions, reactions other than oligomerization, such as cracking, take place, leading to the substantial formation of odd carbon number products, such as propene[23].

The overall objective of this research is to model the kinetics of ethylene oligomerization over the Ni-H-Beta using the Langmuir-Hinshelwood-Hougen-Watson (LHHW) kinetics focused on the oligomerization of ethylene into butene, hexene, and octene. To achieve significant yields in this product range and minimize side reactions, such as cracking, we performed the ethylene

oligomerization over the Ni-H-Beta under mild temperatures ranging from 50 to 100ºC and ethylene inlet partial pressures ranging between 5 and 28 atm; conditions which have been previously screened by our research group for ethylene oligomerization[13], [24]–[26].

3.2 EXPERIMENTAL METHOD

3.2.1 *Catalyst synthesis*

NH_4-Beta zeolite (SiO_2/Al_2O_3 = 25) was purchased from Zeolyst International (product number: CP814E) and used as the catalyst support. The nickel-impregnated catalyst was produced by contact with a 0.51 M aqueous solutions of $Ni(NO_3)_2$ purchased from Sigma-Aldrich (purity: 99.999%). The impregnation process led to a Ni-H-Beta catalyst with a nickel loading of 4.1 wt. %. The Ni-H-Beta catalyst was synthesized according to a procedure described in previous publications from our research group[13], [24]–[26].

3.2.2 *Ethylene oligomerization experiments*

The ethylene oligomerization was performed in a fixed-bed reactor (FBR) shown in Figure 3.1. Prior to the reaction, we loaded 0.25 g of catalyst inside the FBR. Quartz wool (ACROS Organics) was used as packing material to secure the catalyst in place. Two thermocouples, one located at the center of the catalyst bed (Figure 3.1 – TC1) and another one located on top of the catalyst bed (Figure 3.1 – TC2), were used to control the reactor temperature and measure the temperature gradient across the catalyst bed, respectively. The temperature difference between the radial center and the top of the catalyst bed remained below 5ºC for all experiments. The catalyst bed used in the experiments had a diameter of 1 cm and a height of 0.7 cm. We controlled the pressure of the system with a dome loaded back-pressure regulator (Figure 3.1 – BPR, ZF1 series, Equilibar). The reactor inlet consisted of pure ethylene. In order to quantify the molar flow rate of

products leaving the reactor, we mixed the reactor outlet stream (Figure 3.1 – Mixing point) with nitrogen (Figure 3.1 – N_2, purity: 99.998%, Praxair), which was used as internal standard (the nitrogen was only added after the reactor in order to prevent dilution of the ethylene during the reaction). The mixture was fed continuously to a GC-2014 (Shimadzu) via a 6-way valve mounted with a 1 ml sample loop. The GC-2014 was equipped with a capillary column (Agilent 19091-QO4 - ID=0.32 mm, L=30 m and film=20 µm), coupled with FID and TCD detectors.

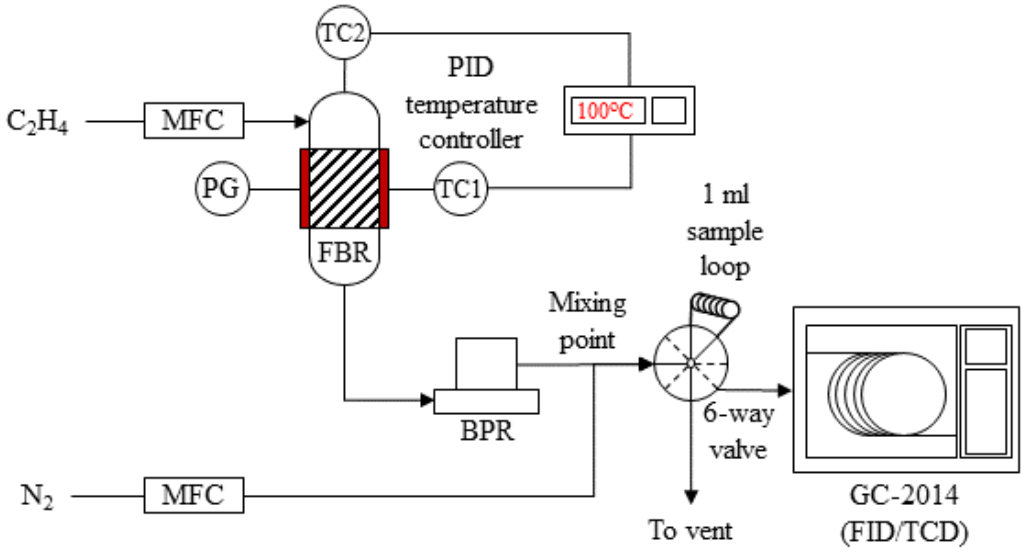

Figure 3.1. Process flow diagram of the fixed-bed reactor used in the kinetic study.

Fresh Ni-H-Beta (nickel loading = 4.1 wt. %) was pretreated overnight at 300°C under nitrogen flow. After pretreatment, we decreased the reactor temperature to the reaction set-point and pressurized the reactor to the pressure set-point with pure ethylene (Figure 3.1 – C_2H_4, purity = 99.5%, Praxair). A flow rate of 700 ml/min was used to pressurize the reactor so as to minimize the extent of chemical reactions at this point. After the reactor pressure reached the set-point, we decreased the ethylene flow rate from 700 ml/min to the reaction flow rate set-point and started the GC acquisition. The ethylene flow rate for most of the experiments reported in the present work was set to 160 ml/min, with few exceptions where we used a variable ethylene flow rate to study the effect of weight hourly space velocity (WHSV) on the reaction. In those cases, we varied

the flow rate from 50 ml/min to 200 ml/min. We measured the outlet composition from the reactor until the composition of the species reached steady-state. Mass balance closure remained within ±4% for all experiments reported in this work. We calculated the ethylene consumption rate and products formation rate according to the following equation:

$$\frac{dF_i}{dW} = r_i \tag{3.1}$$

Where r_i is the consumption or production rate (in g.g of cat.$^{-1}$.h^{-1}), F_i is the mass flow rate of species leaving the reactor (in g.h^{-1}), and W is the mass of catalyst (in g of cat.). The reaction rates were measured under steady-state conditions with a negligible extent of catalyst deactivation. Figure S1-A shows a sample plot of the ethylene conversion as a function of time-on-stream. The experimental reaction rates were calculated by accounting for the total amount of products formed over the reaction time and mass of fresh catalyst. The ethylene conversion was calculated based on the total quantification of products (in g.min^{-1}) according to Equation 3.2:

$$X = \frac{F_{products}}{F_{a0}} \tag{3.2}$$

Where X is the ethylene conversion, F_{a0} is the ethylene mass feed rate (g.min^{-1}), and $F_{products}$ is the sum of mass flow rate of all products downstream of the reactor (g.min^{-1}). Because a great portion of the reactor effluent consisted of ethylene (molar fraction > 90 %), small errors in the measurement of the ethylene molar fraction led to great uncertainty in ethylene consumption rates. Thus, we quantified the ethylene conversion based on the quantification of products. This approach is valid due to the small mass balance error obtained in the present work. We used Equation 3 to calculate the product selectivity, where $S_i\ (wt.\%)$ is the selectivity for species i in wt. %:

$$S_i\ (wt.\%) = 100\% \times \left(\frac{mass\ of\ species\ i\ (grams)}{total\ mass\ of\ products\ (grams)}\right) \tag{3.3}$$

3.2.3 *Kinetic model development*

3.2.3.1 Reaction order

The reaction order of a heterogeneous catalytic reaction can be defined as follows[68]:

$$n_{y,x} = \frac{\partial \ln r_y}{\partial \ln [C]} \tag{3.4}$$

where $n_{y,x}$ is the reaction order of component y with respect to component x, r_y is the reaction rate of consumption or production of component y (in g.g of cat.$^{-1}$.h^{-1}), and $[C]$ is the concentration of component x. The reaction order is a function of temperature and pressure and it is only valid under the conditions for which the data was collected.

3.2.3.2 Reaction rates

The reaction rate expressions were developed according to the reaction network proposed based on the analysis of the experimental results obtained in the present work (discussed later). We used the Langmuir-Hinshelwood-Watson-Hougen (LHHW) kinetics, a common model that allows for the development of reaction rate expressions for elementary steps in heterogeneous catalysis, to develop reaction rate expressions, assuming the chain-growth steps as reaction limiting steps (RLS); the adsorption and desorption steps are in *quasi-equilibrium*. We show later that this assumption is valid under the conditions employed in this study.

The relationship between the ratios of adsorption and desorption constants can be expressed by the sorption parameter K_{eq} (in atm^{-1}):

$$K_{eq} = \frac{k^+}{k^-} \tag{3.5}$$

Where k^+ and k^- (both in atm^{-1}) are the adsorption and desorption constants, respectively.

The equations associated with the reaction network proposed in the present study are presented later in Sections 3.3.2 and 3.3.3 when we discuss the kinetic model. Kinetic parameters were estimated by minimizing the following objective function:

$$f_{min} = \sum_{j=1}^{n} \sum_{i=1}^{s} \left(r_{i,j\ (exp.)} - r_{i,j\ (calc.)} \right)^2 \quad (3.6)$$

In Equation 3.6, $r_{i,j\ (exp.)}$ and $r_{i,j\ (calc.)}$ are the experimental and calculated reaction rates (in g.g of cat.$^{-1}$.h^{-1}), respectively, n is the number of experimental data points, and s is the number of species included in the kinetic model. The model is presented in more detail throughout this Chapter. It accounts for the rate of ethylene (abbreviated as C_2) consumption and butene (abbreviated as C_4), hexene (abbreviated as C_6), and octene (abbreviated as C_8) formation. High molecular weight alkenes, such as decene (abbreviated as C_{10}) and higher alkenes (abbreviated as C_{10+}) were not included because their formation rates did not follow a clear trend with respect to the ethylene partial pressure, which is the independent variable chosen in the present kinetic study (Figure S1-B - Supplementary Information). Replicates at 6.8 and 28 atm, 100^{o}C, and WHSV = 48.4 g ethylene.g cat.$^{-1}$.h^{-1} were used to calculate the standard deviations reported in the manuscript (Table S1 – Appendix A). We used the *Excel Solver* tool to fit the kinetic parameters of the model.

The kinetic model presented in this work was fine-tuned by assessing the sensitivity of the reaction rates relative to the parameters involved in the model. Details on the sensitivity analysis are presented later in the discussion of the results. We estimated the confidence intervals for the calculated reaction rates and kinetic parameters by applying a bootstrap method[69]. We generated a total of 100 data sets by resampling the modeled data and assuming the model error is randomly distributed among the calculated rates. The error was calculated according to the following equation:

$$\varepsilon_{i,j} = r_{i,j\ (exp.)} - R_{i,j\ (calc.)} \quad (3.7)$$

In the above equation, $\varepsilon_{i,j}$, $r_{i,j\ (exp.)}$, and $R_{i,j\ (calc.)}$ are the model error, experimental reaction rate, and calculated reaction rate, respectively, for species i at condition j (reactor temperature and ethylene partial pressure at steady-state). Therefore, the error $\varepsilon_{i,j}$ for species *i* at

condition *j* is the difference between calculated and experimental rates at condition *j*. A data set with size $i \times j$ was obtained from Equation 3.7. The rates used to calculate the model error are given in g.g of cat.$^{-1}$.h^{-1}. A random function was used to determine the error attributed to each resampled data point (*i.e.*, each rate of species *i* at condition *j*), where the ethylene partial pressure at steady-state was selected as the independent variable. The reaction rates were resampled according to the following equation:

$$r_{i,j} = r_{i,j\ (calc.)} + \varepsilon_r \tag{3.8}$$

Where $r_{i,j\ (calc.)}$ is the original calculated reaction rate of species i at condition *j* (according to the kinetic model), ε_r is the error randomly chosen from the data set of errors calculated according to Equation 3.7 (data set with size $i \times j$), and $r_{i,j}$ is the resampled reaction rate given at the same condition *j* as $r_{i,j\ (calc.)}$. Note that conditions for $R_{i,j\ (calc.)}$ in ε_r (Equation 3.7) and $r_{i,j\ (calc.)}$ (in Equation 3.8) are different. After generating the resampled data sets, we recalculated the kinetic parameters for each data set by minimizing the objective function given by Equation 3.6. This process generated a data set of 100 values for each parameter. The uncertainty of the optimized parameters and calculated reaction rates were determined with a confidence level of 95%.

3.3 RESULTS AND DISCUSSION

3.3.1 *Kinetic parameters assessment*

3.3.1.1 Effect of weight hourly space velocity (WHSV)

We assessed the optimum range of WHSV to study the kinetics of ethylene oligomerization over the Ni-H-Beta. Figure 3.2 shows the ethylene conversion as a function of WHSV^{-1}. Ethylene conversion increases linearly with WHSV^{-1} for values of WHSVs between 36.5 and 72.9 g of ethylene.g cat.$^{-1}$.h^{-1} (WHSV^{-1} between 0.014 and 0.027 g cat.h.g of ethylene^{-1}). According to

Equation 3.1, this linear relationship suggests that the rates of ethylene consumption and product formation are constant throughout the length of the catalyst bed for this range of WHSVs. In other words, the reactor operates under differential regime. Therefore, ethylene consumption and alkene production rates can be approximated by Equations 3.9 and 3.10, respectively:

$$\frac{F_{a0}X}{\Delta W} = -r_{C_2H_4} \tag{3.9}$$

$$\frac{F_i}{\Delta W} = r_i \tag{3.10}$$

where F_{a0} is the inlet mass flow rate of ethylene (in g of ethylene.h^{-1}), ΔW is the mass of catalyst (in g of cat.), X is the ethylene conversion, $-r_{C_2H_4}$ is the ethylene consumption rate (in g of ethylene.g of cat.$^{-1}$.h^{-1}), r_i is the formation rate of product i (in g of product i.g of cat.$^{-1}$.h^{-1}), and F_i is the mass flow rate of product i downstream of the reactor (in g of product i.h^{-1}).

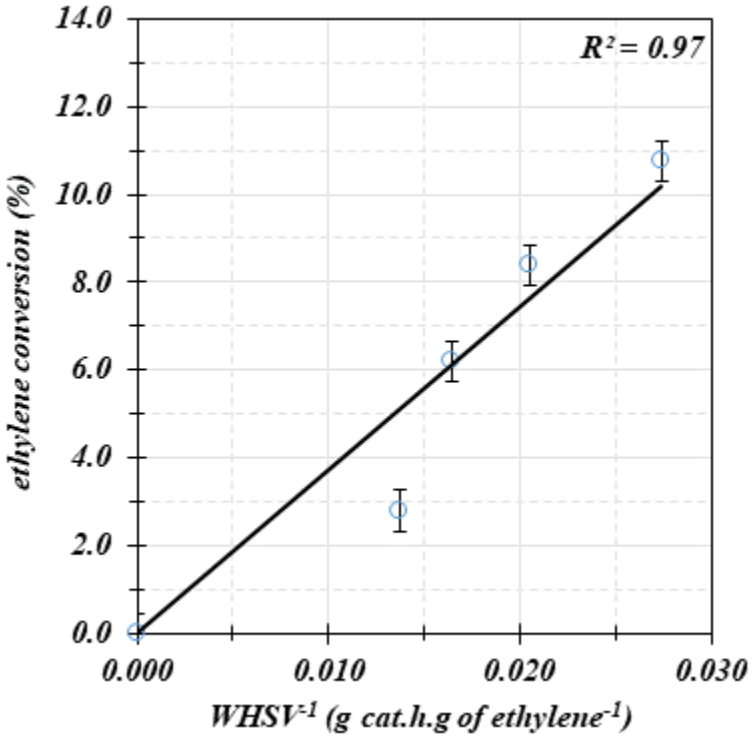

Figure 3.2. Ethylene conversion (%) as a function of the inverse of WHSV (g cat.h.g of ethylene^{-1}) at P = 28 atm and T = 100^{o}C. Solid line shows the linear fitting of ethylene conversion as a function of the WHSV^{-1}.

The linear fitting shown in Figure 3.2 (solid line, R^2 = 0.92) validates the differential behavior of the reaction system. For WHSVs lower than 36.5 g of ethylene.g $cat^{-1}.h^{-1}$ (not shown in Figure 3.2), the reactor operates under integral mode. In this case, $-r_{C_2H_4}$ and r_i are not constant across the catalyst bed and Equations 3.9 and 3.10 are no longer valid under such conditions. This occurs because the ethylene concentration throughout the catalyst bed is not constant at low WHSV, due to the high rates of ethylene consumption at low space velocities[70]. Later we show that the model proposed in the present work is able to fit the data shown in Figure 3.2 under various WHSVs.

3.3.1.2 Effect of temperature

Figure 3.3 shows the selectivity for C_4, C_6, C_8, and C_{10} at 28 atm and temperatures ranging from 50 to 200°C. As the temperature increases from 50 to 100°C, there is a decrease in butene selectivity from 50.0 to 28.5 wt. %. This decrease suggests that chain-growth rates increase with increasing temperature at the expense of butenes, which are converted into higher molecular weight hydrocarbons given the increase in selectivity for C_6 and C_8. On the other hand, for temperatures above 100°C, butene selectivity reaches a plateau. This indicates that chain growth affects longer molecules, such as hexene and octene, to a greater extent relative to butenes above 100°C. However, the selectivity to hexene and octene also reaches a plateau above 100°C.

Figure 3.4 shows the Arrhenius plot for the ethylene oligomerization over the Ni-H-Beta at 28 atm and temperatures ranging from 50 to 200°C. The solid lines show the linear regression of the experimental points. According to the Arrhenius plot, the slope of the fitted line decreases with increasing temperature for temperatures greater than 100°C. The change in the slope of the Arrhenius plot shown in Figure 3.4 might be associated either with a mass transfer limitation effect or a change in the reaction mechanism above 100°C, consistent with the trend shown in Figure 3.3.

We used pure ethylene for the oligomerization experiments. Therefore, ethylene transport from the gas-phase to the outer surface of the catalyst particles proceeds mainly via bulk fluid motion. However, internal mass transfer limitation of ethylene is still possible since the ethylene molecules need to reach the active sites inside the catalyst pores, which contains products diffusing out.

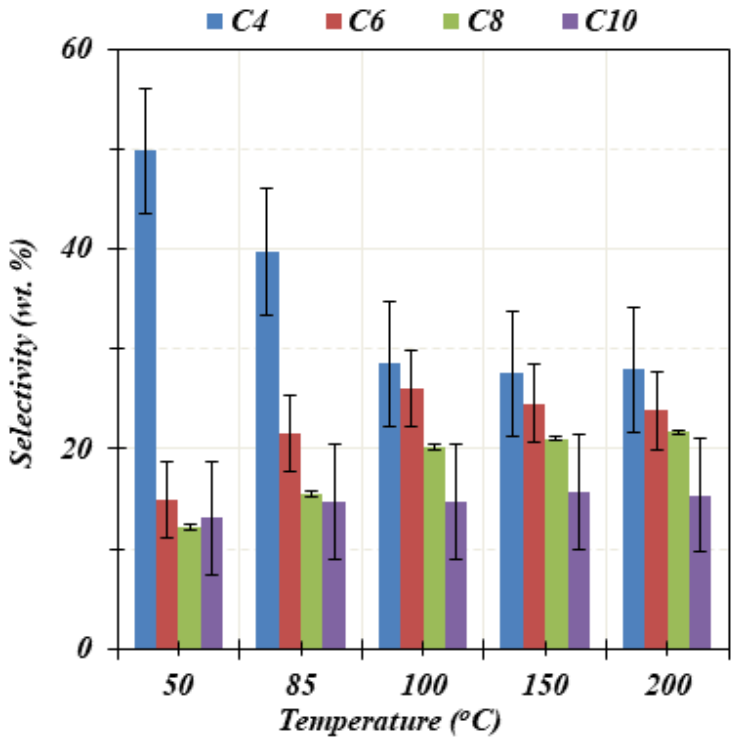

Figure 3.3. Product selectivity given in wt. % for products ranging from C_4 to C_{10} under different temperatures.

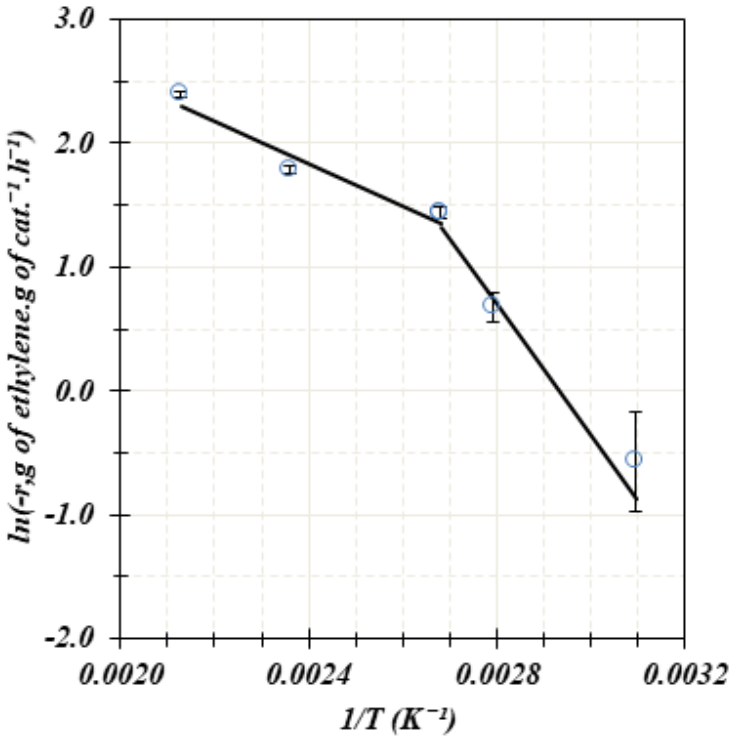

Figure 3.4. Arrhenius plot for the ethylene oligomerization over the Ni-H-Beta catalyst for temperatures ranging from 50 to 200ºC at 28 atm (ethylene partial pressure) and WHSV of 48.4 g ethylene g cat.$^{-1}$ h^{-1}.

Therefore, the counter diffusion of products and ethylene can potentially create a concentration gradient inside the pores of the catalyst. To assess the existence of an internal diffusion limitation regime, we used the Weisz-Prater criterion[70] presented in Equation 3.11:

$$C_{wp} = \frac{-r_{ethylene}\rho_c R^2}{D_e C_{ethylene}} \tag{3.11}$$

Where $-r_{ethylene}$ is the rate of ethylene consumption (in g of ethylene.kg of cat.$^{-1}$.h^{-1}), ρ_c is the density of the catalyst (in kg of cat.m^{-3}), R is the catalyst particle radius (in m), D_e is the effective diffusivity (in m^2.h^{-1}), and $C_{ethylene}$ is the concentration ethylene on the outer surface of the catalyst particle (in g of ethylene.m^{-3}). If C_{wp} is less than unity, internal diffusion limitations are negligible. We approximated the ethylene concentration at the outer surface of the catalyst by the concentration of ethylene in the bulk of the gas assuming ideal gas. We used the Chapman-Enskog[71] equation to calculate the diffusivity coefficient based on an approximation of ethylene

diffusing into a mixture of 1-butene, 1-hexene, and 1-octene. More details about the diffusion model can be found in Section 2 of Appendix A. Results and parameters used to calculate the diffusivities are shown in Table S2 (Section 2 – Appendix A).

Table S2 (Section 2 – Appendix A) shows that C_{wp} is much lower than unity for all temperatures, including the temperatures where the change in the slope is observed (Figure 3.4). This analysis indicates that the reaction is not limited by diffusion of ethylene inside the pores of the Ni-H-Beta for any of the temperatures studied in the present study. Therefore, based on the change in product selectivity shown in Figure 3, we suggest a change in reaction mechanism driven by a decrease in the conversion of butene into hexene and octene above 100°C. Recently, Ehrmaier et al. reported the oligomerization of linear butenes into *n*-octenes and methylheptene over a Ca-Ni-LTA catalyst[72]. According to the authors, nickel sites are responsible for the conversion of butene into high molecular weight products. Isolated Brønsted sites and Ni^{+}-H sites can also catalyze the conversion of butenes into hexene and octene[23], [73]. The Ni-H-Beta used in the present work possesses both sites. Therefore, the conversion of butene into hexene and octene can take place via multiple simultaneous pathways over the Ni-H-Beta, including both Ni and Brønsted sites.

Our hypothesis is that butene is consumed to form hexenes and octene, which is supported by the plateau in butene selectivity above 100°C as shown in Figure 3.3. To validate our hypothesis, we performed the ethylene adsorption over the Ni-H-Beta at 1 atm and -80°C. At these conditions, reaction rates are almost negligible. Even so, trace amounts of products were identified after ethylene adsorption over the Ni-H-Beta. Figure S3 (Section 3 – Appendix A) shows the GC-FID spectrum of the gas analyzed after the ethylene adsorption. The result shows that peaks for C_4 are substantially lower than the ones for C_6, C_8, and C_{10}. This result is unexpected, since the

transport of long-chain molecules (*i.e.*, C_8 and C_{10}) from the catalyst surface to the gas is slower than the transport of butene, especially at low temperatures. One explanation for the low concentration of butene among the gaseous products is its re-adsorption over nickel and Brønsted sites. Therefore, butene can undergo re-adsorption on the catalyst and eventually participate as a co-reactant in chain-growth reactions with ethylene. In the following discussion, we limited the kinetic study to the temperature range at which butene is consumed to form hexenes and octenes. For this reason, we only considered data collected between 50 and 100°C for the development of the kinetic model.

Table 3.1. Apparent activation energies for consumption of ethylene and formation of butene, hexene, and octene in the range of 50 to 100°C (lines with highest slope in Figure 3.4 and Figure S4)

	E_{app} (kJ.mol^{-1})		
	average	lower end[1]	upper end[1]
ethylene consumption	44	43	45
butene formation	44	42	46
hexene formation	78	74	82
octene formation	60	59	61

[1] Calculated by resampling the data using the bootstrap method with a 95% confidence level.

Table 3.1 lists the apparent activation energies (E_{app}) calculated from the linear regression of data points shown in Figure 3.4 and Figure S4 (Section 3 – Appendix A) for temperatures ranging from 50 to 100°C. We calculated apparent activation energies for ethylene consumption and butene, hexene, and octene formation of 44, 44, 78, and 60 kJ.mol^{-1}, respectively. Note that the calculated range of activation energy for butene formation is significantly lower than the ones for hexene and octene formation. Brogaard and Olsbye[15] calculated an intrinsic enthalpy of activation of 77 kJ.mol^{-1} for the conversion of ethylene into butene over a nickel-exchanged H-SSZ-24 zeolite, at 120°C and 1 atm, via density functional theory (DFT) calculations. As noted by the authors, the use of a nickel-exchanged H-SSZ-24 zeolite as model catalyst for simulations allows direct comparison with the Ni-H-Beta because both catalysts contain straight channels with

rings formed by 12 T atoms. More recently, Brogaard et al.[14] reported an experimental activation energy of 33±3 and 37±4 kJ.mol^{-1} involved in the dimerization of ethylene (selectivity > 98%) at 150^{o}C and pressures of 4 and 26 atm, respectively. While the activation energy for butene formation calculated in the present work is much lower than the intrinsic value obtained by Brogaard and Olsbye via DFT calculations, our value agrees with the experimental activation energies recently reported by the same author for butene formation.

Toch et al. reported the overall E_{app} of 76[23] and 74[34] kJ.mol^{-1} for the ethylene oligomerization over nickel-exchanged amorphous silica-alumina and Ni-H-Beta catalysts, respectively. In both cases, the ethylene oligomerization was highly selective towards butene (selectivity > 80 wt. %). The activation energy for ethylene consumption obtained in the present work is lower than the ones reported by Toch et al. This difference is due to the consumption of butene by reaction observed in the present work, which leads to a lower butene selectivity (28.5 wt. % at 100^{o}C and 28 atm).

3.3.1.3 Effect of pressure

In addition to the effect of reaction temperature, we investigated the effect of ethylene partial pressure and products' partial pressure on the consumption of ethylene and the formation of butene, hexene, and octene. According to Equation 3.4, the slopes of the fitted linear functions shown in Figure 3.5 correspond to the reaction order of ethylene consumption and butene, hexene, and octene formation with respect to the ethylene partial pressure and products' partial pressure. Note that the dependence of hexene and octene formation relative to the product's partial pressure is merely an observed dependence since the true reaction order can only be obtained by co-feeding ethylene with these products at varying partial pressures.

The linear fitting of the experimental data shown in Figure 3.5-A indicates a reaction order of 1.7 for the consumption of ethylene relative to the ethylene partial pressure (from 5 to 28 atm) at 100^{o}C. Henry et al. found a second-order relationship for the consumption of ethylene relative to the ethylene partial pressure at 120^{o}C and pressures ranging from 11 to 25 atm[10]. Therefore, a second-order relationship is consistent with the value obtained in the present work under similar conditions.

In addition to the effect of ethylene partial pressure on ethylene consumption, we investigated the effect of ethylene partial pressure on the formation rates of butene, hexene, and octene. We also considered the effect of the concentration of each product on the rates of formation of the other products. Figure 3.5-B, Figure 3.5-C, and Figure 3.5-D show *log-log* plots of the rates of butene, hexene, and octene formation as a function of the partial pressure of species involved in their formations (ethylene, butene, and hexene). Figure 3.5-B shows a reaction order of 1.3 for the rate of butene formation relative to the ethylene partial pressure. According to literature reports[10], [14], a second-order relationship is expected for the formation of butene with respect to ethylene. As pointed by Henry et al.[10], the reaction order for butene formation relative to ethylene has mechanistic implications. The authors showed that a higher reaction order of 2.0 is expected for microporous catalysts, while a lower reaction order of 1.5 is expected for mesoporous catalysts, such as $NiSO_4$-Al_2O_3[10]. According to the authors, micropores provide higher stability to alkyl chains as opposed to mesopores. As shown in our previous publication[13], the Ni-H-Beta catalyst used in the present study contains both types of pore structures (micropores and mesopores), which could explain the low reaction order observed for the formation of butene. We note that the consumption of butene, as discussed in section 3.3.1.2, can also result in a low reaction

order for butene formation, providing evidence of an increase in butene consumption with increasing ethylene partial pressure.

Figure 3.5-C shows that the log of hexene formation rate increases faster with the log of ethylene partial pressure than it does with the log of butene partial pressure. The slopes of the fitted linear functions suggest reaction orders of 2.2 and 1.0 for the formation of hexene relative to ethylene and butene partial pressures, respectively. The reaction order for the formation of hexene relative to ethylene calculated in the present work agrees with the value reported by Brogaard et al.[14].

A possible pathway for the formation of butene and hexene involves a series of ethylene coordination-insertion steps. This way, the reaction order for these products can be expressed by the number of ethylene molecules (repeating units) involved in the chain-growth process. An additional route for the formation of hexene may involve the co-oligomerization of ethylene with re-adsorbed butene on the catalyst, thus establishing a first-order dependency relative to butene partial pressure.

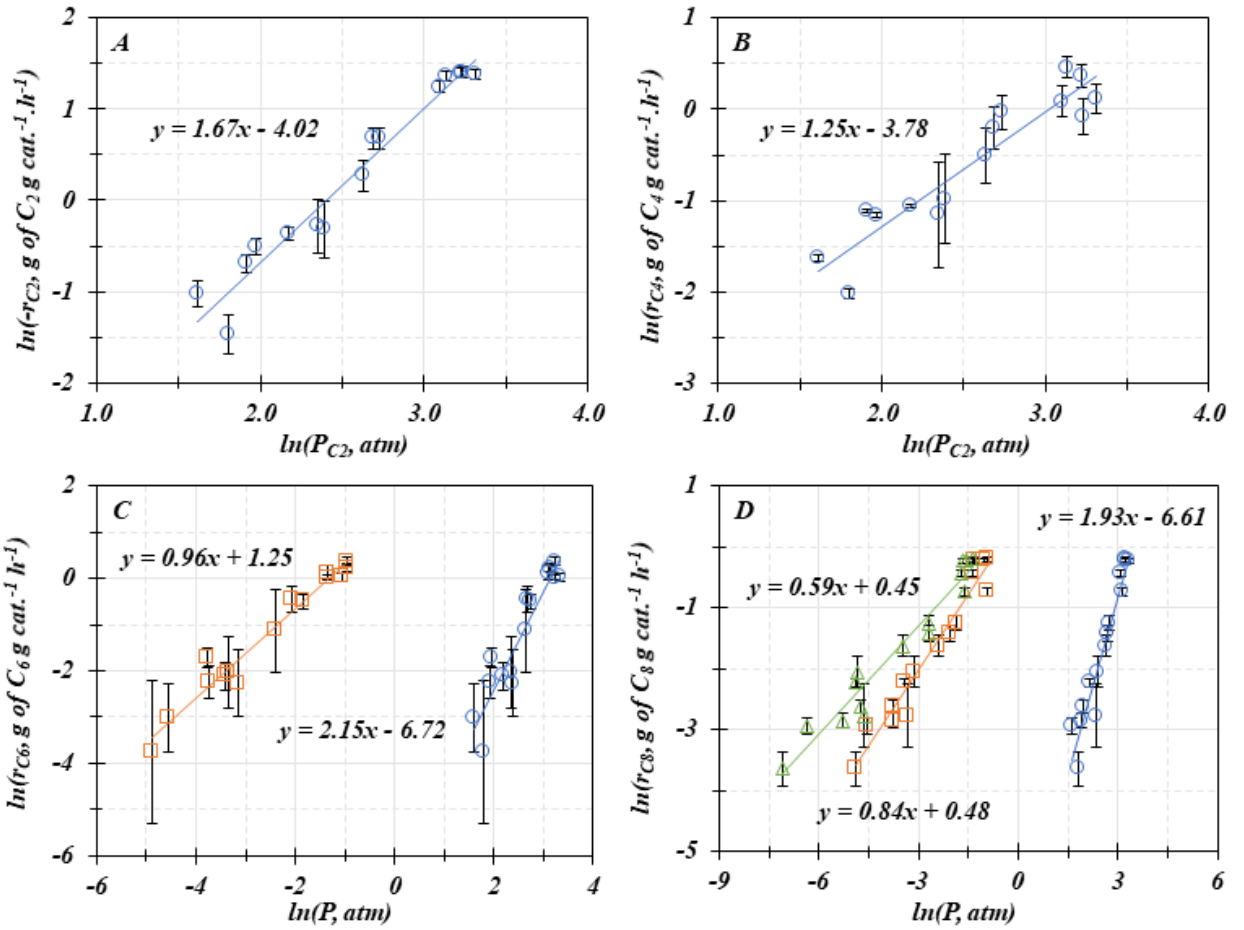

Figure 3.5. Log-log plots of ethylene consumption and butene, hexene, and octene formation rates versus partial pressures of (○) ethylene, (□) butenes, and (△) hexene. Data collected at 100°C and WHSV = 48.4 g ethylene g cat.$^{-1}$ h^{-1}.

Figure 3.5-D shows a second-order dependency for the formation of octene relative to ethylene. Therefore, species other than ethylene may be involved in the formation of octene. Figure 3.5-D suggests a first-order relationship between the formation of octene and butene partial pressure, which supports the involvement of butene in the formation of octenes. The formation of octene from butene can proceed via coordination of 2 ethylene molecules over re-adsorbed butene or via coordination of 2 butene molecules over the active site. Because ethylene is the main reactant in the process, the first possibility is very likely to take place. To assess the second possibility, we performed a butene oligomerization experiment over the Ni-H-Beta in the absence of ethylene in the feed. Figure S5 (Section 3 – Appendix A) shows that octene was formed, suggesting that

dimerization of butene cannot be neglected. Figure 3.5-D shows a reaction order of 0.6 for the formation of octene relative to hexene partial pressure. The low reaction order may indicate a small contribution of hexene to the formation of octene. We show later in Section 3.3.3 that the formation of octene proceeds mainly via butene re-adsorption on the catalyst and this route outcompetes hexene re-adsorption. In Section 3.3.4, we show that the proposed kinetic model is able to predict the reaction orders shown in Figure 3.5.

3.3.2 *Reaction network*

Analysis of the reaction order for species consumed and produced during the process suggests participation of desorbed products, such as butene and hexene, on the formation of octene. In both cases, these products have to undergo desorption followed by re-adsorption over another active site not involved in their formation. Because of that, we denominate the pathways involving consumption of re-adsorbed products *"cascade co-oligomerization"* pathways.

While several pathways can be involved in the conversion of ethylene into butene, hexene, and octene, modeling of reaction rates over distinct sites would lead to a complex reaction network. To simplify the reaction network, we considered that Ni^{2+} charge-compensating two aluminum atoms is the precursor to the nickel active site, which is later transformed into the $[Ni^{2+}\text{-}H^{-}]^{+}$ active site involved in chain-growth reactions. This assumption agrees with previous studies reported in the literature[15], [17]. It is important to highlight that other species, such as isolated Ni^{2+}[15], [16], have been considered in the literature as active sites for ethylene oligomerization. Also, butene and hexene can undergo chain growth over Brønsted sites via carbenium formation[23]. Note that the nature of the active site involved in chain-growth reactions does not affect the kinetic model develop in the present study.

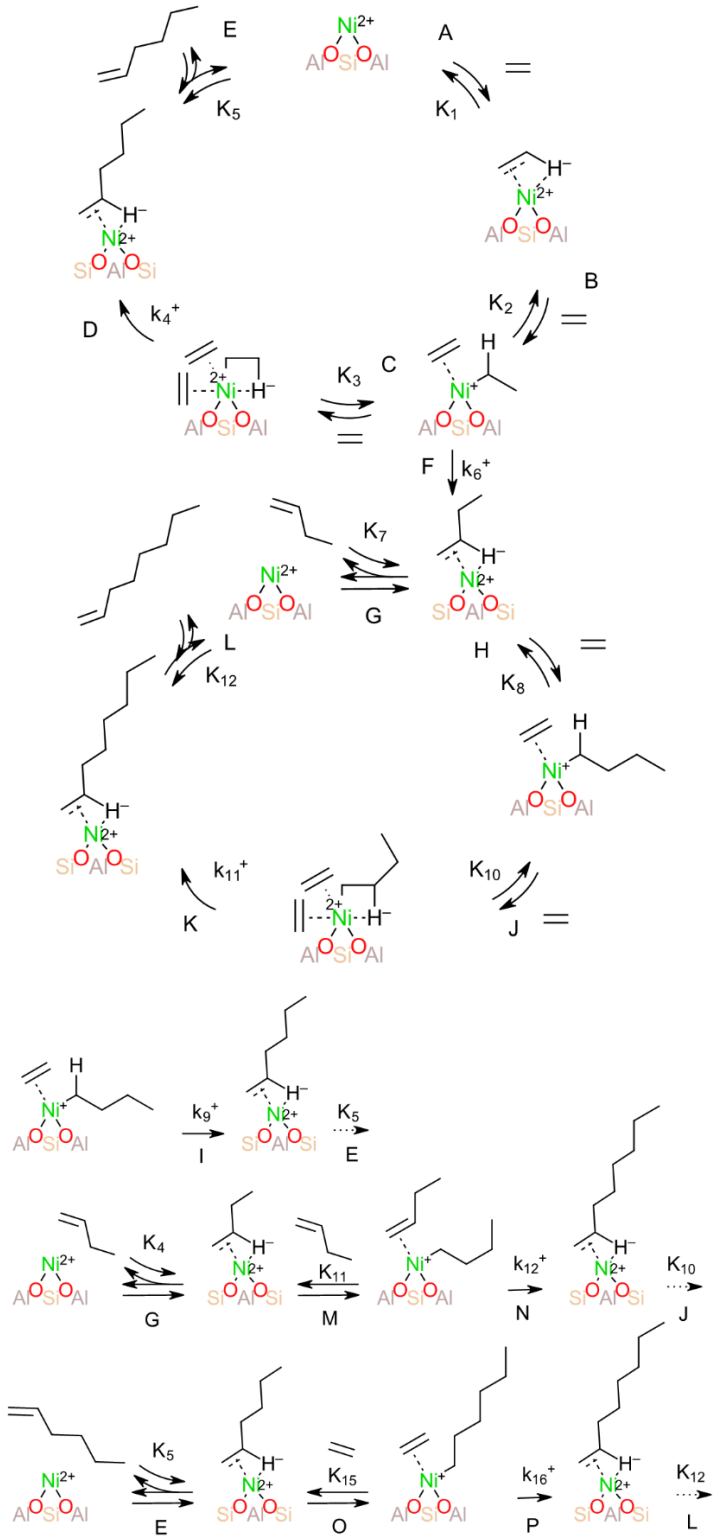

Figure 3.6. *"Cascade co-oligomerization"* pathway proposed based on the results obtained in the present work. The pathways assume the formation of a Cossee-Arlman center in agreement with reports from the literature.

Based on the results presented, we developed the reaction network shown in Figure 3.6, which consists of two cycles of coordination-insertion steps – one involving only ethylene (Figure 6 – A, B, C, D, and E) and the other involving butene and ethylene (Figure 6 – G, H, J, K, and L). The chain-growth process takes place via a Cossee-Arlman mechanism, in agreement with reports from the literature[15], [16]. In the proposed reaction network, ethylene dissociates over a Ni^{2+} site to form an ethenyl-$[Ni^{2+}\text{-}H^{-}]^{+}$ Cossee-Arlman site (Figure 3.6 – A). Then, another ethylene molecule coordinates over the ethenyl-$[Ni^{2+}\text{-}H^{-}]^{+}$ site to form ethene-Ni-ethyl (Figure 3.6 – B). At this point, butene can be formed by the insertion of ethene into the adsorbed ethyl (Figure 3.6 – F). If the insertion step to produce butene does not take place, ethene-Ni-ethyl undergoes another ethylene coordination step to form $[(ethene)_2\text{-Ni-ethyl}]^{+}$ (Figure 3.6 – C). Then, adsorbed hexene can be formed by the insertion of ethene into adsorbed ethyl (Figure 3.6 – D). We propose three different pathways for the formation of octene. The first pathway involves the re-adsorption of gaseous butene (Figure 3.6 – G) to form hexene and octene via series of ethylene coordination on re-adsorbed butene products (Figure 3.6 – H, I, J, K, and L). The second pathway involves re-adsorption of hexene (Figure 3.6 – E) to form octene via coordination and insertion of an additional ethylene molecule on the re-adsorbed hexene (Figure 3.6 – E, O, P, and L). The third pathway involves dimerization of desorbed butenes (Figure 3.6 – G, M, N, and L) to form octene. We used the Langmuir-Hinshelwood-Hougen-Watson (LHHW) kinetics to model the ethylene oligomerization over the Ni-H-Beta catalyst using the reaction network proposed in Figure 3.6.

Table 3.2. Rate expressions developed using the LHHW kinetics based on the *"cascade co-oligomerization"* pathway presented in Figure 3.6

	Kinetic expressions
ethylene consumption	$-r_{Ni-C_2H_4+H} = \frac{k_6^+ K_1 K_2 P_{C_2H_4}^2 + k_4^+ K_1 K_2 K_3 P_{C_2H_4}^3 + k_9^+ K_7 K_8 P_{C_2H_4} P_{C_4H_8} + k_{11}^+ K_7 K_8 K_{10} P_{C_2H_4}^2 P_{C_4H_8} + k_{16}^+ K_5 K_{15} P_{C_2H_4} P_{C_6H_{12}}}{1 + K_1 P_{C_2H_4} + K_7 P_{C_4H_8} + K_5 P_{C_6H_{12}} + K_{12} P_{C_8H_{16}}}$
butene production	$r_{Ni-C_4H_8+H} = \frac{k_6^+ K_1 K_2 P_{C_2H_4}^2 - k_9^+ K_7 K_8 P_{C_2H_4} P_{C_4H_8} - k_{11}^+ K_7 K_8 K_{10} P_{C_2H_4}^2 P_{C_4H_8} - k_{14}^+ K_7 K_{13} P_{C_4H_8}^2}{1 + K_1 P_{C_2H_4} + K_7 P_{C_4H_8} + K_5 P_{C_6H_{12}} + K_{12} P_{C_8H_{16}}}$
hexene production	$r_{Ni-C_6H_{12}+H} = \frac{k_4^+ K_1 K_2 K_3 P_{C_2H_4}^3 + k_9^+ K_7 K_8 P_{C_2H_4} P_{C_4H_8} - k_{16}^+ K_5 K_{15} P_{C_2H_4} P_{C_6H_{12}}}{1 + K_1 P_{C_2H_4} + K_7 P_{C_4H_8} + K_5 P_{C_6H_{12}} + K_{12} P_{C_8H_{16}}}$
octene production	$r_{Ni-C_8H_{16}+H} = \frac{k_{11}^+ K_7 K_8 K_{10} P_{C_2H_4}^2 P_{C_4H_8} + k_{14}^+ K_7 K_{13} P_{C_4H_8}^2 + k_{16}^+ K_5 K_{15} P_{C_2H_4} P_{C_6H_{12}}}{1 + K_1 P_{C_2H_4} + K_7 P_{C_4H_8} + K_5 P_{C_6H_{12}} + K_{12} P_{C_8H_{16}}}$

3.3.3 *Kinetic model analysis*

Table 3.2 shows the rate expressions for the consumption of ethylene and production of butene, hexene, and octene based on the *"cascade co-oligomerization"* pathway presented in Figure 3.6. Table S3 (Section 4 – Appendix A) presents the chemical equations and kinetic expressions used to develop the reaction rates shown in Table 3.2. Initial assessment of the *"cascade co-oligomerization"* model including all pathways shown in Figure 3.6 indicates that the kinetic model was able to predict the experimental rates (at 100ºC and WHSV of 48.4 g ethylene.g cat.$^{-1}$.h^{-1}) for the full range of ethylene partial pressures (5-28 atm, Figure S6 – Appendix A).

Table 3.3. Kinetic constant values calculated for the *"cascade co-oligomerization"* model via minimization of the objective function (Equation 3.6)

reaction constant	value (g.g.cat.$^{-1}$.h^{-1})
k_4^+	0.2
k_6^+	1.8
k_9^+	16.0
k_{11}^+	2.4
k_{14}^+	1.0
k_{16}^+	0.0
sorption parameters	value (atm^{-1})
K_1	2.0x10^{-2}
K_2	0.2
K_3	0.2
K_5	0.0
K_7	1.4x10^{-4}
K_8	7.8
K_{10}	3.0
K_{12}	9.2
K_{13}	0.0
K_{15}	0.5

Table 3.3 shows reaction rate constants (k^+) and sorption parameters (K) for the *"cascade co-oligomerization"* model shown in Figure 3.6. Although values for sorption constants are hardly available in the literature for ethylene oligomerization over nickel-based solid catalysts, one can calculate those values via Equation S4 (Section 5 – Appendix A). To apply Equation S4, one needs to determine values for the pre-exponential factor and enthalpy of adsorption, which are available in the literature. Toch et al. estimated that pre-exponential values associated with the physisorption of ethylene over the Ni-H-Beta range between 10^{-10} and 10^{-9} Pa^{-1}[23]. Additionally, as pointed out by Toch, actual values for pre-exponential factors depend on the reaction temperature. Adsorption is an exothermic process with values for the heat of adsorption (ΔH_{ads}) of ethylene, butene, hexene, and octene over the Ni-H-Beta ranging between -10 and -95 $kJ.mol^{-1}$, respectively[15], [23], [74], [75]. Therefore, based on the values for pre-exponential factor and heat of adsorption reported in the literature, sorption constant values may range between 10^{-4}-10^{9} atm^{-1}. Most of the values calculated in the present work fall within this range.

3.3.3.1 Sensitivity study

To reduce the number of parameters in the *"cascade co-oligomerization"* model (rate expressions shown in Table 3.2), we performed a sensitivity analysis of the adjusted parameters shown in Table 3.3. The sensitivity analysis consisted of disturbing one kinetic parameter at a time and calculating the change in the reaction rates caused by the disturbance. We chose a disturbance of 5% for each variable shown in Table 3.3. We used Equation 12 to calculate the deviation of the reaction rate values after disturbance relative to their original values:

$$S_{i,j} = \frac{\partial \ln r_i}{\partial \ln k_j} = \frac{\Delta r_i / r_i}{\Delta k_j / k_j} \tag{3.12}$$

Where $S_{i,j}$ represents the disturbance coefficient, r_i is the original reaction rate value, and k_j is the disturbed kinetic parameter. We considered the disturbance coefficients with absolute values

greater than 0.10 to be significant for the model proposed. Therefore, based on this criterion we excluded kinetic parameters that produced a disturbance lower that 0.10 or 10% in the reaction rate values. Table S4 (Section 6 – Appendix A) shows the significance of each kinetic parameter used in the *"cascade co-oligomerization"* model. The sensitivity analysis indicates that parameters k_9^+, k_{14}^+, k_{16}^+, K_5, K_{13}, and K_{15} have negligible effect of the model. Therefore, we removed these parameters from the rate expressions shown in Table 3.2. These parameters are involved in the co-oligomerization of desorbed butene and ethylene into hexene (Figure 3.6 – pathway I and E), dimerization of desorbed butene into octene (Figure 3.6 – pathway G, M, N, and L), and co-oligomerization of desorbed hexene and ethylene into octene (Figure 3.6 – pathway E, O, P, and L). According to the sensitivity analysis, the formation of hexene proceeds via a series of ethylene coordination-insertion steps (Figure 3.6 – pathway A, B, C, D, and E) and the formation of octene proceeds via co-oligomerization of desorbed butene with ethylene (Figure 3.6 – pathway G, H, J, K, and L). We show later that the simplified model provides an accurate description of the experimental data.

To further simplify the model, we combined the sorption constant K_2 and K_1. These constants describe the formation of the Cossee-Arlman site. After simplifying the model, we performed the regression of the data. In total, 15 experiments were adjusted with the remaining 9 parameters. The upper and lower limits for each parameter were calculated according to the method described in Section 3.2.3.2. The revised results are presented in Table 3.4. We present the simplified reaction rate expressions in Table 3.5. Figure 3.7 shows the experimental rate of ethylene consumption and the rates of butene, hexene and octene formation compared against the calculated rates using the *"cascade co-oligomerization"* model.

Table 3.4. Revised kinetic constant values calculated for the *"cascade co-oligomerization"* model via minimization of the objective function presented in Equation 3.6

Reaction constant (g.g cat.$^{-1}$.h^{-1})	average	upper limit[1]	lower limit[1]
k_4^+	2.6x10^{-1}	3.2x10^{-1}	2.0x10^{-1}
k_6^+	1.5	2.2	0.8
k_{11}^+	1.9	2.1	1.7
sorption parameters (atm^{-1})	average	upper limit[1]	lower limit[1]
K_1	4.6x10^{-2}	5.5x10^{-2}	3.6x10^{-2}
K_3	0.3	0.4	0.1
K_7	1.5x10^{-4}	1.8x10^{-4}	1.2x10^{-4}
K_8	13.0	13.6	12.5
K_{12}	10.5	10.9	10.1
K_{10}	4.7	5.1	4.2

[1] upper and lower limits calculated according to the method described in Section 3.2.3.2 with a 95% confidence level.

Table 3.5. Revised rate expressions developed using the LHHW kinetics based on the *"cascade co-oligomerization"* model presented in Figure 6

	kinetic expressions
ethylene consumption	$-r_{Ni-C_2H_4+H} = \frac{k_6^+ K_1 P_{C_2H_4}^2 + k_4^+ K_1 K_3 P_{C_2H_4}^3 + k_{11}^+ K_7 K_8 K_{10} P_{C_2H_4}^2 P_{C_4H_8}}{1 + K_1 P_{C_2H_4} + K_7 P_{C_4H_8} + K_{12} P_{C_8H_{16}}}$
butene production	$r_{Ni-C_4H_8+H} = \frac{k_6^+ K_1 P_{C_2H_4}^2 - k_{11}^+ K_7 K_8 K_{10} P_{C_2H_4}^2 P_{C_4H_8}}{1 + K_1 P_{C_2H_4} + K_7 P_{C_4H_8} + K_{12} P_{C_8H_{16}}}$
hexene production	$r_{Ni-C_6H_{12}+H} = \frac{k_4^+ K_1 K_3 P_{C_2H_4}^3}{1 + K_1 P_{C_2H_4} + K_7 P_{C_4H_8} + K_{12} P_{C_8H_{16}}}$
octene production	$r_{Ni-C_8H_{16}+H} = \frac{k_{11}^+ K_7 K_8 K_{10} P_{C_2H_4}^2 P_{C_4H_8}}{1 + K_1 P_{C_2H_4} + K_7 P_{C_4H_8} + K_{12} P_{C_8H_{16}}}$

The sorption constant K_1 associated with the initial adsorption of ethylene on the catalyst (Figure 3.6 – pathway A and B) has an average value of 6.2x10^{-2} atm^{-1}, which suggests a small number of Cossee-Arlman sites on the catalyst. This is consistent with previous literature reports[15], [17]. The sorption constant K_7 is a ratio between butene adsorption and desorption constants at *"quasi-equilibrium",* and it has an average value of 7.7x10^{-6} atm^{-1}. The low value for K_7 indicates a greater extent of butene desorption over adsorption. Note that there is still some extent of butene re-adsorption on the catalyst, since this is the only pathway for octene formation

(Figure 3.6 – pathway G, H, J, K, and L). Therefore, it is not surprising that the ethylene sorption parameters K_8 and K_{10} involved in co-oligomerization of ethylene with butene to form octene have the highest values among the fitted sorption constants shown in Table 3.4. Note that these values are orders of magnitude higher than K_1.

The calculated values for the kinetic parameters shown in Table 3.4 can be explained by the highly favorable adsorption of ethylene over re-adsorbed butene. According to Brogaard and Olsbye[15], the adsorption of ethylene over [Ni-butene]$^+$ (Figure 3.6 – Pathway H) has a Gibbs free energy value of -10 kJ.mol^{-1}, thus indicating that the adsorption of ethylene over sites occupied by re-adsorbed butene is thermodynamically favorable. Although butene desorbs and becomes a gaseous product, a fraction of butene re-adsorbs over the active sites of the catalyst. Once this step takes place, the adsorption of ethylene over re-adsorbed butene is favorable, thus leading to the formation of octene. Note that the reaction constants involved in the dimerization of ethylene into butene (k_6^+) and co-oligomerization of ethylene with butene (k_{11}^+) are higher than the reaction constant involved in the formation of hexene (k_4^+). Also, a K_{12} value of 4.1 atm^{-1} suggests that a fraction of octene remains adsorbed on the catalyst surface, thus indicating a potential pathway for coke production.

This analysis strongly supports our initial hypothesis that the consumption of butene on reactions to form octene lowers the activation energy for butene formation relative to the calculated values for hexene and octene. Also, this result is consistent with the octene reaction orders of 2.0 and 1.0 relative to ethylene and butene, respectively, shown in Figure 3.5. Figure 3.7 shows that the model captures the data trends with good precision.

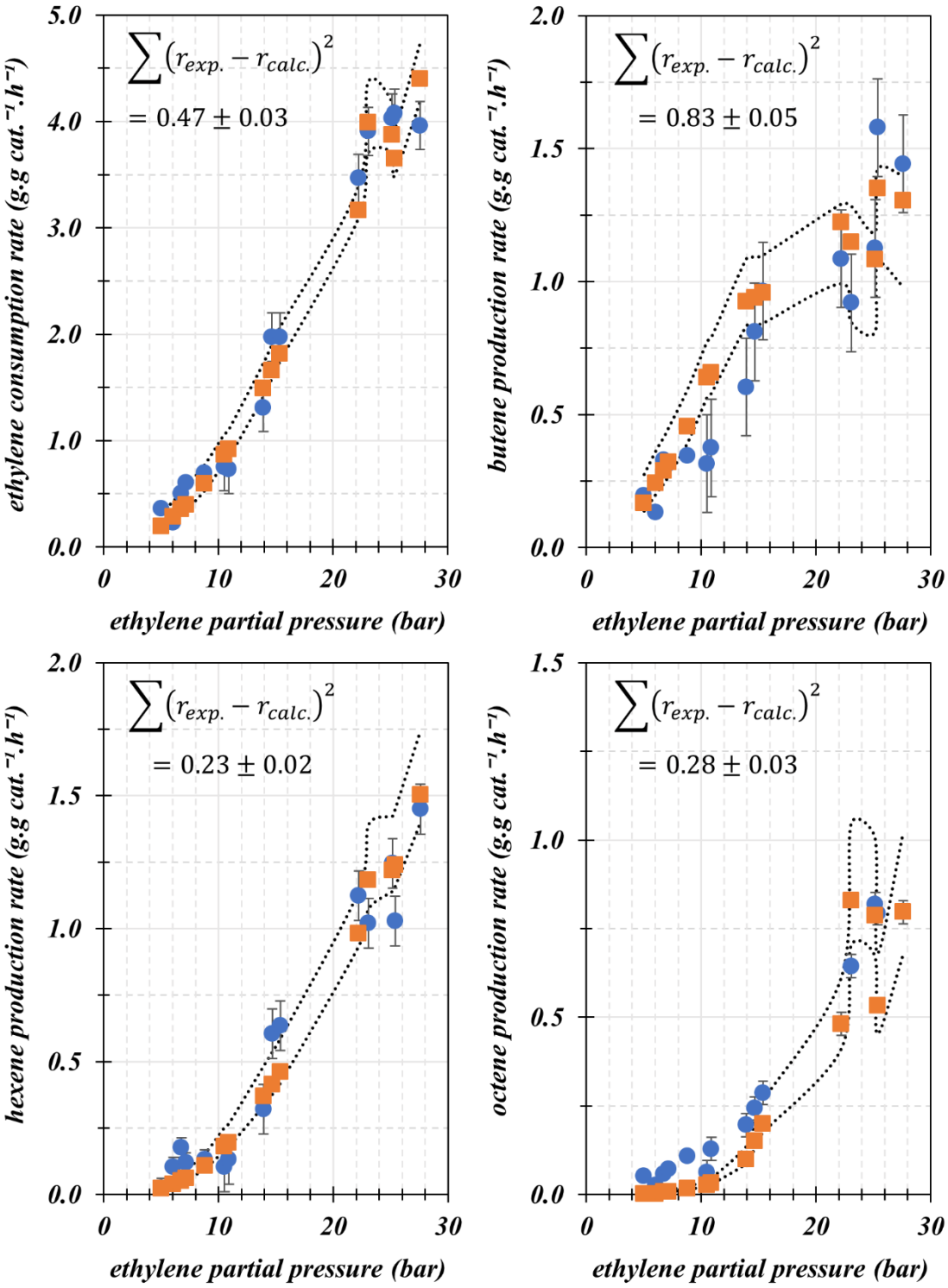

Figure 3.7. (■) Calculated rates of ethylene consumption and butene, hexene and octene formation using the *"cascade co-oligomerization"* model. Dotted lines show the rates upper and lower limits calculated based on the confidence interval of the parameters reported in Table 3.4. (●) Experimental rates with their respective standard deviations calculated from the replicates shown in Table S1. The sum of the squared difference is shown as a representation of the total error after regression.

3.3.4 *Comparison between "cascade co-oligomerization" and "solely ethylene coordination-insertion steps"*

We compared the "*cascade co-oligomerization"* model proposed in the present work with a model assuming only ethylene coordination-insertion steps (without involving re-adsorption of products on the catalyst) as an additional validation step. In the following discussion, we denominate this model *"solely ethylene coordination-insertion steps"*. This is one of the current accepted pathway considered in the literature for the ethylene oligomerization over nickel-based solid catalysts[16], [47]. The reaction pathway based on a simple coordination-insertion process is shown in Figure S7 (Section 7 – Appendix A) and the rate expressions used to model the experimental rates are shown in Table S5 (Section 7 – Appendix A). We considered the adsorption over a Ni^{2+} site to keep the model consistent with the *"cascade co-oligomerization"* model proposed in this work. After performing the initial regression of the *"solely ethylene coordination-insertion steps"* model using the rate expressions shown in Table S5, we performed a sensitivity analysis to remove unnecessary kinetic constants. The approach used for the sensitivity analysis is the same described in Section 3.3.3.1 for the *"cascade co-oligomerization"* model. According to the sensitivity analysis shown in Table S6 (Section 7 – Appendix A) all the parameters considered in the *"solely ethylene coordination-insertion steps"* model are significant. Table 3.6 shows the revised adjusted kinetic constants and Table 3.7 shows the revised rate expressions, for the *"solely ethylene coordination-insertion steps"* model. Figure 3.8 shows the experimental rate of ethylene consumption and the rates of butene, hexene and octene formation compared against the calculated rates using the *"solely ethylene coordination-insertion steps"* model.

Table 3.6. Revised kinetic constant values calculated for the *"solely ethylene coordination-insertion steps"* model via minimization of the objective function presented in Equation 6

Reaction constant (g.g cat.$^{-1}$.h^{-1})	average	upper limit[1]	lower limit[1]
k_3^+	0.5	0.6	0.4
k_5^+	0.7	1.0	0.4
k_7^+	75.5	75.8	75.2
sorption parameters (atm^{-1})	average	upper limit[1]	lower limit[1]
K_1	0.4	0.7	0.1
K_2	1.0	1.2	0.7
K_4	0.9	1.2	0.6
K_6	75.5	76.0	75.1
K_8	12.0	15.6	8.4

[1] upper and lower limits calculated according to the method described in Section 3.2.3.2 with a 95% confidence level.

Table 3.7. Revised rate expressions developed using the LHHW kinetics based on the *"solely ethylene coordination-insertion steps"* model presented in Figure S7

	kinetic expressions
ethylene consumption	$-r_{C_2H_4} = \frac{k_3^+ K_1 K_2 P_{C_2H_4}^2 + k_5^+ K_4 K_{10} P_{C_2H_4} P_{C_4H_8} + k_7^+ K_6 K_9 P_{C_2H_4} P_{C_6H_{12}}}{1 + K_1 P_{C_2H_4} + K_{10} P_{C_4H_8} + K_9 P_{C_6H_{12}} + K_8 P_{C_8H_{16}}}$
butene production	$r_{C_4H_8} = \frac{k_3^+ K_1 K_2 P_{C_2H_4}^2}{1 + K_1 P_{C_2H_4} + K_{10} P_{C_4H_8} + K_9 P_{C_6H_{12}} + K_8 P_{C_8H_{16}}}$
hexene production	$r_{C_6H_{12}} = \frac{k_5^+ K_4 K_{10} P_{C_2H_4} P_{C_4H_8}}{1 + K_1 P_{C_2H_4} + K_{10} P_{C_4H_8} + K_9 P_{C_6H_{12}} + K_8 P_{C_8H_{16}}}$
octene production	$r_{C_8H_{16}} = \frac{k_7^+ K_6 K_9 P_{C_2H_4} P_{C_6H_{12}}}{1 + K_1 P_{C_2H_4} + K_{10} P_{C_4H_8} + K_9 P_{C_6H_{12}} + K_8 P_{C_8H_{16}}}$

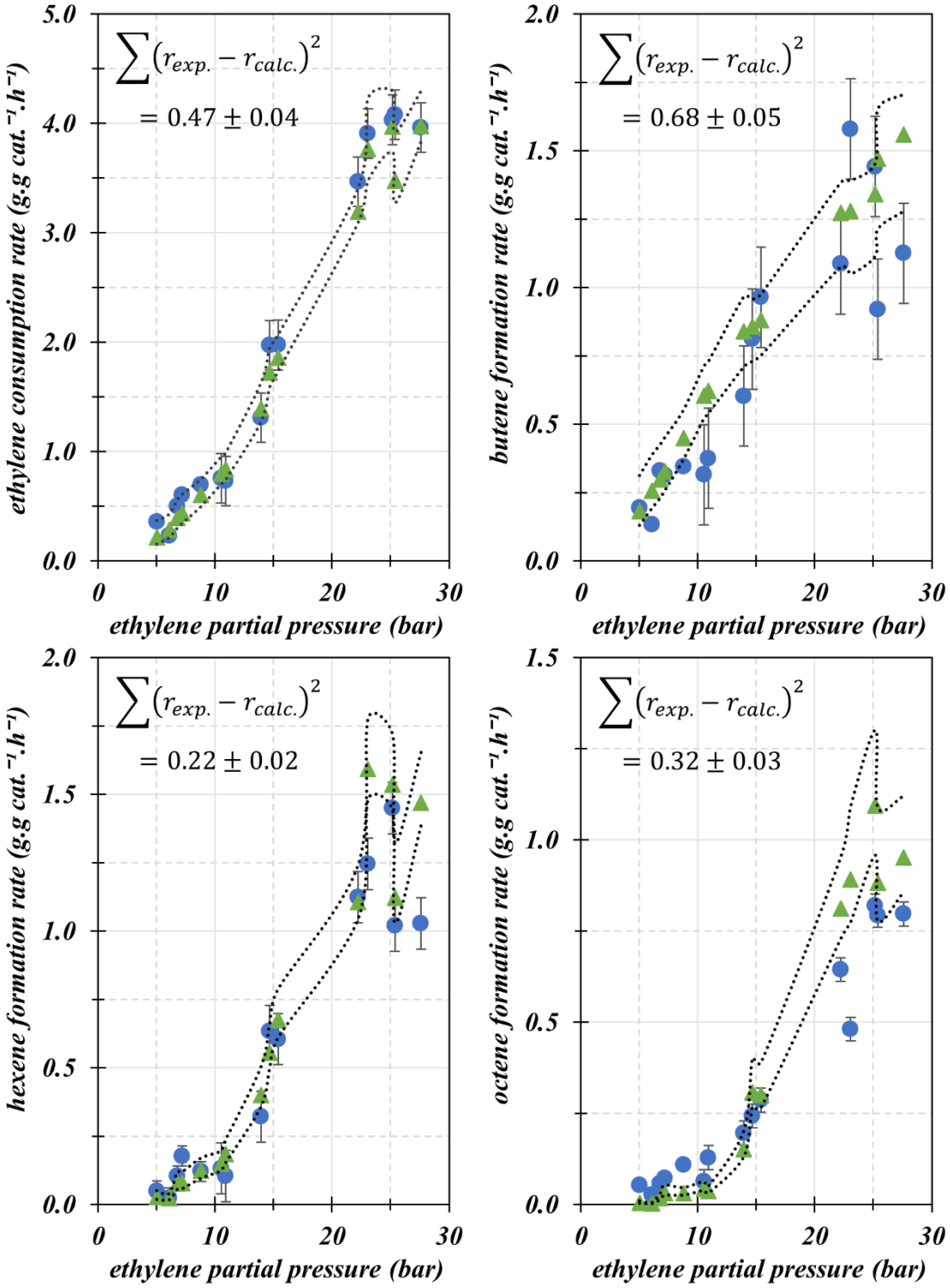

Figure 3.8. (▲) Calculated rates of ethylene consumption and butene, hexene and octene formation using the *"solely ethylene coordination-insertion steps"* model. Dotted lines show the rates upper and lower limits calculated based on the confidence interval of the parameters reported in Table 3.6. (●) Experimental rates with their respective standard deviations calculated from the replicates shown in Table S1. The sum of the squared difference is shown as a representation of the total error after regression.

The results indicate that the *"solely ethylene coordination-insertion steps"* model is able to describe the trends in the experimental rates. The minimized errors for the rates of ethylene consumption and hexene and octene formation are not significantly different than the ones obtained with the *"cascade co-oligomerization"* model (Figure 3.7). For the rates of butene formation, the *"solely ethylene coordination-insertion steps"* model shows a statistically significantly better prediction of the rates than the *"cascade co-oligomerization"*. Still, the latter is able to predict the trends for butene formation obtained experimentally with good accuracy.

To further elucidate differences between the *"cascade co-oligomerization"* and *"solely ethylene coordination-insertion steps"* models, we calculated the reaction order based on the modeled rate expressions for both models according to Equation 3.4. The revised rate expressions shown in Table 3.5 and Table 3.7 were used to develop the reaction order equations.

Table 3.8 summarizes the expressions for the reaction orders of butene, hexene, and octene formation as a function of ethylene partial pressure for the *"cascade co-oligomerization"* and *"solely ethylene coordination-insertion steps"* models. Equations S5-S12 (Section 8 – Appendix A) show the derivative of the fraction of free sites (θ^*) relative to ethylene partial pressure used to calculate the reaction orders reported in Table 3.8. Figure 3.9 shows the squared difference between experimental and calculated reaction orders of butene, hexene, and octene as a function of ethylene partial pressure. We note that the reaction orders were calculated based on the kinetic parameters reported in Table 3.4 and Table 3.6 without further regression of the parameters to fit the experimental reaction orders shown in Figure 3.5. Table S7 (Section 8 – Appendix A) shows the sum of the squared difference between experimental and calculated reaction orders for both models.

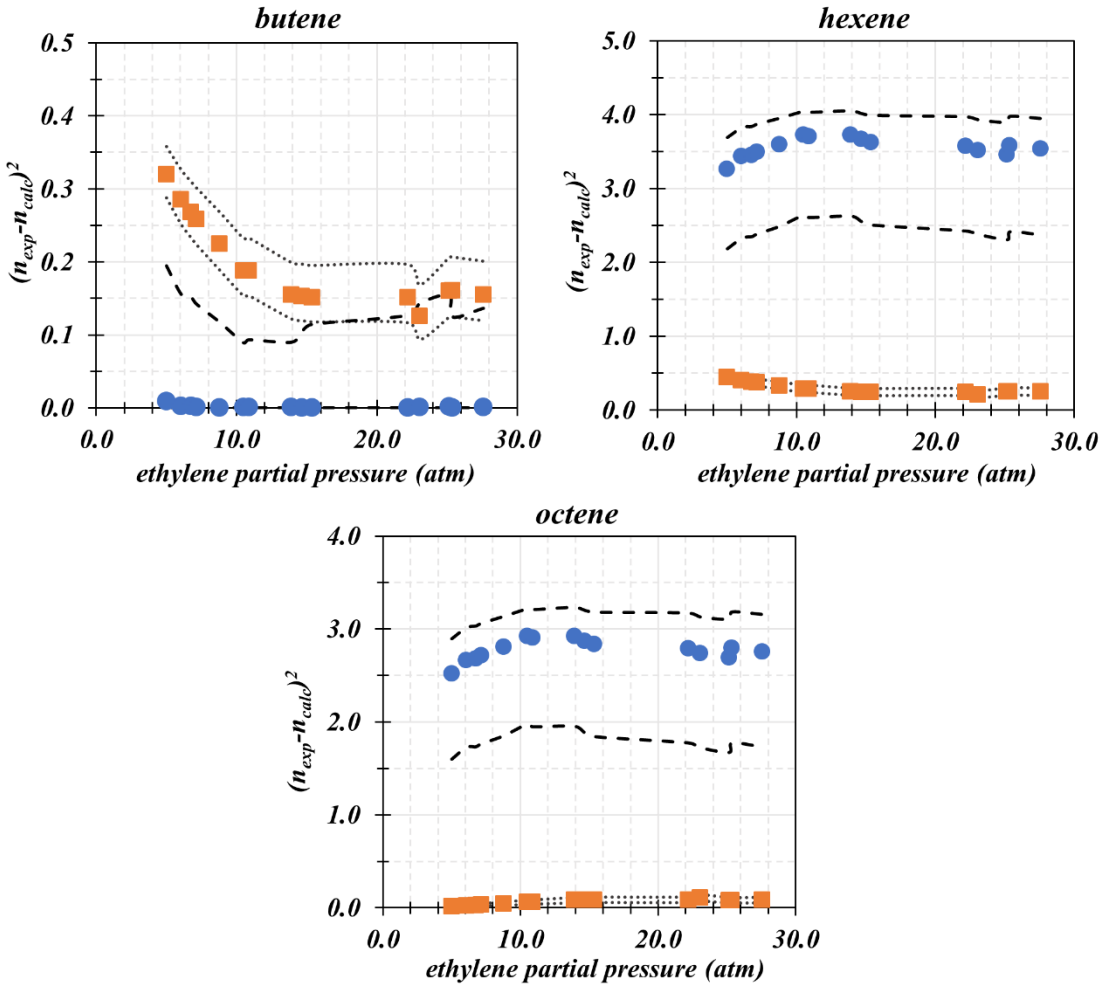

Figure 3.9. Square of the difference between experimental and calculated reaction orders of butene, hexene, and octene relative to ethylene for the (■) *"cascade co-oligomerization"* and (●) *"solely ethylene coordination-insertion steps"* models. Dotted lines (*"cascade co-oligomerization"* = ⋯⋯ and *"solely ethylene coordination-insertion steps"* = ╍╍) show the errors upper and lower limits calculated based on the confidence interval of the parameters reported in Table 3.4 and Table 3.6.

Figure 3.9 clearly shows that the *"cascade co-oligomerization"* model provides a better prediction of the experimental reaction order reported in Figure 3.5 than the *"solely ethylene coordination-insertion steps"* model. The *"solely ethylene coordination-insertion steps"* model performs better than the *"cascade co-oligomerization"* when predicting the reaction orders of butene. It is important to highlight that both models display similar performances when predicting the reaction orders of butene at ethylene partial pressures greater than 12 bar, with no statistical difference between the calculated residues. For the reaction orders of hexene and octene formation, the

"solely ethylene coordination-insertion steps" model shows a stark deviation from the experimental reaction order. The sum of the squared difference shown in Table S7 indicates that the *"cascade co-oligomerization"* model yields a much lower total error compared to the *"solely ethylene coordination-insertion steps"* model. Therefore, the *"cascade co-oligomerization"* model provides better consistency to the data relative to the *"solely ethylene coordination-insertion steps"* model.

This analysis shows that in order to remain consistent with the experimental reaction order of octene, butene must desorb and re-adsorb on the catalyst. If this process does not take place, then the formation of octene proceeds via simple ethylene coordination over Ni-butyl to form adsorbed Ni-hexyl, which is later transformed into octene via another ethylene coordination-insertion step, leading to a lower reaction order dependence with respect to ethylene partial pressure.

Table 3.8. Reaction order for the production of butene, hexene, and octene as a function of the ethylene partial pressure

Reaction order[1]	*"cascade co-oligomerization"*[2,4]	*"solely ethylene coordination-insertion steps"*[3,4]
n_{C_4,C_2}	$\frac{2k_6^+K_1K_2P_{C_2H_4}^2 - 2k_{11}^+K_7K_8K_{10}P_{C_2H_4}^2P_{C_4H_8}}{k_6^+K_1K_2P_{C_2H_4}^2 - k_{11}^+K_7K_8K_{10}P_{C_2H_4}^2P_{C_4H_8}} + P_{C_2H_4}\frac{\partial \ln(\theta^*)}{\partial P_{C_2H_4}} = 2 + P_{C_2H_4}\frac{\partial \ln(\theta^*)}{\partial P_{C_2H_4}}$	$2 + P_{C_2H_4}\frac{\partial \ln(\theta^*)}{\partial P_{C_2H_4}}$
n_{C_6,C_2}	$\frac{3k_4^+K_1K_2K_3P_{C_2H_4}^3}{k_4^+K_1K_2K_3P_{C_2H_4}^3} + P_{C_2H_4}\frac{\partial \ln(\theta^*)}{\partial P_{C_2H_4}} = 3 + P_{C_2H_4}\frac{\partial \ln(\theta^*)}{\partial P_{C_2H_4}}$	$1 + P_{C_2H_4}\frac{\partial \ln(\theta^*)}{\partial P_{C_2H_4}}$
n_{C_8,C_2}	$\frac{2k_{11}^+K_7K_8K_{10}P_{C_2H_4}^2P_{C_4H_8}}{k_{11}^+K_7K_8K_{10}P_{C_2H_4}^2P_{C_4H_8}} + P_{C_2H_4}\frac{\partial \ln(\theta^*)}{\partial P_{C_2H_4}} = 2 + P_{C_2H_4}\frac{\partial \ln(\theta^*)}{\partial P_{C_2H_4}}$	$1 + P_{C_2H_4}\frac{\partial \ln(\theta^*)}{\partial P_{C_2H_4}}$

[1] $n_{x,y}$ is the reaction order of species x relative to species y.

[2] $P_{C_2H_4}\frac{\partial \ln(\theta^*)}{\partial P_{C_2H_4}}$ is defined in Section 8.1 of the Appendix A.

[3] $P_{C_2H_4}\frac{\partial \ln(\theta^*)}{\partial P_{C_2H_4}}$ is defined in Section 8.2 of the Appendix A.

[4] θ^* indicates the fraction of free sites.

3.3.5 *Model performance*

The parity plot presented in Figure 3.10 shows that the proposed model is able to predict the rates of ethylene consumption and product formation for reactions performed at WHSVs (data shown in Figure 3.2) and temperatures (data show in Figure 3.3 and Figure 3.4) not included in the data set used to fit the kinetic parameters shown in Table 3.4. This result is expected since we demonstrated previously that the reaction rates remained approximately constant for temperatures varying from 50 and 100°C and WHSVs varying from 36.5 and 72.9 g of ethylene.g cat.$^{-1}$.h^{-1}.

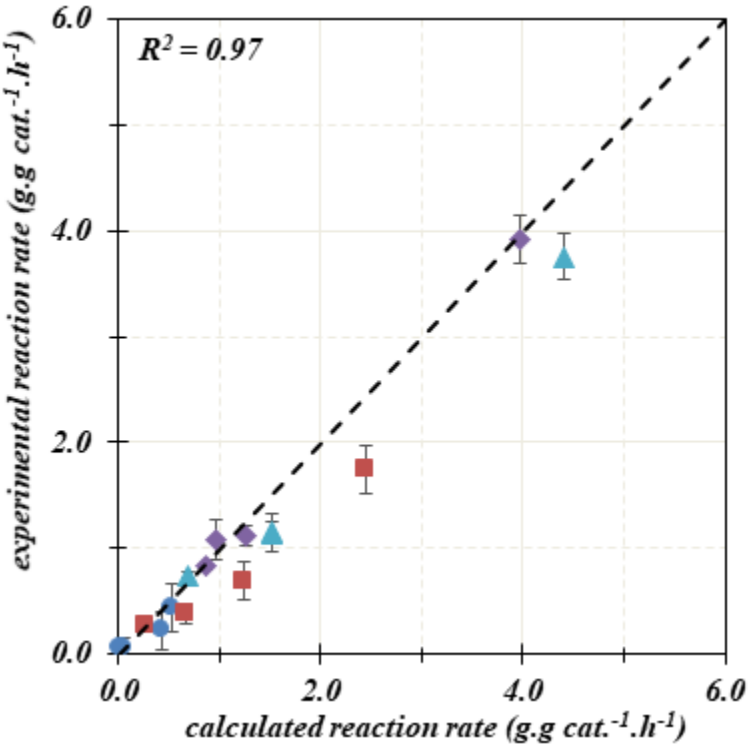

Figure 3.10. Parity plot showing experimental rates of ethylene consumption and products formation against the calculated values according to the rate expressions shown in Table 3.5 and kinetic parameters shown in Table 3.4. (●) 28 atm and 50°C, (■) 28 atm and 75°C, (◆) 28 atm, 100°C, and WHSV = 36.5, and (▲) 28 atm, 100°C, and WHSV = 60.8.

3.4 CONCLUSION

The present work addresses the kinetics of ethylene oligomerization over the Ni-H-Beta. Only a few studies reported the development of kinetic models for the ethylene oligomerization over nickel-exchanged acidic inorganic catalysts. The present work uses a systematic approach to develop a reaction network consistent with experimental data. We report activation energies for formation of butene, hexene, and octene of 44, 78, and 60 $kJ.mol^{-1}$, respectively. The lower activation energy for butene formation suggests the involvement of butene in co-oligomerization pathways over the Ni-H-Beta catalyst.

Study of the effect of ethylene partial pressure on the formation of butene, hexene, and octene indicates that while the reaction orders for butene and hexene formation are consistent with the ethylene coordination-insertion mechanism, the reaction order for octene formation points to the participation of butene and hexene as co-reactants. Based on this observation, we hypothesized a pathway involving co-oligomerization of butene and hexene products denominated *"cascade co-oligomerization"* pathway. Based on this pathway, we developed a kinetic model using the LHHW kinetics and generated rate expressions for the consumption of ethylene and production of butene, hexene, and octene. The fitting of kinetic parameters was performed according to experimental rates obtained at 100°C and pressures ranging from 5 to 28 atm.

The proposed *"cascade co-oligomerization"* model is consistent with the experimental rates. According to the results, the pathway involving butene co-oligomerization is more selective towards octene than the pathway involving consumption of hexene. Comparison between the *"cascade co-oligomerization"* pathway and a simple *"solely ethylene coordination-insertion steps"* model suggests that while the latter is able to fit the experimental rates, it cannot predict the reaction order for octene formation. This comparison provides another indication that desorbed

butene participates on the formation of octene. Therefore, during the ethylene oligomerization over nickel-based solid catalysts, hexene is formed via a series of ethylene coordination-insertion steps, and octene is formed via coordination-insertion of re-adsorbed butene with ethylene.

Previous studies from our research group provided evidence of butene consumption in chain-growth reactions to promote formation of higher alkenes based on the change in product selectivity with WHSV[26]. However, this is the first work to provide a kinetic description of this phenomenon and address this mechanism over a wide range of ethylene partial pressures. Finally, the study presented in this work can contribute to the development of solid catalysts tailored to the production of higher alkenes.

Chapter 4. EFFECT OF COKE SOLUBILITY ON THE OLIGOMERIZATION OF SUPERCRITICAL ETHYLENE OVER HETEROGENEOUS CATALYSTS[5,6]

Abstract

We investigated the effect of coke solubility in supercritical ethylene on the ethylene oligomerization over nickel-based heterogeneous catalysts. The approach uses *n*-decane as a model compound to simulate coke formed during the catalytic process. We report the solubility of *n*-decane in ethylene at 30, 50, and 75^{o}C and pressures ranging from 1 to 68 bar; conditions previously screened by our research group for ethylene oligomerization. We reproduced previous literature data on the solubility of *n*-decane in nitrogen to validate the flow system designed in the present work.

The present study is the first to report the solubility of *n*-decane in ethylene under a broad range of conditions, including subcritical and supercritical conditions. We found that the ethylene – *n*-decane system deviates from ideality very quickly with increasing pressure. Beyond the ethylene critical point (P = 50.3 bar and T = 9.4^{o}C) the solubility of *n*-decane in ethylene at 30^{o}C reaches a maximum value of 3.0%; close to the value observed at 50 and 75^{o}C, under the same pressure. We used the solubility data to estimate the rate of coke dissolution and compared these values with kinetic data under supercritical conditions. Analysis of coke dissolution rates in supercritical ethylene under different temperatures indicates that the transport of products from the catalyst surface to the bulk of supercritical ethylene controls the catalytic process at supercritical

[5] To be submitted to the Journal of Supercritical Fluids, Gabriel V. S. Seufitelli, Fernando L. P. Resende, Rick Gustafson.

[6] Work presented at the American Institute of Chemical Engineers (AIChE) Annual Meeting in 2019.

conditions. The approach used in the present work is novel because it accounts for the contribution of coke dissolution rates on the ethylene oligomerization over nickel-based solid catalysts.

Keywords: Ethylene Oligomerization; Solubility; Supercritical Fluids; Coke; Ni-H-Beta.

4.1 INTRODUCTION

Ethylene oligomerization is currently carried out over homogeneous catalysts[12], [76], requiring the use of co-catalysts, such as methylaluminoxane (MAO)[16], [32], [65]. MAO is a pyrophoric solid and is commonly dissolved in aromatic solvents, such as toluene. Use of toluene as the reaction medium requires expensive separation processes to recover the catalyst and reaction products and has potential safety and environmental implications because of toluene's toxicity. For these reasons, ethylene oligomerization over heterogeneous catalysts has received attention due to the potential of employing a more environmentally-friendly and user-friendly process for the production of light and heavy alkenes[65], [76]. Several works reported the development of novel heterogeneous catalysts for ethylene oligomerization comprising mostly nickel-exchanged aluminosilicates, such as Ni-H-Beta[7], [10], [11], [13], [16], [23]–[26], Ni-MCM-41[9], [11], Ni-SBA-15[18], [25], [77], [78], and Ni-SIRAL30[11], [58]. Although these catalysts show good stability and high ethylene conversion, the high selectivity to light alkenes, such as butene and hexene, still hinders the use of heterogeneous catalysts in large scale ethylene oligomerization processes relative to its homogeneous counterpart.

Catalyst deactivation is another concern with heterogeneous catalysts[79]. Deactivation of heterogeneous catalysts can occur by diverse processes[80]. Usual mechanisms include fouling and poisoning[79], [81], [82]. Fouling is mechanical in nature and results from the deposition of material on the catalyst. Poisoning is a chemical deactivation process caused by strongly adsorbed species on active sites[79], [81], [82]. A common cause of deactivation is the accumulation of coke

on the catalyst. Catalyst deactivation requires expensive and complicated regeneration processes[81], which are estimated to cost the industry billions of dollars annually[82].

It has been proposed that supercritical fluids could promote the solvation of coke in heterogeneous oligomerization processes, which in turn reduces catalyst deactivation by coke[13], [25], [83], [84]. A supercritical fluid is any fluid above its critical temperature and pressure, and ethylene has the lowest critical temperature among light alkenes (9.4^{o}C), and a relatively mild critical pressure (50.3 bar). Added to the fact that ethylene is the reactant for the ethylene oligomerization, its mild critical point could make supercritical ethylene a medium for coke mitigation. In previous publications[13], [25], we provided visual evidence for the dissolution of coke in supercritical ethylene during the ethylene oligomerization over the Ni-H-Beta[13]. Our results suggested an increase in the formation of C_{10+} alkenes as a consequence of the dissolution of coke molecules in supercritical ethylene and the increased rates of oligomerization under supercritical conditions. In addition to the solvation effect, the oligomerization of supercritical ethylene could shift the product distribution towards high molecular weight alkenes. This is especially desirable to increase the production of liquid hydrocarbons from ethylene oligomerization over heterogeneous catalysts.

While supercritical ethylene can be used under mild conditions to promote coke dissolution during the ethylene oligomerization over heterogeneous catalysts, mild conditions can limit the production of alkenes due to the low extent of chain-growth reactions[68], [70]. Several works reported the increase in ethylene oligomerization rates with increasing temperature and pressure[7], [10], [11], [13], [18], [23]–[26], [37], [39]. Tuning the conditions to minimize coke production and simultaneously maximize the extent of chain-growth reactions is necessary to ensure stable catalyst activity and high alkene productivity.

The extent of coke production depends on the rates of coke deposition and coke removal (via dissolution). Information currently available on the quantification of coke deposition and dissolution rates over heterogeneous catalysts is limited. In the present work, we used a systematic approach to quantify the dissolution rates of coke in subcritical and supercritical ethylene. This approach required a solubility study using a coke model compound in subcritical and supercritical ethylene. In previous works, coke produced via subcritical ethylene oligomerization over nickel-exchanged aluminosilicate catalysts has been characterized as aliphatic molecules[11], [13]. Additionally, we characterized the coke formed under supercritical conditions as high molecular weight linear and cyclic alkanes connected via sp^3 bonds[13]. We found that the CH_2/CH_3 ratio of the coke formed under supercritical conditions was a function of temperature with values varying between 3.0 and 6.5. Therefore, we chose *n*-decane as a coke model compound because of its aliphatic nature and its CH_2/CH_3 ratio, which falls within the range of values reported in our previous study (3.0 - 6.5)[13].

The solubility of liquids, such as *n*-decane, in compressed gases has been extensively reported in the literature[27]–[30], [85]–[87]. Prausnitz et al. studied the solubility of *iso*-octane, *n*-decane, carbon tetrachloride, and toluene in nitrogen, hydrogen, and carbon monoxide[30]. They concluded that the solubility deviates from ideality very quickly with increasing pressure, especially for pressures above 10 atm. Diepen et al. studied the solubility of naphthalene in subcritical and supercritical ethylene and reported a sharp increase in solubility beyond the ethylene critical point, which can be attributed to the reduction in the ethylene dielectric constant above the critical point leading to a decrease in the polarity of the supercritical fluid[27]. Kurnik et al. reported the same phenomena for the solubility of 2,3-dimethyl-naphthalene, 2,6-dimethyl-naphthalene, phenanthrene, benzoic acid, and hexachloroethane in carbon dioxide and

ethylene.[87] The present work focused on the solubility of *n*-decane in ethylene because of the potential to minimize catalyst coking under supercritical conditions.

The overall objective of this research is to assess and model *n*-decane solubility in subcritical and supercritical ethylene. The information obtained in the solubility study will be used to provide insight on the solvation of the coke formed over the solid catalyst during the ethylene oligomerization under supercritical conditions, thereby assessing its contribution to the transport of high molecular weight products from the catalyst surface to the gas. This investigation is an essential first step in an on-going broader study on the kinetics of ethylene oligomerization under supercritical conditions.

4.2 THERMODYNAMICS

4.2.1 *Solubility modeling*

We adopted a thermodynamic modeling approach similar to Prausnitz's[28], [88], [89] based on virial and Peng-Robinson equations of state (EOS) to describe the experimental solubility data. Description of the model can be found elsewhere[28]. Briefly, the model accounts for both gas and liquid phases and assumes that the solubility of gaseous species in *n*-decane is negligible. This assumption is valid for nitrogen, which has low solubility in *n*-decane. Even though the solubility of ethylene in n-decane cannot be neglected, the conditions used in the present study are sufficient to ensure that the amount of ethylene in the gas is much larger than the amount of ethylene solubilized in *n*-decane. According to our simulations, the mole fraction of ethylene in n-decane in all experiments remained below 10%, which is lower than the threshold of 20% for liquid-phase non-ideality. Therefore, at ethylene mole fractions below 10% the liquid phase is an ideal solution with respect to the solvent (*n*-decane)[30]. Also, as noted by D'Avila and Prausnitz[29], [30], if the mole fraction of the gas in the liquid is much lower than unity, it is not

necessary to know its value accurately, since the mole fraction of *n*-decane in ethylene is not sensitive to the mole fraction of ethylene in *n*-decane.

The molar fraction of *n*-decane in the gas can be expressed by the following equation:

$$y_2 = \frac{(1-x_1).P_2^S.\phi_2^S.\exp\left(\int_{P_2^S}^{P}\frac{\vartheta_2^L}{R.T}dP\right)}{\phi_2.P} \quad (4.1)$$

Where y_2 is the molar fraction of *n*-decane in the gas, P_2^S, ϕ_2^S, and ϑ_2^L are the saturation pressure, liquid-phase fugacity coefficient at saturation, and molar volume of pure *n*-decane, respectively, ϕ_2 is the gas-phase fugacity coefficient of *n*-decane, *P* and *T* are the pressure and temperature, respectively, and x_1 is the molar fraction of the volatile component in *n*-decane, calculated according to the following equation:

$$x_1 = \frac{\phi_1.y_1.P}{H_{1,2}.\exp\left(\int_{P_2^S}^{P}\frac{\overline{\vartheta_1}^{\infty}}{R.T}dP\right)} \quad (4.2)$$

In Equation 4.2, ϕ_1 and y_1 are the gas-phase fugacity coefficient and molar fraction of the less-volatile component in the gas, respectively, and $H_{1,2}$ is the Henry's constant. For the fitting of the solubility data, we assumed Henry's constant for the solubility of ethylene in *n*-decane of 48 bar^{-1}[90]. Equations 4.1 and 4.2 provide the basis to obtain the composition of a binary vapor-liquid system under any *P* and *T*. However, fugacity coefficients ϕ_1 and ϕ_2 are also a function of the gas-phase composition. Therefore, the calculation of solubility requires an iterative process with the EOS.

4.2.2 *Equations of state (EOS)*

In the present study, we used the virial and Peng-Robinson EOS to calculate the fugacity coefficients for the components in the gas phase. For the nitrogen – *n*-decane system, a quadratic virial EOS was sufficient to predict the solubility data under the conditions used in the present

study. For the ethylene – *n*-decane system, a cubic EOS was required to calculate the solubilities at high pressures. For this reason, we used the Peng-Robinson EOS to calculate the solubility of *n*-decane in ethylene.

4.2.2.1 Virial

We used Prausnitz's approach to model the solubility of *n*-decane in nitrogen as a validation method of the solubility system designed in this work. For this system, a quadratic equation of state was able to predict the experimental solubility. Therefore, we adopted the virial EOS truncated in the second term for the solubility calculations. A detailed description of the virial equation used in the present work can be found in [29], [30], [91].

4.2.2.2 Peng-Robinson

The Peng-Robinson EOS was used to model the solubility of *n*-decane in ethylene. The Peng-Robinson EOS is given by Equations 4.3-4.8[92], [93]:

$$P = \frac{R.T}{v-b} - \frac{a(T)}{v.(v+b)+b.(v-b)} \tag{4.3}$$

$$b = 0.07780.\frac{R.T_c}{P_c} \tag{4.4}$$

$$a(T) = a(T_c).\alpha(T_r, \omega) \tag{4.5}$$

$$a(T_c) = 0.45724.\frac{R^2.T_c^2}{P_c} \tag{4.6}$$

$$\alpha(T_r, \omega) = \left[1 + \beta\left(1 - T_r^{1/2}\right)\right]^2 \tag{4.7}$$

$$\beta = 0.37464 + 1.54226.\omega - 0.26992.\omega^2 \tag{4.8}$$

Composition calculation of a multi-component system using the Peng-Robinson EOS requires the use of mixing rules, which provide a relationship between the properties of the pure components present in the mixture. The conventional mixing rule for a binary system is given by:

$$\alpha(T_r, \omega) = \left[1 + \beta\left(1 - T_r^{1/2}\right)\right]^2 \tag{4.9}$$

$$\beta = 0.37464 + 1.54226.\omega - 0.26992.\omega^2 \quad (4.10)$$

Where a and b for the pure components are defined by Equations 4.4-4.8. Absolute values for parameters c_{12} and k_{12} are smaller than unity. For mixtures comprising non-polar components, $c_{12} = 0$, and k_{12} can then be estimated from binary equilibrium data. It is usual to assume that k_{12} does not vary with temperature, although studies have shown the contrary[94]. Equation 4.11 gives the fugacity coefficient of component k in the mixture as a function of the parameters in the Peng-Robinson EOS[28]:

$$\ln \phi_k = \frac{b_k}{b}\left(\frac{P.v}{R.T} - 1\right) - \ln\frac{P.(v-b)}{R.T} - \frac{a}{2.\sqrt{2}.b.R.T}\left[\frac{2\sum_i z_i.a_{ik}}{a} - \frac{b_k}{b}\right].\ln\frac{v+(1+\sqrt{2}).b}{v+(1-\sqrt{2}).b} \quad (4.11)$$

4.3 EXPERIMENTAL SECTION

4.3.1 *Materials*

We purchased glass-wool from Acros Organics, *n*-decane from TCI. All chemicals used had a purity higher than 98%. We purchased nitrogen (purity > 99.999%) and ethylene (purity > 99.5%) from Praxair. All chemicals were used without further purification.

4.3.2 *Solubility system setup*

We used a transpiration flow method technique [29], [30], [87], [88] to study the solubility of *n*-decane in compressed nitrogen and ethylene. This technique uses a saturator, where the less-volatile phase stays stationary while it is striped by the moving volatile phase. This technique provides a good model for the dissolution process of heterogeneous catalytic conversion of ethylene into higher alkenes because the coke (less-volatile phase) stays adsorbed in the catalyst bed, while the flowing supercritical ethylene (volatile phase) solubilizes it. The flow system provides a consistent tool to quantify the solubility of coke in ethylene, in the absence of the catalytic process.

The transpiration system used in the present work is a modification of the reactor presented in Chapter 3 (Figure 3.1). Briefly, the solubility setup consisted of a packed bed constructed with stainless-steel tubes and Swagelok fittings (Figure 4.1). We used a Swagelok Tee (SS-8-VCR-T) to construct a saturator, where we mounted a bed of glass-wool along the total length of the tee. Then, we pipetted *n*-decane on the glass-wool until the wool was fully saturated with liquid (~ 3-4 ml of *n*-decane) and mounted the saturator in the flow system. A gas manifold mounted with mass flow controllers (Parker) controlled ethylene and nitrogen flow rates and a back-pressure regulator (BPR - Equilibar ZF) downstream controlled the pressure of the system. The gas exiting the saturator through the back-pressure regulator flowed through a transfer line packed with glass-wool followed by a coalescing filter to remove entrained liquid from the gas before analysis. We measured the *n*-decane gas-phase molar fraction online using a GC-2014 (Shimadzu) coupled with TCD and FID detectors. We used an H-PLOTQ (Agilent, 30 m x 0.25 x 0.25µm) and DB-1 column (Agilent, 30 m x 0.53 m x 3µm) to study the solubility of *n*-decane in nitrogen and ethylene. We controlled the temperature of the system, saturator and transfer line, with heating tapes connected to PID controllers and measured the temperature using type K thermocouples (Figure 4.1 - TC).

4.3.3 *Solubility experiments*

We measured the solubility of *n*-decane in compressed nitrogen and ethylene at temperatures ranging from 30 to 100 ^{o}C and pressures ranging from 1 to 68 bar. We measured the temperature and pressure during the experiments with a variation of ± 2%, and for each experiment, we measured the concentration of the less-volatile component in the gas phase until it reached a steady value (steady-state). For the experiments reported in the present study, we used flow rates ranging from 20 to 100 ml/min. To confirm that equilibrium was attained, we measured the mole fraction of n-decane in the gas at varying flow rates to ensure that the concentration of *n*-

decane remained constant. We also measured the solubility under ambient pressure, in which the composition of the mixture can be calculated with good precision assuming ideal gas.

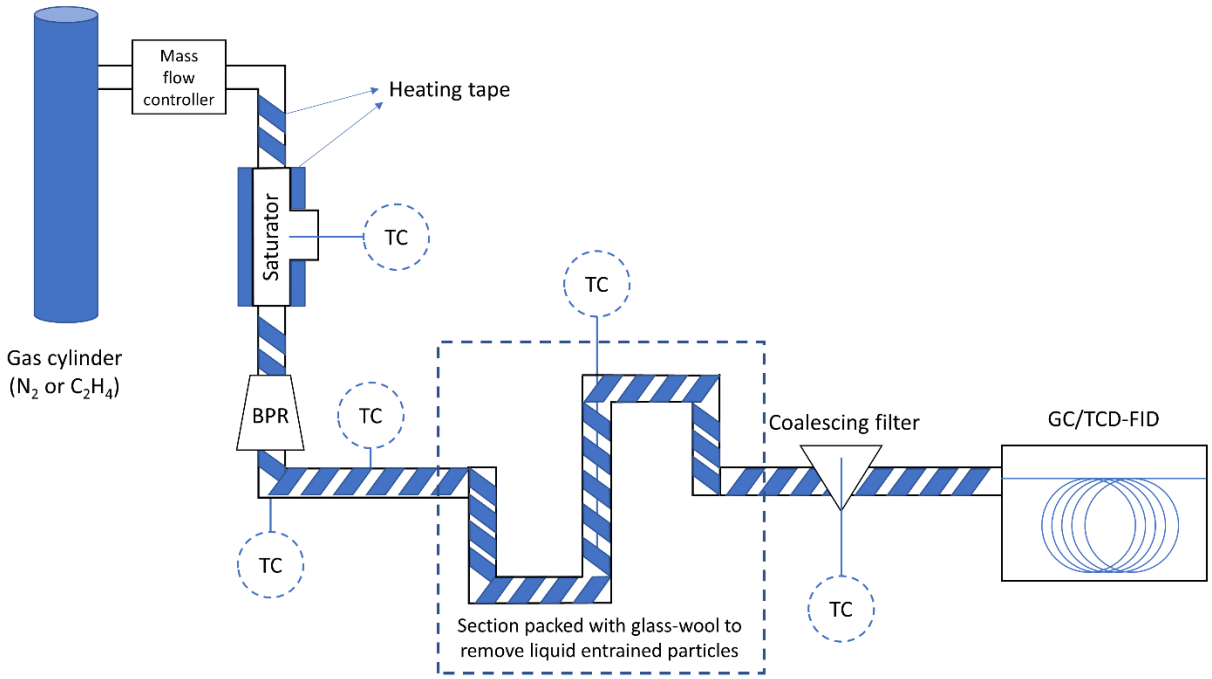

Figure 4.1. Schematic process flow diagram of the saturator system.

4.3.4 *Data treatment*

We used the thermodynamic model and EOS presented in Section 4.2 to fit the experimental data and calculate the equilibrium parameters for the virial and Peng-Robinson EOS. To obtain numerical values for the binary interaction parameters, we minimized the objective function F given by:

$$F = \sum_{i=1}^{n} \left(y_i^{exp.} - y_i^{calc.} \right)^2 \tag{4.12}$$

Where n is the number of experimental data points, and $y_i^{exp.}$ and $y_i^{calc.}$ are the experimental and calculated mole fractions of *n*-decane in the gas mixture, respectively.

4.3.5 *Pyridine sorption*

To measure the concentration of sites on the catalyst, we performed pyridine adsorption in a Shimadzu Prestige 21 FTIR mounted with a Harrick Scientific *in-situ* chamber. Prior to the adsorption, we pretreated the catalyst under vacuum (10^{-3} bar) at 300^{o}C for 30 min. Then, we reduced the temperature to 30^{o}C and introduced 20 µL of pyridine onto the catalyst. Afterward, we evacuated the catalyst at 250^{o}C for 30 min under vacuum to remove physically adsorbed pyridine from the catalyst surface and recorded the FTIR spectra under the same temperature. We determined the concentration of Brønsted and Lewis sites from the peak areas at 1450 and 1545 cm^{-1}, using the extinction coefficients reported by Emeis [53].

4.4 RESULTS AND DISCUSSION

4.4.1 *Nitrogen – n-decane system*

4.4.1.1 System validation

We evaluated the effect of gas flow rate on the mole fraction of *n*-decane in nitrogen. This step is important to ensure that the gas phase at the outlet of the saturator was at equilibrium with the liquid phase. We also verified the steady-state behavior of the system under long periods (>10 hours) to ensure reproducibility of data. A final assessment of the system employed solubility measurements under ambient pressure since the composition can be easily verified assuming ideal gas behavior.

Figure 4.2-A shows the effect of nitrogen flow rate on the molar fraction of *n*-decane in nitrogen at 75^{o}C and 38.8 bar. Changes in nitrogen flow rate had little impact on the steady-state mole fraction of *n*-decane in the nitrogen (mole fraction ~ 0.14%). Figure 4.2-B shows the long-term steady-state behavior of the solubility system at 75^{o}C and 27.0 bar. The system shows good stability even after 15 hours of time-on-stream (TOS) starting with an initial *n*-decane volume of

3000 µL. Prausnitz et al. reported that the solubility of *n*-decane in nitrogen[29], [30] did not change with changes in gas flow rates from 140 to 566 ml/min and *n*-decane volume when studying the solubility of *n*-decane in nitrogen using a flow-type solubility apparatus. For the rest of the experiments reported in the present Chapter, we used flow rates varying between 20 and 100 ml/min and an initial liquid paraffin volume of 3000 µL. The constant molar fraction with varying flow rate demonstrates that the system rapidly reaches equilibrium and that the flow system is well suited to measure the solubility of *n*-decane in compressed gases under equilibrium conditions. As an additional precaution to ensure that the system attained equilibrium, we measured the solubility of *n*-decane in nitrogen under ambient pressure. The experimental value obtained at 30°C (0.13%) and 1 atm is in good agreement with the calculated value assuming ideal-gas behavior (0.16%).

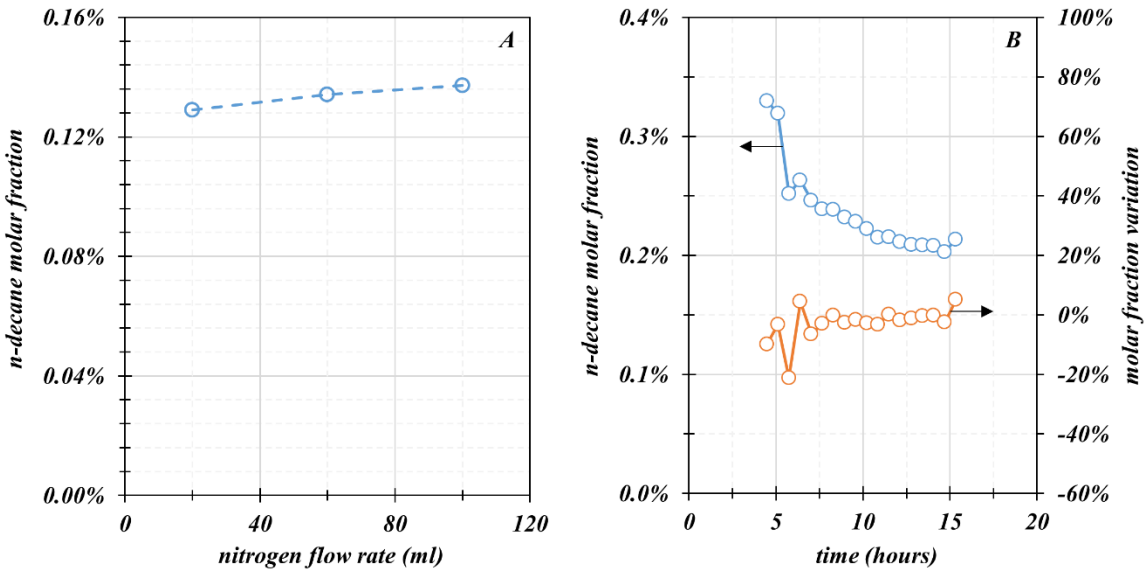

Figure 4.2. A – Effect of flow rate on the mole fraction of n-decane in nitrogen. Data collected under 75°C and 38.8 bar. B – Long term steady-state behavior of the solubility system. Data collected under 75°C and 27 bar.

4.4.1.2 Solubility of n-decane in nitrogen

The solubility of *n*-decane in nitrogen was extensively studied by Prausnitz et al.[29], [30]. As an additional validation step, we measured the solubility of *n*-decane in nitrogen under conditions similar to the ones studied by Prausnitz. Figure 4.3-A shows the vapor-phase solubility

of *n*-decane in nitrogen under pressures ranging between 1 and 110 bar. For comparison, we also present the data reported by Prausnitz et al. The results obtained with the flow system designed in the present work agree with the results reported by Prausnitz et al. Figure 4.3-B shows the n-decane vapor-phase fugacity coefficients as a function of temperature and pressure. Both temperature and pressure have a significant effect on the fugacity coefficient of n-decane in the gas phase. We used the experimental solubility data to calculate the second virial cross-coefficient according to the model and data treatment described in Sections 4.2.1 and 4.3.4, respectively.

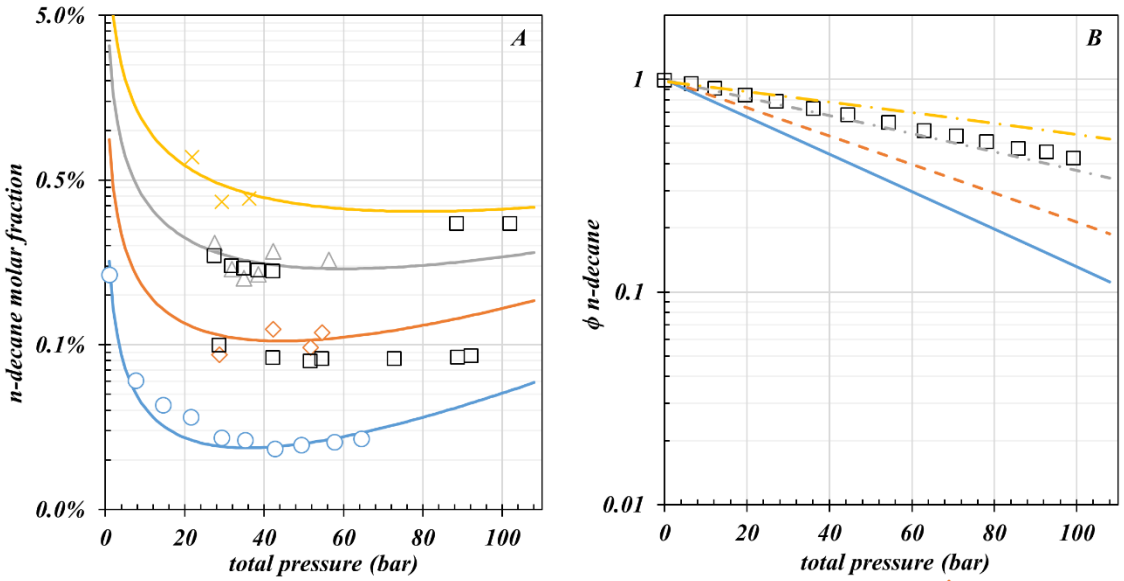

Figure 4.3. A – Vapor-phase solubility of n-decane in nitrogen at (○) 30, (◇) 50, (△) 75, and (×) 100 °C. (□) experimental solubility data reported by Prausnitz et al. in [30] and [29]. Solid lines show the calculated solubilities from the fitting of the thermodynamic model described in Section 4.2.1. B – n-decane vapor-phase fugacity coefficients calculated using the virial EOS at (—) 30, (– –) 50, (– –) 75, and (–·–) 100 °C. (□) Values reported by Prausnitz et al. at 75°C [29].

Table 4.1 shows the second virial cross-coefficients obtained from the fitting of the isotherms shown in Figure 3-A. We also show the second virial cross-coefficients reported by Prausnitz et al. under different temperatures for comparison.

Table 4.1. Second virial cross coefficients calculated from the solubility data shown in the present work compared with the values reported by Prausnitz et al. in [29]

Temperature (°C)	B_{12} ($cm^3.mol^{-1}$)	
	This work	Prausnitz et al.[29]
30	-256	-
50	-204	-148
75	-135	-111
100	-79	-82

The results show that the calculated second virial cross-coefficients are in good agreement with the values obtained by Prausnitz et al. It is important to note that the second virial cross-coefficient is negative for all temperatures and its value increases with increasing temperature. The second virial cross-coefficient is associated with the extent of attractive and repulsive forces between two molecules[95]. Large negative B_{12} values are associated with attraction between distinct molecules[28]. The trend shown in Table 4.1 is in support of the results present in Figure 4.3. At 30°C, the system shows a great extent of non-ideality associated with the presence of attractive forces between molecules of different species. In contrast, at high temperatures, repulsive forces prevail, increasing the extent of ideal gas behavior and consequently leading to an ideal mixture with fugacity coefficients equal to one. This is corroborated by the greater B_{12} value obtained at 100°C (B_{12} = -79 $cm^3.mol^{-1}$) compared to the value calculated at 30°C (B_{12} = -256 $cm^3.mol^{-1}$).

4.4.2 *Ethylene – n-decane system*

4.4.2.1 System validation

As shown in Section 4.4.1, the solubility system designed in the present study provides reliable measurements for the solubility of *n*-decane in nitrogen. To demonstrate that the flow system can also be used to measure the solubility of *n*-decane in ethylene, we measured the solubility of *n*-decane in ethylene at 30, 50, 75°C and ambient pressure, in which the solubilities

can be easily estimated assuming ideal gas behavior. Table 4.2 shows that the experimental solubilities are in good agreement with the predictions assuming ideal gas, which indicates that the ethylene – *n*-decane attained equilibrium at these conditions.

Table 4.2. Measured and calculated solubilities assuming ideal gas at 30, 50, and 75°C and 1 atm

	n-decane mole fraction (%)	
Temperature (°C)	Measured	Calculated assuming ideal gas
30	0.12	0.16
50	0.48	0.86
75	2.79	2.71

4.4.2.2 Solubility of n-decane in ethylene

Figure 4.4-A shows the solubility of *n*-decane in ethylene at 30, 50, and 75°C, and the modeled isotherms obtained using the Peng-Robinson EOS. Figure 4.4-B shows the calculated *n*-decane fugacity coefficient as a function of temperature and pressure. Modeled isotherms obtained from the fitting of the solubility data shows that the model agrees with the experimental results.

Analysis of the isotherms shown in Figure 4.4-A and the *n*-decane fugacity coefficients shown in Figure 4.4-B indicates that the solubility of *n*-decane in ethylene deviates from ideality very quickly with increasing ethylene pressure, driven by the increase in attractive forces between ethylene and *n*-decane. This behavior becomes even more pronounced at 30 °C, consistent with the analysis for the solubility of *n*-decane in nitrogen shown in Section 4.4.1. The *n*-decane fugacity coefficients calculated in nitrogen and ethylene show that the non-ideal behavior of *n*-decane in ethylene is much more pronounced than the one observed in nitrogen under the conditions used in the present study. For example, at 30°C and 68 bar, the *n*-decane fugacity coefficient in ethylene is 99% lower than the fugacity coefficient calculated in nitrogen under the same conditions. This difference is due to the great extent of attractive forces (potential energy) between *n*-decane molecules and ethylene relative to nitrogen.

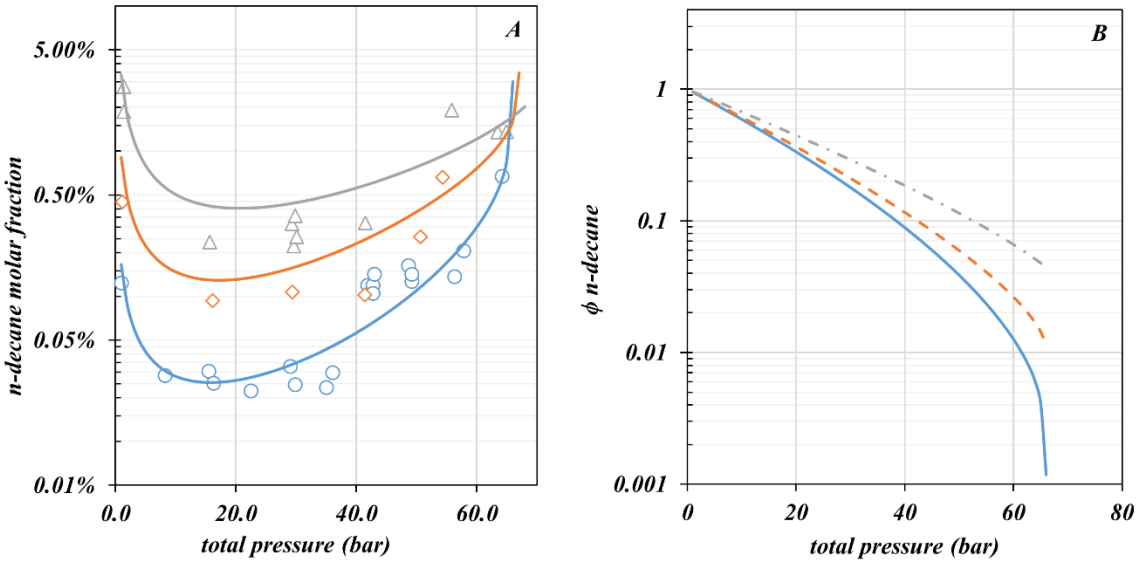

Figure 4.4. A – Vapor-phase solubility of n-decane in ethylene at (○) 30, (◇) 50, and (△) 75°C. Solid lines show modeled solubility isotherms from the fitting of the thermodynamic model described in Section 4.2.1 using the Peng-Robinson EOS. B – n-Decane vapor-phase fugacity coefficients calculated using Peng-Robinson EOS at (—) 30, (– –) 50, and (-··-) 75°C.

As the ethylene pressure increases, the mole fraction of *n*-decane in ethylene at 30°C approaches the values obtained at 50 and 75°C, Figure 4.4-A. Such behavior has been reported by Diepen at al. and Kurnik et al. when studying the solubility of naphthalene in ethylene and can be ascribed to the increased solvation power of ethylene beyond its critical point (T = 9.4°C, and P = 50.3 bar)[27], [87]. Figure 4.4-B shows that the calculated *n*-decane fugacity coefficient decreases rapidly (approximately 85%) beyond the ethylene critical pressure under 30°C, in agreement with the trends shown in Figure 4.4-A. The solubility enhancement at 30°C and pressures greater than 50.3 bar is associated with the increase in potential energy and decrease in kinetic energy of the gas[28]. The increase in potential energy leads to a substantial increase in attractive forces between *n*-decane and ethylene.

4.4.3 *Effect of the n-decane solubility on the ethylene oligomerization process*

The overall objective of the solubility study presented in Section 4.4.2 is to estimate the amount of coke solubilized during the ethylene oligomerization over the Ni-H-Beta catalyst. More

specifically, we are interested in the quantification of coke dissolution rates from the catalyst surface as a function of temperature and pressure. As presented in Section 4.4.2, *n*-decane was used as a model compound for coke based on its aliphatic nature and chain-length (CH_2/CH_3 ratio). Therefore, data for the solubility of *n*-decane in ethylene can be used to inform coke solubility in supercritical ethylene.

In addition, we can obtain coke production rate and alkene production rates from kinetic data at different conditions. A comparison of all the rates involved in the catalytic process provides a unique approach to elucidate the contribution of coke dissolution during the heterogeneous catalytic process. In Section 4.4.3.1, we discuss how coke dissolution rates affect reaction kinetics.

Figure 4.5 shows a simplified pathway considered in the present work for the oligomerization of supercritical ethylene. The simplified pathway includes *(1) transport* and *(2) coke production*. ***Pathway 1 – transport*** accounts for supercritical ethylene assisted dissolution of intermediates from the catalyst. ***Pathway 2 - coke production*** refers to intermediates that neither desorbed from the catalyst surface nor dissolved in supercritical ethylene. In the present work, we define coke as any intermediate that remained adsorbed on the catalyst surface after the reaction, and we used the mass of coke quantified after the reaction to calculate the average coke production rates, assuming a constant rate of coke production over time. It is important to note that the coke defined in the present work is apparent because the true amount of coke produced during the reaction is affected by the rates of chain-growth and intermediate desorption and dissolution[80]. Also, by assuming an average coke production rate over time, we are approximating the true coke production rate during the catalytic process, which can vary over time. Average coke production rates are given in g of coke.g of catalyst^{-1}.h^{-1} and were calculated by dividing the mass of coke on the catalyst measured after the reaction by the mass of catalyst and the total reaction time.

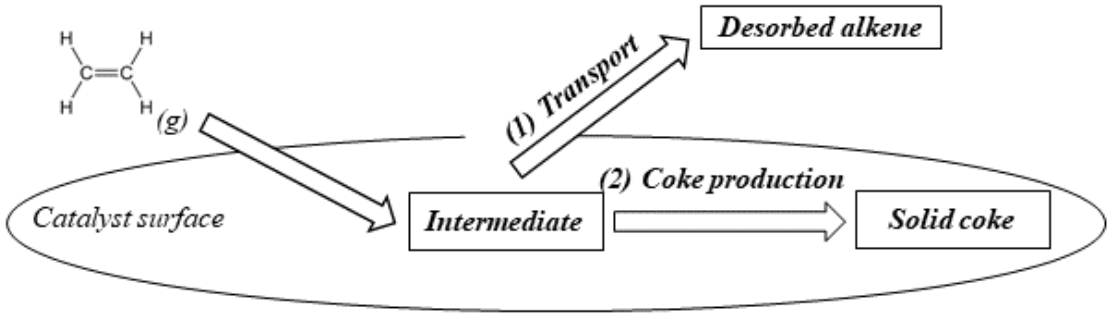

Figure 4.5. Simplified reaction pathway for the oligomerization of supercritical ethylene over the Ni-H-Beta.

Coke dissolution rates were calculated based on the thermodynamic model developed from solubility data. We calculated coke dissolution rates based on the following equation:

$$r = \frac{F.x.MW}{W} \quad (4.13)$$

Where F is the ethylene flow rate (in moles.h^{-1}) used during the ethylene oligomerization, x is the mole fraction of dissolved coke in the gas (at T and P) calculated from the thermodynamic model described in the present work based on *n*-decane as a model compound for coke, W is the mass of catalyst used during the reaction (in g), and MW is the molecular weight of *n*-decane = 142.29 g.moles^{-1}. Equation 4.13 gives coke dissolution rates in g of coke (based on *n*-decane as model compound).g of catalyst^{-1}.h^{-1}. We note that the coke dissolution rate based on solubility data expresses the maximum rate of coke dissolution since the system reaches thermodynamic equilibrium.

Alkene production rates were calculated based on the mass of ethylene converted according to the following equation:

$$r = \frac{F_{e,0}.X}{W} \quad (4.14)$$

Where $F_{e,0}$ is the inlet mass flow rate of ethylene (in g of ethylene.h^{-1}), W is the mass of catalyst (in g), X is the ethylene conversion, and r is the total rate of alkene production (in g of alkene.g

catalyst^{-1}.h^{-1}). The alkene production rate refers to alkenes that desorbed from the catalyst and were identified via gas chromatograph.

4.4.3.1 Effect of coke dissolution under supercritical conditions

We used kinetic data reported in previous works from our research group[25] in combination with the solubility data reported in the present work to investigate the effect of supercritical ethylene on the ethylene oligomerization over the Ni-H-Beta. Figure 4.6 shows the average coke production rate (g of coke.g catalyst^{-1}.h^{-1}), the coke dissolution rate (g of coke.g catalyst^{-1}.h^{-1}), and the alkene production rate (in g of alkene.g catalyst^{-1}.h^{-1}) as a function of temperature for the ethylene oligomerization under supercritical conditions (ethylene partial pressure = 52.5 bar).

Figure 4.6 shows the rates of alkene production, coke production, and coke dissolution at 30, 60, and 90^{o}C under supercritical conditions. At 30^{o}C, the reaction leads to a significant rate of production of desorbed alkene products, which can be attributed to (1) the high reaction rates under supercritical ethylene conditions, even at low temperatures and (2) the high ethylene solvation power above its critical point already observed and described in Section 4.4.2 via solubility data. At 30^{o}C, the coke dissolution rate is four-fold relative to the apparent coke production rate. If we assume that coke molecules solubilized by the supercritical fluid become gaseous products, then Figure 4.6 implies that 0.05 g of coke.g catalyst^{-1}.h^{-1} are formed at 30^{o}C, out of which 0.04 g of coke.g catalyst^{-1}.h^{-1} desorb as products, and 0.01 g of coke.g catalyst^{-1}.h^{-1} remains adsorbed on the catalyst. Products formed via coke dissolution correspond to almost 10% of total alkenes formed at 30^{o}C (0.04 out of 0.45 g of alkene.g catalyst^{-1}.h^{-1}).

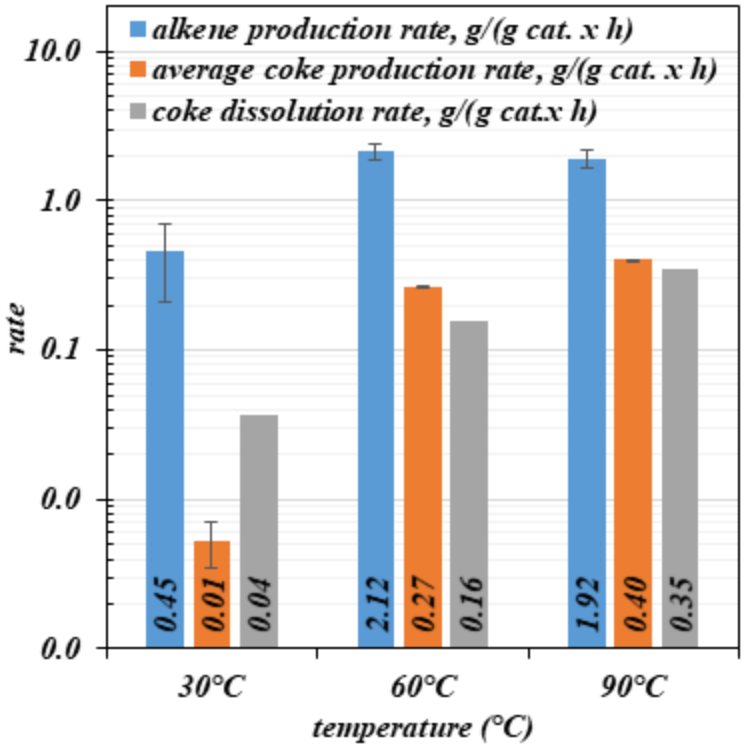

Figure 4.6. Semi-log plot showing the rates of alkene production, average coke production, and coke dissolution as a function of temperature for the oligomerization of supercritical ethylene (ethylene total pressure = 52.5 bar). Data extracted from [25].

The alkene production rate increases from 0.45 to 2.12 g of alkene.g catalyst^{-1}.h^{-1} as the temperature increases from 30 to 60^{o}C. The average coke production and coke dissolution rates follow a similar trend, with increases from 0.01 and 0.04 g of coke.g catalyst^{-1}.h^{-1} to 0.27 and 0.16 g of coke.g catalyst^{-1}.h^{-1}, respectively. The results show that the increase in coke solubility with temperature did not outcompete the increase in intermediate formation, and a substantial fraction of the products remained on the catalyst (approximately 11% of the products). With increasing temperature from 60 to 90^{o}C, the alkene production rate remained constant, while both the average coke production and coke dissolution rates increased from 0.27 and 0.16 g of coke.g catalyst^{-1}.h^{-1} to 0.40 and 0.35 g of coke.g catalyst^{-1}.h^{-1}, respectively. In this case, the selectivity to coke increased from 11% at 60^{o}C to 17% at 90^{o}C.

Figure 4.6 shows that catalyst activity increased with an initial increase in temperature from 30 to 60^{o}C, as one would expect, leading to increase in the rates of production of desorbed alkenes. The average coke production also increased, despite the increase in coke solubility. However, with an additional increase in temperature to 90^{o}C, the process favored coke production, which suggests that the transport of products from the catalyst surface to the gas does not outcompete the increase in rates of intermediate formation. We note that even though coke dissolution is enhanced at 60 and 90^{o}C, high chain-growth rates favor the production of intermediate products on the catalysts surface, which eventually leads to coke production.

Accumulation of coke on the catalyst at 60 and 90^{o}C may cause pore plugging. As we showed in our previous publication[25], there is a substantial decrease in catalyst surface area from 677 m^2/g for the fresh Ni-H-Beta to 550 and 78 m^2/g for the spent catalysts at 30 and 120^{o}C, respectively. Plugging of catalyst pores may prevent ethylene from reaching active sites, which can explain the small increase in alkene production rate with temperature from 60 to 90^{o}C.

In the case that pore plugging does not limit accessibility to active sites, we hypothesize that the active sites may become populated by high molecular weight products at high temperature under supercritical conditions, contributing to the production of coke on the catalyst and eventually poisoning of active sites. To validate this hypothesis, we measured the concentration of sites available for reaction via pyridine adsorption. The Ni-H-Beta contains a concentration of Brønsted and Lewis sites of 54 and 213 μmol/g, respectively. It is well accepted that nickel exchange on acidic inorganic supports leads to the formation of additional Lewis sites, consequently causing a reduction in the number of Brønsted sites[7], [10], [11], [16]. Both Lewis and Brønsted sites interact with ethylene molecules and desorbed products. We estimate that the number of moles of ethylene inside the reactor (~ 1-2 moles) under supercritical conditions is orders of magnitude

higher than the moles of active sites available for reaction (~ $1.6x10^{-3}$ moles). Furthermore, based on the experimental results reported in [25], we estimate that the number of moles of alkene products inside the reactor varies between 0.1 and 0.5 moles. The greater amount of ethylene and alkene products compared to active sites available for reaction supports our hypothesis that the active sites may become occupied quickly under supercritical conditions.

Therefore, even though supercritical ethylene might contribute to transport of products via supercritical fluid extraction of the coke from the catalyst surface, coke dissolution rates cannot outcompete the high reaction rates under supercritical conditions at high temperatures. As a result, coke accumulates on the catalyst pores causing pore plugging and deactivation of the active sites. Based on the pathway proposed in Figure 4.5, under supercritical conditions and low temperatures (30^oC) ***(1) transport*** of products from the catalyst to the bulk of the gas is fast. However, at high temperatures ***(1) transport*** limits the catalytic process. Note that the transport limitation is associated with the catalyst inability to keep its surface clean under high temperatures, due to the high rates of intermediate formation, which can cause pore plugging. This process leads to ***(2) coke production*** at high temperatures.

Even though coke is appreciably soluble in supercritical ethylene at low and high temperatures under supercritical conditions, coke dissolution rates are not enough to offset the high rates of coke production on the catalyst surface at high temperatures. Figure 4.7 summarizes the main conclusions of the present work by showing the preferential pathways involved in the oligomerization of supercritical ethylene over the Ni-H-Beta as a function of reaction conditions.

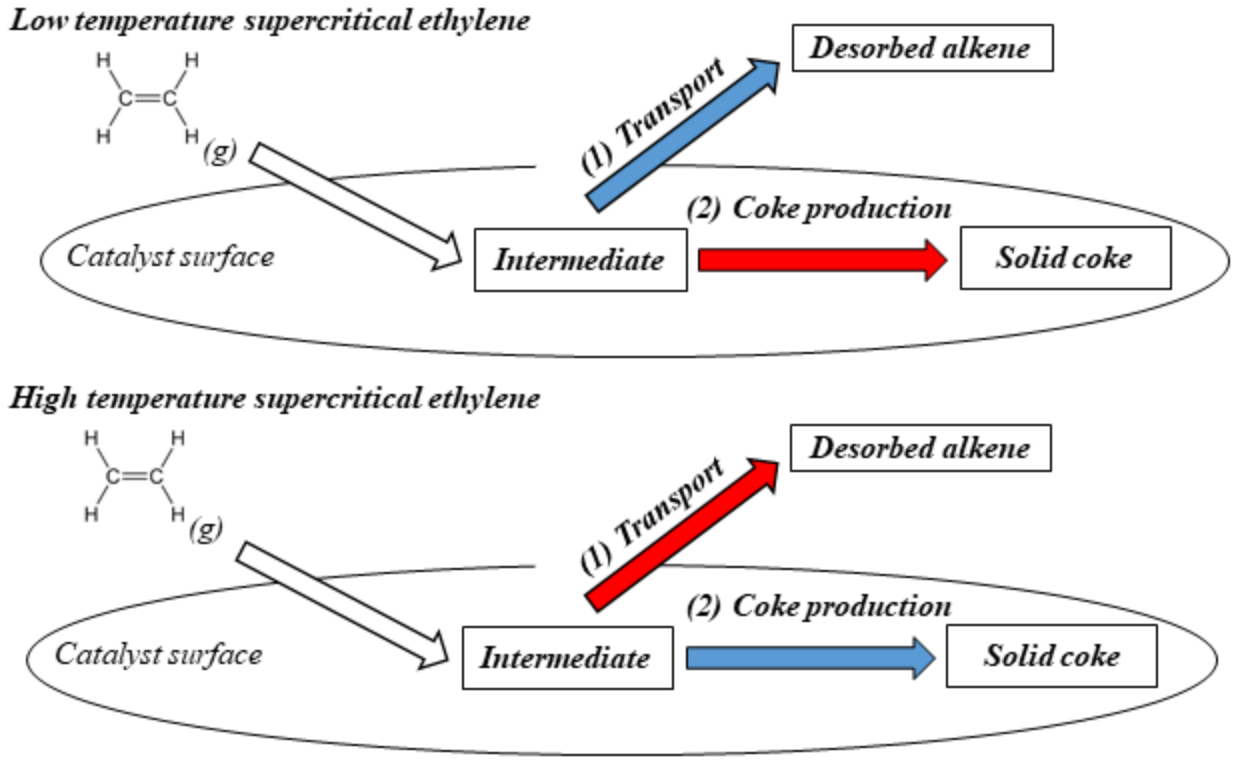

Figure 4.7. Preferential pathways involved in the oligomerization of supercritical ethylene at low and high temperatures. Blue arrows: More selective pathways. Red arrows: Less selective pathways.

4.5 CONCLUSION

In this study, we discuss the effects of coke solubility on the oligomerization of supercritical ethylene. To study the solubility of coke in ethylene, we used *n*-decane as a model compound for the coke. We reported the solubility of *n*-decane in nitrogen and ethylene. Data obtained for the nitrogen – *n*-decane system indicates that the results are in good agreement with the results reported in the literature[28]–[30]. The experiments on the solubility of *n*-decane in ethylene show that the system deviates from ideality very quickly with increasing ethylene partial pressure. Beyond the ethylene critical point, we found that the solubility of *n*-decane in ethylene at 30^{o}C approaches the solubility values observed at 50 and 75^{o}C under the same pressures.

Comparison of kinetic and solubility data in supercritical ethylene suggests that at low temperatures (30^{o}C), coke dissolution actively promotes the removal of coke from the catalyst. However, increase in temperature from 30 to 60 and 90^{o}C causes a large increase in both alkene production and coke production rates, causing occupation of most or all active sites by products. At high temperatures (90^{o}C), this process can lead to pore plugging. Therefore, we hypothesize that under supercritical conditions and high temperatures, transport of products from the catalyst surface limits the catalytic process, thus, favoring the production of coke on the catalyst. Even though coke dissolution still aids transport of products from the catalyst surface to the gas, coke dissolution by supercritical ethylene cannot outcompete the high reaction rates under supercritical conditions and high temperatures.

Chapter 5. KINETICS OF SUPERCRITICAL ETHYLENE OLIGOMERIZATION OVER THE NI-H-BETA[7,8]

Abstract

We discuss the kinetics of supercritical ethylene oligomerization over the Ni-H-Beta at 30, 50, 75, and 100°C and ethylene partial pressures ranging between 53 and 62 atm. At 30°C, the selectivity for C_4 decreases from 65.0 to 19.7 wt. % with increasing ethylene partial pressure from 53 to 62 atm, while the selectivity for C_{16} increases with pressure, with a maximum of 49.8 wt. % at 60 atm. At an ethylene partial pressure of 60 atm, the selectivity for C_{16} decreases from 49.8 to 4.3 wt. % with increasing temperature from 30 to 100°C. The trend in product selectivity suggests that low temperatures favor the formation of long-chain products, while high temperature favors the formation of light products under supercritical conditions.

The activation energies for ethylene oligomerization decreases from 75.9 to 37.8 kJ/mol with increasing ethylene partial pressure from 53 to 62 atm. The decrease in activation energy with pressure may be attributed to the accumulation of products on the catalyst at high pressures, as discussed in Chapter 4. In this case, the consumption of ethylene and the formation of products becomes dependent on how much the catalyst surface is exposed, thus decreasing the effect of temperature on ethylene consumption rates.

We propose 3 models for the oligomerization of supercritical ethylene over the Ni-H-Beta assuming different reaction limiting steps (adsorption, chain-growth, and desorption). The Langmuir-Hinshelwood-Hougen-Watson kinetics was used to model the rate expressions for the

[7] To be submitted to the Journal of Supercritical Fluids, Gabriel V. S. Seufitelli, Fernando L. P. Resende, Rick Gustafson.

[8] Work presented at the American Institute of Chemical Engineers (AIChE) Annual Meeting in 2019.

formation of C_4, C_6, C_8, C_{10}, C_{12}, C_{14}, and C_{16} alkenes. The model that assumes desorption of products as the reaction limiting step provides the best fit of the kinetic data among the models proposed in the present work. Therefore, the results indicate that the slow desorption of products from the catalyst surface under supercritical conditions limits the reaction. This result agrees with results presented in the coke solubility research (Chapter 4) and helps to understand the effects of supercritical medium during ethylene oligomerization over the Ni-H-Beta.

Keywords: Supercritical fluid, ethylene oligomerization, kinetic model, desorption.

5.1 INTRODUCTION

In recent years, the crude oil price has been fluctuating, affecting the price of transportation fuels. Environmental implications also contribute to the price increase in crude oil-derived fuels due to carbon taxes in oil refineries. Therefore, technologies that can produce liquid fuels via alternative routes are becoming necessary. Over the years, ethylene oligomerization has been a process of interest in both industry and academia. The special interest in this technology lies in the possibility to produce high-value molecules (alkenes) that could be transformed into drop-in fuels after a simple hydrogenation process.

Most of the ethylene produced worldwide comes from the thermal cracking of refinery gas and naphtha[96]. Refinery off-gas (dry gas) from fluid catalytic cracking (FCC) and delayed cocker units in oil refineries can also supply ethylene[97]. These are low-value diluted streams usually burned to recover energy, which can be transformed into high-value chemicals via oligomerization. Ethylene can also be produced via steam reforming of ethane from shale gas[31], [98]. This route is becoming popular in the U.S. and several cracking facilities are opting to crack ethane instead of naphtha. A more environmentally-friendly route uses lignocellulosic ethanol to produce ethylene via dehydration, which can then be used to produce high-value alkenes[76].

Commercial ethylene oligomerization processes use homogeneous catalysts[99]. These catalysts are usually dissolved in organic solvents[100], which creates technical and environmental implications since the products need to be separated from the reaction medium. As an alternative, heterogeneous catalysts have been investigated for ethylene oligomerization. These catalysts are more environmentally-friendly because they do not require mixing with solvents. Also, product separation in heterogeneous catalytic reactions is relatively easier and cheaper than product separation in its homogeneous counterpart[2]. Several heterogeneous catalysts have been reported for ethylene oligomerization, such as Ni-H-Beta[7], Ni-MCM-41[44], Ni-SBA-15[18], and Ni-SIRAL[58].

It has been shown that nickel-based solid catalysts can achieve high ethylene conversions with good stability over long reaction times. However, selectivity for butene is still high over these catalysts, which imposes limitations for the commercial implementation of this technology since higher molecular weight alkenes are desirable. To increase the molecular weight of the final product, LanzaTech in partnership with the Pacific Northwest National Laboratory (PNNL) designed a two-steps oligomerization process[66]. In this process, ethylene oligomerization takes place over the Ni-H-Beta in two consecutive reactors, where the light alkenes downstream of the first reactor undergo further oligomerization in a second reactor. In addition to drop-in fuels, these high molecular weight alkenes can be used in a wide range of applications including plasticizers (C_8 and C_{10}), lubricants (C_{10}), detergents (C_{12}, C_{14}, and C_{16}), sanitizers (C_{12}, C_{14}, and C_{16}), and even sizing agents for the paper industry (C_8-C_{16})[1], [99].

As a novel alternative to produce long-chain alkenes, our research group proposed in previous publications oligomerization of supercritical ethylene[13], [25]. We showed that the oligomerization of supercritical ethylene increases the selectivity for C_{10+} alkenes[13]. Also,

depending on the reaction conditions, supercritical ethylene may dissolve coke molecules, thus, promoting *in-situ* catalyst regeneration during the reaction[13], [25], [27], [83]. This is especially desirable since catalyst deactivation is a major problem in heterogeneous catalytic reactions.

To further understand the dissolution of coke in supercritical ethylene, in Chapter 4, we modeled the solubility of coke in subcritical and supercritical ethylene using *n*-decane as a coke model compound. Our results suggest a great increase in coke solubility beyond the ethylene critical point, with a more perceptible increase at low temperatures (30^{o}C). Comparison of solubility and kinetic data at 30^{o}C indicates that transport of molecules from the catalyst surface to the gas is faster relative to the rates of alkene production due to the high solubility of long-chain molecules in supercritical ethylene and low temperatures. However, at high temperatures (90^{o}C), coke dissolution rates are not able to outcompete the high rates of oligomerization, thus, favoring the accumulation of products on the catalyst.

Production of high molecular weight products in heterogeneous ethylene oligomerization is especially challenging because: (1) product selectivity decreases with increasing product molecular weight, in other words, carbon number[33], [101] and (2) long-chain products have lower diffusivities compared to light products, which favors the accumulation of carbon deposits on the catalyst (coke).

This Chapter presents the continuation of on-going research to elucidate the effects of the supercritical ethylene in the oligomerization of ethylene over the Ni-H-Beta. To continue the work towards the development of a supercritical ethylene oligomerization process, we propose in the present study a kinetic model for the oligomerization of supercritical ethylene.

Kinetic models for ethylene oligomerization over nickel-based solid catalysts have been discussed in only few publications over the years[19], [20], [23], [34], [67]. Riekert et al.

investigated the ethylene oligomerization over a NiNaY zeolite at 350^{o}C and low ethylene pressures[20]. They found that desorption controls the overall catalytic process due to the slow release of butene from the catalyst surface. Reikert et al. calculated a true activation energy of 88 kJ.mol^{-1}. Espinoza et al. studied the ethylene oligomerization over nickel-exchanged amorphous silica-alumina and used a random dimerization/co-dimerization model to fit experimental kinetic data to a first-order kinetic model[67]. Ng and Creaser studied the kinetics of ethylene dimerization over a NiNaY catalyst and reported apparent activation energy ranging between 58.6 and 42.1 kJ/mol[19]. The authors used a first-order kinetic model to fit the experimental data. More recently, Toch et al. studied the kinetics of ethylene oligomerization over nickel-exchanged amorphous silicate and H-Beta[23], [34]. The authors used Single-Event MicroKinetic modeling to develop a complex kinetic model for the process. According to Toch et al., the activation barrier involved in the conversion of ethylene into alkenes is 74 kJ.mol^{-1}[23], [34]. In Chapter 3, we developed a kinetic model for ethylene oligomerization over a Ni-H-Beta catalyst using the Langmuir-Hinshelwood-Hougen-Watson kinetics. We provided indications that butene participates as a co-reactant in oligomerization reactions in subcritical ethylene. We note that the present study is the first to model the kinetics of supercritical ethylene oligomerization over nickel-based solid catalysts.

We developed a kinetic model for the oligomerization of supercritical ethylene at 30, 50, 75, and 100 ^{o}C and ethylene partial pressures ranging between 53 and 62 atm. Similar to the approach used in Chapter 3, we used the Langmuir-Hinshelwood-Hougen-Watson kinetics to model reaction rate expressions for the consumption of ethylene and formation of even carbon numbered products ranging between C_4 and C_{16}. The overall objective of this study is to develop

a kinetic model that helps to understand the formation of high molecular weight alkenes during the oligomerization of supercritical ethylene over nickel-based solid catalysts.

5.2 EXPERIMENTAL SECTION

5.2.1 *Catalyst synthesis*

The catalyst used in this study is the Ni-H-Beta already reported in several publications from our group[13], [24]–[26]. Briefly, the NH_4-Beta support (Si/Al = 12.5) was purchased from Zeolyst International. The Ni-H-Beta catalyst was prepared via impregnation of NH_4-Beta with a 0.51 M solution of $Ni(NO)_3$ for 6 hours. After impregnation, the solids were recovered via vacuum filtration and dried overnight at 100^{o}C. Finally, the solids were calcined at 550^{o}C for 6 hours to obtain the Ni-H-Beta catalyst. The nickel loading of the Ni-H-Beta catalyst was 4.1 wt. %. The same catalyst was already characterized in previous publications from our group[13], [24]–[26]. Nitrogen (purity = 99.9 %) and ethylene (purity = 99.5 %) were purchased from Praxair and used without further purification.

5.2.2 *Ethylene oligomerization experiments*

We used a fixed-bed reactor already described in Chapter 3 (Figure 3.1). The reactor was designed to work at temperatures up to 500^{o}C and pressures up to 68 atm. Heating tapes connected to PID temperature controllers were used to control both reactor and transfer line temperatures. The transfer line used to sample the gas from the outlet stream of the reactor was kept at 200^{o}C to avoid condensation of products before they reached the sample valve. A dome loaded back-pressure regulator (Equilibar ZF series) was used to control the pressure of the reactor. In a usual run, 250 mg of catalyst (average particle diameter = 750 μm) was loaded into the reactor. Quartz-wool (Acros Organics) was used as support to hold the catalyst powder in place. Then, the reactor

was pretreated overnight (>15 hours) at 300^{o}C at a nitrogen flow of 100 ml/min. After pretreatment, we cooled-down the reactor to the reaction temperature and admitted a mixture of ethylene and nitrogen (ethylene mole percent = 93%) into the reactor at a flow rate greater than 700 ml/min to pressurize the reactor. After the reactor reached the reaction pressure, we reduced the total flow rate to 300 ml/min (ethylene = 280 ml/min and nitrogen = 20 ml/min) to start the reaction.

We used a GC-FID/TCD (Shimadzu GC-2014) equipped with a DB-1 column (Agilent 125-1034, 30-m × 0.53-mm × 3.00 µm) to analyze the gas at the outlet of the reactor. We quantified alkenes ranging from C_4 to C_{16}. We measure the composition of the reactor outlet stream online using a pneumatic 6-way valve mounted with a 1 ml sample loop, sampled every 25 min. Each experiment was performed until the product composition reached steady-steady (~6 hours). Because of the mild temperatures employed in the present study, cracking products with odd carbon number were negligible. The mass balance closure for the experiments remained within ±2% with the exception of the experiments performed at 100oC, in which the mass balance closure was ±9%.

5.2.3 *Kinetic metrics*

We calculated the ethylene conversion and selectivities for products according to the following equations:

$$X = \frac{F_{products}}{F_{a0}} \tag{5.1}$$

$$S_i\ (wt.\%) = \frac{\text{mass of product i}}{\text{total mass of products}} \tag{5.2}$$

$$S_i\ (mole\ \%) = \frac{\text{moles of product i}}{\text{total moles of products}} \tag{5.3}$$

Where X is the ethylene conversion, $F_{products}$ is the mass flow rate of products at the outlet stream of the reactor, and F_{a0} is the inlet mass flow rate of ethylene into the reactor. We chose to calculate the ethylene conversion based on the products due to the unreliable measurement of ethylene mole fraction via GC. In Equations 5.2 and 5.3, S_i is the product selectivity for alkene i in wt. % and mole %, respectively. All measurements were performed at steady-state conditions.

We showed in Chapter 3 that under the conditions used in the present study, the reactor operates at differential mode. Therefore, the rates of ethylene consumption and alkene formation can be approximated by the following equations:

$$-r_{C_2H_4} = \frac{F_{a0}X}{\Delta W} \tag{5.4}$$

$$r_i = \frac{F_i}{\Delta W} \tag{5.5}$$

Where F_{a0} is the inlet mass flow rate of ethylene, ΔW is the mass of catalyst, X is the ethylene conversion, $-r_{C_2H_4}$ is the ethylene consumption rate, r_i is the production rate of alkene i, and F_i is the mass flow rate of alkene i downstream of the reactor.

5.2.4 *Kinetic model development*

The reaction rates developed in the present work are based on the Langmuir-Hinshelwood-Hougen-Watson (LHHW) kinetics. We compare three models assuming different reaction limiting steps (RLS). We discuss each model in more detail throughout the chapter. Due to the large number of isomers, we lumped the products according to their carbon number. We developed rate expressions for the consumption of ethylene and production of butene (abbreviated as C_4), hexene (abbreviated as C_6), octene (abbreviated as C_8), decene (abbreviated as C_{10}), dodecene (abbreviated as C_{12}), tetradecene (abbreviated as C_{14}), and hexadecene (abbreviated as C_{16}). We calculated the kinetic parameters for each model by minimizing the following objective function:

$$f_{min} = \sum_{j=1}^{n} \sum_{i=1}^{s} \left(r_{i,j\ (exp.)} - r_{i,j\ (calc.)} \right)^2 \quad (5.6)$$

Where, $r_{i,j\ (exp.)}$ and $r_{i,j\ (calc.)}$ are the experimental and calculated reaction rates, respectively, for species *i* at condition *j*, *s* is the number of species, and n is the number of experimental data points.

5.2.5 *Model treatment and statistics*

The confidence intervals for calculated kinetic parameters were estimated by applying the bootstrap method[69]. In total, 100 data sets were generated for each model by resampling the modeled data. We assumed that the error propagation of the model was randomly distributed among the calculated rates. The error was calculated according to the following equation:

$$\varepsilon_{i,j} = r_{i,j\ (exp.)} - r_{i,j\ (calc.)} \quad (5.7)$$

In the above equation, $\varepsilon_{i,j}$, $r_{i,j\ (exp.)}$, and $r_{i,j\ (calc.)}$ are the model error, experimental reaction rate, and calculated reaction rate, respectively, for species i at condition j (reactor temperature and ethylene partial pressure at steady-state). A data set with size $i \times j$ was obtained from Equation 5.7. Rates used to calculate the model error are given in mmole.g of cat.$^{-1}$.h^{-1}. We used a random function to attribute the error for each resampled data point. We chose the ethylene partial pressure at steady-state as the independent variable for this analysis. The rates where resampled according to the following equation:

$$r_{i,j} = r_{i,j\ (calc.)} + \varepsilon_r \quad (5.8)$$

Where $r_{i,j\ (calc.)}$ is the original calculated reaction rate of species i at condition j (according to the kinetic model), ε_r is the error randomly chosen from the data set of errors calculated according to Equation 5.7 (data set with size $i \times j$), and $r_{i,j}$ is the resampled reaction rate given at the same condition j as $r_{i,j\ (calc.)}$. We recalculated all kinetic parameters for each data set after resampling the data, by minimizing the objective function given by Equation 5.6. A total of 100 values for

each parameter were generated, from which we estimated the parameter uncertainty with a confidence level of 95% [69].

5.3 RESULTS AND DISCUSSION

5.3.1 *Effect of temperature and pressure*

Table 5.1 summarizes the selectivities for C_4, C_6, C_8, C_{10}, C_{12}, C_{14}, and C_{16} alkenes as a function of temperature and pressure. The results presented in Table 5.1 are also plotted in Figure 5.1 for better visualization of the trends in the data. Note that for all conditions listed in Table 5.1, ethylene is a supercritical fluid. Table 5.1 also shows the selectivity for C_{10+} alkenes, which comprises the sum of selectivities for C_{12}, C_{14}, and C_{16} alkenes. At 30^{o}C, there is a sharp decrease in C_4 selectivity from 65.0 to 19.7 wt. % with increasing ethylene partial pressure from 53 to 62 atm, which indicates an increase in the consumption of butene with increasing pressure. On the other hand, the selectivity for C_{16} increases with increasing pressure at 30^{o}C, with a maximum of 49.8 wt. % at 60 atm. At this pressure, the selectivity for C_{10+} also reaches a maximum of 69.6 wt. % at 30^{o}C. The increase in C_{16} selectivity corresponds to an 8-fold increase relative to selectivity observed at 53 atm. The evident increase in product molecular weight with increasing pressure at 30^{o}C may be attributed to the increase in chain-growth rates with pressure combined with the high solubility of long-chain hydrocarbons in supercritical ethylene as discussed in Chapter 4. This process helps to keep the catalyst surface "clean"[13] by reducing the rates of product accumulation on the catalyst.

At 50 ^{o}C, the increase in C_{16} and C_{10+} selectivities are less steep relative to the increases observed at 30^{o}C. The maximum selectivity for C_{16} and C_{10+} at 50^{o}C takes place at an ethylene partial pressure of 56 atm, lower than the pressure where the maximum selectivities for C_{16} and C_{10+} are observed at 30^{o}C. In Chapter 4, we compared the solubility of *n*-decane in supercritical

ethylene at 30, 50, and 75°C, and found a greater increase in *n*-decane solubility with pressure at lower temperatures. Therefore, the higher selectivities for C_{16} and C_{10+} at 30°C relative to 50°C shown in Table 5.1 may be explained by the high solubility of long-chain alkenes in supercritical ethylene and low temperatures.

Table 5.1. Overview of ethylene conversion and product selectivity as a function of temperature and pressure

T (°C)	ethylene partial pressure (atm)	ethylene conversion (%)	product selectivity (wt. %)								
			C_4	C_6	C_8	C_{10}	C_{12}	C_{14}	C_{16}	C_{10+}	m.b. (%)
30	53	0.1	65.0	1.0	0.3	2.7	9.8	14.7	6.5	31.0	98.5
	56	0.2	29.0	4.9	3.5	5.5	6.5	6.5	44.1	57.1	98.9
	60	0.2	19.9	4.4	1.8	4.3	0.8	19.0	49.8	69.6	101.2
	62	0.2	19.7	4.9	3.1	5.0	4.2	22.3	40.7	67.2	101.8
50	53	0.2	49.7	2.5	0.5	2.5	14.0	19.1	11.8	44.8	98.8
	56	0.5	18.3	5.1	4.0	2.8	1.4	29.9	38.5	69.8	98.9
	60	0.2	29.6	9.8	8.1	6.6	4.8	14.8	26.3	45.9	101.5
	62	0.3	36.5	10.0	6.2	3.1	1.7	15.3	27.2	44.2	102.1
75	53	1.2	11.3	4.3	5.1	4.3	8.8	41.1	24.9	74.9	99.7
	56	2.1	17.5	5.2	6.4	4.4	10.8	36.1	19.6	66.4	101.2
	60	1.0	14.6	9.1	8.3	7.2	7.5	36.3	16.9	60.7	102.1
	62	0.9	23.5	11.7	10.7	8.7	5.6	23.4	16.4	45.5	102.2
100	53	9.2	24.2	19.0	17.6	14.0	11.3	10.1	3.8	25.2	107.1
	56	9.6	20.2	20.5	17.5	12.3	11.2	17.3	1.0	29.5	107.1
	60	10.6	23.8	26.5	20.1	12.5	5.7	7.1	4.3	17.1	109.3
s.d.[1]		0.2	5.6	1.1	0.8	3.0	2.9	6.4	1.4		

[1] standard deviation.

With a further increase in temperature from 50 to 75°C, the selectivities for C_{16} and C_{10+} decrease from 24.9 and 74.9 wt. % at 53 atm to 16.4 and 45.5 wt.% at 62 atm, respectively. On the other hand, with increasing pressure from 53 to 62 atm at 75°C, the selectivities for C_4, C_6, and C_8 increase from 11.3, 4.3, and 5.1 wt. % to 23.5, 11.7, and 10.7 wt. %, respectively. Although the selectivities for C_{16} and C_{10+} is still high at 75°C, the trends in selectivities with pressure indicate

that as pressure increases, product formation rates outcompete the rates of product dissolution from the catalyst surface. A similar trend is observed at 100°C, where the selectivities for C_4 and C_{16} remain constant with pressure. Note that the selectivities for C_{16} and C_{10+} at 100°C are the lowest among the temperatures studied in the present work.

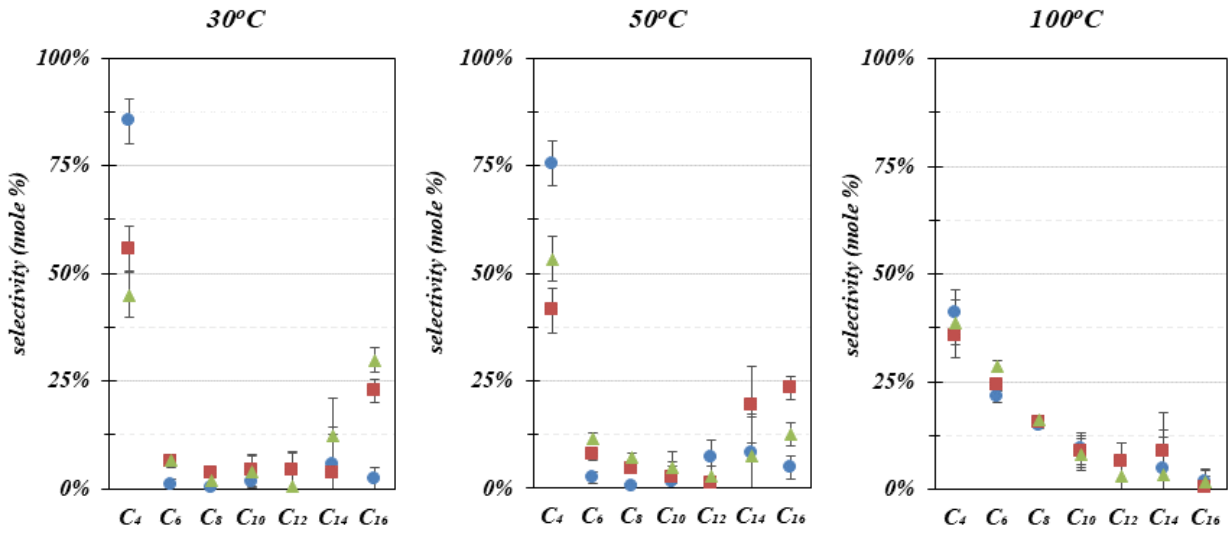

Figure 5.1. Selectivity (in mole %) for C_4-C_{16} alkenes at 30, 50 and 100°C and ethylene partial pressures of (●) 53, (■) 56, and (▲) 60 atm. Same data shown in Table 5.1.

Analysis of the effect of temperature and pressure in the oligomerization of supercritical ethylene over the Ni-H-Beta suggests that product dissolution rates outcompete the rates of product formation at 30 and 50°C. This contributes to the high selectivities for C_{16} and C_{10+} at these temperatures. However, with an increase in temperature from 50 to 75°C, the rates of product formation start to outcompete the rates of product dissolution from the catalyst. At 100°C, product formation rates are high, which causes the accumulation of products on the catalyst, leading to a decrease in C_{16} and C_{10+} selectivity.

Figure 5.2 shows the Arrhenius plots for the ethylene consumption at 53, 56, 60, and 62 atm and temperatures varying between 30 and 100°C. Table 5.2 shows the apparent activation

energies as a function of ethylene partial pressure. Toch et al. reported a value of 74.0 kJ/mol for the apparent activation energy in the oligomerization of subcritical ethylene over the Ni-H-Beta at an ethylene partial pressure of 3.5 bar[23]. At 53 atm, we calculated a value for the apparent activation energy of 70.8 kJ/mol under supercritical conditions. As shown in Table 5.2, the upper-end value for the apparent activation energy at 53 atm is above the value reported by Toch et al. It is important to note that although the activation energy calculated in the present work agrees with the value reported by Toch et al., the values were calculated at different conditions.

One can see in Table 5.2 that the apparent activation energies decrease from 70.8 to 34.7 kJ/mol with increasing ethylene partial pressure from 53 to 62 atm. In Chapter 3, we calculated a value of 43.7 kJ/mol for the apparent activation energy of the oligomerization of subcritical ethylene at 28 atm and 100^{o}C. Since the conditions used in the work described in Chapter 3 were similar to the conditions used by Toch et al., we justified the lower activation energy obtained in Chapter 3 to the consumption of butene by reaction. One evidence for this conclusion was the steep decrease in butene selectivity with the temperature obtained in Chapter 3 (Figure 3.3). However, the selectivities reported in Table 5.1 show that the selectivity for C_4 remains constant with the temperature at 56, 60, and 62 atm. Therefore, an alternative explanation for the decrease in ethylene consumption rates with the temperature at high ethylene partial pressures could be attributed to internal diffusion limitations of ethylene on the catalyst's pores.

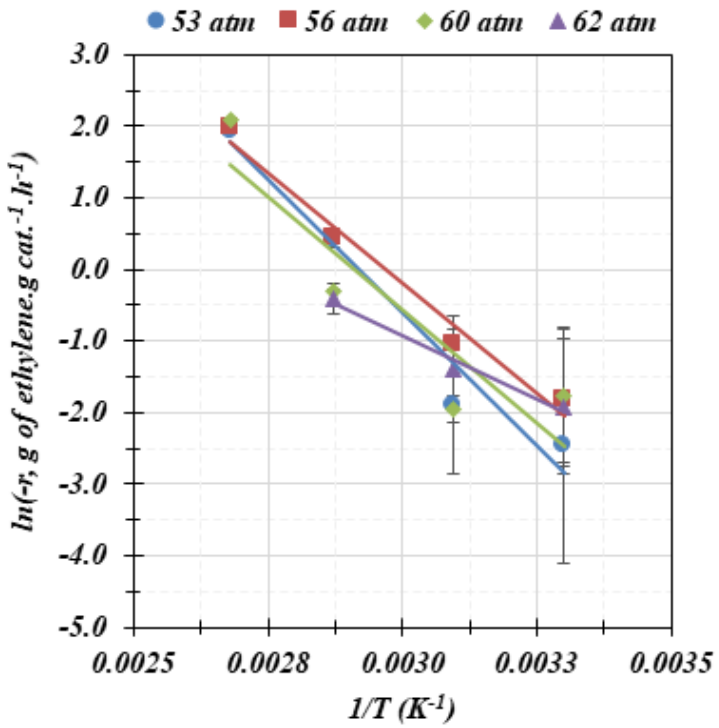

Figure 5.2. Arrhenius plot at different pressures.

Table 5.2. Activation energies as a function of ethylene partial pressure. Values calculated from the data shown in Figure 5.2. Upper-end and lower-end values calculated with a confidence level of 95%

	apparent activation energy (kJ/mol)		
ethylene partial pressure (atm)	average	upper end	lower end
53	70.8	75.9	65.7
56	54.8	57.8	51.8
60	56.7	59.6	53.7
62	34.7	37.8	20.6

To strengthen our hypothesis, we used the Weisz-Prater criterion[68] to evaluate for internal transport limitations on the catalytic process. The criterion is defined by the following equation:

$$C_{wp} = \frac{-r_{ethylene}\rho_c R^2}{D_e C_{ethylene}} \tag{5.9}$$

Where $-r_{ethylene}$ is the rate of ethylene consumption at stead-state, ρ_c is the density of the catalyst, R is the catalyst particle radius, D_e is the effective diffusivity, and $C_{ethylene}$ is the concentration ethylene at the outside of the catalyst particle surface. Catalyst density and particle

radius were reported in Chapter 3. For the calculations, we assumed that ethylene diffuses into a mixture of products, whose composition is given as the composition measured at steady-state. According to the criterion, if C_{wp} is less than unity, internal diffusion limitations are negligible. We estimated C_{wp} values ranging between 2.7×10^{-4} and 2.1×10^{-2} for all experiments reported in the present study. Note that we used the pore volume of the fresh catalyst to calculate C_{wp}. Based on the analysis, we can rule out the diffusion limitation of ethylene in the catalyst's pore.

The decrease in activation energy with pressure shown in the Arrhenius plot can be explained by the accumulation of products on the catalyst surface. The high rates of oligomerization at high temperatures and pressures can cause the accumulation of hydrocarbons on the catalyst surface, thus reducing available catalyst surface area. In extreme scenarios, a substantial fraction of the catalyst's pores may be blocked by carbon deposits and ethylene may not be able to reach active sites inside of the catalyst particle. In this case, the release of products from the catalyst becomes dependent on how fast the surface is exposed, making the reaction rates less sensitive to temperature. Still, despite the accumulation of products on the catalyst surface at 62 atm, the process still reaches steady-state, suggesting that a portion of the catalyst's surface is still available for reaction.

5.3.2 *Schulz-Flory distribution of product selectivity*

It is widely reported in the literature[2], [7], [8], [34], [43], [102], that the product distribution for the ethylene oligomerization over nickel-based solid catalysts follows a Schulz-Flory-type distribution. The Schulz-Flory distribution is a first-order recurrence relation given by the following equations[102]:

$$T_{n+1} = \alpha T_n \tag{5.10}$$

$$T_n = c\alpha^n \tag{5.11}$$

$$c = \frac{(1-\alpha)R}{\alpha} \tag{5.12}$$

Equation 5.10 gives the rate of termination for an alkene (T_{n+1}) as a function of the rate of termination of the previous step (T_n), with general solution given by Equation 5.11, where n represents the number of monomeric units. In Equation 5.11, c is given by Equation 5.12, where α is the propagation probability, and R is the total number of moles of product produced.

In Figure 5.4, the solid dots show the experimental product selectivities (in mole %) and the lines show the calculated product selectivity based on the Schulz-Flory distribution. One can see that the modeled selectivities for C_4, C_6, and C_8 agree with the experimental results. However, the Schulz-Flory model fails to predict the selectivities for middle-range (C_{10}-C_{12}) and diesel-range alkenes (C_{14}-C_{16}). Note that the model deviates up to 20% from the experimental selectivities for high molecules weight alkenes (C_{10}-C_{16}). This result supports the discussion present in the previous section. The greater selectivity for C_{10}-C_{16} fractions, beyond the expected Schulz-Flory distribution for nickel-based solid catalysts, may be attributed to the removal of coke precursors from the catalyst by supercritical ethylene, especially at low temperatures.

At 100^{o}C, the Schulz-Flory model predicts the selectivity for all product fractions. In this case, the dissolution of long-chain products in supercritical ethylene and high temperatures does not seem to contribute to the final product distribution. Therefore, we can assume that the formation of high molecular weight products at 100^{o}C is exclusively due to the kinetics of the reaction.

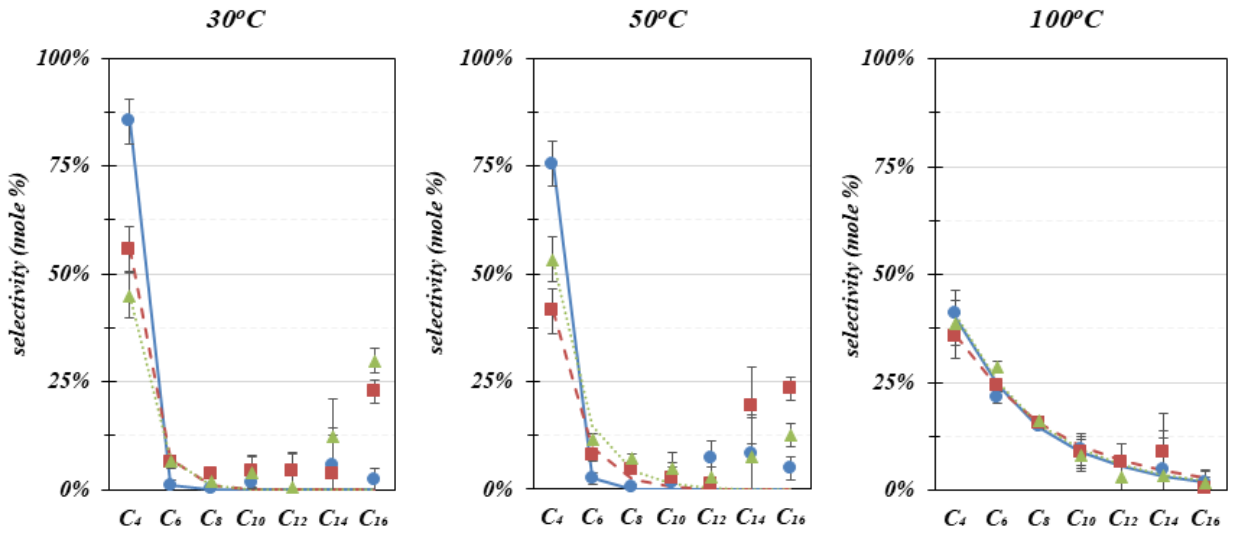

Figure 5.3. Selectivity (in mole %) for C_4-C_{16} alkenes at 30, 50 and 100°C and ethylene partial pressures of (●) 53, (■) 56, and (▲) 60 atm. Lines show modeled selectivities at ethylene partial pressures of (—) 53, (- -) 56, and (····) 60 atm based on a Schulz-Flory-type distribution according to Equations 5.10-5.12.

5.3.3 *Kinetic model development*

Based on the results presented in Figure 5.3, the formation of products during the oligomerization of supercritical ethylene over the Ni-H-Beta can be modeled by coupling the dissolution of long-chain products in supercritical ethylene to a product distribution that follows the Schulz-Flory model. The dissolution of products in supercritical ethylene increases the selectivity for long-chain alkenes (C_{10}-C_{16}) and its contribution decreases with increasing temperature. In Chapter 4, we measured the solubility of *n*-decane in supercritical ethylene at conditions similar to the ones used in the present work. However, the rates of product dissolution measured in reported in Chapter 4 produce a much greater increase in selectivities for C_{10}-C_{16} products than the increase shown in Figure 5.3. We anticipated this discrepancy, given that the solubility measured in Chapter 4 reflected the maximum solubility of long-chain hydrocarbons in supercritical ethylene since the measurements were obtained in the equilibrium. Therefore, we used the difference between the experimental and modeled product selectivities shown in Figure

5.3 to calculate the fraction of C_{10}-C_{16} products solubilized in supercritical ethylene. The rates of product formation were modeled according to the following equation:

$$r_{i,calc.} = r_{i,Shulz-Flory} + r_{i,dissolution} \quad (5.13)$$

In Equation 5.13, $r_{i,calc.}$ is the modeled rates of product formation for species i, $r_{i,Shulz-Flory}$ is the rate of product formation assuming that its selectivity follows the Schulz-Flory distribution, and $r_{i,dissolution}$ is the rate of product dissolution in supercritical ethylene calculated by the difference between experimental and modeled selectivities shown in Figure 5.3. We used the Langmuir-Hinshelwood-Hougen-Watson kinetics[68], [70] to model reaction rate expressions for $r_{i,Shulz-Flory}$ based on the partial pressures of products and reactants.

Due to the complexity and number of products formed, we proposed a simplified reaction pathway to model rate expressions for product formation. The proposed reaction pathway is shown in Figure 5.4. We showed previously that internal diffusion limitations are negligible. Therefore, we assumed that only elementary steps can control the catalytic process (*i.e.*, *adsorption*, *chain-growth*, and *desorption*). Also, since kinetic measurements were performed at steady-state, the kinetic model does not account for the initial catalyst deactivation due to the production of carbon deposits.

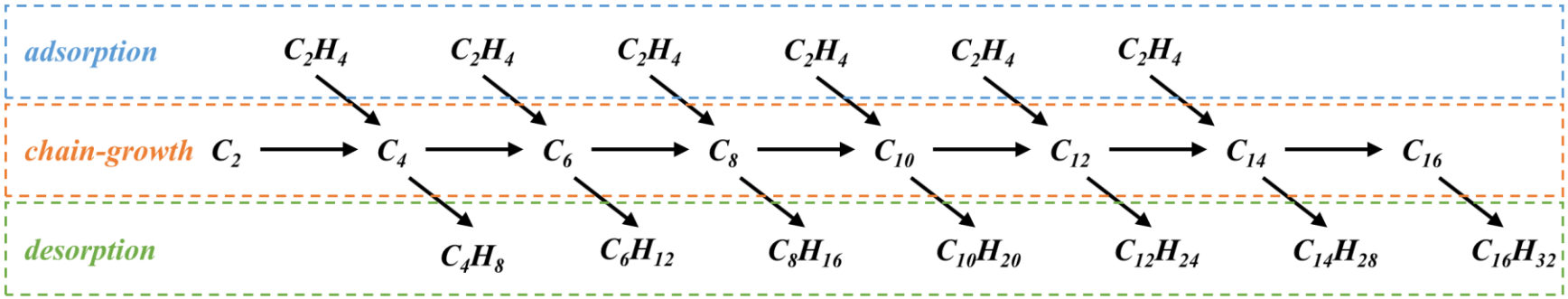

Figure 5.4. Simplified reaction pathway proposed in the present study to model the ethylene oligomerization over the Ni-H-Beta under supercritical conditions.

The proposed reaction pathway starts with the initial adsorption of ethylene on the catalyst surface. Then, an *insertion* step takes place, via the coupling of one ethylene molecule with the adsorbed C_2 species. Once *insertion* takes place, then a *chain-growth* step converts two adsorbed C_2 species into an adsorbed C_4 species. In the proposed reaction pathway, adsorbed species can either undergo desorption, forming products, or they may undergo additional *insertion* steps followed by *chain-growth* to produce longer adsorbed species. If *desorption* takes place, the catalytic process is complete, and the products are then released from the catalyst surface to the bulk of the supercritical fluid.

Table 5.3. Reaction rate expressions developed using the Langmuir-Hinshelwood-Watson-Hougen kinetics, assuming different RLS (Adsorption, chain-growth, and desorption)

Product	***Model 1***	***Model 2***	***Model 3***
	Adsorption*	Chain-growth*	Desorption*
C_4	$r_{C_4} = k_1 P_{C_2}^2$	$r_{C_4} = k_1 P_{C_2}^2$	$r_{C_4} = k_1 P_{C_2}^2$
C_6	$r_{C_6} = k_2 P_{C_2} P_{C_4}$	$r_{C_6} = k_2 P_{C_2} P_{C_4}$	$r_{C_6} = k_2 P_{C_2}^3$
C_8	$r_{C_8} = k_3 P_{C_2} P_{C_6}$	$r_{C_8} = k_3 P_{C_2} P_{C_6}$	$r_{C_6} = k_3 P_{C_2}^4$
C_{10}	$r_{C_{10}} = k_4 P_{C_2} P_{C_8}$	$r_{C_{10}} = k_4 P_{C_2} P_{C_8}$	$r_{C_6} = k_4 P_{C_2}^5$
C_{12}	$r_{C_{12}} = k_5 P_{C_2} P_{C_{10}}$	$r_{C_{12}} = k_5 P_{C_2} P_{C_{10}}$	$r_{C_6} = k_5 P_{C_2}^6$
C_{14}	$r_{C_{14}} = k_6 P_{C_2} P_{C_{12}}$	$r_{C_{14}} = k_6 P_{C_2} P_{C_{12}}$	$r_{C_6} = k_6 P_{C_2}^7$
C_{16}	$r_{C_{16}} = k_7 P_{C_2} P_{C_{14}}$	$r_{C_{16}} = k_7 P_{C_2} P_{C_{14}}$	$r_{C_{16}} = k_7 P_{C_2}^8$

* Reaction limiting step (RLS).

Different reaction rate expressions can be obtained depending on the reaction limiting step (RLS). Table 5.3 shows three sets of reaction rate expressions for the production of C_4, C_6, C_8, C_{10}, C_{12}, C_{14}, and C_{16}, assuming in each set of equations that one of the elementary steps (*insertion, chain-growth,* or *desorption*) is the RLS. We assumed that RLS are irreversible, while the other steps are in *quasi-equilibrium.* To reduce the number of kinetic parameters, we lumped parameters involved in intermediate steps. Therefore, the model proposed includes one kinetic parameter for each reaction rate.

Kinetic constants k_i (with $1 < i < 7$) shown in Table 5.3 are a function of temperature given by the Arrhenius equation[68], [70]:

$$k_i = k_{i,0} e^{-\frac{E_a}{RT}} \quad (5.14)$$

Where $k_{i,0}$ is the pre-exponential factor and E_a is the activation energy.

5.3.4 *Kinetics under supercritical conditions*

Table 5.4 summarizes the results obtained from the fitting of the kinetic models shown in Table 3. Because ***Model 1*** (RLS = adsorption) and ***Model 2*** (RLS = chain-growth) have the same reaction rate expressions for all pathways, we report their results together. Calculated kinetic parameters for ***Models 3*** converged to values different than the ones obtained for ***Models 1 and 2***. Initial assessment indicates that most of the activation energies calculated for ***Models 1 and 2*** are not physically possible, since apparent activation energies cannot be 0.0 kJ/mol. According to the Arrhenius relationship given by Equation 5.14, if activation energies are 0.0 kJ/mol, reaction rates depend only on pre-exponential factors, which misleadingly suggests that reaction rates are not a function of temperature.

Table 5.4. Initial fitting of kinetic data based on the minimization of the objective functions given in Equation 5.6

	Model 1 and 2		***Model 3***	
Product	k (mmole.g cat^{-1}.h^{-1}.atm^{-2})	E_a (kJ/mol)	k (mmole.g cat^{-1}.h^{-1}.atm^{i+1})*	E_a (kJ/mol)
C_4	6.9x10^{11}	98.5	7.9x10^{11}	98.9
C_6	3.3x10^{5}	40.7	7.1x10^{14}	133.6
C_8	5.9x10^{-1}	0.0	1.6x10^{12}	128.5
C_{10}	6.0x10^{-1}	0.0	7.5x10^{5}	97.1
C_{12}	7.1x10^{-1}	0.0	1.8x10^{3}	92.1
C_{14}	8.0x10^{-1}	0.0	3.2x10^{0}	86.3
C_{16}	1.0x10^{0}	78.3	3.7x10^{-2}	86.3
f_{min}	86.9		73.6	

On the other hand, calculated kinetic parameters for ***Model 3*** converged to physically meaningful values. It is possible that C_{8+} products are formed via butene co-oligomerization

reactions as proposed in Chapter 3. In this case, the formation of these products becomes less dependent on ethylene. Note that activation energies were not forced to converge to the values shown in Table 5.4. Kinetic parameters were obtained from the minimization of the objective function given in Equation 5.6, with varying initial guesses to ensure reliability for the fitted parameters. The total error, given by f_{min} in Table 5.4, suggests that ***Model 3*** provides a lower error compared with ***Models 1 and 2***.

To elucidate differences between the models, we used the bootstrap method to quantify the parameter confidence intervals and the variation of the model error. As discussed in the Section 5.2, the bootstrap method is a resampling technique that estimates the parameter confidence intervals by assuming a randomized error distribution among the calculated rates.

Table 5.5 shows the average value, upper-end, and lower-end for the kinetic parameters included in each model proposed in the present work. Table 5.5 also shows the average model error, f_{min}, and its upper and lower end values. As one can see, ***Model 3*** leads to the lowest f_{min} among the models tested in the present work. Based on the results shown in Table 5.5, ***Model 3*** provides the best fitting of the kinetic data among the models tested in this work. This may be an indication that the desorption of products from the catalyst surface to the bulk of the fluid controls the reaction under supercritical conditions.

Overall, the calculated apparent activation energies for ***Model 3*** are high. It has been reported in the literature that intrinsic activation energies involved in the formation of butene (C_4), hexene (C_6), and octene (C_8), range between 72 and 77 kJ.mol^{-1} for the oligomerization of subcritical ethylene over the Ni-H-Beta and similar catalysts[15]. The higher values obtained in the present work may suggest that conversion of supercritical ethylene into C_4, C_6, and C_8 over the Ni-H-Beta is slower than the formation of these products under subcritical conditions.

Table 5.5. Kinetic parameters calculated from the fitting of the models shown in Table 5.3

Product	***Model 1 and 2***						***Model 3***					
	k (mmole.g cat^{-1}.h^{-1}.atm^{-2})			E_a (kJ/mol)			k (mmole.g cat^{-1}.h^{-1}.atm^{i+1})*			E_a (kJ/mol)		
	mean	upper end	lower end	Mean	upper end	lower end	mean	upper end	lower end	mean	upper end	lower end
C_4	$1.2x10^{12}$	$1.9x10^{12}$	$6.2x10^{11}$	93.1	94.5	91.6	$1.4x10^{12}$	$2.1x10^{12}$	$8.3x10^{11}$	94.2	95.6	92.8
C_6	$3.0x10^{5}$	$4.0x10^{5}$	$2.0x10^{5}$	37.0	38.0	36.0	$1.8x10^{15}$	$2.4x10^{15}$	$1.1x10^{15}$	132.6	133.5	131.6
C_8	$6.1x10^{-1}$	$6.2x10^{-1}$	$6.1x10^{-1}$	0.0	0.0	0.0	$7.5x10^{11}$	$9.6x10^{11}$	$5.4x10^{11}$	122.7	123.9	121.6
C_{10}	$6.3x10^{-1}$	$6.4x10^{-1}$	$6.3x10^{-1}$	0.0	0.0	0.0	$9.6x10^{5}$	$1.4x10^{5}$	$4.7x10^{5}$	90.2	91.8	88.6
C_{12}	$7.4x10^{-1}$	$7.5x10^{-1}$	$7.4x10^{-1}$	0.0	0.0	0.0	$2.3x10^{3}$	$3.6x10^{3}$	$9.9x10^{2}$	81.9	84.0	79.8
C_{14}	$7.9x10^{-1}$	$8.0x10^{-1}$	$7.8x10^{-1}$	0.0	0.0	0.0	$2.0x10^{0}$	$2.7x10^{0}$	$1.3x10^{0}$	74.0	76.4	71.5
C_{16}	$1.0x10^{0}$	$1.0x10^{0}$	$1.0x10^{0}$	78.4	78.5	78.3	$3.4x10^{-2}$	$4.8x10^{-2}$	$2.1x10^{-2}$	75.6	78.1	73.0
	mean		upper end		lower end		mean		upper end		lower end	
f_{min}	65.9		68.9		62.8		58.6		62.2		55.0	

*i is the subscript assigned to the k values in Table 5.3.

For ***Model 3***, activation energies decrease with increasing product carbon number. This trend shows that hydrocarbon formation becomes less sensitive to temperature with increasing chain length. The accumulation of products on the catalyst due to the high rates of chain growth at supercritical conditions can slow down the release of products from the catalyst. This process can lead to a reaction controlled by the desorption of products from the catalyst surface, as assumed in ***Model 3***. Note that the accumulation of products on the catalyst surface can also cause pore plugging, increasing the desorption controlling aspect of the reaction.

In Chapter 4, the comparison between coke dissolution rates and product formation rates provided indications that the transport of molecules from the catalyst surface to the bulk of the fluid is slow under supercritical conditions. The results obtained in the present work provide further indications for the slow transport of molecules promoted by the slow desorption of products from the catalyst surface.

Figure 5.5-A shows the calculated residues $r_{exp.} - r_{calc.}$ in mmole.g cat.$^{-1}$.h^{-1} for C_4, C_6, and C_8, with calculated rates given by ***Model 3***. Figure 5.5-B shows the experimental selectivities (in mole %) for C_{10}, C_{12}, C_{14}, and C_{16} and calculated selectivities based on the rates obtained from ***Model 3***. There is a high correlation between the calculated rates of C_4, C_6, and C_8 formation and the experimental rates. Also, estimated selectivities for C_{10}, C_{12}, C_{14}, and C_{16} are in good agreement with the experimental values. Based on the results, ***Model 3*** provides a solid description of the kinetic trends reported in the present work.

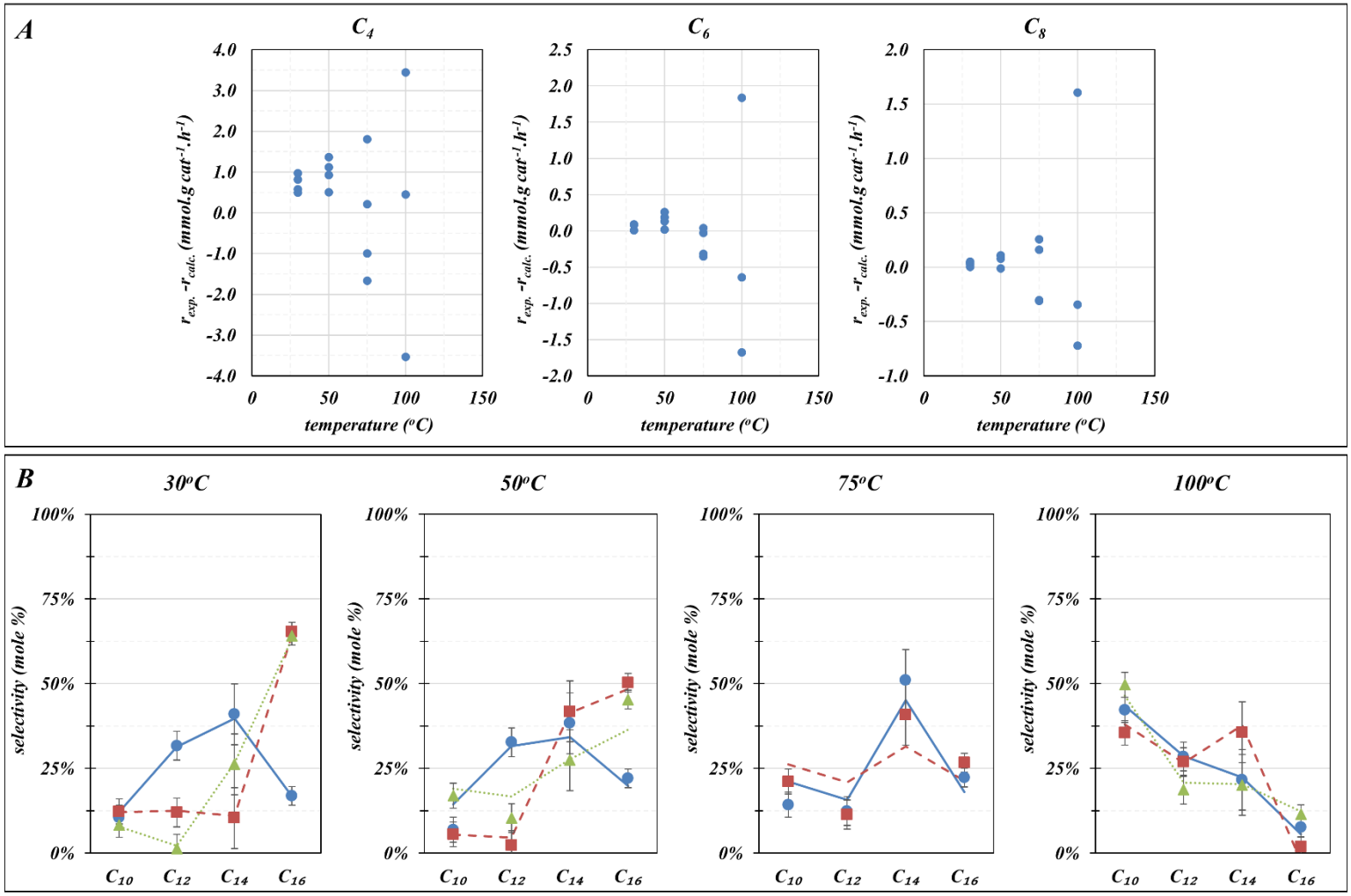

Figure 5.5. A – Calculated residues ($r_{exp.} - r_{calc.}$) for the rates of C_4, C_6, and C_8 formation as a function of temperature for ***Model 3***. B – Selectivities (in mole %) for C_{10}-C_{16} alkenes at 30, 50, 75°C, and 100°C and ethylene partial pressures of (●) 53, (■) 56, and (▲) 60 atm. Lines show modeled selectivities at ethylene partial pressures of (—) 53, (- -) 56, and (····) 60 atm based on calculated rates of formation from ***Model 3***.

5.4 GUIDELINES

Based on the results obtained in the present work, we propose the following guidelines to improve the rates of product desorption from the catalyst surface during the oligomerization of supercritical ethylene over nickel-based solid catalysts:

1- Use of supports with larger pore volumes, such as SBA-15[18] or SIRAL[11], [58], to minimize the extent of product accumulation on the catalyst surface.

2- Control the concentration of nickel sites on the catalyst to reduce the extent of chain-growth reactions[103], thus avoiding the accumulation of products on the catalyst surface.

3- Cycle between low-temperature and high-temperature cycles under supercritical conditions to promote the dissolution of products from the catalyst surface, thus, maintaining the catalyst surface clean.

5.5 CONCLUSION

We discussed the kinetics of supercritical ethylene oligomerization over the Ni-H-Beta. At low temperatures, supercritical ethylene promotes the dissolution of long-chain products from the catalyst surface, contributing to the increased selectivity for C_{16} alkenes, with a maximum selectivity of 49.8 wt. % at an ethylene partial pressure of 60 atm. The dissolution of products at low temperatures is aided by the high solubility of these products in supercritical ethylene. As temperature increases, the rates of product formation outcompete the rates of product dissolution, thus, leading to the accumulation of products on the catalyst surface. This process leads to a reduction in C_{10+} selectivity, driven by the reduction in C_{14} and C_{16} selectivities.

The apparent activation energy for the consumption of ethylene decreases from 70.8 to 34.4 kJ/mol with increasing ethylene partial pressure from 53 to 62 atm. According to the Weisz-Prater criterion, the internal diffusion limitation of ethylene on the catalyst pores are negligible. However, in the case of pore plugging, ethylene may not be able to access active sites available for reaction. Therefore, we hypothesize that the decrease in activation energy with pressure may be ascribed to the accumulation of products on the catalyst surface.

A comparison of the kinetic models proposed in this work suggests that ***Model 3***, which assumes desorption as the RLS, provides the best fitting of the experimental data among the models tested. We highlight that ***Model 3*** converged to physically meaningful kinetic parameters. Analysis of calculated activation energies for ***Model 3*** indicates higher values than the ones reported in the literature. We attribute the high activation energy values to the slow formation of products under supercritical conditions. The trend also points to a decrease in activation energies with temperature, which may be ascribed to the competition between chain-growth and dissolution rates. At high temperatures, chain-growth reactions may outcompete the rates of product dissolution in supercritical ethylene. Finally, we attribute the desorption controlling process to the accumulation of products on the catalyst, which can cause plugging of the catalyst's pores.

Chapter 6. A NOVEL ROUTE FOR ALKENES AND CYCLOALKANES VIA ETHYLENE OLIGOMERIZATION OVER NI-SIRAL CATALYSTS[9,10]

Abstract

We describe a novel route for the production of alkenes and cycloalkanes via the oligomerization of subcritical and supercritical ethylene over a Ni-SIRAL catalyst. We report the production of liquid products at 50, 100, and 200ºC and 40 and 65 bar operating at both single and dual reactor configurations. The screening of reaction temperature at supercritical conditions (65 bar) indicates the highest liquid yield (liquid at ambient conditions) of 41.7 wt. % at 200ºC with a single reactor. Under supercritical conditions, at 200ºC, the liquid yield increased from 41.7 to 60.8 wt. % after the addition of a second oligomerization reactor. The ethylene oligomerization under subcritical conditions led to a much lower yield for liquid products relative to the yield obtained at supercritical conditions, at both reactor configurations (single and dual). At subcritical conditions, we obtained liquid yields of 19.3 wt. % with a single reactor and 35.9 wt. % with a dual reactor. The dual reactor configuration proved to be the better configuration for the production of cycloalkanes, with a yield of 7.3 wt. % at subcritical conditions and 8.5 wt. % at supercritical conditions. These results indicate that supercritical ethylene may not be necessary for the production of cycloalkanes. In our previous work[13], we hypothesized that supercritical ethylene promoted the formation of cycloalkanes via dissolution of coke, which contains linear and cyclic

[9] Provisional patent filed on March 19, 2021: A MESOPOROUS CATALYST AND PROCESS FOR ALKENE, ALKANE, AND CYCLOALKANE SYNTHESIS VIA OLIGOMERIZATION OF ETHYLENE. Gabriel V. S. Seufitelli, Fernando L. P. Resende, Rick Gustafson.

[10] To be submitted to Applied Catalysis B: Environmental, Gabriel V. S. Seufitelli, Fernando L. P. Resende, Rick Gustafson.

alkanes. However, the production of cycloalkanes at subcritical conditions reported in the present study may point to an additional pathway for their formation involving cyclization of long-chain products on the second oligomerization reactor. This is evident when comparing the yield for cycloalkane under subcritical conditions using a single reactor, 0.6 wt. %, with the yield obtained with a dual reactor, 7.3 wt. %. Based on the results we proposed a reaction pathway that agrees with the results presented in this work. The pathway involves oligomerization, isomerization, co-oligomerization, cyclization, and dissolution of cycloalkanes from coke fractions assisted by supercritical ethylene.

Keywords: Ethylene oligomerization; supercritical ethylene; cycloalkanes; pore volume; nickel.

6.1 INTRODUCTION

The aviation sector is forecasted to grow at a yearly rate of 2% until 2040[104]. According to the U.S. Department of energy, this growth is expected to increase commercial jet fuel consumption by 31% until 2050[105]. In 2019, 26.7 billion gallons of jet fuel were consumed in the U.S., corresponding to a total expenditure of $52.7 billion[106]. With the imminent increase in jet fuel consumption and environmental implication of fossil fuels, the aviation sector proposed to reduce CO_2 emissions by 50% until 2050[107]. Currently, the aviation sector contributes approximately 2-3% of the total human-induced greenhouse gas (GHG) emissions in the U.S.[108] and this number is expected to double by 2040[109]. In this scenario, sustainable jet fuel becomes a promising alternative to reduce GHG emissions[110]. In 2012, the Federal Aviation Administration (FAA) set the goal to use 1 billion gallons of biomass-derived jet fuel annually in U.S. aviation by 2018[111]. Currently, 7.3% of commercial jet fuel is from renewable resources, and it is estimated that this fraction will increase to 13.5% by 2040[105].

Until now, seven sustainable jet fuels have been approved by the American Society for Testing and Materials (ASTM)[112], [113]: Fisher Tropsch (FT-SPK) from syngas, Hydrotreated esters and fatty acids synthetic paraffinic kerosene (HEFA), Hydroprocessed fermented sugar-synthetic iso-paraffins (SIP), Fisher Tropsch synthetic kerosene with aromatics (FT-SKA), Alcohol-to-jet from iso-butanol (ATJ-SPK), Catalytic hydrothermolysis jet from lipids via supercritical hydrothermal process (CHJ), and Hydroprocessed hydrocarbons, esters, and fatty acids synthetic paraffinic kerosene (HC-HEFA-SPK). According to ASTM's specifications, commercial jet fuels can be blended with most of these sustainable jet fuels by up to 50% v/v. Pires et al. published extensive work on the analysis of the sustainable jet fuels approved by ASTM[113]. Most of the jet fuel blends are composed of *n*-alkanes (4.0-44.0 wt. %) and iso-alkanes (6.9-96.4 wt. %) with small fractions of aromatics (8.8 wt. %). Among the sustainable processes approved by ASTM, only CHJ provides a jet fuel blendstock that contains cycloalkanes in its composition (32.9 wt. %). The cycloalkane fraction in commercial jet fuels, such as Jet-A, varies between 4.9 and 32.0 wt. %[112], [113]. For conventional military jet fuel, such as JP-5 and JP-8, the fraction of cycloalkanes varies between 11.5 and 22.0 wt. %[112], [113].

Jet fuel is a complex mixture of *n*-alkanes, iso-alkanes, cycloalkanes, and aromatics[112]. Alkanes are responsible for most of the energy content of jet fuels. While aromatic molecules possess lower specific energy than alkanes, they provide seal-swelling capacity, thus, preventing leaks in the fuel system. However, aromatic molecules generate soot when burned, contributing to the majority of emissions from jet fuel combustion. A study from the Boeing Company and the University of Dayton showed that the swelling of O-rings is not only dependent on the concentration of aromatics, but it also depends on the overall composition of jet fuel[114]. Recent studies also indicate that cycloalkanes can provide seal-swelling capacity[112], [115].

Cycloalkanes have higher specific energy than aromatics. Therefore, the replacement of aromatic molecules with cycloalkanes can increase the energy content of jet fuel, reduce soot generation, and improve O-rings' seal[112]. In this work, we present a novel route for the production of linear and cyclic hydrocarbons via ethylene oligomerization.

Ethylene is widely available and it is the main feedstock in several industries[116]. The majority of the ethylene produced worldwide is via the hydrocracking of ethane and naphtha from crude oil[117]. The advancement of shale-gas extraction technologies in the U.S. increased the production of ethane, making it a cheaper feedstock for hydrocracking than naphtha[31]. Ethylene can also be produced from biomass via ethanol dehydration[118]. In the U.S., most of the ethanol produced is from corn grains[119], but a promising low carbon pathway for ethanol production is from agricultural residues, such as corn stover, or dedicated energy crops such as poplar wood. Until 2014, there were 3 facilities under development in the U.S. to convert biomass residues into ethanol: Abengoa in Hugoton, Kansas (25-million gallons per year); Dupont in Nevada, Iowa (30-million gallons per year); and POET-DSM in Emmetsburg, Iowa (770 tons of corn stover per day)[120]. Until November 2019, POET-DSM was the only refinery in the U.S. producing ethanol from crop waste, before pausing its operations[121]. In 2019, 142.7 billion gallons of motor gasoline were consumed in the U.S. According to the current regulation, the maximum percentage of ethanol in motor gasoline is 10%, reaching an ethanol "blend wall" of 14.3 billion gallons. The vast availability of corn and crop waste in the U.S. coupled with the "blend wall" limitation makes ethanol a feasible feedstock for the ethylene production. It is important to note that the production of ethanol from lignocellulosic biomass (corn stover) in the U.S. still requires further development due to the recent unsuccessful attempts to implement competitive lignocellulosic ethanol production on a large scale.

A life-cycle assessment study indicates that the production of ethylene via ethanol from corn grain and corn stover generates negative GHG emissions of -0.5 and -1.0 kg CO_2-equiv/kg ethylene, respectively[122]. On the other hand, the production of ethylene via hydrocracking of ethane from shale-gas leads to a positive GHG emission of 1.4 kg CO_2-equiv/kg ethylene[122]. From an economic standpoint, a comparison between lignocellulosic biomass, corn grain, and shale gas as feedstock for ethylene production shows that ethane from shale-gas is the cheapest feedstock, followed by corn grain, and lignocellulosic biomass is the most expensive feedstock[122]. The negative GHG emissions coupled with the production of high-value products from ethylene may justify the higher cost for ethylene production from corn grain, crop residues, and dedicated energy crops, relative to shale-gas. In this context, jet fuel becomes a suitable high-value product, thus, creating an alternative to put the aviation sector on track to reduce CO_2 emissions by 2050. The oligomerization of ethylene is one of the main routes considered for the conversion of ethylene into a hydrocarbon mixture similar to the one found in jet fuel[66], [123], [124]. This process provides a wide spectrum of n-alkenes and iso-alkenes with varying carbon number[7], [23]. Alkenes are not suitable for aviation fuel because they are highly unstable and undergo polymerization[112]. Therefore, a hydrogenation step is necessary to convert the product mixture into n-alkanes and iso-alkanes[123], [125], [126].

Commercial ethylene oligomerization processes employ organometallic, primarily nickel based[127]–[129], homogeneous catalysts[3], [12], [45]. The major drawbacks of this technology are the environmental implications associated with the use of organic solvents and high operating costs for product separation and catalyst recovery[2]. There has been great interest in the development of heterogeneous catalysts for ethylene oligomerization since these catalysts do not require the use of solvents and allow for a much easier product separation than in their

homogeneous counterpart. Nickel-based solid catalysts have been proposed since they incorporate the same active metal used in the organometallic homogeneous catalyst. Supports for nickel-based solid catalysts include amorphous silica-alumina[130], [131] and microporous[7], [39] and mesoporous[8], [11], [18], [44] inorganic zeolites. Catalyst deactivation is the main issue during the ethylene oligomerization over nickel-based amorphous silica-alumina and microporous inorganic catalysts[39]. An exception is the Ni-H-Beta, which shows good stability and it is resistant to deactivation[7]. Nickel-based mesoporous catalysts, such as NiSBA-15[18] and Ni-MCM-41[44], are also resistant to deactivation, which may be attributed to the greater pore volume of mesoporous supports relative to microporous ones.

Our research group has extensively studied the oligomerization of ethylene over nickel-based solid catalysts[13], [24]–[26]. To minimize coke production and consequent catalyst deactivation, we proposed in previous publications the use of supercritical ethylene. We reported the production of liquid products over the Ni-H-Beta and provided visual evidence that supercritical ethylene promotes coke dissolution during the reaction[13]. The majority of the liquid obtained under supercritical conditions was comprised of C_{10+} alkenes with a small fraction of cycloalkanes.

For the coke solubility effect to take place, the rates of coke dissolution in supercritical ethylene have to surpass the rates of product formation on the catalyst, otherwise, carbon deposits may form on the catalyst surface[13]. High reaction rates at supercritical conditions over a catalyst that contains a low pore volume led to the accumulation of products on the catalyst, thus causing pore plugging. Catalyst deactivation was observed even when we used the Ni-H-Beta for the oligomerization of supercritical ethylene. The catalyst deactivation under supercritical conditions compromised the formation of liquid products and impacted the catalyst lifetime.

This work is part of on-going research to design a sustainable process for the production of high-value liquid fuels from ethylene. Potential sources for ethylene include lignocellulosic biomass, such as corn stover and corn grain. The route involves the dehydration of cellulosic ethanol into ethylene and employs subcritical and supercritical ethylene oligomerization over a newly developed Ni-SIRAL® 40 HPV catalyst for the production of alkenes and cycloalkanes. The final step of this process involves the hydrogenation of the liquid product. The process for the production of jet fuel employing these 3 steps (ethanol dehydration, ethylene oligomerization, and alkene hydrogenation) is denominated alcohol-to-jet (ATJ). While Gevo[5] and LanzaTech [66], [124] are the two main companies producing sustainable jet fuel blends on a large scale via ATJ, LanzaTech is the only one employing ethanol dehydration to ethylene. Byogy and Swedish Biofuels are currently seeking approval from ASTM for their jet fuel from lignocellulosic ethanol[112], [132]. The current ATJ technologies are not able to produce cycloalkanes.

In this work, we focus solely on the development of an ethylene oligomerization process to produce liquid products from ethylene. To increase the production of liquids and reduce catalyst deactivation, we designed a new mesoporous nickel-based solid catalyst. We choose the SIRAL® 40 HPV for catalyst support, which has a pore volume of 1.5 cm^3/g, twice the pore volume of SBA-15 reported in the literature, 0.8 cm^3/g[18]. We show that the oligomerization of subcritical and supercritical ethylene over the Ni-SIRAL® 40 HPV catalyst leads to a liquid product comprised of n-alkenes, iso-alkenes, and cycloalkanes. Hydrogenation of this liquid can provide a liquid mixture with a composition similar to commercial and military jet fuel.

6.2 EXPERIMENTAL SECTION

6.2.1 *Materials*

The SIRAL® 40 HPV (Al_2O_3/SiO_2 = 60/40) support, abbreviated as SIRAL40, was obtained from Sasol. Nickel nitrate hexahydrate (purity = 99.999%) and pyridine (purity > 99.0%) were purchased from Sigma-Aldrich and TCI, respectively. Ethylene (purity = 99.5%) and Nitrogen (purity = 99.999%) were purchased from Praxair and used without further purification.

6.2.2 *Catalyst synthesis*

The Ni-SIRAL® 40 HPV catalyst, abbreviated as Ni-SIRAL40, was produced via impregnation of SIRAL40 with $Ni(NO_3)_2.6H_2O$. A 0.548 M solution of $Ni(NO_3)_2.6H_2O$ was prepared by mixing 15.89 grams of $Ni(NO_3)_2.6H_2O$ with 100 ml of deionized water. Then, the $Ni(NO_3)_2$ solution was dripped onto the SIRAL40 support under agitation at room temperature for 6 hours. Afterward, the solution was vacuum filtered to recover the solid fraction. The solid was dried overnight at 100^{o}C. After drying, the solid was calcined at 550^{o}C in the presence of air for 6 hours to yield the Ni-SIRAL40 catalyst. The Ni-SIRAL40 catalyst was sieved to a particle diameter ranging between 250 and 500 μm.

6.2.3 *Catalysis characterization*

The concentration of nickel on the Ni-SIRAL40 catalyst was measured via Inductively coupled plasma atomic emission spectroscopy (ICP-AES) using EPA protocol 200.7, where the catalyst samples were digested in a solution of nitric acid and hydrochloric acid.

X-ray powder diffractions were obtained in a Bruker D8 Discover Microfocus diffractometer mounted with a IμS 2.0 microfocus X-ray source (Incoatec) using Cu K-α radiation and a Pilatus 3R 100K-A 2D detector. The samples were pressed flat onto a silicon wafer substrate.

X-ray photoelectron spectra (XPS) were collected in a Surface Science Instrumental S-Probe spectrometer (Service Physics, Bend OR). We used a monochromatized Al X-Ray source with a spot size of 800 x 800 µm. The catalyst powders were pressed onto a piece of double Scotch tape. We ran all samples as insulators, and a charge neutralizer was used during the measurements. For the high-resolution spectra, all binding energies were referenced to the C 1s C-C bonds at 285.0 eV.

Pyridine adsorption was performed in a Harrick Sci. diffuse reflectance chamber mounted with ZnSe windows. Spectra were collected in a Shimadzu Prestige-21 Fourier Transform Infrared Spectroscope (FTIR) equipped with a DLaTGS detector. We pretreated the catalysts (5 mg – diluted in KBr with a 5% dilution) at 300^{o}C under vacuum (10^{-3} bar) for 30 min before sorption. After pretreatment, we reduced the temperature to 30^{o}C and admitted 20 µL of pyridine into the chamber under vacuum. Then, we evacuated the chamber for 30 min to remove physisorbed pyridine species from the catalyst surface and ramped the reactor chamber temperature to 250^{o}C. We collected the spectra of the catalyst surface with a resolution of 8 cm^{-1} and used the peaks located at 1450 and 1545 cm^{-1} to measure the concentration of Lewis and Brønsted acid sites using the extinction coefficients reported by Emeis[53].

6.2.4 *Reaction system*

The reactor used for the ethylene oligomerization experiments is shown in Figure 6.1. The reaction system consisted of two consecutive packed-bed reactors (Figure 6.1 – Reactors #1 and #2) each capable of holding 1 gram of Ni-SIRAL40 catalyst. Quartz-wool was used to hold the catalyst inside the reactors. A double pipe condenser (Figure 6.1 – Condenser) mounted downstream of the second reactor was used to condense the liquid products. The condenser was connected to a water chillers (ThermoFlex900 – Thermo Scientific) that kept cold water

recirculating through the condenser at a temperature of 5.0°C during the reaction. Condensed liquid products were collected in a 1'' diameter collector (Figure 6.1 – Liquid collector) capable of holding approximately 100 ml of liquid. A back-pressure regulator (Equilibar ZF series) was used to keep both reactors and the condenser at the reaction pressure. Heating tapes connected to PID temperature controllers were used to keep both reactors at the reaction temperature. The reactors were insulated with quartz-wool jackets to prevent heat loss (Figure 6.1 – Red rectangles around Reactors #1 and #2).

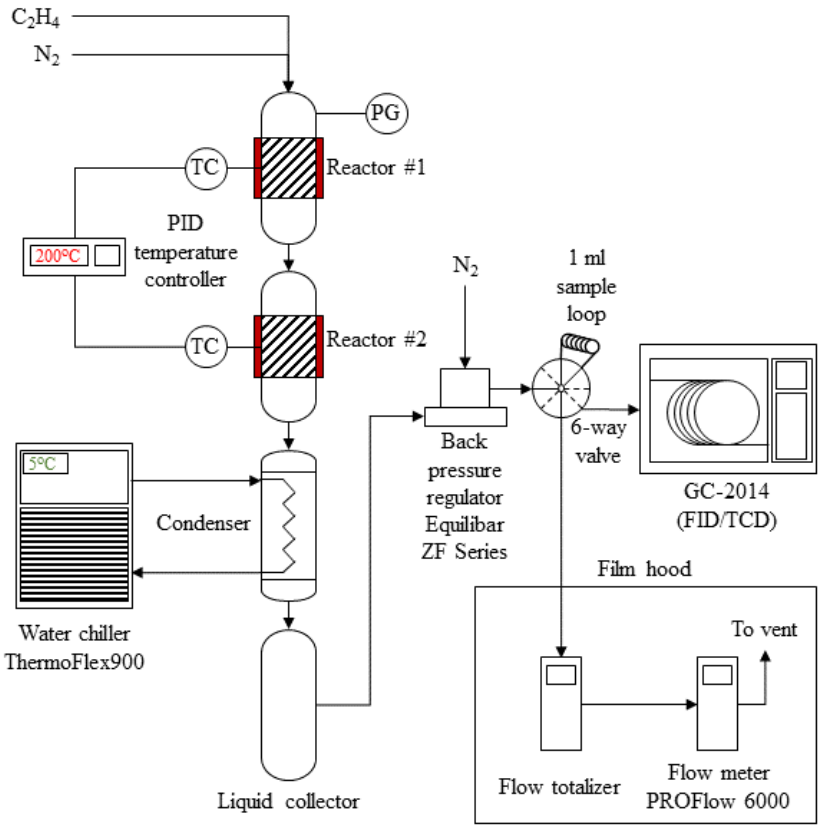

Figure 6.1. Process flow diagram for the ethylene oligomerization system used in the present study. In Reactors #1 and #2, the shaded area represents the catalyst bed location.

The outlet of the back-pressure regulator was connected to a pneumatic 6-way valve mounted with a 1 ml sample loop to analyze the gas products. The gases were analyzed via GC-FID/TCD. Mass flow controllers (201 series – Parker) were used to feed ethylene and nitrogen

into the reactor. A flow totalizer (Figure 6.1 – Flow totalizer) was installed downstream of the 6-way valve to account for the total volume of gases downstream of the reactor at the end of the experiments. Also, the gas flow rate downstream of the reactor was measured online with a flow meter (ProFLOW 6000 – Restek). The reaction system was designed to operate at a maximum reaction temperature of 500^{o}C and total pressure up to 69 bar.

6.2.5 *Ethylene oligomerization experiments*

The ethylene oligomerization was performed at 50, 100, and 200^{o}C and total pressure of 40.0 and 65.0 bar. We also tested single and dual reactor configurations. The dual reactor configuration was tested to promote oligomerization of long-chain alkenes, such as butene, hexene, and octene, in the second reactor with the objective to increase the molecular weight of the liquid product.

A mixture of ethylene and nitrogen (89 mole % ethylene, balanced nitrogen) was used for the experiments. Ethylene was fed at a rate of 163 ml (STD)/min and nitrogen was used as an internal standard for mass balance closure. The reactions were performed for at least 5 hours. Ethylene conversion was calculated based on the mass of ethylene consumed during the reaction:

$$X_{ethylene}(\%) = \left(\frac{\dot{n}_{in} - \dot{n}_{out}}{\dot{n}_{in}}\right) \times 100\% \quad (6.1)$$

Where $X_{ethylene}$ is the ethylene conversion, $\dot{n}_{in}$ is the molar flow rate of ethylene at the inlet of the reactor, and $\dot{n}_{out}$ is the molar flow rate of ethylene at the outlet of the reactor. At the end of the experiments, we accounted for the yields of gas, liquid, and coke. The gas yield was calculated according to the following equation:

$$Y_{gas}(\%) = \left(\frac{total\ mass\ of\ gas\ after\ reaction(g)}{total\ mass\ of\ ethylene\ fed\ into\ reactor\ (g)}\right) \times 100\% \quad (6.2)$$

The gaseous product consisted mostly of butene with trace amounts of hexene and octene. The total mass of gas was quantified online via GC-FID/TCD.

The condensed liquid in the collector was weighed and the total liquid yield was calculated according to the following equation:

$$Y_{liquid}(\%) = \left(\frac{total\ mass\ of\ liquid\ weighed\ after\ reaction\ (g)}{total\ mass\ of\ ethylene\ fed\ into\ reactor\ (g)}\right) \times 100\% \quad (6.3)$$

The composition of the liquid was determined via GC-MS/FID. For all experiments reported in this work, we identified *n*-alkenes, iso-alkenes, aromatics, and cycloalkanes among the liquid products. The GC-MS/FID was calibrated for *n*-pentane, *n*-hexane, *n*-heptane, *n*-octane, *n*-decane, *n*-dodecane, *n*-tetradecane, ethyl cyclohexane, di-methyl cyclohexane, and cyclooctane. We assumed the same response factor for alkanes and alkenes. The yields for *n*-alkenes, iso-alkenes, aromatics, and cycloalkanes were calculated based on the calibrations as follow:

$$Y_i(wt.\%) = \left(\frac{total\ mass\ of\ i\ in\ liquid\ (g)}{total\ mass\ of\ liquid\ (g)}\right) \times 100\% \quad (6.4)$$

In the above equation, i refers to *n*-alkenes, iso-alkenes, aromatics, and cycloalkanes. The selectivities for butene (abbreviated as C_4), pentene (abbreviated as C_5), hexene (abbreviated as C_6), heptene (abbreviated as C_7), octene (abbreviated as C_8), nonene (abbreviated as C_9), decene (abbreviated as C_{10}), undecene (abbreviated as C_{11}), dodecane (abbreviated as C_{12}), tridecene (abbreviated as C_{13}), tetradecene (abbreviated as C_{14}), pentadecane (abbreviated as C_{15}), hexadecene (abbreviated as C_{16}), and heavier products (abbreviated as C_{16+}) in the liquid were calculated according to the following equation:

$$S_i(wt.\%) = \left(\frac{total\ mass\ of\ i\ in\ liquid\ (g)}{total\ mass\ of\ liquid\ (g)}\right) \times 100\% \quad (6.5)$$

Where *i* refers to the product fractions mentioned above. The selectivity for butene in the liquid was calibrated based on *n*-pentane. Heavier product fractions, such as C_{15}, C_{16}, and C_{16+}, were calibrated based on *n*-tetradecane. Note that the response factor for calibrated hydrocarbons remained almost unchanged relative to their carbon numbers. The coke yield was measured by weighing the reactor before and after the reaction:

$$Y_{coke}(\%) = \left(\frac{mass\ of\ reactor\ after\ reaction - mass\ of\ reactor\ before\ reaction}{total\ mass\ of\ ethylene\ fed\ into\ reactor\ (g)}\right) \times 100\% \quad (6.6)$$

According to the above equation, we considered coke as any species that remained on the catalyst after the reaction. The mass balance closure was calculated by accounting for the total mass of ethylene and nitrogen fed into the reactor and the total mass of nitrogen, unreacted ethylene, gaseous products (butene, hexene, and octene) at the outlet of the reactor, liquid products, and coke produced at the end of the reaction according to the following equation:

$$m.b.(\%) = \left(\frac{total\ mass\ of\ products, unreacted\ C_2H_4, and\ N_2\ after\ reaction}{total\ mass\ fed\ to\ reactor\ (C_2H_4\ and\ N_2)}\right) \times 100\% \quad (6.7)$$

6.3 RESULTS AND DISCUSSION

6.3.1 *Catalyst characterization*

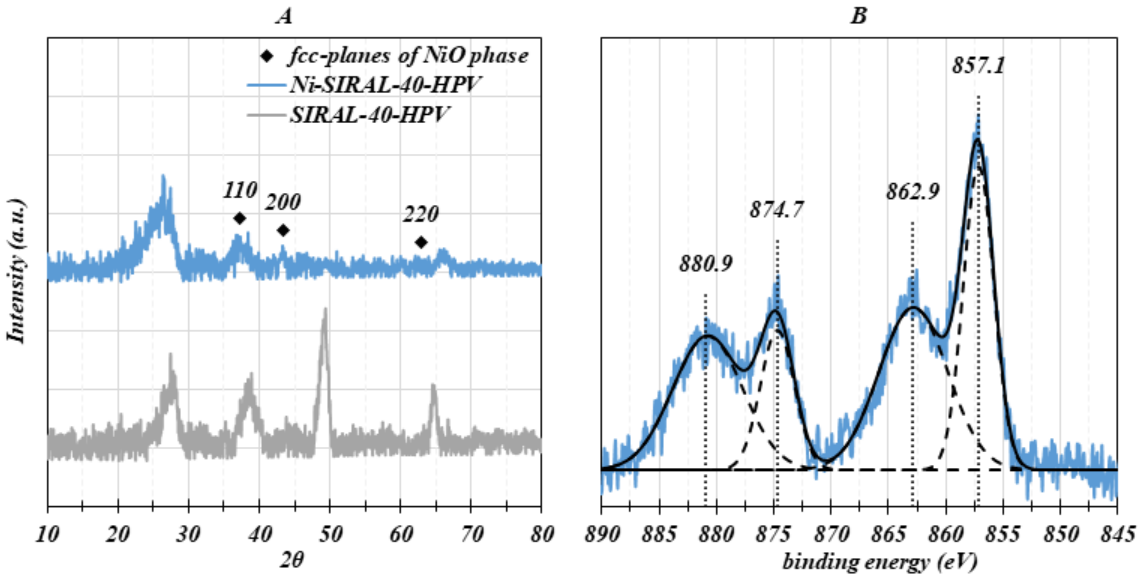

Figure 6.2. A – X-Ray Diffraction pattern of the fresh Ni-SIRAL catalyst (4.9 wt. % nickel) and the pristine SIRAL40-HPV support. B – Ni 2p X-Ray Photoelectron spectrum of the 4.9 wt. % nickel Ni-SIRAL catalyst.

The nickel impregnation of the SIRAL40-HPV support produced a Ni-SIRAL catalyst with a nickel loading of 4.9 wt. %. Figure 6.2-A shows the X-Ray powder diffraction (XRD) pattern of the Ni-SIRAL catalyst and the pristine SIRAL40-HPV support. The pristine support shows a broad peak at 20-30º characteristic of the amorphous silica phase[133]. The XRD pattern of the nickel catalyst indicates the absence of diffractions at 37.3º, 43.3º, and 62.9º, characteristic of (110), (200), and (220) fcc-planes of NiO phase[7]. The absence of these peaks suggests that if NiO crystallites were formed during impregnation, their sizes are relatively small[13].

The peak fitting of the $Ni2p_{3/2}$ region of the X-Ray photoelectron spectrum shown in Figure 6.2-B confirms the absence of free NiO phase on the catalyst, which would produce a component at 854.3 eV[16], [60], [134], [135]. Instead, the peak fitting produced two components at higher

biding energies of 857.1 and 862.9 eV. The first component at 857.1 eV has been assigned to either highly dispersed tetrahedral Ni^{2+} interacting with the catalyst's lattice oxygen or Ni silicate/aluminate[16], [60], [136]–[140] and the second peak at 862.9 eV has been assigned to the shake-up satellite peak of isolated Ni^{2+} species[134]. Note that these two peaks are shifted to higher binding energy values (~ 0.4 eV), which provides indications for the presence of Ni^{2+} in exchanging positions[136]. The peak fitting of the $Ni2p_{1/2}$ region shows two components at 874.7 and 880.9 eV, which have been ascribed to tetrahedral Ni^{2+} species coordinated with lattice oxygen and the shake-up satellite of isolated Ni^{2+} species, respectively[60].

Pyridine sorption over the pristine SIRAL40-HPV support and Ni-SIRAL catalyst indicates that the concentration of Brønsted sites decreased from 139 to 43 μmol/g and the concentration of Lewis sites increased from 108 to 138 μmol/g after nickel impregnation. The decrease in the concentration of Brønsted sites followed by the formation of additional Lewis sites suggests that nickel exchanges Brønsted sites on the catalyst[7].

Based on the characterization results, most of the nickel present on the catalyst surface is in ionic form. Also, the results strongly advocate for the presence of highly dispersed Ni^{2+} species tetrahedrally coordinated with lattice oxygen on the catalyst. These ionic nickel species are characterized as Lewis acids[7].

Note that while X-ray penetration is usually more than 100 nm, detectable photoelectrons are at a much shorter depth (~ 2 nm)[141]. Therefore, it is possible that very small NiO crystallites are still present deep at the inner walls of the catalyst, despite the absence of Ni^{2+} components for free NiO phase in the $Ni2p_{3/2}$ region of the X-ray photoelectron spectrum[134]. The very week diffractions for the free NiO in the XRD pattern also indicates these NiO crystallites are very small and highly dispersed inside of the catalyst.

6.3.2 *Ethylene oligomerization over Ni-SIRAL40*

Table 1 shows the summary of experimental results obtained in this work. In the following sections we discuss in detail the effects of reactor temperature, pressure, and configuration (single vs dual reactor) on product distribution, liquid composition, and liquid selectivity.

6.3.2.1 Effect of reaction temperature under supercritical conditions

Table 6.1 (Tests 1, 2, and 3) shows that the ethylene conversion increased from 16.3 to 42.2% with an increase in temperature from 50 to 100°C, and then it increases from 42.2 to 90.6% with an increase in temperature from 100 to 200°C. Also, the yield for liquid hydrocarbons increased from 0.5 and 2.9% at 50 and 100°C, respectively, to 41.7% at 200°C. The majority of the liquid product obtained at 200°C is composed of *n*-alkenes (56.4 wt. %) followed by iso-alkenes (42.1 wt. %) and small fractions of 3.4 and 0.5 wt. % of cycloalkanes and aromatics, respectively. Based on the results, the oligomerization of supercritical ethylene over the Ni-SIRAL40 catalyst at 200°C and 65 bar total pressure led to the greatest yield for liquids among all temperatures tested in this work. However, the yield for cycloalkanes is still low at this condition, and most of the liquid is composed of n-alkenes and iso-alkenes.

Table 6.1. Summary of experimental results reported in the present work[11]

Test	1	2	3	4	5	6
Reaction conditions						
# of reactors	1	1	1	1	2	2
Total catalyst mass	1.00	1.00	1.00	1.00	2.01	2.01
Temperature (°C)	50	100	200	200	200	200
Pressure (bar)	65.0	65.0	65.0	40.0	40.0	65.0
Time (h)	6	6	5	6	6	5
C_2H_4 flow rate (ml STD/min)	163	163	163	163	163	163
N_2 flow rate (ml STD/min)	20	20	20	20	20	20
WHSV (h^{-1})	12.3	12.3	12.3	12.3	12.3	12.3

[11] Liquid collected at ambient pressure for Tests 1 and 2. Liquid phase composition and selectivity for Tests 1 and 2 not available.

Conversion						
Ethylene (%)	16.3	42.2	90.6	54.1	74.2	94.3
Mass balance closure for the process (%)	96.2	104.6	77.5	83.3	88.0	94.3
Yield (wt. %)						
Liquid	0.5	2.9	41.7	19.3	35.9	60.8
Gas	10.8	41.5	27.2	13.0	18.7	30.6
Coke	1.3	3.1	2.4	2.0	4.9	4.5
Composition of liquid phase (wt. %)						
n-alkenes	-	-	56.4	29.0	31.1	51.5
iso-alkenes	-	-	42.1	18.0	36.9	48.4
cycloalkanes	-	-	3.4	0.6	7.3	8.5
aromatics	-	-	0.5	0.1	0.0	0.2
mass balance closure for liquid composition (wt. %)	-	-	102.4	47.8	75.2	108.6
Selectivity of liquid phase (wt. %)						
C_4	-	-	20.7	15.5	19.3	19.8
C_5	-	-	1.0	0.7	0.3	0.2
C_6	-	-	36.0	18.6	18.2	35.6
C_7	-	-	6.9	0.4	0.2	0.9
C_8	-	-	24.4	8.7	17.8	27.1
C_9	-	-	0.5	0.9	1.1	1.6
C_{10}	-	-	8.5	2.9	10.7	15.1
C_{11}	-	-	0.4	0.1	1.3	1.3
C_{12}	-	-	3.6	0.2	5.2	5.3
C_{13}	-	-	0.0	0.1	0.2	0.2
C_{14}	-	-	0.2	0.0	0.2	0.3
C_{15}	-	-	0.0	0.0	0.0	0.4
C_{16}	-	-	0.0	0.0	0.1	0.0
C_{16+}	-	-	0.1	0.0	0.6	0.8
mass balance closure for liquid selectivity (wt. %)	-	-	102.4	47.8	75.2	108.6

In our previous publication, we hypothesized the supercritical ethylene promoted the formation of cycloalkanes over the Ni-H-Beta via dissolution of coke fractions from the catalyst surface[13]. To validate this hypothesis and further our understanding of the reaction pathway involved in the formation of cycloalkanes over the Ni-SIRAL40 catalyst, we investigated the effect of ethylene pressure on the composition of the liquid.

6.3.2.2 Effect of reaction pressure

Table 6.1 (Tests 3 and 4) shows that a change from supercritical (total pressure = 65 bar) to subcritical (total pressure = 40 bar) conditions caused a reduction in ethylene conversion and liquid yield from 90.6 to 54.1% and 41.7 to 19.3%, respectively. The composition of the liquid indicates a reduction in the ratio of iso-alkenes to *n*-alkenes from 0.74 under supercritical conditions to 0.62 under subcritical conditions. Also, there was a reduction in the yield for cycloalkanes from 3.4 to 0.6 wt. % after the change from supercritical to subcritical conditions.

The trend indicates that supercritical ethylene promote the formation of cyclic molecules as we previously hypothesize, and it also favors the formation of alkylated products. Table 6.1 shows that the liquid produced under supercritical conditions contains a much greater fraction of C_6, C_8, C_{10}, and C_{12}, than the liquid collected at subcritical conditions. However, this analysis is limited by the poor mass balance closure of the quantified fractions in the liquid collected at 40 bar.

As explained in the Section 6.2, the yields and selectivities of the fractions present in the liquid were quantified based on calibrations given in mass%. This is the reason why the sum of quantified fractions in the liquid does not add to 100%. As noted by Pires et al.[113], the poor mass balance closure for GC-MS analysis of the liquid is due to the small number of standards used to quantify the several species in the liquid. Ideally, one would want to use standards that match physical and chemical characteristics of each components in the liquid. However, the liquid products contain more than 100 components, for which some of the commercial standards are not even available.

Table 6.2 shows the relative content of the liquid fractions based on the quantified yields and selectivities shown in Table 6.1. The normalized composition shown in Table 6.2 supports our

analysis that the formation of cycloalkanes and alkylated products is favored at supercritical conditions (Tests 3 and 4). Except for C_6, the normalized data indicates an increase in the selectivity for C_8, C_{10}, and C_{12} fractions with change from subcritical to supercritical conditions. We note that the normalized content of C_4 in the liquid is much higher at subcritical conditions, suggesting that the formation of high molecular weight products is favored in supercritical ethylene.

Table 6.2. Relative content of the fractions (wt. % of total quantified liquid)

Test	1	2	3	4	5	6
Reaction conditions						
# of reactors	1	1	1	1	2	2
Temperature (°C)	50	100	200	200	200	200
Pressure (bar)	65.0	65.0	65.0	40.0	40.0	65.0
Composition of liquid phase (wt. %)						
n-alkenes			55.1	60.7	41.3	47.4
iso-alkenes			41.1	37.7	49.1	44.6
cycloalkanes			3.3	1.3	9.7	7.8
aromatics			0.5	0.3	0.0	0.1
Selectivity of liquid phase (wt. %)						
C_4			20.2	32.4	25.3	18.2
C_6			35.2	39.0	24.3	32.7
C_8			23.8	18.2	23.7	25.0
C_{10}			8.3	6.1	14.2	13.9
C_{12}			3.5	0.5	6.9	4.9
C_{14}			0.2	0.0	0.3	0.3
C_{16}			0.0	0.0	0.1	0.0
C_{16+}			0.1	0.0	0.8	0.7

6.3.2.3 Single vs. dual reactor configuration

According to the results, the oligomerization of supercritical ethylene over the Ni-SIRAL40 at 200°C and 65 bar produced the maximum amount of liquid, 41.7%, with the maximum composition of cycloalkanes, 3.4 wt. %, and C_6-C_{16+}, 80.6 wt. %, among the conditions tested in this work. However, a substantial amount of gas was formed, 27.2%, and 20.7 wt. % of the liquid consisted of C_4. The majority of the gas formed consisted of C_4, with trace amounts of C_6 and C_8.

The results at 200°C and 65 bar indicate that the Ni-SIRAL40 catalyst was able to consume virtually all the ethylene introduced into the reactor. To increase liquid yield and its molecular weight, we decided to introduce a second reactor downstream of the first one. We hypothesized that the gaseous C_4 fraction produced in the first reactor would undergo further oligomerization in the second reactor. This way, we would be able to reduce the formation of gaseous C_4, thus increasing liquid yield and its high molecular weight fractions (C_6-C_{16+}) via conversion of C_4 into C_6, C_8, C_{10}, C_{12}, C_{14}, C_{16}, and C_{16+}.

Table 6.1 (Tests 3 and 6) shows that the introduction of a second reactor led to an increase in liquid yield from 41.7 to 60.8%. However, gas yield also increased after the addition of the second reactor. Note that the mass balance closure with a single reactor was 77.5%, while the mass balance closure with two reactors was 94.3%. Therefore, the apparent increase in gas yield after the introduction of a second reactor can be ascribed to the insufficient collection of gases formed in the experiment with a single reactor.

The cycloalkane yield in the liquid increased from 3.4 to 8.5 wt. % after the addition of a second reactor. Since almost all the ethylene was consumed in the first reactor, the increase in liquid and cycloalkane yields may be ascribed to the oligomerization and cyclization of long-chain alkenes (formed in the first reactor) in the second reactor. Table 6.1 shows that except for C_{10}, the selectivity for all products remained unchanged after the addition of a second reactor. Table 6.3 shows the mass yield (in grams) of fractions in the liquid calculated by multiplying the selectivities shown in Table 6.1 by the total mass of liquid collected after the reaction.

Although the selectivities remained unchanged after the introduction of a second reactor in the reaction system, the masses of C_6, C_8, C_{10}, C_{12} in the liquid increased between 35 and 144%. We estimate that 12.5 grams of gaseous C_4 were not collected in the experiment with a single

reactor, which corresponds to almost the same increase in liquid mass after the introduction of the second reactor. Based on this analysis, it is reasonable to assume that out of the total mass of C_4 produced in Test 3 (single reactor), 29.3 grams, 12.5 grams were converted into C_6, C_8, C_{10}, C_{12} in the second reactor, which corresponds to a C_4 conversion of approximately 30%.

Table 6.3. Yield of the fractions in the liquid (in grams)

Test	1	2	3	4	5	6
Reaction conditions						
# of reactors	1	1	1	1	2	2
Temperature (^{o}C)	50	100	200	200	200	200
Pressure (bar)	65.0	65.0	65.0	40.0	40.0	65.0
Yield of liquid phase (grams)						
C_4			5.2	4.6	6.7	6.8
C_6			9.0	5.6	6.4	12.2
C_8			6.1	2.6	6.3	9.3
C_{10}			2.1	0.9	3.8	5.2
C_{12}			0.9	0.1	1.8	1.8
C_{14}			0.1	0.0	0.1	0.1
C_{16}			0.0	0.0	0.0	0.0
C_{16+}			0.0	0.0	0.2	0.3

There was also an increase in C_4 yield from 5.2 to 6.8 grams, which corresponds to an increase of approximately 30%. The additional C_4 collected in the liquid may be ascribed to the conversion of unreacted ethylene in the second reactor. Note that the conversion of butene over the Ni-SIRAL40 catalyst in the second reactor suggests that this catalyst can oligomerize not only ethylene but also light-olefins, such as butene.

6.3.2.4 Subcritical vs. supercritical ethylene in a dual reactor configuration

The results presented up to this point suggest that oligomerization of supercritical ethylene in a dual reactor favors the formation of liquids and cycloalkanes. One major concern in chemical processes involving supercritical fluids is the high operating costs to pressurize gases. It would be

beneficial to produce cycloalkanes at economically justifiable yields also at subcritical conditions. To assess the effect of subcritical and supercritical conditions in the yields of liquid and cycloalkane at the optimum reactor configuration, we performed the ethylene oligomerization using a dual reactor configuration under subcritical conditions (40 bar) at 200^{o}C.

Table 6.1 (Tests 5 and 6) shows a liquid yield of 35.9 wt. % under subcritical conditions compared to 60.8 wt. % under supercritical conditions. The lower yield for liquid products at subcritical conditions was expected since oligomerization rates increase with reactant pressure. However, analysis of the liquid fractions suggests a yield for cycloalkanes of 7.3 wt. % under subcritical conditions, approximately equal to the yield for cycloalkanes obtained under supercritical conditions. This result is promising because it indicates that supercritical conditions may not be necessary for the production of cycloalkanes. Compared to the experiment performed with a single reactor at subcritical conditions (40 bar), the yield for cycloalkanes in the liquid increased substantially from 0.6 to 7.3 wt. %. This is a much greater increase in cycloalkane fraction than the one after the introduction of the second reactor under supercritical conditions, from 3.3 to 8.5 wt. %. We note that while cycloalkane yields (in wt. %) are similar under subcritical and supercritical conditions, a greater mass of cycloalkanes was obtained under supercritical conditions since more liquid was produced under this condition.

The results presented in this section provide evidence for an additional pathway for cycloalkanes, where not only coke solubilization in supercritical ethylene contributes to the formation of cycloalkanes, but cyclization of higher alkenes also assists the formation of these molecules. We note that the rates of cyclization increase with reaction pressure[142]. Therefore, while cycloalkanes can be formed under subcritical conditions, their formation is favorable under supercritical conditions.

6.3.3 *Liquid characterization*

Table 6.4 shows the most abundant molecules in the liquid collected after the oligomerization of supercritical ethylene at 200^{o}C and 65 bar over the Ni-SIRAL40 catalyst in a dual reactor configuration. Sixty percent of C_6 in the liquid comprises 2-hexene with an additional 4% of 1-hexene, which suggests a small extent of isomerization of n-hexene over the acid sites of the Ni-SIRAL40 catalyst. On the other hand, the fraction of normal molecules in the liquid comprising C_8, C_{10}, and C_{12} varies between 8 and 17%, suggesting a high extent of isomerization of *n*-octene, *n*-decene, and *n*-dodecene over acid sites. Note that the degree of branching among the most abundant C_8, C_{10}, and C_{12} molecules is uniform with the presence of both light and heavy branching (Table 6.4 – aliphatic column for C_8, C_{10}, and C_{12}).

Heavily branched 6-membered cycloalkanes are the most abundant cycloalkanes present in the liquid. Most of these molecules are included in the C_{10} fraction, comprising 35% of the cycloalkanes in the liquid. The second, third, and fourth most abundant fractions of 6-membered cycloalkanes are found among C_{12}, C_{11}, and C_{18}, comprising 15, 12, and 9% of the cycloalkanes in the liquid, respectively. Based on the most abundant cycloalkanes among C_{10} and C_{12} shown in Table 6.4, methyl, ethyl, and propyl are the most common alkyl substituents in these molecules.

Concerning the ring size, a 6-membered ring is the most favorable conformation for cycloalkanes from a thermodynamic standpoint[142]. Therefore, it is not surprising that 71% of cycloalkanes in the liquid are 6-membered cyclic molecules.

Table 6.4. Most abundant molecules in the liquid (T=200°C, P=65 bar, double reactor configuration) identified via GC-MS and their respective yields

species	aliphatic	MS score*	yield (wt. %)	cyclic	MS score*	yield (wt. %)
C_6	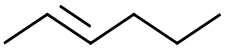 2-hexene	97	21.5	-	-	-
C_8	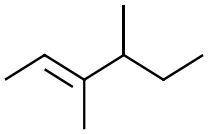 3,4-dimethyl-2-hexene	96	7.4	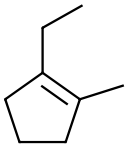 1-ethyl-2-methylcyclopentene	92	0.1
C_{10}	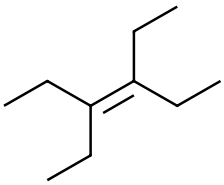 3,4-diethyl-3-hexene	93	2.1	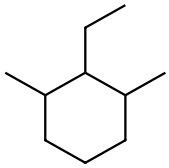 2-ethyl-1,3-dimethylcyclohexane	89	1.6
				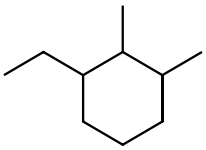 1-ethyl-2,3-dimethyl cyclohexane	91	0.6
				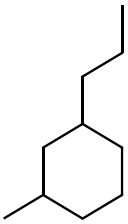 1-methyl-3-propylcyclohexane	92	0.5
C_{11}	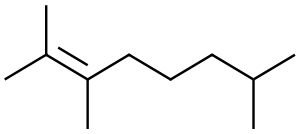 2,3,7-trimethyl-2-octene	83	0.3	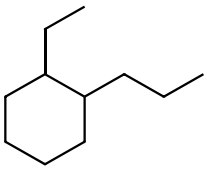 1-ethyl-2-propylcyclohexane	88	0.9

C_{12}	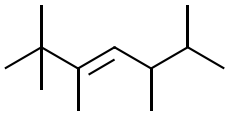 2,2,3,5,6-pentamethyl-3-heptene	84	0.7	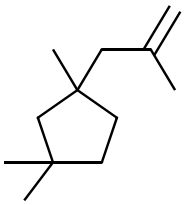 1,1,3-trimethyl-3-(2-methyl-2-propenyl)-cyclopentane	86	0.5
				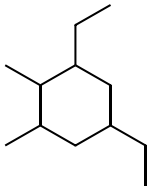 1,5-diethyl-2,3-dimethylcyclohexane	86	0.3
C_{15}				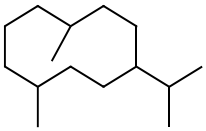 1,7-dimethyl-4-(1-methylethyl)cyclodecane	85	0.4

* GC-MS similarity score.

Some of the molecules obtained in this work are similar to the molecules already present in commercial jet fuel. For instance, 2,3,7-trimethyl-2-octene and 2,2,3,5,6-pentamethyl-3-heptene are very similar to 2,5,6-trimethyl-octane and 2,2,4,6,6-pentamethyl-heptane found in Jet-A, JP-5, and JP-8, and some of the sustainable jet fuels approved by ASTM[113]. It is important to emphasize that a hydrogenation step is required to convert the alkenes into alkanes and that this process is not expected to change the degree of branching and size of the molecules present in the liquid. With respect to cycloalkanes, 1-methyl-3-propyl-cyclohexane is similar to 1-methyl-2-propyl-cyclohexane, already present in commercial jet fuels[113].

One important aspect concerning the cycloalkanes obtained in this work is their degree of branching. The cycloalkanes are heavily branched as shown in Table 6.4. The effect of

cycloalkane's degree of branching in jet fuel properties is still a topic that requires further investigation[112].

6.3.4 *Reaction pathway*

We developed a reaction pathway to explain the formation of the several molecules obtained in the present work. This pathway combines previous results reported by our research group[13] and the results obtained in this work. The proposed pathway is mostly based on the composition of the liquid and gas products via GC-MS/FID and GC-FID/TCD.

Figure 6.3 shows the reaction pathways identified in the present work for the ethylene oligomerization over the Ni-SIRAL catalyst: oligomerization, isomerization, co-oligomerization, cyclization, and cycloalkanes originated from dissolved coke by supercritical ethylene. The pathway agrees with results obtained at 50, 100, and 200^{o}C, total pressures of 40 and 65 bar, and single and dual reactor configurations. Note that the proposed reaction pathway has the objective to highlight the routes involved in the formation of the several products obtained in the present work.

For a single reactor configuration, operating at subcritical conditions, oligomerization, and isomerization are the main reaction pathways contributing to the composition of the liquid and product selectivity reported in Table 6.1. Co-oligomerization and cyclization of higher alkenes may also take place; however, to a much lower extent relative to oligomerization and isomerization pathways. The introduction of a second reactor under subcritical conditions promotes co-oligomerization and cyclization of higher alkenes, thus, contributing to the increase in cycloalkanes and long-chain alkenes yields.

Under supercritical conditions, oligomerization, isomerization, co-oligomerization, cyclization, and cycloalkane formation from dissolved coke take place at both single and dual

reactor configurations. Co-oligomerization of higher alkenes, especially C_4, in the second reactor, increases the molecular weight of the liquid. Because almost all the ethylene is consumed in the first reactor, ethylene oligomerization pathway is negligible in the second reactor. We hypothesize that both linear and branched alkenes may undergo cyclization as shows in Figure 6.3. For instance, 2-decene and 3-decene can form 1,2-diethylcyclohexane and 3-ethyl-2-methyl-1-hepetene can form 1-ethyl-2,4-dimethylcyclohexane. All species considered in the cyclization pathway were identified via GC-MS/FID in the liquid.

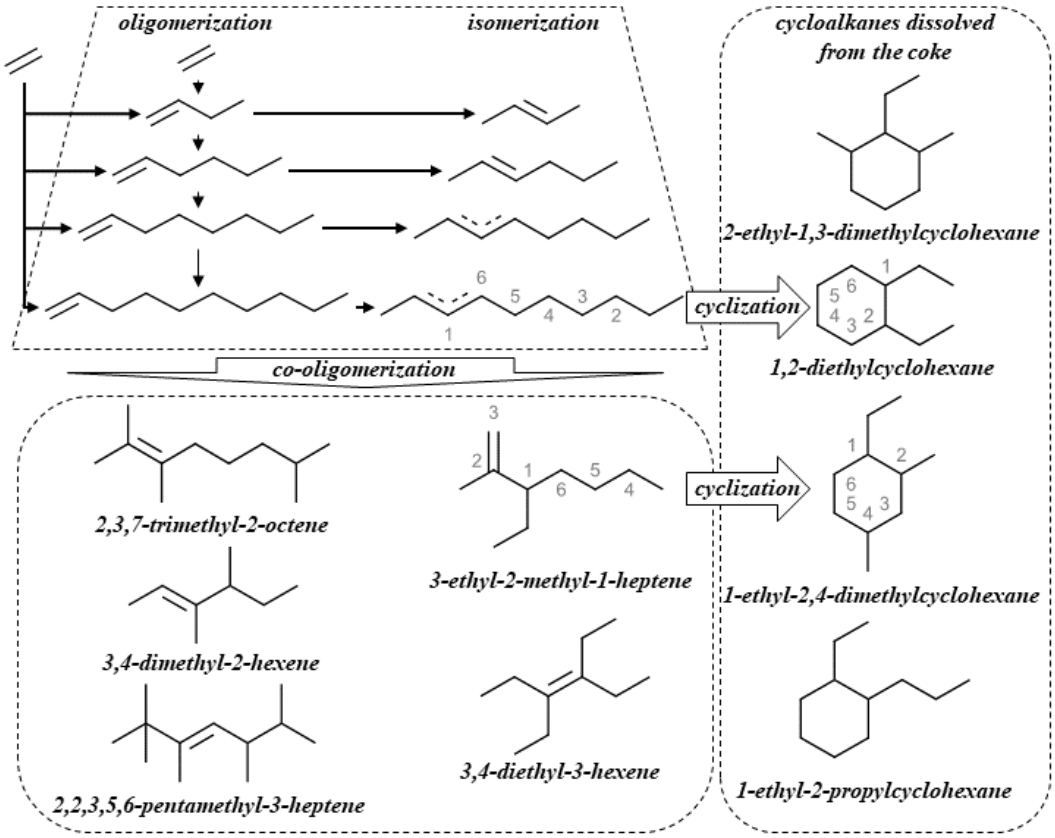

Figure 6.3. Proposed reaction pathway for the ethylene oligomerization over the Ni-SIRAL catalyst.

6.4 CONCLUSION

In the present work, we present a novel route for the production of alkenes and cycloalkanes via oligomerization of ethylene over a Ni-SIRAL catalyst. This route takes place at both subcritical and supercritical ethylene. We report the production of liquid products at 50, 100, and 200^{o}C, pressures of 40 and 65 bar in a reaction system set up for single and dual reactor. At supercritical conditions (65 bar), the production of liquid products increases with reaction temperature reaching a maximum of 41.7 wt. %, with a single reactor, and 60.8 wt. % with a dual reactor, at 200^{o}C. Supercritical ethylene also favors the formation of cycloalkanes, with a maximum yield of 8.5 wt. % at 200^{o}C with 2 consecutive reactors. We show that the production of cycloalkenes is also possible with a dual reactor configuration under subcritical conditions (40 bar) leading to a yield for cycloalkanes of 7.3 wt. %, at 200^{o}C.

We proposed a reaction pathway based on the experimental results, which considers the following reaction routes: oligomerization, isomerization, co-oligomerization, cyclization, and formation of cycloalkanes from coke dissolution by supercritical ethylene. According to the results, the formation of cycloalkanes at subcritical conditions with a dual reactor proceeds via cyclization of higher alkenes, while cycloalkanes from coke dissolution by ethylene also takes place under supercritical conditions.

Chapter 7. TECNO-ECONOMIC ASSESSMENT OF POPLAR CONVERSION INTO JET FUEL VIA ALCOHOL-TO-JET TECHNOLOGY

7.1 PROCESS OVERVIEW

The overall goal of the present Chapter is to evaluate the process economics for the production of jet fuel (liquid hydrocarbon mixture of alkanes and cycloalkanes) via oligomerization of ethylene over an environmentally friendly heterogeneous catalyst. A sustainable route for ethylene was adopted, starting from renewable resources via dehydration of lignocellulosic ethanol. The process presented in this work uses poplar as the feedstock for the production of jet fuel. Poplar has excellent characteristics for biofuel production – poplar has high productivity, requires little fertilizer input, and can re-sprout from the same stem after multiple harvests[143]. The process designed for the conversion of poplar into jet fuel is shown in Figure 7.1. Initially, the biomass undergoes dilute acid pretreatment in Area 100 (Figure 7.1 – A100) to fractionate the raw biomass into its individual components: lignin, cellulose, and hemicellulose. The liquid fraction contains monomeric sugars from the hydrolyzed hemicellulose and sugar degradation products (*i.e.*, furfural), and the solid fraction contains the unhydrolyzed lignin and cellulose. The outlet stream from Area 100 goes to Area 200 (Figure 7.1 – A200), which combines the enzymatic hydrolysis and overliming steps. The cellulose in the solid stream from Area 100 is hydrolyzed into glucose via enzymatic hydrolysis. In the overliming step, calcium hydroxide is used to remove sugar degradation products and phenolic components, which are undesirable during the fermentation step[144]. While overliming is necessary to remove troublesome components in the fermentation step, it promotes side reactions at high pH responsible for causing

sugar losses up to 30%[144]. Also, a solid fraction, gypsum, forms during this process from calcium hydroxide reaction with sulfuric acid, which requires an additional separation step to separate the sugars from the gypsum[144]. The outlet stream from hydrolysis is then mixed with the outlet stream from the overliming step and sent to fermentation.

The liquid stream from Area 200 goes to Area 300 (Figure 7.1 – A300), where most of the monomeric sugars are fermented into ethanol, and a smaller fraction of the fermentable sugars are lost to co-fermentation reactions into acetic acid. Area 300 also includes the seed fermenters used to grow the *Zymomonas mobilis* strain microorganisms used during fermentation. The outlet stream from Area 300 – denoted beer – contains water, microorganisms, monomeric and oligomeric sugars, furfural, acetic acid, ethanol, dissolved solids, and lignin. The beer is sent to Area 400 (Figure 7.1 – A400), where the ethanol is separated from the other components present in the beer via fractional distillation in the beer column. The ethanol stream from Area 400, which contains water and CO_2, is sent to Area 600 (Figure 7.1 – A600). The bottom stream from the beer column, which contains water, microorganisms, monomeric and oligomeric sugars, furfural, acetic acid, dissolved solids, and lignin, goes to a separator to recover the solid and liquid fractions. The liquid stream (mostly water mixed with furfural, acetic acid, and dissolved solids) goes to Area 900 (Figure 7.1 – A900) for wastewater treatment. The solid fraction (mostly lignin mixed with water, microorganisms, monomeric and oligomeric sugars, furfural, acetic acid, and dissolved solids) goes to the boiler in Area 500 (Figure 7.1 – A500) for steam production and electricity generation.

Areas 600, 700, and 800 are responsible for the conversion of ethanol into ethylene, conversion of ethylene into alkenes, and conversion of alkenes into alkanes and cycloalkanes, respectively. In Area 600, ethanol is dehydrated into ethylene over an HZSM-5 catalyst at 1 atm

and 205^{o}C. The outlet stream from the dehydration reactor, which contains ethylene, unreacted ethanol, CO_2, and water, is alkali-treated with sodium hydroxide to remove the CO_2 as sodium carbonate. Then, unreacted ethanol and water are recycled back to the dehydration reactor and high purity ethylene is sent to Area 700 (Figure 7.1 – A700) for oligomerization.

Before entering the oligomerization reactor, high purity ethylene from Area 600 is sent to a compressor and pressurized to 100 bar. Then, pressurized ethylene is oligomerized over the Ni-SIRAL 40 HPV catalyst presented in Chapter 6. Fractional distillation is used to separate the liquid products (C_6+ alkenes and cycloalkanes) from butene, pentene, and unreacted ethylene, which are recycled back to the oligomerization reactor.

The liquid alkenes from Area 700 are then hydrogenated into alkanes in Area 800 (Figure 7.1 – A800). The hydrogenation step is a relatively simple process, where the double bonds of the alkenes are hydrogenated in the presence of hydrogen and a solid catalyst at 17 bar and 100^{o}C. After that, unreacted hydrogen is separated from the liquid mixture to obtain the jet fuel product that contains alkanes and cycloalkanes.

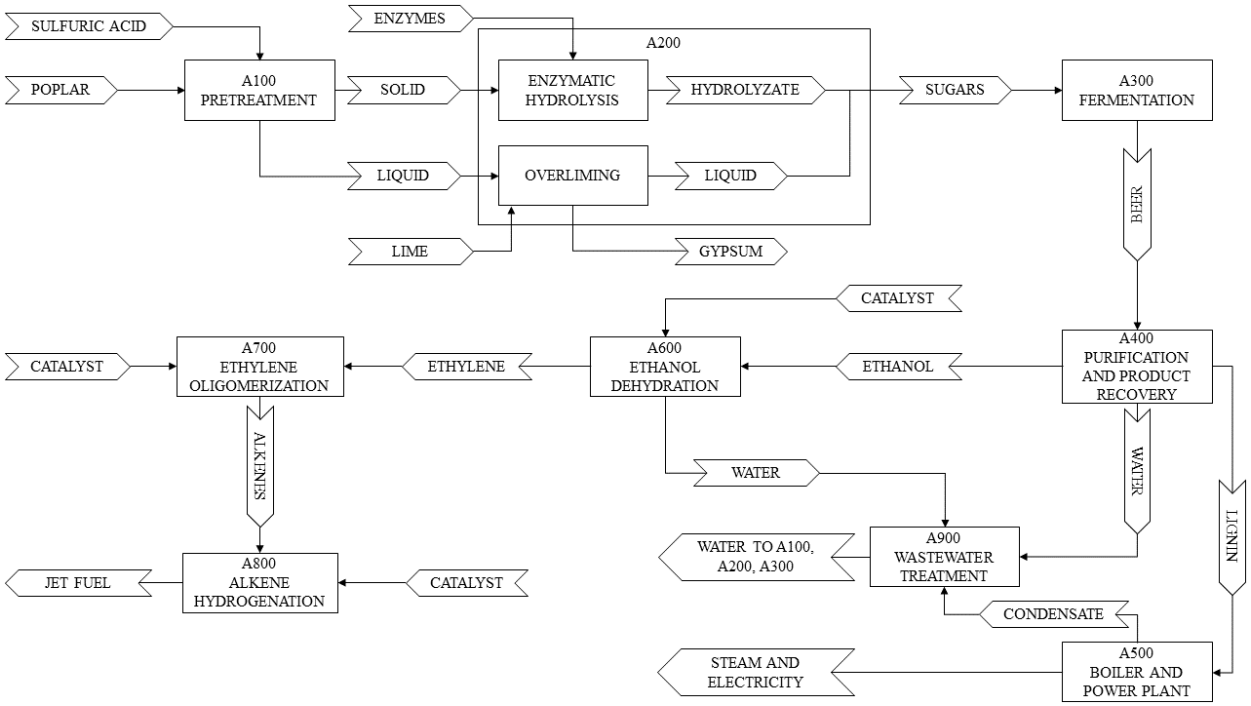

Figure 7.1. Process flow diagram of the designed process for the production of jet fuel from poplar. Only main component streams are shown.

7.2 PROCESS DESIGN AND COST ESTIMATING

The process design and specifications are presented. The assumptions used in the design of the areas are based on NREL's report from 2002[145] and 2011[146]. The design presented in this section is a baseline for estimating operating and capital costs, which assumes a scale of 2,000 dry metric tons of biomass/day. Later, a sensitivity analysis is performed to show the effect of process conditions on the minimum jet fuel selling price.

7.2.1 *Area 100: Pretreatment*

In Area 100, the biomass is deconstructed into its main fractions (cellulose, hemicellulose, and lignin) via dilute-acid hydrolysis. The hydrolysis is catalyzed by dilute sulfuric acid at the conditions shown in Table 7.1. In the biomass pretreatment step, the hemicellulose (mannan, galactan, xylan, and arabinan) is hydrolyzed into monomeric sugars. Most of the hemicellulose in poplar is xylan with small fractions of mannan, galactan, and arabinan[144]. Also, the acetyl groups of the hemicellulose are converted into acetic acid and a small fraction of the hydrolysate sugars can become degradation products (*i.e.*, HMF and furfural)[144]. In the present design, it is assumed that 90% of the xylan is hydrolyzed into xylose, a small fraction (9.9%) of the cellulose is hydrolyzed into glucose, and most of the lignin (95%) remains solid during hydrolysis[146]. Table 7.2 presents the chemical reactions and conversions used to model Area 100.

The pretreatment reactor considered in the present work is similar to the one reported in a previous NREL report[145], [146]. It consists of a single horizontal reaction vessel designed to operate at temperatures up to 190°C, sulfuric acid loading up to 1.1 wt. %, and residence time up to 10 minutes. The pretreatment system and solid-liquid separator used in Area 100 were previously quoted at $20MM (2009$)[146] and $30MM (2009$)[146], respectively.

Table 7.1. Conditions used for pretreatment

Sulfuric acid loading	35.3 mg/g dry biomass
Steam loading (at 190°C and 13.7 atm)	3.2 kg/kg dry biomass
Temperature	190°C
Pressure	13 atm

Table 7.2. Dilute acid pretreatment hydrolysis reactions and conversions

Reaction	Reactant	% Converted to product
$(Cellulose)_n + nH_2O \rightarrow nGlucose$	Cellulose	9.9%
$(Xylan)_n + nH_2O \rightarrow nXylose$	Xylan	90.0%
$(Xylan)_n \rightarrow nFurfural + 2nH_2O$	Xylan	5.0%
$Acetate \rightarrow Acetic\ acid$	Acetate	100.0%
$(Lignin)_n \rightarrow n\ Soluble\ Lignin$	Lignin	5.0%

7.2.2 *Area 200: Enzymatic hydrolysis and overliming*

In the present design, the cellulose in the solid stream from Area 100 is hydrolyzed into glucose before fermentation in Area 300. This process is known as separate hydrolysis and fermentation (SHF). It is assumed that the hydrolysis takes place at a temperature of 48^{o}C, and a cellulase loading of 20 mg/g of cellulose producing a cellulose conversion of 90%[146]. Most of the operating cost for Area 200 is from enzyme production with cellulase production costs reported at $4.24/kg of cellulase[146]. For a more conservative design, an enzyme production cost of $10.14/kg of cellulase was adopted[147] since a production cost of $4.24/kg of cellulase seems too optimistic and assumes zero cost with transportation and formulation[146]; assumptions not included in the present design. Capital investment for enzyme production was not modeled in the present design and is estimated based on a previous NREL report; $18.3MM (2007$) for the Base Case (2,000 dry metric tons of biomass/day)[146].

The liquid stream from Area 100 is sent to an overliming unit, where calcium hydroxide is added to precipitate components that can upset the fermentation of sugars. From 20 to 30% of the fermentable sugars are lost during overliming[144]–[146]. The mechanisms involved in the removal of degradation products and the loss of sugars during overliming are unknown[144]. In the present design, a sugar loss of 30% is assumed in the overliming step. Table 7.3 shows the reaction and conversion assumed for gypsum formation during the overliming step. At the end of the overliming process, the liquid stream from hydrolysis is mixed with the liquid stream from the overliming unit to produce the sugar-rich stream that goes to Area 300 for fermentation. Costs for the saccharification and overliming tanks were obtained from [145], [146].

Table 7.3. Overliming reactions and conversions

Reaction	Reactant	% Converted to product
$Ca(OH)_2 + H_2SO_4 \rightarrow CaSO_4.2H_2O\ (Gypsum)$	$Ca(OH)_2$	100.0%

7.2.3 *Area 300: Fermentation*

Area 300 includes the seed fermenters used to inoculate the bacteria used during fermentation and the main fermenters. In the present design, the co-fermentation of xylose and glucose to ethanol is performed using the *Zymomonas mobilis* strain microorganisms[146]. Eight percent of the sugar stream from Area 200 is sent to the seed fermenters for inoculation of the bacteria. The bacteria are first grown in a progressively scaled series of seed fermenters (seed train) at 41°C. Diammonium phosphate (DAP) is added to the seed fermenters as a nitrogen source for *Zymomonas mobilis* growth at a concentration of 0.67g/L of broth. A price of $967/ton of DAP is assumed. After growth, the inoculated cells are fed into the main fermenters for the fermentation of sugars from Area 200, where the fermentation process takes place at a temperature of 41°C. It is assumed that 3.0% of xylose and glucose available for conversion are lost to acetic acid due to contamination in the seed fermenter. The scale and number of fermenters and seed fermenters assumed in the present design are the same reported in previous NREL reports. Table 7.4 and Table 7.5 list the chemical reactions and conversions assumed for the seed fermenters and main fermenters, respectively.

Table 7.4. Seed fermenters reactions and conversions

Reaction	Reactant	% Converted to product
$Glucose \rightarrow 2\ CO_2 + 2\ Ethanol$	Glucose	90.0%
$3\ Xylose \rightarrow 5\ CO_2 + 5\ Ethanol$	Xylose	80.0%
$Glucose \rightarrow 3 Acetic\ acid$	Glucose	3.0%
$2\ Xylose \rightarrow 5\ Acetic\ acid$	Xylose	3.0%

Table 7.5. Main fermenters reactions and conversions

Reaction	Reactant	% Converted to product
$Glucose \rightarrow 2\ CO_2 + 2\ Ethanol$	Glucose	95.0%
$Galactose \rightarrow 2\ CO_2 + 2\ Ethanol$	Galactose	32.5%
$Mannose \rightarrow 2\ CO_2 + 2\ Ethanol$	Mannose	32.5%
$3\ Xylose \rightarrow 5\ CO_2 + 5\ Ethanol$	Xylose	85.0%
$3\ Arabinose \rightarrow 5\ CO_2 + 5\ Ethanol$	Arabinose	80.0%

The outlet stream from Area 300 – denoted beer – contains ethanol at a concentration of 2.6 wt. % and it is mixed with impurities, solids, uncovered sugars, and water. This stream goes to Area 400 for purification and recovery. The seed fermenters and the main fermenter were quoted at $1.8MM (2009$) and $10MM (2009$), respectively[146].

7.2.4 *Area 400: Purification and product recovery*

In this area, ethanol is separated from the other components present in the beer stream via fractional distillation in the beer column. The beer column contains 32 plates and works at a reflux ratio of 3 and a bottom to feed ratio of 0.82[146]. The beer is fed into the beer column on the fourth tray. The overhead stream contains mostly water (40.2%), CO_2 (23.7%), and ethanol (36.0%). All the CO_2 in the overhead stream and a small fraction of the ethanol (0.9%) is vented, and the remaining stream is fed back into the beer column at tray number eight. The outlet ethanol stream is side drawn from the beer column at 97^{o}C and contains 72.8 wt. % of water, 26.3 wt. % of ethanol, 0.53 wt. % of CO_2, and trace amounts of furfural and acetic acid. The high concentration of water in the outlet stream of Area 400 has no impact on the dehydration of ethanol into ethylene in Area 600 since the minimum ethanol concentration designed at the inlet of the dehydration reactor is 10 wt. %[148]. The bottom stream contains water, dissolved solids, acetic acid, sulfuric acid, monomeric sugars (glucose, mannose, galactose, xylose, and arabinose), DAP, lignin, cellulose, xylan, cellulase, oligomeric sugars, and ash. The bottom is sent to a press to separate the aqueous fraction from the solids; the solids are recovered at a consistency of 60%. The aqueous fraction is sent to Area 900 for wastewater treatment and the solid fraction is fed into the boiler in Area 500 for steam production and energy generation.

The quote from Megtec for a beer column (14’ diameter x 76’ tall with 32 trays and a 24’’ spacing) and a rectifying column, including pumps, heat exchangers, and reflux drums is $3.4MM

(2009$)[146]. This price was assumed as a conservative estimation of the cost of the beer column used in the present design. It is assumed that the cost for the solid-liquid separator unit is in the vicinity of $5MM (2002$)[145], [146].

7.2.5 *Area 500: Boiler and power plant*

Table 7.6. Boiler reactions

Reaction	Reactant
$Lignin + 10.125O_2 \rightarrow 6.95H_2O + 7.3CO_2$	Lignin
$Glucose + 6O_2 \rightarrow 6H_2O + 6CO_2$	Glucose
$Xylose + 5O_2 \rightarrow 5H_2O + 5CO_2$	Xylose
$Cellulose + 6O_2 \rightarrow 5H_2O + 6CO_2$	Cellulose
$Mannan + 6O_2 \rightarrow 5H_2O + 6CO_2$	Mannan
$Galactan + 6O_2 \rightarrow 5H_2O + 6CO_2$	Galactan
$Arabinan + 5O_2 \rightarrow 4H_2O + 5CO_2$	Arabinan
$Xylan + 5O_2 \rightarrow 4H_2O + 5CO_2$	Xylan
$Cellulase + 1.2445O_2 \rightarrow 0.785H_2O + 1CO_2 + 0.145N_2 + 0.007SO_2$	Cellulase
$Dissolved\ solids + 1.2763O_2 \rightarrow 0.74H_2O + 1CO_2 + 0.0013SO_2$	Dissolved solids
$Microorganism + 1.2O_2 \rightarrow 0.9H_2O + 1CO_2 + 0.1N_2$	Microorganisms
$Furfural + 5O_2 \rightarrow 2H_2O + 5CO_2$	Furfural
$Methane + 2O_2 \rightarrow 2H_2O + 1CO_2$	Methane

Steam and power are generated from the combustion of the solid stream from Area 400 and biogas from Area 900. The boiler operates at 454ºC and air is fed at an excess of 61.6%. Complete combustion of the organic matter in the boiler is assumed in the design. The inorganic matter in the solid inlet stream (ash from Area 400) is not combusted in the boiler. Instead, this material is recovered and sent to waste disposal – the additional operating cost for ash disposal is $35/ton of ash[149]. Superheated steam at 454ºC and 62 atm is produced in the boiler and fed into a turbine, which operates at 10 atm, to produce electricity. The outlet stream from the turbine, superheated steam at 277ºC and 10 atm, is used to heat the ethanol outlet stream from Area 400, the inlet liquid water stream in Area 500, and the butene recycle stream in Area 700. Additional steam is necessary for the process. It is important to highlight that the steam cost is determined by

the method used for steam production[150]. A steam cost of $7/ton of steam is assumed in the present design[150]. The costs for the boiler and the turbogenerator are estimated at $28.6MM (2009$) and $9.5MM (2010$), respectively[146]. Table 7.6 shows the reactions used in the combustion of organic matter in the boiler. Conversion of 100% is assumed for all reactions.

7.2.6 *Area 600: Ethanol dehydration*

Ethanol dehydration into ethylene takes place over a trifluoromethanesulfonic-modified HZSM-5 catalyst at 205ºC and 1 atm[148]. According to a previous report, 98.2% of the ethylene is converted into ethylene for a diluted ethanol stream (90 wt. % water)[148]. It is assumed that no side reactions take place during ethanol dehydration into ethylene. As mentioned previously, the high concentration of water in the outlet ethanol stream from Area 400 has no impact on the catalytic dehydration process because it meets the specifications (water composition = 72.8 wt. %) for the dehydration over the modified HZSM-5 catalyst proposed. It is also assumed that CO_2 and furfural, present in the ethanol inlet stream, have a negligible effect on the catalytic process. The outlet stream from the dehydration reactor goes into an alkali-treatment unit, where sodium hydroxide is added to remove the CO_2 as sodium carbonate. Then, the ethylene is vented and the water, unreacted ethylene, and impurities (i.e., furfural) remaining in the aqueous stream are recycled back to the dehydration reactor. In the last step of the process, ethylene passes through a series of absorbent columns (packed sieve) to remove trace amounts of water and impurities. Costs for the dehydration reaction and packed sieve absorbent columns are $3.7MM (1999$)[151] and $2.6MM (2009$)[146].

7.2.7 *Area 700: Ethylene oligomerization*

High purity ethylene from Area 600 is pressurized to 100 bar using a centrifugal compressor. During compression, the ethylene temperature increases from 50^{o}C to 442^{o}C. Therefore, no additional heating is required before feeding ethylene into the oligomerization reactor. For the Base Case scenario, ethylene oligomerization takes place over the Ni-SIRAL 40 HPV catalyst at 200^{o}C and 100 bar. Values for ethylene conversion and product yields used in the present design are reported in Chapter 6. The outlet stream from the oligomerization reactor goes into a distillation column to separate the liquid alkenes (C_6+ alkene and cycloalkanes products) from butene, pentene, and unreacted ethylene, which are recycled back to the oligomerization reactor via another centrifugal compressor. Recovery of liquid products is achieved in a distillation column mounted with 18 trays, operating at a reflux ratio of 6 and a bottom-to-feed ratio of 0.75. The concentration of butene and pentene in the distillate product is negligible. In some scenarios, cycloalkanes are recovered from the liquid alkenes before hydrogenation due to their high value. The current price of JP-10 – a military jet fuel composed mostly of one bicyclic alkane molecule – is $7,091/ton[152]. Later, we discuss the impact of cycloalkane recovery on process economics. In the present design, two consecutive distillation columns are used to separate the cycloalkanes from the alkenes. In the first column, the cycloalkanes, and light alkenes (C_6, C_7, and C_8 alkenes) are separated from the C_9+ alkene fraction. Then, the overhead from the first column, which contains the cycloalkanes and C_6, C_7, and C_8 alkenes, is fed into the second column, where the cycloalkanes are recovered in the bottom stream, and the overhead (C_6, C_7, and C_8 alkenes) is mixed with the distillate from the first column (C_9+ alkene) and sent to hydrogenation. Table 7.7 shows the number of trays, reflux ratio, and bottom to feed ratio designed for the recovery of cycloalkanes. The cycloalkane recovery using the present design is 99.9%.

Table 7.7. Parameters designed for the distillation columns used for the recovery of cycloalkanes

	First column	Second column
Number of trays	46	70
Reflux ratio	15	15
Bottom-to-feed ratio	0.81	0.94

Compressor costs were estimated based on the power necessary to pressurize the gas according to the following correlation:

$$Cost(\$) = 5{,}840 \times (Power)^{0.82} \quad (7.1)$$

Costs with reactor and distillation columns were obtained from previous NREL reports. A catalyst lifetime of 6 months was assumed. This is a conservative estimate since the lifetime of heterogeneous catalysts can range from 5 to 10 years. A catalyst cost of $500/ton was assumed in the present design.

7.2.8 *Area 800: Alkene hydrogenation*

Hydrogenation of alkanes is a fairly simple process. It was assumed that the hydrogenation takes place of a solid-based catalyst at 100^{o}C and 17 bar. The main operating cost of this area is associated with hydrogen purchase. Therefore, it was assumed a stoichiometric amount of hydrogen necessary to hydrogenate the mass of alkene in the inlet stream. The final jet fuel contains a mixture of cycloalkanes and alkanes – if cycloalkanes are recovered in Area 800, the jet fuel from Area 900 contains only linear alkanes. A more detailed design requires recycling and make-up hydrogen to achieve complete conversion of alkenes into alkanes. Also, two consecutive packed beds are usually used to protect the catalyst bed and avoid additional costs with catalyst replacement. The costs with a second reactor, recycle, and hydrogen compression are not considered in the present design, and these would account for a small fraction of the total capital investment. A hydrogen cost of $1,508/ton is assumed[149].

7.2.9 *Area 900: Wastewater treatment*

Wastewater from Areas from 400, 500, and 600 are sent to an anaerobic pond where the organic matter is decomposed by anaerobic microorganisms. This process produces 10 g of biogas/L of wastewater feed, which is fed into the boiler in Area 500. The aqueous outlet stream from the anaerobic pond is then sent to aerobic digesters, where aerobic microorganisms finish decomposing the organic matter in the wastewater stream. This process produces a sludge that can be either burned in the boiler to recover energy or disposed. Twenty percent of the outlet stream from the aerobic digester is recycled into the anaerobic pond and the remaining stream is alkali-treated to remove CO_2. Other impurities (*i.e.*, SO_2) can also be removed via alkali treatment. Additional treatments (not included in the present design) may be necessary to remove other impurities from the water stream[146]. A transfer pump is used to send the treated water to Areas 100, 200, and 300. Costs for anaerobic pond, aerobic digester, and pumps were obtained from NREL[146].

7.3 PROCESS ECONOMICS

7.3.1 *Cost-year indices*

The cost-year of 2019 was chosen for this analysis. Equipment and operating costs were obtained in their base year and corrected to 2019$ using the Chemical Engineering Plant cost index (CEI) according to the following equation:

$$Cost(2019\$) = Cost(base\$) \times \left(\frac{CEI_{2019}}{CEI_{base}}\right) \tag{7.2}$$

Where $Cost(2019\$)$ is the equipment or operating cost in 2019$, $Cost(base\$)$ is the cost at a given base year, and CEI_{2019} and CEI_{base} are the cost indexes for 2019, 619.2[153], and the base year, respectively.

7.3.2 *Equipment cost*

Purchased costs were obtained from the literature[145], [146], [149], [151] and used to estimate equipment costs for each area and the total capital investment for the biorefinery described in the present design. The installed equipment cost is based on the factored value of the equipment purchase cost, according to the following equation:

$$Installed\ cost = (purchased\ equipment\ cost) \times (multiplier) \quad (7.3)$$

Installed costs calculated using Equation 7.3 do not take into consideration installation costs associated with foundation, piping, and wiring[146]. These costs are important for a more detailed analysis of the process economics, which goes beyond the scope of the analysis presented in this design.

A power law equation was used to estimate the cost of the scaled equipment relative to its base cost and size:

$$New\ cost = (Base\ cost) \times \left(\frac{New\ size}{Base\ size}\right)^{n} \quad (7.4)$$

In Equation 7.4, *n* is the characteristic scaling exponent, which is a positive fraction (usually below 1.0) and depends on the characteristics of the equipment (capacity, heat duty, or flow rate)[146]. Installed cost multipliers and characteristic scaling exponents were obtained from the literature for the different units used in the present design[145], [146], [149], [151]. These values are shown in Table 7.8.

Table 7.8. Installation factors and exponents used for installation and scaling cost estimations

Equipment	Installation factors	Exponent
Mixer	1.00	0.50
Tank	2.00	0.70
Main fermenter	1.50	1.00
Seed fermenter	1.80-2.00	0.70
Heater	2.20	0.70
Boiler	1.80	0.60
Turbine	1.80	0.60
Molecular sieve package	1.80	0.60
Anaerobic basin	1.00	0.60
Aerobic digester	1.00	0.60
Solid-liquid separator	1.70	0.70
Filter	1.40	0.39
Hydrotreating facility	2.00	0.50
Column		
Beer	2.40	0.80
Hydrocarbon separation column	2.47	0.68
Condenser package	2.47	0.44
Reboiler package	2.47	0.68
Reactor		
Pretreatment	1.50	0.60
Dehydration and oligomerization	2.47	0.65
Pump		
Water	3.10	0.80
Transfer	2.30	0.80
Hydrocarbons	2.47	0.79

The total installed equipment costs for each area is only a portion of the total direct costs (TDC). The TDC also includes site development, warehouse, and additional piping. These costs can be factored in based on the total installed equipment cost. The total indirect costs (TIC) – proratable costs, field expenses, home office and construction, project contingency, and other costs – are based on the TDC. The sum of TDC and TIC gives the fixed capital investment (FCI). The total capital investment (TCI) is the sum of the FCI and the working capital. In the present design, the working capital is 5% of the FCI. The assumptions and costs used to estimate the TDC and TIC were the same reported in a previous NREL report[146].

7.3.3 *Variable and fixed operating costs*

Table 7.9 shows the variable costs associated with raw materials, waste disposal, and by-products. Material balances from Aspen simulations were used to estimate the total variable cost for the biorefinery. The fixed operating costs include direct supervisory labor, operating labor, laboratory charges, operating supplies, property insurance, and maintenance. Table 7.10 lists the assumptions used for the estimation of fixed operating costs.

Table 7.9. Costs for raw materials, waste disposal, and by-products

Item	Cost ($/ton)	Cost ($/kWh)	Base year	Source
Poplar	77[a]		2016	[143]
Sulfuric acid, 93%	88		2007	[146]
Diammonium phosphate	967		2007	[146]
Enzyme production cost	10,140		2011	[147]
Caustic	149		2007	[146]
Lime	199		2007	[146]
Freshwater	0.2		2007	[146]
Electricity		0.06	2016	[143]
HZSM-5 catalyst	25,000		2020	
SIRAL 40 HPV	500,000		2020	
Hydrogen	1,508		2013	[149]
Waste disposal	35		2013	[149]
Steam (280^{o}C and 1310 kPa)	7		2014	[150]

a: $/dry ton

Table 7.10. Fixed operating cost assumptions

Item	Cost assumption	Source
Operating labor	Total of 10 Areas with 2 employees per area working at 3 shifts a day (each shift = 8 hours) at an average hourly rate of $26.7.	U.S. Bureau of labor statistics
Direct supervisory labor	15% of the operating labor	
Laboratory charges	15% of the operating labor	
Maintenance	3% of ISBL	[149]
Operating supplies	1 % of FCI	
Insurance	0.7% of FCI	[149]

7.3.4 *Discounted cash flow analysis and minimum jet fuel selling price*

The approach used in the present design to calculate the minimum jet fuel selling price assumes a project net present value of zero (break-even point), based on a fixed annual discount rate (15% for the Base Case) over the project lifespan (10 years). For the Base Case, the project is assumed to be 40% equity-financed with an annual percentage rate (APR) of 8% for 10 years. Due to the uncertain tax situation in a corporate with low tax rates and favorable depreciation schedules a tax rate of 0% over taxable income is assumed. Complete depreciation of the assets is assumed at the end of the project lifespan (10 years) at a constant annual depreciation rate. During the start-up period – assumed as one year in the present design – the biorefinery operates at 50% reduced capacity.

7.4 RESULTS AND DISCUSSION

Initially, the analysis presents the breakdown of the capital investment and operating expenses, and the minimum selling price of jet fuel for the Base Case scenario – biorefinery operating at a capacity of 2,000 dry metric tons of poplar/day. Then, the effect of scale, raw material cost, and cycloalkane recovery on the minimum jet fuel selling price are discussed.

7.4.1 *Base case: 2,000 dry metric tons of poplar per day*

Table 7.11 shows the project cost, including TDC, TIC, and working capital. The combined installed cost of Areas 100, 500, and 700 correspond to 55% of the total installed cost (30% of the TCI) of the biorefinery, which is mostly due to the high prices of pretreatment and oligomerization reactors, compressors, boiler, and turbogenerator. TIC corresponds to 36% of the TCI.

Table 7.11. Project cost worksheet

Process Area	Description	Installed Cost ($MM)
A100	Pretreatment	74.8
A200	Enzymatic hydrolysis and Overliming	28.3
A300	Fermentation	14.6
A400	Purification and Product Recovery	14.3
A500	Boiler and Power Plant	86.5
A600	Ethanol Dehydration	31.2
A700	Ethylene Oligomerization	50.9
A800	Alkene Hydrogenation	23.5
A900	Wastewater Treatment	63.2
Total		***387.3***
Warehouse	4.0% ISBL	9.5
Site development	9.0% ISBL	21.4
Additional piping	4.5% ISBL	10.7
Total Direct Costs (TDC)		***428.9***
Proratable expenses	10% TDC	42.9
Field expenses	10% TDC	42.9
Home office and construction fees	20% TDC	85.8
Project contingency	10% TDC	42.9
Other costs (start-up, permits, etc.)	10% TDC	42.9
Total Indirect Costs (TIC)		***257.4***
Fixed Capital Investment (FCI)		***686.3***
Working capital	5% FCI	34.3
Total Capital Investment (TCI)		***720.6***

Table 7.12 shows the yields, rates, and conversion costs of the process. The designed biorefinery has an annual capacity of 38.8 MMgal and the break-even minimum jet fuel selling price is $8.51/gal at a discount rate of 15%. The jet fuel yield of 55.4 gal/dry metric ton of poplar corresponds to 70% of the theoretical yield based on the carbohydrates in the poplar feedstock.

Table 7.12. Summary of yields, rates, and conversion costs

Feedstock rate	2,000 dry metric tons/day
On-line time	350 days/year
Jet fuel yield	55.4 gal/dry metric ton of poplar
Annual jet fuel production	38.8 MMgal
Total equipment cost	$387MM
TCI	$721MM
TCI per annual gallon	$18.58/gal
Minimum jet fuel selling price (15% discount rate)	$8.51/gal

Figure 7.2 shows the variable operating cost breakdown per gallon of jet fuel. The total operating cost is estimated at $4.41/gal of jet fuel, with the fixed cost accounting for 12.5% of the total operating cost. The poplar feedstock, enzyme, and steam are the most contributors to the total variable operating cost of the biorefinery. The poplar cost of $77/dry metric ton assumed in the present design is optimistic since feedstock handling and transport are not included in the design, which can contribute to an even higher operating cost. However, lower feedstock costs may be possible if poplar is harvested close to the biorefinery. Also, lower enzyme production costs may be possible if the enzymes are formulated with stability for a lower lifespan and are not stored for prolonged periods of time[146]. Later, the effects of lower feedstock and enzyme costs are discussed.

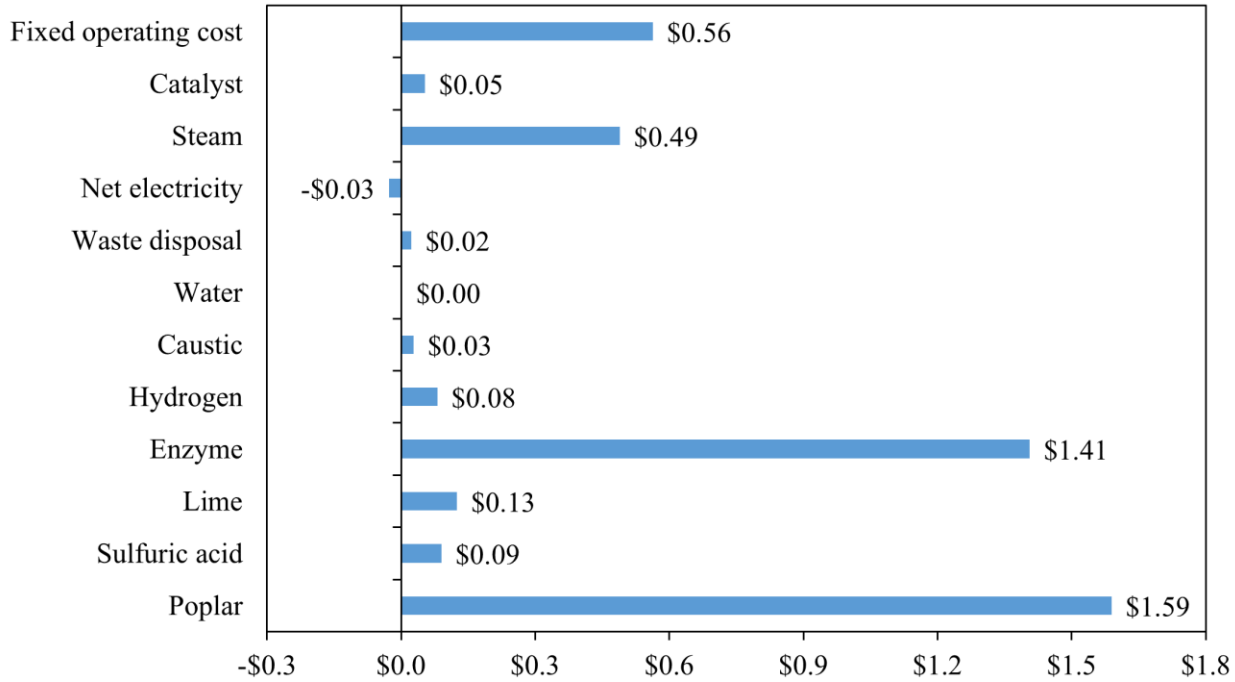

Figure 7.2. Variable operating cost breakdown per gallon of jet fuel.

7.4.2 *Economy of scale*

It has been reported that the increase in biorefinery scale has the potential to reduce the minimum selling price of biofuel[143]. In this work, two additional scales – 4,000 and 8,000 dry metric tons of poplar/day – are investigated. Figure 7.3 shows the minimum jet fuel selling price as a function of biorefinery capacity and discount rate. Scale-up of the biorefinery capacity leads to a reduction in minimum jet fuel selling price as expected. The cash cost selling price shown in Figure 7.3 is the sum of the variable and fixed operating costs to produce the jet fuel, not including discount, interest, and depreciation. The minimum selling price at a lower discount rate of 10% is also shown. Although scales larger than 2,000 dry metric tons of biomass/day are currently not feasible in the U.S., future development of bioresource technologies may pose a feasible scenario for the large-scale production of bio-jet fuel at low selling prices. Even so, the lowest minimum price obtained in the present design is $5.91/gal (8,000 dry metric tons of poplar/day), 2.1 times

higher than the minimum selling price target of $3.00/gal set by the U.S. Department of Energy[154].

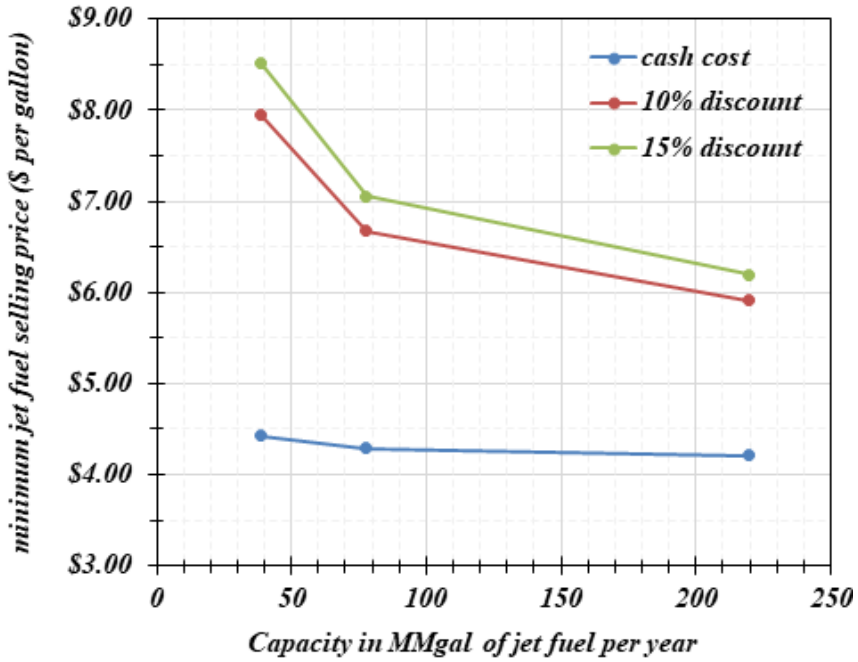

Figure 7.3. Minimum jet fuel selling price as a function of biorefinery capacity and discount rate.

7.4.3 *Sensitivity analysis*

An alternative scenario is discussed in this section, where the cycloalkanes are produced separately. Cycloalkanes have a high value and could be potentially sold at $7,091/ton. In this scenario, the remaining alkane mixture containing the linear alkanes is sold as a jet-fuel blend. In this analysis, the price of cycloalkanes is fixed at $7,091/ton (the same price of JP-10) and the minimum selling price of the linear alkane mixture is calculated. Also, the effect of biomass cost, enzyme cost, and discount rate on the minimum jet fuel price is discussed. The discussion is focused on the Base Case scenario for a daily biomass feed rate of 2,000 dry metric tons of poplar.

Based on the work presented in Chapter 6, the cycloalkane content in the liquid product from the oligomerization reactor is 8.5 wt. %. The separation is performed according to the description in Section 7.2.7 of the present Chapter. The additional separation adds $2.4MM to the

installed capital cost of the ethylene oligomerization area (Area 700) and $3.4MM to the TCI of the biorefinery (Table 7.13). The minimum selling price of the jet fuel blend for the scenario where the cycloalkanes are sold separately is $8.01/gal (Table 7.14). Even though this price is lower than that of the Base Case scenario, the difference is below 10%.

Table 7.13. Comparison of capital investment between the Base Case scenario and the scenario where the cycloalkanes are recovered and sold separately

Area	Description	Base Case (B.C.) $MM	Δ (Selling cycloalkanes – B.C.) $MM
A100	Pretreatment	74.8	0.0
A200	Hydrolysis and Overliming	28.3	0.0
A300	Fermentation	14.6	0.0
A400	Purification Recovery	14.3	0.0
A500	Boiler and Power Plant	86.5	0.0
A600	Ethanol Dehydration	31.2	0.0
A700	Ethylene Oligomerization	50.9	+2.4
A800	Alkene Hydrogenation	23.5	-0.7
A900	Wastewater Treatment	63.2	0.0
Total		***387.3***	***+1.7***
TCI		***720.6***	***+3.4***

Table 7.14. Summary of yields, rates, and conversion costs for the scenario where the cycloalkanes are recovered and sold separately

Feedstock rate	2,000 dry metric tons/day
On-line time	350 days/year
Jet fuel blend yield (linear alkanes)	52.3 gal/dry metric ton of poplar
Annual jet fuel production	36.6 MMgal
Total equipment cost	$389MM
TCI	$724MM
TCI per annual gallon	$19.78/gal
Minimum jet fuel selling price (15% discount rate)	$8.01/gal

Figure 7.4 shows the change in minimum jet fuel selling price with biomass, process configuration (a scenario where cycloalkanes are selling separately), discount rate, and enzyme relative to the Base Case scenario. According to the sensitivity analysis, a lower enzyme cost of $4.24/kg has the highest impact on the minimum jet fuel price, followed by the discount rate, process configuration, and biomass cost. Even at the most optimistic scenario, where biomass cost, discount rate, and

enzyme cost, are the lowest, and cycloalkanes are recycled and sold separately, the variation in minimum selling price is -$2.23/gal, leading to a final value of $6.28/gal relative to the Base Case. This analysis shows the challenge of achieving a competitive jet fuel selling price from woody biomass, in which investors can obtain a reasonable rate of return. Even at the most optimistic conditions, further optimization is necessary for the production of jet fuel at a scale that is feasible.

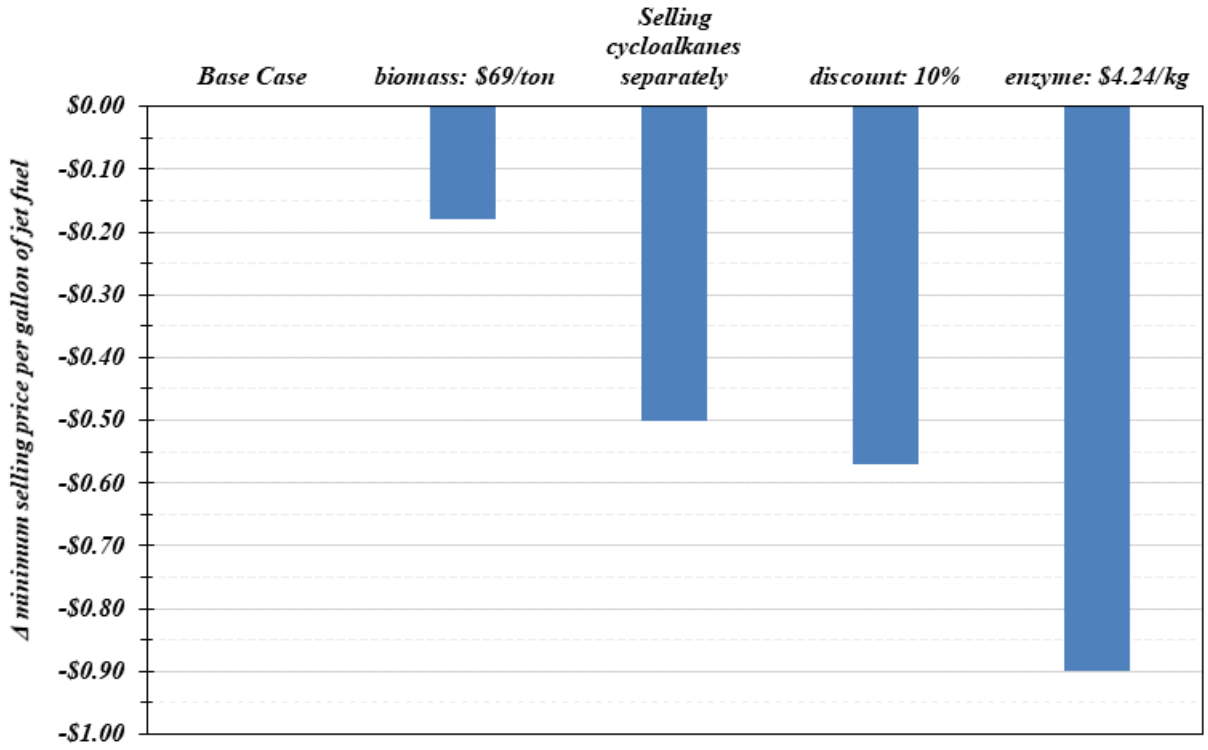

Figure 7.4. Change in minimum jet fuel selling price for biomass, process configuration, discount rate, and enzyme variation relative to the Base Case scenario.

7.4.4 *Comparison with previous techno-economic studies*

Table 7.15 shows the minimum fuel selling price (MFSP) for some of the technologies considered for the conversion of woody biomass into liquid hydrocarbons. The MFSP obtained in the present design for the Base Case at a discount rate of 10% ($7.94/gal) is lower than the value reported in [155] for the conversion of forest residue into liquid hydrocarbons via alcohol-to-jet technology. However, these values are still higher than the ones reported for other technologies,

such as hydrothermal liquefaction and pyrolysis. The main challenge in the conversion of biomass using alcohol-to-jet processing lies in the poor biomass usage. The lignin fraction is not converted into useful hydrocarbon products. Instead, it is used for energy generation. Also, 39% of the ethanol mass is lost as water during the dehydration step, leading to a major decrease in the overall process yields. Another pathway for alcohol-to-jet uses acetogenic microorganisms during the fermentation of sugars, converting 100% of the sugars from biomass into useful carbon. The acetic acid can be converted into ethanol via ethyl acetate intermediate[143]. Crawford et al.[143] reported an MFSP of $6.80/gal of jet fuel using the acetogenic pathway, leading to a jet fuel yield of 87.3 gal/dry metric ton of poplar; much higher than the yield reported in the present design, 55.4 gal/dry metric ton of poplar. Nevertheless, note that when assuming a scenario where cycloalkanes are sold as a high-value product, and biomass, enzyme, and discount are the lowest, the jet fuel price ($6.28/gal) is lower than the value reported in [143].

Table 7.15. Overview of techno-economic studies on biomass conversion into hydrocarbon fuel

Feedstock	MFSP[a] ($/gal)	Scale (MMgal /year)	Feed price ($/dry ton)	Jet fuel yield (gal/dry ton)	Process pathway	Source
Poplar	8.01	36.6	77	52.3	Sugar fermentation to ethylene followed by Alcohol-to-jet	This work[b]
Poplar	6.80[c]	20.1	77	87.3	Acetogenic fermentation followed acetone to ethanol and ethanol-to-jet fuel	[143]
Forest residue	4.84[d]	39.7	108.3	119.0	Hydrothermal liquefaction	[143], [155]
Forest residue	5.52[d]	39.7	108.3	89.3	Pyrolysis	[143], [155]
Forest residue	8.62[d]	39.7	108.3	44.4	Alcohol-to-jet	[143], [155]

Wood chips	5.52[d]	18.5	69	56.9	Alcohol-to-jet	[143], [156]

[a] Minimum fuel selling price.
[b] results obtained in the present work with a discount rate of 15%.
[c] calculated at a discount rate of 15%.
[d] calculated at a discount rate of 10%.

7.5 CONCLUSION

The techno-economic assessment of jet fuel production from poplar is discussed. The designed process involves biomass fractionation into sugars, sugar fermentation into ethanol, ethanol dehydration into ethylene, ethylene oligomerization into alkenes, and alkene hydrogenation into alkanes. For the Base Case scenario, a minimum jet fuel selling price of $8.51/gal was calculated. If cycloalkanes are sold separately at $7,091/ton, the jet fuel blend (linear alkanes) can be sold at a minimum selling price of $8.01/ton. The sensitivity analysis shows that the minimum fuel selling price is highly sensitive to biomass cost, discount rate, and enzyme production cost. A scenario where cycloalkanes are sold separately as a high-value product, and biomass, enzyme, and discount rate are the lowest, can substantially reduce the minimum fuel selling price to $6.28/gal.

Chapter 8. CONCLUSION AND FUTURE WORK

8.1 CONCLUSION

The present research describes the fundamental aspects of the ethylene oligomerization over nickel-based solid catalysts under subcritical and supercritical conditions. First, the mechanism and kinetics of the oligomerization of subcritical ethylene are described. The results indicate that the oligomerization takes place over two active sites that we hypothesize as a combination of a Ni^{2+} cation and a Brønsted site. The concentrations of both sites on the catalyst have great implications on the extent of ethylene oligomerization. Equal amounts of nickel and Brønsted sites are required to promote ethylene oligomerization reactions. Low concentrations of Ni^{2+} and high concentrations of Brønsted sites decrease the probability of forming the active center involved in the initial step of the ethylene oligomerization process over nickel-based solid catalysts. Also, the excess of nickel relative to Brønsted sites can also decrease the probability for the formation of $[Ni\text{-}H]^{+}$ sites.

Then, the kinetics of the ethylene oligomerization over the Ni-H-Beta are investigated. It is shown that the formation of butene and hexene proceeds via a series of ethylene coordination insertion steps, and the formation of octene proceeds via co-oligomerization of ethylene and desorbed butene. In the present research, the co-oligomerization route is denoted *"cascade co-oligomerization"*.

After the investigation of the mechanisms and kinetics of the ethylene oligomerization over the Ni-H-Beta, the kinetics of the oligomerization of supercritical ethylene are presented. A thermodynamic model for the solubility of *n*-decane – a model compound for coke used in the present research – in subcritical and supercritical ethylene is developed. As described in Chapter

1, supercritical ethylene promotes the removal of coke molecules from heterogeneous catalysts. Comparison of the solubility and the kinetic data under supercritical conditions indicate that at low temperatures, the rates of coke dissolution by the supercritical ethylene higher than the apparent rates of coke production on the catalyst. However, at higher temperatures, the rates of coke dissolution are not sufficient to offset the high rates of coke production on the catalyst. Therefore, the transport of products from the catalyst surface to the bulk of the supercritical fluid is slow, causing a build-up of products on the catalyst. This process can lead to catalyst deactivation by tying up active sites or by pore plugging. The kinetics of the ethylene oligomerization under supercritical conditions agree with the analysis presented in the solubility study. According to the results, desorption of products controls the catalytic process, causing accumulation of products on the catalyst and consequent catalyst deactivation.

Based on the results presented in Chapters 2, 3, 4, and 5, a novel catalyst was developed for the oligomerization of supercritical ethylene. The catalyst has a high nickel-exchanging capability and a high pore volume. These features are important to increase the probability for the formation of the active sites in the initial step of the oligomerization and avoid accumulation of products on the catalyst in the case of a reaction controlled by the desorption of products from the catalyst.

The novel catalyst is able to convert virtually all the ethylene without exhibiting deactivation under supercritical conditions, with high yields for liquid products. A dual reactor configuration was used to promote oligomerization of butene to increase the formation of liquid products. The novel catalyst shows outstanding characteristics for ethylene oligomerization and can pave a solid path for the commercialization of this technology in the near future.

A complementary techno-economic study for the conversion of poplar into jet fuel is also presented, where the data obtained in the present research for the ethylene oligomerization over the novel Ni-SIRAL 40 catalyst was used to model the ethylene oligomerization. The results show that even the high liquid yields obtained with this catalyst lead to a minimum selling price much higher ($9.41/gal of jet fuel) than the goal of $3.00/gal of jet fuel.

8.1 FUTURE WORK

Future research on the ethylene oligomerization over heterogeneous catalysts may involve the investigation of new active metals and novel mesoporous supports for this reaction. Mechanistic and kinetic approaches similar to the ones presented in this research may help identify opportunities to control the product selectivity and increase yields for liquid products. Future steps are necessary to optimize conditions, especially focusing on cycloalkane production during the oligomerization of supercritical ethylene over the novel Ni-SIRAL 40 catalyst.

REFERENCE

[1] E. G. Derouane, *Catalysts for Fine Chemical Synthesis*, 4th ed. John Wiley & Sons, Ltd, 2006.

[2] A. Finiels, F. Fajula, and V. Hulea, "Nickel-based solid catalysts for ethylene oligomerization - a review," *Catal. Sci. Technol.*, vol. 4, no. 8, pp. 2412–2426, 2014, doi: 10.1039/C4CY00305E.

[3] A. Forestière, H. Olivier-Bourbigou, and L. Saussine, "Oligomerization of Monoolefins by Homogeneous Catalysts," *Oil Gas Sci. Technol. - Rev. l'IFP*, vol. 64, no. 6, pp. 649–667, 2009, doi: 10.2516/ogst/2009027.

[4] John Wiley & Sons, *Industrial Organic Chemistry*, 4th ed., vol. 4. 2008.

[5] W. Wang *et al.*, "Review of Biojet Fuel Conversion Technologies," no. July, p. 98, 2016, doi: 10.1016/j.rser.2015.09.016.

[6] F. T. T. Ng and D. C. Creaser, "Ethylene dimerization over modified nickel exchanged Y-zeolite," *Appl. Catal. A, Gen.*, vol. 119, no. 2, pp. 327–339, 1994, doi: 10.1016/0926-860X(94)85200-6.

[7] A. Martínez, M. A. Arribas, P. Concepción, and S. Moussa, "New bifunctional Ni-H-Beta catalysts for the heterogeneous oligomerization of ethylene," *Appl. Catal. A Gen.*, vol. 467, pp. 509–518, 2013, doi: 10.1016/j.apcata.2013.08.021.

[8] M. Lallemand, A. Finiels, F. Fajula, and V. Hulea, "Continuous stirred tank reactor for ethylene oligomerization catalyzed by NiMCM-41," *Chem. Eng. J.*, vol. 172, no. 2–3, pp. 1078–1082, 2011, doi: 10.1016/j.cej.2011.06.064.

[9] V. Hulea and F. Fajula, "Ni-exchanged AlMCM-41 - An efficient bifunctional catalyst for ethylene oligomerization," *J. Catal.*, vol. 225, no. 1, pp. 213–222, 2004, doi: 10.1016/j.jcat.2004.04.018.

[10] R. Henry *et al.*, "Ethene oligomerization on nickel microporous and mesoporous-supported catalysts: Investigation of the active sites," *Catal. Today*, vol. 299, no. February 2017, pp. 154–163, 2018, doi: 10.1016/j.cattod.2017.04.029.

[11] S. Moussa, M. A. Arribas, P. Concepción, and A. Martínez, "Heterogeneous oligomerization of ethylene to liquids on bifunctional Ni-based catalysts: The influence of support properties on nickel speciation and catalytic performance," *Catal. Today*, vol. 277, pp. 78–88, 2016, doi: 10.1016/j.cattod.2015.11.032.

[12] D. S. McGuinness, "Olefin oligomerization via metallacycles: Dimerization, trimerization, tetramerization, and beyond," *Chem. Rev.*, vol. 111, no. 3, pp. 2321–2341, 2011, doi: 10.1021/cr100217q.

[13] G. V. S. Seufitelli and F. L. P. Resende, "Study of the catalytic reactions of ethylene oligomerization in subcritical and supercritical media over a NiBEA catalyst," *Appl. Catal. A Gen.*, vol. 576, pp. 96–107, Apr. 2019, doi: 10.1016/j.apcata.2019.01.015.

[14] R. Y. Brogaard *et al.*, "Ethene Dimerization on Zeolite-Hosted Ni Ions: Reversible Mobilization of the Active Site," *ACS Catal.*, vol. 9, no. 6, pp. 5645–5650, 2019, doi: 10.1021/acscatal.9b00721.

[15] R. Y. Brogaard and U. Olsbye, "Ethene Oligomerization in Ni-Containing Zeolites: Theoretical Discrimination of Reaction Mechanisms," *ACS Catal.*, vol. 6, no. 2, pp. 1205–1214, 2016, doi: 10.1021/acscatal.5b01957.

[16] S. Moussa, P. Concepción, M. A. Arribas, and A. Martinez, "Nature of active nickel sites and initiation mechanism for ethylene oligomerization on heterogeneous Ni-beta

catalysts," *ACS Catal.*, p. acscatal.7b03970, 2018, doi: 10.1021/acscatal.7b03970.
[17] A. Brückner, U. Bentrup, H. Zanthoff, and D. Maschmeyer, "The role of different Ni sites in supported nickel catalysts for butene dimerization under industry-like conditions," *J. Catal.*, vol. 266, no. 1, pp. 120–128, 2009, doi: 10.1016/j.jcat.2009.05.021.
[18] R. D. Andrei, M. I. Popa, F. Fajula, and V. Hulea, "Heterogeneous oligomerization of ethylene over highly active and stable Ni-AlSBA-15 mesoporous catalysts," *J. Catal.*, vol. 323, pp. 76–84, 2015, doi: 10.1016/j.jcat.2014.12.027.
[19] F. T. T. Ng and D. C. Creaser, "Ethylene Dimerization: Kinetics and Selectivity for 1-Butene," *Stud. Surf. Sci. Catal.*, vol. 73, pp. 123–131, 1992.
[20] L. Riekert, "The kinetics of ethylene polymerization in nickel-Y zeolite," *J. Catal.*, vol. 19, no. 1, pp. 8–14, 1970, doi: 10.1016/0021-9517(70)90291-5.
[21] R. A. Alberty, "Kinetics of the polymerization of alkenes on zeolites," *J. Chem. Phys.*, vol. 87, no. 6, pp. 3660–3667, 1987, doi: 10.1063/1.452963.
[22] R. L. Espinoza, C. P. Nicolaides, C. J. Korf, and R. Snel, "Catalytic oligomerization of ethene over nickel-exchanged amorphous silica-alumina; Effect of the nickel concentration," *Appl. Catal.*, vol. 31, no. 2, pp. 259–266, 1987, doi: 10.1016/S0166-9834(00)80695-8.
[23] K. Toch, J. W. Thybaut, M. A. Arribas, A. Martínez, and G. B. Marin, "Steering linear 1-alkene, propene or gasoline yields in ethene oligomerization via the interplay between nickel and acid sites," *Chem. Eng. Sci.*, vol. 173, pp. 49–59, 2017, doi: 10.1016/j.ces.2017.07.025.
[24] O. Jan and F. L. P. Resende, "Liquid hydrocarbon production via ethylene oligomerization over Ni-HB," *Fuel Process. Technol.*, vol. 179, no. May, pp. 269–276, 2018, doi: 10.1016/j.fuproc.2018.07.004.
[25] O. Jan, K. Song, A. Dichiara, and F. L. P. Resende, "Oligomerization of supercritical ethylene over nickel-based silica-alumina catalysts," *Chem. Eng. Sci.*, vol. 197, pp. 212–222, Apr. 2019, doi: 10.1016/j.ces.2018.12.018.
[26] O. Jan, K. Song, A. B. Dichiara, and F. L. P. Resende, "Ethylene Oligomerization over Ni-Hβ Heterogeneous Catalysts," *Ind. Eng. Chem. Res.*, vol. 57, pp. 10241–10250, 2018, doi: 10.1021/acs.iecr.8b01902.
[27] G. A. M. Diepen and F. E. C. Scheffer, "The Solubility of Naphthalene in Supercritical Ethylene," *J. Am. Chem. Soc.*, vol. 70, no. 12, pp. 4085–4089, 1948, doi: 10.1021/ja01192a035.
[28] J. M. Prausnitz, R. N. Lichtenthaler, and E. G. de Azevedo, *Molecular Thermodynamics of Fluid-Phase Equilibria*, 3rd ed. 1998.
[29] S. G. D. Avila, B. K. Kaul, and J. M. Prausnitz, "Solubilities of Heavy Hydrocarbons in Compressed Methane and Nitrogen," vol. 21, no. 4, pp. 488–491, 1976, doi: 10.1021/je60071a017.
[30] J. M. Prausnitz and P. R. Benson, "Solubility of liquids in compressed hydrogen, nitrogen, and carbon dioxide," *AIChE J.*, vol. 5, no. 2, 1959, doi: https://doi.org/10.1002/aic.690050208.
[31] P. C. A. Bruijnincx and B. M. Weckhuysen, "Shale gas revolution: An opportunity for the production of biobased chemicals?," *Angew. Chemie - Int. Ed.*, vol. 52, no. 46, pp. 11980–11987, 2013, doi: 10.1002/anie.201305058.
[32] C. O'connor and M. Kojima, "Alkene oligomerization," *Catal. today*, vol. 6, pp. 329–349, 1990.

[33] J. Skupińska, “Oligomerization of α-Olefins to Higher Oligomers,” *Chem. Rev.*, vol. 91, no. 4, pp. 613–648, 1991, doi: 10.1021/cr00004a007.
[34] K. Toch, J. W. Thybaut, and G. B. Marin, “Ethene oligomerization on Ni-SiO2-Al2O3: Experimental investigation and Single-Event MicroKinetic modeling,” *Appl. Catal. A Gen.*, vol. 489, pp. 292–304, 2015, doi: 10.1016/j.apcata.2014.10.036.
[35] A. Lacarriere *et al.*, “Distillate-range products from non-oil-based sources by catalytic cascade reactions,” *ChemSusChem*, vol. 5, no. 9, pp. 1787–1792, 2012, doi: 10.1002/cssc.201200092.
[36] M. Lallemand, A. Finiels, F. Fajula, and V. Hulea, “Nature of the active sites in ethylene oligomerization catalyzed by ni-containing molecular sieves: Chemical and IR spectral investigation,” *J. Phys. Chem. C*, vol. 113, no. 47, pp. 20360–20364, 2009, doi: 10.1021/jp9082932.
[37] M. Lallemand, A. Finiels, F. Fajula, and V. Hulea, “Continuous stirred tank reactor for ethylene oligomerization catalyzed by NiMCM-41,” *Chem. Eng. J.*, vol. 172, no. 2–3, pp. 1078–1082, 2011, doi: 10.1016/j.cej.2011.06.064.
[38] M. Lallemand, A. Finiels, F. Fajula, and V. Hulea, “Catalytic oligomerization of ethylene over Ni-containing dealuminated Y zeolites,” *Appl. Catal. A Gen.*, vol. 301, no. 2, pp. 196–201, 2006, doi: 10.1016/j.apcata.2005.12.019.
[39] M. Lallemand, O. A. Rusu, E. Dumitriu, A. Finiels, F. Fajula, and V. Hulea, “NiMCM-36 and NiMCM-22 catalysts for the ethylene oligomerization: Effect of zeolite texture and nickel cations/acid sites ratio,” *Appl. Catal. A Gen.*, vol. 338, no. 1–2, pp. 37–43, 2008, doi: 10.1016/j.apcata.2007.12.024.
[40] Y. Wang *et al.*, “Synthesis and properties of MFI zeolites with microporous, mesoporous and macroporous hierarchical structures by a gel-casting technique,” *New J. Chem.*, vol. 40, no. 5, pp. 4398–4405, 2016, doi: 10.1039/C5NJ03387J.
[41] J. Heveling, C. P. Nicolaides, and M. S. Scurrell, “Identification of novel catalysts and conditions for the highly efficient and stable heterogeneous oligomerization of ethylene,” *J. Chem. Soc. Chem. Commun.*, no. 2, pp. 126–127, 1991, doi: 10.1039/C39910000126.
[42] J. Heveling, C. P. Nicolaides, and M. S. Scurrell, “Catalysts and conditions for the highly efficient and stable heterogeneous oligomerization of ethylene,” *Am. Chem. Soc. Div. Pet. Chem. Prepr.*, vol. 36, no. 4, pp. 578–584, 1991, doi: 10.1039/c39910000126.
[43] M. D. Heydenrych, C. P. Nicolaides, and M. S. Scurrell, “Oligomerization of ethene in a slurry reactor using a nickel(II)-exchanged silica-alumina catalyst,” *J. Catal.*, vol. 197, no. 1, pp. 49–57, 2001, doi: 10.1006/jcat.2000.3035.
[44] M. Hartmann, A. Pöppl, and L. Kevan, “Ethylene dimerization and butene isomerization in nickel-containing MCM-41 and AlMCM-41 mesoporous molecular sieves: An electron spin resonance and gas chromatography study,” *J. Phys. Chem.*, vol. 100, no. 23, pp. 9906–9910, 1996, doi: 10.1021/jp9602181.
[45] S. Forget, H. Olivier-Bourbigou, and D. Delcroix, “Homogeneous and Heterogeneous Nickel-Catalyzed Olefin Oligomerization: Experimental Investigation for a Common Mechanistic Proposition and Catalyst Optimization,” *ChemCatChem*, vol. 9, no. 12, pp. 2408–2417, 2017, doi: 10.1002/cctc.201700348.
[46] E. D. Metzger, R. J. Comito, C. H. Hendon, and M. Dincă, “Mechanism of single-site molecule-like catalytic ethylene dimerization in Ni-MFU-4l,” *J. Am. Chem. Soc.*, vol. 139, no. 2, pp. 757–762, 2017, doi: 10.1021/jacs.6b10300.
[47] R. Joshi, G. Zhang, J. T. Miller, and R. Gounder, “Evidence for the Coordination-Insertion

Mechanism of Ethene Dimerization at Nickel Cations Exchanged onto Beta Molecular Sieves," *ACS Catal.*, vol. 8, no. 12, pp. 11407–11422, 2018, doi: 10.1021/acscatal.8b03202.

[48] P. Cossee, "Ziegler-Natta catalysis I. Mechanism of polymerization of α-olefins with Ziegler-Natta catalysts," *J. Catal.*, vol. 3, no. 1, pp. 80–88, 1964, doi: 10.1016/0021-9517(64)90095-8.

[49] E. J. Arlman and P. Cossee, "Ziegler-Natta catalysis III. Stereospecific polymerization of propene with the catalyst system TiCl3AlEt3," *J. Catal.*, vol. 3, no. 1, pp. 99–104, 1964, doi: 10.1016/0021-9517(64)90097-1.

[50] I. V. Elev, B. N. Shelimov, and V. B. Kazansky, "The Role of Ni+ Ions in the activity of NiCaY Zeolite catalysts for Ethylene Dimerization," *J. Catal.*, vol. 89, no. 2, pp. 470–477, 1984, doi: 10.1016/0021-9517(84)90323-3.

[51] A. A. Davydov, M. Kantcheva, and M. L. Chepotko, "FTIR spectroscopic study on nickel(II)-exchanged sulfated alumina: Nature of the active sites in the catalytic oligomerization of ethene," *Catal. Letters*, vol. 83, no. 1–2, pp. 97–108, 2002, doi: 10.1023/A:1020669818242.

[52] T. Cai, "Studies of a new alkene oligomerization catalyst derived from nickel sulfate," *Catal. Today*, vol. 51, no. 1, pp. 153–160, 1999, doi: 10.1016/S0920-5861(99)00018-8.

[53] C. A. Emeis, "Determination of Integrated Molar Extinction Coefficients for Infrared Absorption Bands of Pyridine Adsorbed on Solid Acid Catalysts," *J. Catal.*, vol. 141, no. 2, pp. 347–354, Jun. 1993, doi: 10.1006/jcat.1993.1145.

[54] K. Y. Foo and B. H. Hameed, "Insights into the modeling of adsorption isotherm systems," *Chem. Eng. J. J.*, no. 156, pp. 2–10, 2010, doi: 10.1016/j.cej.2009.09.013.

[55] V. R. Choudhary and S. Mayadevi, "Sorption Isotherms of Methane, Ethane, Ethylene, and Carbon Dioxide on ALPO-5 and SAPO-5," *Langmuir*, vol. 12, no. 17, pp. 980–986, 1996, doi: 10.1039/ft9959102935.

[56] I. Langmuir, "The adsorption of gases on plane surfaces of glass, mica and platinum," *J. Am. Chem. Soc.*, vol. 40, no. 9, pp. 1361–1403, 1918, doi: 10.1021/ja02242a004.

[57] K. P. Burnham and D. R. Anderson, *Model Selection and Inference: A Practical Information-Theoretic Approach*, 2nd ed. New York: Springer, 2002.

[58] M. Lee *et al.*, "Ni/SIRAL-30 as a heterogeneous catalyst for ethylene oligomerization," *Appl. Catal. A Gen.*, vol. 562, no. June, pp. 87–93, 2018, doi: 10.1016/j.apcata.2018.06.004.

[59] M. I. Vázquez, A. Corma, and V. Fornés, "Characterization of NiO supported on zeolite Y, by pyridine adsorption," *Zeolites*, vol. 6, no. 4, pp. 271–274, Jul. 1986, doi: 10.1016/0144-2449(86)90080-1.

[60] R. Baran, I. I. Kamińska, A. Śrębowata, and S. Dzwigaj, "Selective hydrodechlorination of 1,2-dichloroethane on NiSiBEA zeolite catalyst: Influence of the preparation procedure on a high dispersion of Ni centers," *Microporous Mesoporous Mater.*, vol. 169, pp. 120–127, 2013, doi: 10.1016/j.micromeso.2012.11.005.

[61] R. Domnick, G. Held, P. Witte, and H. P. Steinrück, "The transition from oxygen chemisorption to oxidation of ultra-thin Ni layers on Cu(111)," *J. Chem. Phys.*, vol. 115, no. 4, pp. 1902–1908, 2001, doi: 10.1063/1.1379534.

[62] H. Vidas and B. Hugman, "Availability, Economics, and Production Potential North American Unconventional Natural Gas Supplies," Fairfax, 2008.

[63] G. R. Lappin, L. H. Nemec, J. D. Sauer, and J. D. Wagner, "Olefins, Higher," in *Kirk-*

Othmer Encyclopedia of Chemical Technology, Hoboken, NJ, USA: John Wiley & Sons, Inc., 2010, pp. 1–20.

[64] A. M. Al-Jarallah, J. A. Anabtawi, M. A. B. Siddiqui, and A. M. Aitani, "Part 1 Dimebization Ofethylene To Butene-1," *Catal. TodayToday*, vol. 14, no. 1992, pp. 1–124, 1992, doi: 10.1186/1472-6823-13-53.

[65] A. Finiels, F. Fajula, and V. Hulea, "Nickel-based solid catalysts for ethylene oligomerization – a review," *Catal. Sci. Technol.*, vol. 4, no. 8, pp. 2412–2426, 2014, doi: 10.1039/C4CY00305E.

[66] M. A. Lilga, R. T. Hallen, K. O. Albrecht, A. R. Cooper, J. G. Frye, and K. Ramasamy, "System and Processes for Conversion of Ethylene Feedstocks to Hydrocarbon Fuels," US 2016/01942.57 A1, 2016.

[67] R. L. Espinoza, C. J. Korf, C. P. Nicolaides, and R. Snel, "Catalytic oligomerization of ethene over nickel-exchanged amorphous silica-alumina; effect of the reaction conditions and modelling of the reaction.," *Appl. Catal.*, vol. 29, no. 1, pp. 175–184, 1987, doi: 10.1016/S0166-9834(00)82615-9.

[68] I. Chorkendorff and J. W. Niemantsverdriet, *Concepts of Modern Catalysis and Kinetics*. Weinheim: WILEY-VCH Verlag GmbH & Co. KGaA, 2003.

[69] W. Hu, J. Xie, H. W. Chau, and B. C. Si, "Evaluation of parameter uncertainties in nonlinear regression using Microsoft Excel Spreadsheet," *Environ. Syst. Res.*, vol. 4, no. 1, 2015, doi: 10.1186/s40068-015-0031-4.

[70] H. S. Fogler, *Elements of Chemical Reaction Engineering*, 4th ed. Prentice Hall, 2006.

[71] R. B. Bird, W. E. Stewart, and E. N. Lightfoot, *Transport Phenomena Wiley*. John Wiley & Sons, 2007.

[72] A. Ehrmaier *et al.*, "Dimerization of Linear Butenes on Zeolite-Supported Ni 2+," *ACS Catal.*, vol. 9, no. 1, pp. 315–324, 2019, doi: 10.1021/acscatal.8b03095.

[73] M. Bjørgen, K. P. Lillerud, U. Olsbye, S. Bordiga, and A. Zecchina, "1-Butene Oligomerization in Bro1nsted Acidic Zeolites: Mechanistic Insights from Low-Temperature in Situ FTIR Spectroscopy," *J. Phys. Chem. B*, vol. 108, no. 23, pp. 7862–7870, 2004, doi: 10.1021/jp0377836.

[74] J. F. Denayer, W. Souverijns, P. A. Jacobs, J. A. Martens, and G. V. Baron, "High-temperature low-pressure adsorption of branched C5-C8 alkanes on zeolite beta, ZSM-5, ZSM-22, zeolite Y, and mordenite," *J. Phys. Chem. B*, vol. 102, no. 23, pp. 4588–4597, 1998, doi: 10.1021/jp980674k.

[75] J. F. M. Denayer and G. V. Baron, "Adsorption of normal and branched paraffins in faujasite zeolites NaY, HY, Pt/NaY and USY," *Adsorption*, vol. 3, no. 4, pp. 251–265, 1997, doi: 10.1007/BF01653628.

[76] V. Hulea, "Toward Platform Chemicals from Bio-Based Ethylene: Heterogeneous Catalysts and Processes," *ACS Catal.*, vol. 8, no. 4, pp. 3263–3279, Apr. 2018, doi: 10.1021/acscatal.7b04294.

[77] R. D. Andrei *et al.*, "Ethylene to Propylene by One-Pot Catalytic Cascade Reactions," *ACS Catal.*, vol. 5, no. 5, pp. 2774–2777, May 2015, doi: 10.1021/acscatal.5b00383.

[78] R. D. Andrei, M. I. Popa, C. Cammarano, and V. Hulea, "Nickel and molybdenum containing mesoporous catalysts for ethylene oligomerization and metathesis," *New J. Chem.*, vol. 40, no. 5, pp. 4146–4152, 2016, doi: 10.1039/c5nj02586a.

[79] C. H. Bartholomew, "Mechanisms of catalyst deactivation," *Appl. Catal. A Gen.*, vol. 212, no. 1–2, pp. 17–60, 2001, doi: 10.1016/S0926-860X(00)00843-7.

[80] D. L. Trimm, “Catalyst design for reduced coking (review),” *Appl. Catal.*, vol. 5, no. 3, pp. 263–290, 1983, doi: 10.1016/0166-9834(83)80156-0.
[81] C. V. Satyanarayana, D. Srikant, and H. R. Gurav, *Catalyst Deactivation and Regeneration*. 2016.
[82] M. D. Argyle and C. H. Bartholomew, “Heterogeneous catalyst deactivation and regeneration: A review,” *Catalysts*, vol. 5, no. 1, pp. 145–269, 2015, doi: 10.3390/catal5010145.
[83] L. Fan, I. Nakamura, S. Ishida, and K. Fujimoto, “Ethylene oligomerization on H-ZSM-5 zeolite catalysts in supercritical phase n-pentane mixtures.” pp. 585–588, 1998, doi: https://doi.org/10.1252/jcej.31.585.
[84] J. Wang, F. Hassan, P. I. Chigada, S. P. Rigby, B. Al-Duri, and J. Wood, “Coke Formation and characterization during 1-hexene isomerization and oligomerization over H-ZSM-5 catalyst under supercritical conditions,” *Ind. Eng. Chem. Res.*, vol. 48, no. 17, pp. 7899–7909, 2009, doi: 10.1021/ie801466d.
[85] K. Chylinski and J. Gregorowicz, “Solubilities of 1-propanol and 1 , 2-propanediol in supercritical carbon dioxide . New analytical procedure and measurements,” pp. 163–172, 1998.
[86] J. Gregorowicz, “Solubility of tetracosane in supercritical ethane and ethylene,” vol. 27, pp. 13–23, 2003.
[87] R. T. Kurnlk, S. J. Holla, and R. C. Reid, “Solubility of Solids in Supercritical Carbon Dioxide and Ethylene,” *J. Chem. Eng. Data*, vol. 26, no. 1, pp. 47–51, 1981, doi: 10.1021/je00023a016.
[88] G. T. Hefter and R. P. T. Tomkins, *Wiley Series in Solution Chemistry 006: The Experimental Determination of Solubilities*, vol. 6. 2003.
[89] S. J. Park, T. Y. Kwak, and G. A. Mansoori, “Statistical mechanical description of supercritical fluid extraction and retrograde condensation,” *Int. J. Thermophys.*, vol. 8, no. 4, pp. 449–471, Jul. 1987, doi: 10.1007/BF00567105.
[90] I. Union, O. F. Pure, and A. Chemistry, “Volume 57 - Ethene,” *Int. Union Pure Appl. Chem. - Solubility Data Ser.*, vol. 57, 1994.
[91] H. K. Onnes, “Expression of the equation of state of gases and liquids by means of series.,” *KNAW, Proc.*, pp. 125–147, 1902, doi: 10.1007/978-94-009-2079-8_6.
[92] D. Y. Peng and D. B. Robinson, “A New Two-Constant Equation of State,” *Ind. Eng. Chem. Fundam.*, vol. 15, no. 1, pp. 59–64, 1976, doi: 10.1021/i160057a011.
[93] D. B. Robinson, D. Y. Peng, and S. Y. K. Chung, “The development of the Peng - Robinson equation and its application to phase equilibrium in a system containing methanol,” *Fluid Phase Equilib.*, vol. 24, no. 1–2, pp. 25–41, 1985, doi: 10.1016/0378-3812(85)87035-7.
[94] F. Mutelet, “VLE predictions with the Peng – Robinson equation of state and temperature dependent k ij calculated through a group contribution method,” vol. 224, pp. 285–304, 2004, doi: 10.1016/j.fluid.2004.06.059.
[95] J. Wisniak, “Interpretation of the Second Virial Coefficient,” *J. Chem. Educ.*, vol. 76, no. 5, pp. 671–675, 1999, doi: 10.1021/ed076p671.
[96] K. Weissermel and H. Arpe, *Industrial Organic Chemistry*, no. 7. Wiley, 2003.
[97] R. D. Andrei *et al.*, “Ethylene Oligomerization from Diluted Stream over Ni-Containing Heterogeneous Catalysts,” *Ind. Eng. Chem. Res.*, vol. 59, no. 5, pp. 1746–1752, 2020, doi: 10.1021/acs.iecr.9b05576.

[98] A. Galadima and O. Muraza, “Revisiting the oxidative coupling of methane to ethylene in the golden period of shale gas: A review,” *J. Ind. Eng. Chem.*, vol. 37, pp. 1–13, 2016, doi: 10.1016/j.jiec.2016.03.027.
[99] G. R. Lappin, L. H. Nemec, J. D. Sauer, and J. D. Wagner, “Olefins, Higher,” in *Kirk-Othmer Encyclopedia of Chemical Technology*, I. John Wiley & Sons, Ed. Hoboken, NJ, USA: John Wiley & Sons, Inc., 2010, pp. 1–20.
[100] W. Keim, “Oligomerization of ethylene to α-olefins: Discovery and development of the shell higher olefin process (SHOP),” *Angew. Chemie - Int. Ed.*, vol. 52, no. 48, pp. 12492–12496, 2013, doi: 10.1002/anie.201305308.
[101] W. Keim *et al.*, “Linear Oligomerization of olefins via nickel chelate complexes and mechanistic considerations based on semi-empirical calculations,” *J. Mol. Catal.*, vol. 6, no. 2, pp. 79–97, 1979, doi: 10.1016/0304-5102(79)80016-4.
[102] G. J. P. Britovsek *et al.*, “Ethylene Oligomerization beyond Schulz-Flory Distributions,” *ACS Catal.*, vol. 5, no. 11, pp. 6922–6925, 2015, doi: 10.1021/acscatal.5b02203.
[103] D. Y. Shin, J. H. Yoon, H. Baik, and S. J. Lee, “A way to avoid polymeric side products during the liquid-phase ethylene oligomerization with SBA-15 supported (bpy)Ni(II)Cl2 heterogeneous catalyst,” *Appl. Catal. A Gen.*, vol. 590, no. November 2019, p. 117363, 2020, doi: 10.1016/j.apcata.2019.117363.
[104] F. A. Administration, “FAA Aerospace Forecasts Fiscal Years 2020-2040,” 2020.
[105] U.S. Department of Energy, “Annual Energy Outlook 2020 with projections to 2050,” 2020.
[106] E. I. Administration, “Jet Fuel Consumption, Price, and Expenditure Estimates,” 2019. https://www.eia.gov/state/seds/data.php?incfile=/state/seds/sep_fuel/html/fuel_jf.html (accessed Nov. 18, 2020).
[107] IATA, “Annual Review 2019,” 2019.
[108] IATA, “Climate Change & CORSIA,” 2018. https://www.iata.org/en/programs/environment/climate-change/.
[109] S. Kosir, R. Stachler, J. Heyne, and F. Hauck, “High-performance jet fuel optimization and uncertainty analysis,” *Fuel*, vol. 281, no. April, p. 118718, 2020, doi: 10.1016/j.fuel.2020.118718.
[110] J. Popp, Z. Lakner, M. Harangi-Rákos, and M. Fári, “The effect of bioenergy expansion: Food, energy, and environment,” *Renew. Sustain. Energy Rev.*, vol. 32, pp. 559–578, 2014, doi: 10.1016/j.rser.2014.01.056.
[111] United States of America, “Aviation Greenhouse Gas Emissions Reduction Plan,” *Aviation*, no. June, 2012, [Online]. Available: https://www.faa.gov/about/office_org/headquarters_offices/apl/environ_policy_guidance/policy/media/Aviation_Greenhouse_Gas_Emissions_Reduction_Plan.pdf.
[112] J. Holladay, Z. Abdullah, and J. Heyne, “Sustainable Aviation Fuel: Review of Technical Pathways,” 2020.
[113] A. P. P. Pires, Y. Han, J. Kramlich, and M. Garcia-Perez, “Chemical composition and fuel properties of alternative jet fuels,” *BioResources*, vol. 13, no. 2, pp. 2632–2657, 2018, doi: 10.15376/biores.13.2.2632-2657.
[114] FAA, Boeing, and University of Dayton Research Institue, “Impact of Alternative Jet Fuel and Fuel Blends on Non-Metallic Materials Used in Commercial Aircraft Fuel Systems CLEEN Project Final Report – Submitted by The Boeing Company.”
[115] S. Kosir, J. Heyne, and J. Graham, “A machine learning framework for drop-in volume

swell characteristics of sustainable aviation fuel," *Fuel*, vol. 274, no. November 2019, p. 117832, 2020, doi: 10.1016/j.fuel.2020.117832.
[116] H. Zimmermann and R. Walzl, "Ethylene," in *Ullmann's Encyclopedia of Industrial Chemistry*, Weinheim, Germany: Wiley-VCH Verlag GmbH & Co. KGaA, 2009.
[117] K. Weissermel and H. Arpe, *Industrial Organic Chemistry*, no. 7. Wiley, 2003.
[118] M. Zhang and Y. Yu, "Dehydration of ethanol to ethylene," *Ind. Eng. Chem. Res.*, vol. 52, no. 28, pp. 9505–9514, 2013, doi: 10.1021/ie401157c.
[119] L. Tao, J. N. Markham, Z. Haq, and M. J. Biddy, "Techno-economic analysis for upgrading the biomass-derived ethanol-to-jet blendstocks," *Green Chem.*, vol. 19, no. 4, pp. 1082–1101, 2017, doi: 10.1039/c6gc02800d.
[120] U. S. E. I. Administration, "Commercial-scale cellulosic ethanol plant opens," 2014. https://www.eia.gov/todayinenergy/detail.php?id=17851 (accessed Nov. 18, 2020).
[121] POET, "EPA Actions Trigger Project Liberty Shift From Production to R&D," 2019. https://poet.com/pr/epa-actions-trigger-project-liberty-shift (accessed Nov. 18, 2020).
[122] M. Yang, X. Tian, and F. You, "Manufacturing Ethylene from Wet Shale Gas and Biomass: Comparative Technoeconomic Analysis and Environmental Life Cycle Assessment," *Ind. Eng. Chem. Res.*, vol. 57, no. 17, pp. 5980–5998, 2018, doi: 10.1021/acs.iecr.7b03731.
[123] BYOGY Renewables, "Alcohol To Jet (ATJ) emerging through ASTM," *ICAO Aviat. Sustain. Altern. fuels Work.*, 2011.
[124] S. Simpson, "A Hybrid Catalytic Route to Fuels from Biomass Syngas," *U.S. Dep. Energy Bioenergy Technol. Off. 2017 Proj. Peer Rev.*, 2017.
[125] B. G. Harvey and R. L. Quintana, "Synthesis of renewable jet and diesel fuels from 2-ethyl-1-hexene," *Energy Environ. Sci.*, vol. 3, no. 3, p. 352, 2010, doi: 10.1039/b924004g.
[126] M. E. Wright, B. G. Harvey, and R. L. Quintana, "Highly efficient zirconium-catalyzed batch conversion on 1-butene: A new route to jet fuels," *Energy and Fuels*, vol. 22, no. 5, pp. 3299–3302, 2008, doi: 10.1021/ef800380b.
[127] M. Hartmann and L. Kevan, "Transition-Metal Ions in Aluminophosphate and Silicoaluminophosphate Molecular Sieves: Location, Interaction with Adsorbates and Catalytic Properties," *Chem. Rev.*, vol. 99, no. 3, pp. 635–663, 1999, doi: 10.1021/cr9600971.
[128] S. Wang, W. H. Sun, and C. Redshaw, "Recent progress on nickel-based systems for ethylene oligo-/polymerization catalysis," *J. Organomet. Chem.*, vol. 751, pp. 717–741, 2014, doi: 10.1016/j.jorganchem.2013.08.021.
[129] F. Speiser, P. Braunstein, and L. Saussine, "Catalytic ethylene dimerization and oligomerization: recent developments with nickel complexes containing P,N-chelating ligands," *Acc. Chem. Res.*, vol. 38, no. 10, pp. 784–793, 2005, doi: 10.1021/ar050040d.
[130] J. R. Sohn and W. C. Park, "Characterization of nickel sulfate supported on γAl2O 3 and its relationship to acidic properties," *Korean J. Chem. Eng.*, vol. 19, no. 4, pp. 580–586, 2002, doi: 10.1007/BF02699299.
[131] J. Heveling, C. P. Nicolaides, and M. S. Scurrell, "Catalysts and conditions for the highly efficient, selective and stable heterogeneous oligomerisation of ethylene," *Appl. Catal. A Gen.*, vol. 173, no. 1, pp. 1–9, 1998, doi: 10.1016/S0926-860X(98)00147-1.
[132] L. Zhang, T. L. Butler, and B. Yang*, "Recent Trends, Opportunities and Challenges of Sustainable Aviation Fuel," *Green Energy to Sustain.*, pp. 85–110, 2020, doi: 10.1002/9781119152057.ch5.

[133] M. Lee *et al.*, “Ni/SIRAL-30 as a heterogeneous catalyst for ethylene oligomerization,” *Appl. Catal. A Gen.*, vol. 562, no. May, pp. 87–93, 2018, doi: 10.1016/j.apcata.2018.06.004.
[134] D. Eliche-Quesada, J. Mérida-Robles, P. Maireles-Torres, E. Rodríguez-Castellón, and A. Jiménez-López, “Hydrogenation and ring opening of tetralin on supported nickel zirconium-doped mesoporous silica catalysts. Influence of the nickel precursor,” *Langmuir*, vol. 19, no. 12, pp. 4985–4991, 2003, doi: 10.1021/la020865l.
[135] C. A. Tolman, W. M. Riggs, W. J. Linn, C. M. King, and R. C. Wendt, “Electron Spectroscopy for Chemical Analysis of Nickel Compounds,” *Inorg. Chem.*, vol. 12, no. 12, pp. 2770–2778, 1973, doi: 10.1021/ic50130a006.
[136] S. Bendezú, R. Cid, J. L. G. Fierro, and A. López Agudo, “Thiophene hydrodesulfurization on sulfided Ni, W and NiW/USY zeolite catalysts: Effect of the preparation method,” *Appl. Catal. A Gen.*, vol. 197, no. 1, pp. 47–60, 2000, doi: 10.1016/S0926-860X(99)00532-3.
[137] B. Pawelec, R. Mariscal, R. M. Navarro, J. M. Campos-Martin, and J. L. G. Fierro, “Simultaneous 1-pentene hydroisomerisation and thiophene hydrodesulphurisation over sulphided Ni/FAU and Ni/ZSM-5 catalysts,” *Appl. Catal. A Gen.*, vol. 262, no. 2, pp. 155–166, 2004, doi: 10.1016/j.apcata.2003.11.037.
[138] G. Poncelet, M. A. Centeno, and R. Molina, “Characterization of reduced α-alumina-supported nickel catalysts by spectroscopic and chemisorption measurements,” *Appl. Catal. A Gen.*, vol. 288, no. 1–2, pp. 232–242, 2005, doi: 10.1016/j.apcata.2005.04.052.
[139] S. R. Kirumakki, B. G. Shpeizer, G. V. Sagar, K. V. R. Chary, and A. Clearfield, “Hydrogenation of Naphthalene over NiO/SiO2-Al2O3 catalysts: Structure-activity correlation,” *J. Catal.*, vol. 242, no. 2, pp. 319–331, 2006, doi: 10.1016/j.jcat.2006.06.014.
[140] M. Wu, L. Chou, and H. Song, “Epoxidation of butadiene over nickel modified TS-1 catalyst,” *Catal. Letters*, vol. 142, no. 5, pp. 627–636, 2012, doi: 10.1007/s10562-012-0792-6.
[141] J. Kawai, H. Adachi, Y. Kitajima, K. Maeda, S. Hayakawa, and Y. Gohshi, “Inelastic Mean Free Path of Photoelectrons in Ag Determined by Total Reflection X-Ray Photoelectron Spectroscopy,” *Anal. Sci.*, vol. 13, no. 5, pp. 797–801, 1997, doi: 10.2116/analsci.13.797.
[142] F. Wurche and F. G. Klärner, “The Effect of Pressure on Organic Reactions: Basic Principles and Mechanistic Applications,” *High Press. Chem. Synth. Mech. Supercrit. Appl.*, pp. 41–96, 2007, doi: 10.1002/9783527612628.ch02.
[143] J. T. Crawford, C. W. Shan, E. Budsberg, H. Morgan, R. Bura, and R. Gustafson, “Hydrocarbon bio-jet fuel from bioconversion of poplar biomass: techno-economic assessment,” *Biotechnol. Biofuels*, vol. 9, no. 1, p. 141, Dec. 2016, doi: 10.1186/s13068-016-0545-7.
[144] D. U. Pascoli, A. Suko, R. Gustafson, H. L. Gough, and R. Bura, “Novel ethanol production using biomass preprocessing to increase ethanol yield and reduce overall costs,” *Biotechnol. Biofuels*, vol. 14, no. 1, pp. 1–18, 2021, doi: 10.1186/s13068-020-01839-0.
[145] A. Aden *et al.*, “Lignocellulosic Biomass to Ethanol Process Design and Economics Utilizing Co-Current Dilute Acid Prehydrolysis and Enzymatic Hydrolysis for Corn Stover,” *Natl. Renew. Energy Lab.*, no. June, 2002, doi: NREL/TP-510-32438.
[146] D. Humbird *et al.*, “Process Design and Economics for Biochemical Conversion of

Lignocellulosic Biomass to Ethanol," *Renew. Energy*, vol. 303, no. May, p. 147, 2011, doi: 10.2172/1013269.

[147] D. Klein-Marcuschamer, P. Oleskowicz-Popiel, B. A. Simmons, and H. W. Blanch, "The challenge of enzyme cost in the production of lignocellulosic biofuels," *Biotechnol. Bioeng.*, vol. 109, no. 4, pp. 1083–1087, 2012, doi: 10.1002/bit.24370.

[148] R. Le Van Mao, T. M. Nguyen, and G. P. McLaughlin, "The bioethanol-to-ethylene (B.E.T.E.) process," *Appl. Catal.*, vol. 48, no. 2, pp. 265–277, 1989, doi: 10.1016/S0166-9834(00)82798-0.

[149] R. Davis *et al.*, "Process Design and Economics for the Conversion of Lignocellulosic Biomass to Hydrocarbons: Dilute-Acid and Enzymatic Deconstruction of Biomass to Sugars and Biological Conversion of Sugars to Hydrocarbons," no. March, 2013, doi: 10.2172/1107470.

[150] U.S. Department of Energy Energy Efficiency and Renewable Energy, "A Best Practices Steam Technical Brief - How To Calculate The True Cost of Steam," p. 13, 2018.

[151] S. D. Phillips, J. K. Tarud, M. J. Biddy, and A. Dutta, "Gasoline from Wood via Integrated Gasification , Synthesis, and Methanol-to- Gasoline Technologies," 2011. doi: NREL/TP-5100-47594.

[152] J. A. Muldoon and B. G. Harvey, "Bio-Based Cycloalkanes: The Missing Link to High-Performance Sustainable Jet Fuels," *ChemSusChem*, vol. 13, no. 22, pp. 5777–5807, 2020, doi: 10.1002/cssc.202001641.

[153] D. Lozowski, "The Chemical Engineering Plant Cost Index," *Chemical Engineering Essentials for the CPI Professional*, Apr. 2019.

[154] R. Davis *et al.*, "Process Design and Economics for the Conversion of Lignocellulosic Biomass to Hydrocarbons: Dilute-Acid and Enzymatic Deconstruction of Biomass to Sugars and Biological Conversion of Sugars to Hydrocarbons," no. October 2013, 2013, doi: 10.2172/1107470.

[155] S. de Jong, R. Hoefnagels, A. Faaij, R. Slade, R. Mawhood, and M. Junginger, "The feasibility of short-term production strategies for renewable jet fuels - a comprehensive techno-economic comparison," *Biofuels, Bioprod. Biorefining*, vol. 9, no. 6, pp. 778–800, Nov. 2015, doi: 10.1002/bbb.1613.

[156] K. Atsonios, M. A. Kougioumtzis, K. D. Panopoulos, and E. Kakaras, "Alternative thermochemical routes for aviation biofuels via alcohols synthesis: Process modeling, techno-economic assessment and comparison," *Appl. Energy*, vol. 138, pp. 346–366, 2015, doi: 10.1016/j.apenergy.2014.10.056.

APPENDIX A

1. KINETIC MODEL DEVELOPMENT

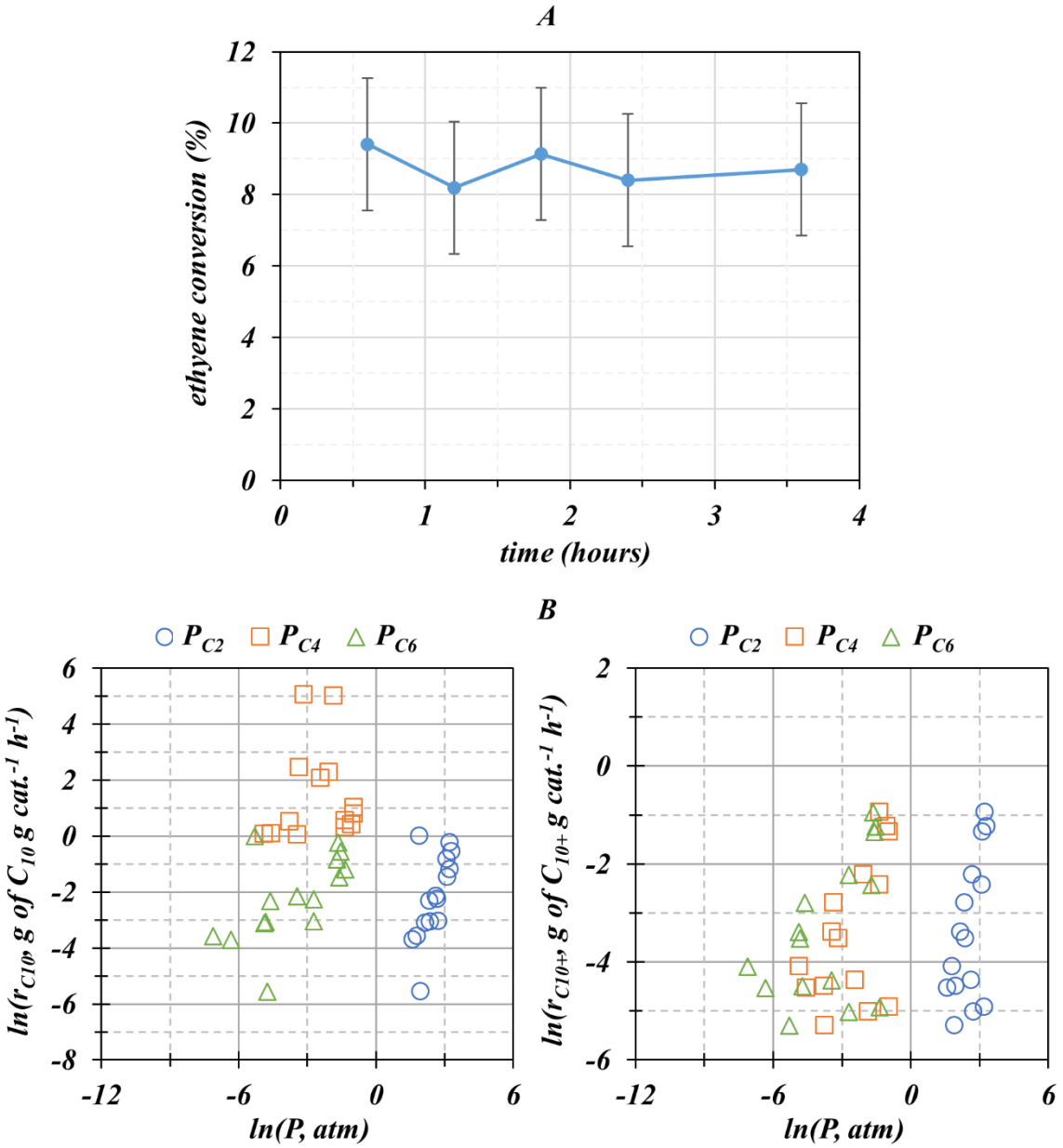

Figure S1: A – ethylene conversion as a function of time-on-stream for the ethylene oligomerization at 100°C and 28 bar. B – Log-log plots of the rates of formation of C_{10} and C_{10+} products as a function of the ethylene, butene, and hexene partial pressures.

Table S1: Replicates performed at 6.8 and 28 bar at 100 ^{o}C and WHSV = 48.4 g ethylene g cat.$^{-1}$ h^{-1}

					r (g.g cat^{-1} h^{-1})								
	T (K)	P (atm)	X[1] (%)	m.b.[2] (%)	C2	C4	C5	C6	C7	C8	C9	C10	C12
	373	28.4	8.15	99.4	3.94	1.12	0.00	1.03	0.0	0.80	0.02	0.58	0.29
	382	26.1	8.39	100.4	4.06	0.92	0.00	1.02	0.01	0.79	0.03	0.79	0.39
	380	26.0	7.30	103.0	3.53	1.37	0.00	1.22	0.01	0.73	0.00	0.22	0.00
s.d.[3]	4.0	1.1	0.23	1.5	0.23	0.18	0.00	0.09	0.00	0.03	0.01	0.24	0.16
	373	6.8	1.03	98.1	0.50	0.33	0.00	0.10	0.00	0.06	0.00	0.00	0.00
	380	7.2	1.24	101.2	0.60	0.31	0.00	0.18	0.00	0.07	0.00	0.00	0.01
s.d.[3]	3.5	0.2	0.10	1.6	0.05	0.01	0.00	0.04	0.00	0.01	0.00	0.00	0.00

[1] ethylene conversion
[2] mass balance
[3] standard deviation

2. ETHYLENE DIFFUSION MODEL INTO A MIXTURE OF ALKENES

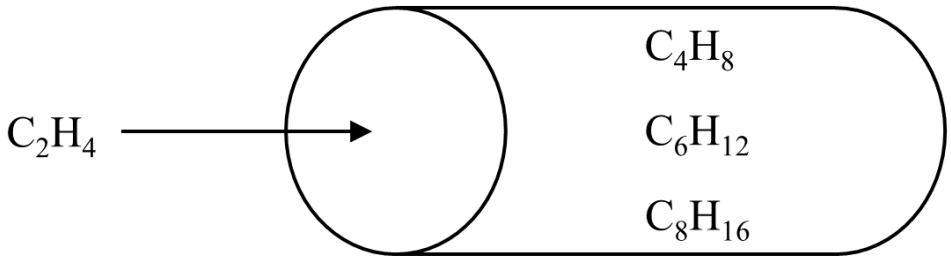

Figure S2: Pore diffusion model used to assess mass transfer limitation effects during ethylene oligomerization over the Ni-H-Beta catalyst.

Application of the Weisz-Prater criterion[71] requires information of the effective diffusivity of reactants into the pores of the catalyst, which contains products formed from the conversion of ethylene into alkenes. Therefore, we considered a model where ethylene diffuses into a mixture of products (1-butene, 1-hexene, and 1-octene). A simplified schematic is shown in Figure S2. We assessed the possibility of Knudsen-diffusion limitation in the system; however, the small gas mean-free path calculated relative to the pore diameter of the catalyst led us to rule out this possibility. We used the Wilker's equation[71] (Equation S1) to calculate the diffusivity of ethylene into a mixture of 1-butene, 1-hexene, and 1-octene.

$$D_{1\rightarrow mixture} = \frac{1}{\frac{y_2'}{D_{1\rightarrow 2}}+\frac{y_3'}{D_{1\rightarrow 3}}+\cdots+\frac{y_n'}{D_{1\rightarrow n}}} \quad \text{(S1)}$$

In Equation S1, subscripts 1 to 4 correspond to ethylene, butene, hexene, and octene, respectively. $D_{1\rightarrow i}$ represents the binary diffusivity coefficient of component 1 into component i and y_i' is the molar fraction of component i in the mixture evaluated on a component-1-free basis:

$$y_i' = \frac{y_i}{1-y_1} \quad \text{(S2)}$$

We calculated the binary diffusivity coefficient using the Chapman-Enskog equation as follow[71]:

$$D_{12} = \frac{0.001858 T^{\frac{3}{2}} \sqrt{\frac{M_1 + M_2}{M_1 M_2}}}{p \sigma_{12}^2 \Omega_{D,12}} \quad \text{(S3)}$$

Where D_{12} is the diffusivity coefficient of species 1 in 2 (in cm^2/s), T is the temperature (in K), M_i is the molecular weight of specie i (in g.mol^{-1}), p is the total pressure of the binary mixture (in atm), σ_{12} is the Lennard-Jones force constant, and $\Omega_{D,12}$ is the collision integral function. Values used for the assessment of the diffusivity and results obtained considering the model described above are shown in Table S2.

Table S2: Diffusivity coefficients calculated from the model described in this section and the parameters applied to the Weisz-Prater criterion to access internal mass transfer limitation regime in the pores of the Ni-H-Beta catalyst

	Temperature (K)				
	323	348	373	423	470
$D_{12}(cm^2.s)$	0.0031	0.0035	0.0041	0.0052	0.0063
$D_{13}(cm^2.s)$	0.0024	0.0028	0.0032	0.0040	0.0049
$D_{14}(cm^2.s)$	0.0018	0.0027	0.0031	0.0039	0.0048
y_2	0.70	0.58	0.44	0.43	0.43
y_3	0.14	0.21	0.27	0.26	0.25
y_4	0.08	0.11	0.15	0.16	0.17
$D_{1\rightarrow mixture}(cm^2.s)$	0.0030	0.0036	0.0041	0.0053	0.0065
$-r_{ethylene}$ (g ethylene.kg cat.$^{-1}$.h^{-1})	567	1967	4215	5966	10979
D_e (m^2.h^{-1})	4.2x10^{-4}	4.9x10^{-4}	5.6x10^{-4}	7.3x10^{-4}	9.0x10^{-4}
$C_{ethylene}$ (g ethylene.m^{-3})	29,601	27,474	25,633	22,555	20,343
C_{wp}	0.002	0.007	0.01	0.02	0.03

3. KINETIC PARAMETERS ASSESSMENT

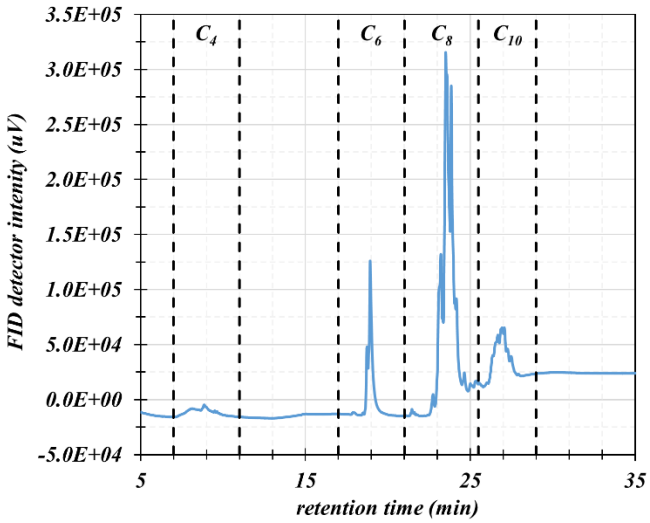

Figure S3: GC-FID spectra of gas products collected after the ethylene adsorption over the Ni-H-Beta catalyst at 1 atm and -80°C. The inlet mixture consisted of nitrogen (molar fraction = 0.991) and ethylene (molar fraction = 0.009).

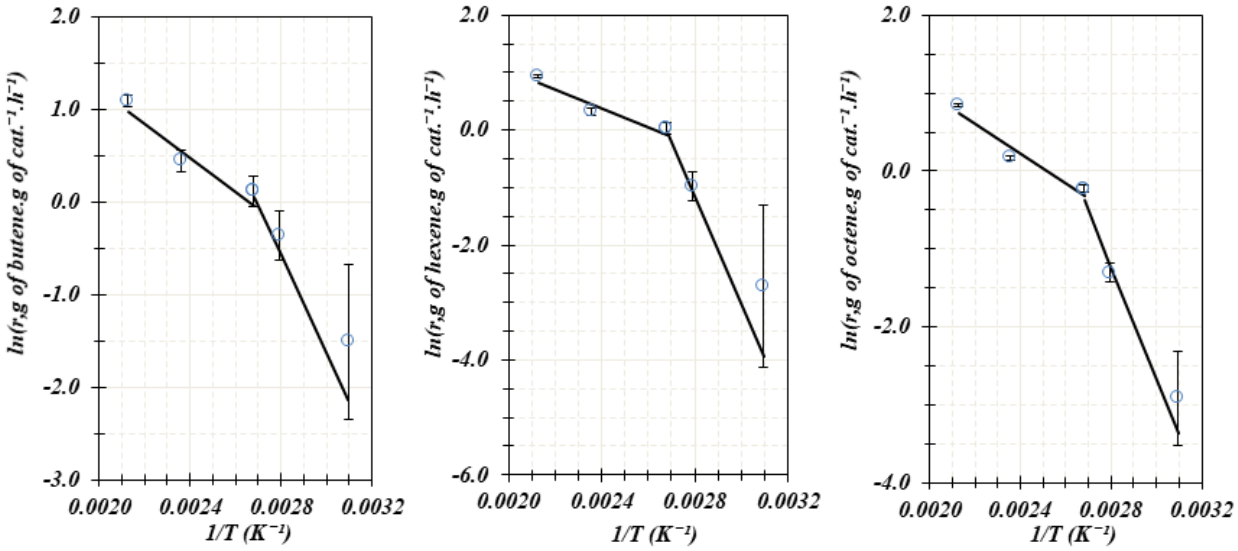

Figure S4: Arrhenius plot for the formation of butene, hexene, and octene.

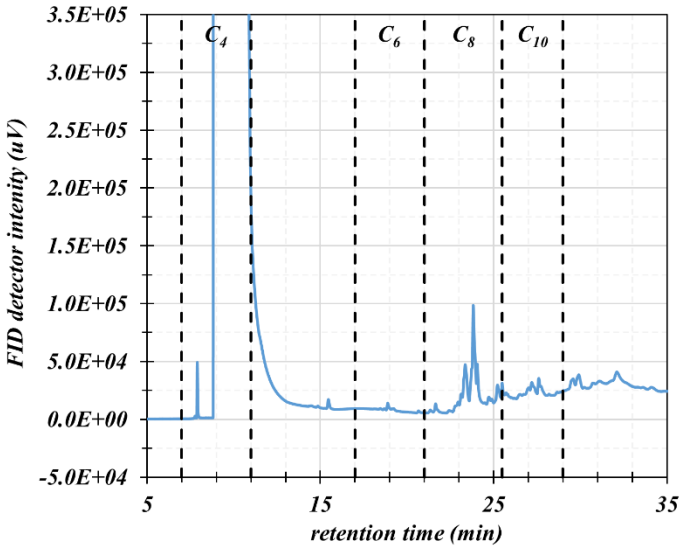

Figure S5: GC-FID spectra of gas products collected after butene oligomerization over the Ni-H-Beta catalyst (nickel loading = 4.1 wt. %) at 1 atm and 100°C. The inlet mixture consisted of nitrogen (molar fraction = 0.96) and butene (molar fraction = 0.04).

4. "BUTENE CO-OLIGOMERIZATION" MODEL

Table S3: Kinetic expressions developed using the LHHW kinetics based on the pathway proposed in Figure 3.6

reaction step[1]	Chemical Equations[2]	Kinetic expressions[3]
A	$C_2H_4 + Ni^{2+} \leftrightarrow [Ni^{2+} - H^-] - C_2H_3$	$\theta_{[Ni^{2+}-H^-]-C_2H_3} = K_1 P_{C_2H_4} \theta_{Ni^{2+}}$
B	$[Ni^{2+} - H^-] - C_2H_3 + C_2H_4 \leftrightarrow C_2H_3 - Ni^+ - C_2H_5$	$\theta_{C_2H_3-Ni^+-C_2H_5} = K_2 P_{C_2H_4} \theta_{[Ni^{2+}-H^-]-C_2H_3} = K_1 K_2 P_{C_2H_4}^2 \theta_{Ni^{2+}}$
C	$C_2H_3 - Ni^+ - C_2H_5 + C_2H_4 \leftrightarrow C_2H_3 - Ni^+ - C_2H_5(C_2H_4)$	$\theta_{C_2H_3-Ni^+-C_2H_5(C_2H_4)} = K_3 P_{C_2H_4} \theta_{C_2H_3-Ni^+-C_2H_5} = K_1 K_2 K_3 P_{C_2H_4}^3 \theta_{Ni^{2+}}$
D	$C_2H_3 - Ni^+ - C_2H_5(C_2H_4) \rightarrow [Ni^{2+} - H^-] - C_6H_{11}$	$r^D_{[Ni^{2+}-H^-]-C_6H_{11}} = k_4^+ \theta_{C_2H_3-Ni^+-C_2H_5(C_2H_4)} = k_4^+ K_1 K_2 K_3 P_{C_2H_4}^3 \theta_{Ni^{2+}}$
E	$[Ni^{2+} - H^-] - C_6H_{11} \leftrightarrow C_6H_{12} + Ni^{2+}$	$\theta_{[Ni^{2+}-H^-]-C_6H_{11}} = K_5 P_{C_6H_{12}} \theta_{Ni^{2+}}$
F	$C_2H_3 - Ni^+ - C_2H_5 \rightarrow [Ni^{2+} - H^-] - C_4H_7$	$r^F_{[Ni^{2+}-H^-]-C_4H_7} = k_6^+ \theta_{C_2H_3-Ni^+-C_2H_5} = k_6^+ K_1 K_2 P_{C_2H_4}^2 \theta_{Ni^{2+}}$
G	$[Ni^{2+} - H^-] - C_4H_7 \leftrightarrow C_4H_8 + Ni^{2+}$	$\theta_{[Ni^{2+}-H^-]-C_4H_7} = K_7 P_{C_4H_8} \theta_{Ni^{2+}}$
H	$[Ni^{2+} - H^-] - C_4H_7 + C_2H_4 \leftrightarrow C_2H_3 - Ni^+ - C_4H_9$	$\theta_{C_2H_3-Ni^+-C_4H_9} = K_8 P_{C_2H_4} \theta_{[Ni^{2+}-H^-]-C_4H_7} = K_7 K_8 P_{C_2H_4} P_{C_4H_8} \theta_{Ni^{2+}}$
I	$C_2H_3 - Ni^+ - C_4H_9 \rightarrow [Ni^{2+} - H^-] - C_6H_{11}$	$r^I_{[Ni^{2+}-H^-]-C_6H_{11}} = k_9^+ \theta_{C_2H_3-Ni^+-C_4H_9} = k_9^+ K_7 K_8 P_{C_2H_4} P_{C_4H_8} \theta_{Ni^{2+}}$
J	$C_2H_3 - Ni^+ - C_4H_9 + C_2H_4 \leftrightarrow C_2H_3 - Ni^+ - C_4H_9(C_2H_4)$	$\theta_{C_2H_3-Ni^+-C_4H_9(C_2H_4)} = K_{10} P_{C_2H_4} \theta_{C_2H_3-Ni^+-C_4H_9} = K_7 K_8 K_{10} P_{C_2H_4}^2 P_{C_4H_8} \theta_{Ni^{2+}}$
K	$C_2H_3 - Ni^+ - C_4H_9(C_2H_4) \rightarrow [Ni^{2+} - H^-] - C_8H_{15}$	$r^K_{[Ni^{2+}-H^-]-C_8H_{15}} = k_{11}^+ \theta_{C_2H_3-Ni^+-C_4H_9(C_2H_4)} = k_{11}^+ K_7 K_8 K_{10} P_{C_2H_4}^2 P_{C_4H_8} \theta_{Ni^{2+}}$
L	$[Ni^{2+} - H^-] - C_8H_{15} \leftrightarrow C_8H_{16} + Ni^{2+}$	$\theta_{[Ni^{2+}-H^-]-C_8H_{15}} = K_{12} P_{C_8H_{16}} \theta_{Ni^{2+}}$
M	$[Ni^{2+} - H^-] - C_4H_7 + C_4H_8 \leftrightarrow C_4H_7 - Ni^+ - C_4H_9$	$\theta_{C_4H_7-Ni^+-C_4H_9} = K_{13} P_{C_4H_8} \theta_{[Ni^{2+}-H^-]-C_4H_7} = K_7 K_{13} P_{C_4H_8}^2 \theta_{Ni^{2+}}$
N	$C_4H_7 - Ni^+ - C_4H_9 \rightarrow [Ni^{2+} - H^-] - C_8H_{15}$	$r^N_{[Ni^{2+}-H^-]-C_8H_{15}} = k_{14}^+ \theta_{C_4H_7-Ni^+-C_4H_9} = k_{14}^+ K_7 K_{13} P_{C_4H_8}^2 \theta_{Ni^{2+}}$
O	$[Ni^{2+} - H^-] - C_6H_{11} + C_2H_4 \leftrightarrow C_2H_3 - Ni^+ - C_6H_{13}$	$\theta_{C_2H_3-Ni^+-C_6H_{13}} = K_{15} P_{C_2H_4} \theta_{[Ni^{2+}-H^-]-C_6H_{11}} = K_5 K_{15} P_{C_2H_4} P_{C_6H_{12}} \theta_{Ni^{2+}}$
P	$C_2H_3 - Ni^+ - C_6H_{13} \rightarrow [Ni^{2+} - H^-] - C_8H_{15}$	$r^P_{[Ni^{2+}-H^-]-C_8H_{15}} = k_{16}^+ \theta_{C_2H_3-Ni^+-C_6H_{13}} = k_{16}^+ K_5 K_{15} P_{C_2H_4} P_{C_6H_{12}} \theta_{Ni^{2+}}$
Balance of active sites[4]	$\theta_* + \theta_{[Ni^{2+}-H^-]-C_2H_3} + \theta_{[Ni^{2+}-H^-]-C_4H_7} + \theta_{[Ni^{2+}-H^-]-C_6H_{11}} + \theta_{[Ni^{2+}-H^-]-C_8H_{15}} = 1$ $\theta_{Ni^{2+}} + K_1 P_{C_2H_4} \theta_{Ni^{2+}} + K_7 P_{C_4H_8} \theta_{Ni^{2+}} + K_5 P_{C_6H_{12}} \theta_{Ni^{2+}} + K_{12} P_{C_8H_{16}} \theta_{Ni^{2+}} = 1$	

Implicit rate expressions[5]	$\sum r_{C_2H_4} = -r^{F}_{[Ni^{2+}-H^{-}]-C_4H_7} - r^{D}_{[Ni^{2+}-H^{-}]-C_6H_{11}} - r^{I}_{[Ni^{2+}-H^{-}]-C_6H_{11}} - r^{K}_{[Ni^{2+}-H^{-}]-C_8H_{15}} - r^{P}_{[Ni^{2+}-H^{-}]-C_8H_{15}}$
	$\sum r_{C_4H_8} = r^{F}_{[Ni^{2+}-H^{-}]-C_4H_7} - r^{I}_{[Ni^{2+}-H^{-}]-C_6H_{11}} - r^{K}_{[Ni^{2+}-H^{-}]-C_8H_{15}} - r^{N}_{[Ni^{2+}-H^{-}]-C_8H_{15}}$
	$\sum r_{C_6H_{12}} = r^{D}_{[Ni^{2+}-H^{-}]-C_6H_{11}} + r^{I}_{[Ni^{2+}-H^{-}]-C_6H_{11}} - r^{P}_{[Ni^{2+}-H^{-}]-C_8H_{15}}$
	$\sum r_{C_8H_{16}} = r^{K}_{[Ni^{2+}-H^{-}]-C_8H_{15}} + r^{N}_{[Ni^{2+}-H^{-}]-C_8H_{15}} + r^{P}_{[Ni^{2+}-H^{-}]-C_8H_{15}}$

[1] Reaction steps refer to the elementary steps shown in Figure 3.6.

[2] $[Ni^{2+} - H^{-}]$ represents the active site where ethylene adsorption and chain-growth reactions take place.

[3] K represents the equilibrium parameters described by Equation 3.5, k^{+} represents the reaction constant associated with the conversion step, and P_i is the partial pressure of species i at steady-state.

[4] $\theta_* =$ Fraction of free active site.

[5] Overall rate expressions for production of C_4, C_6, and C_8 products and consumption of ethylene.

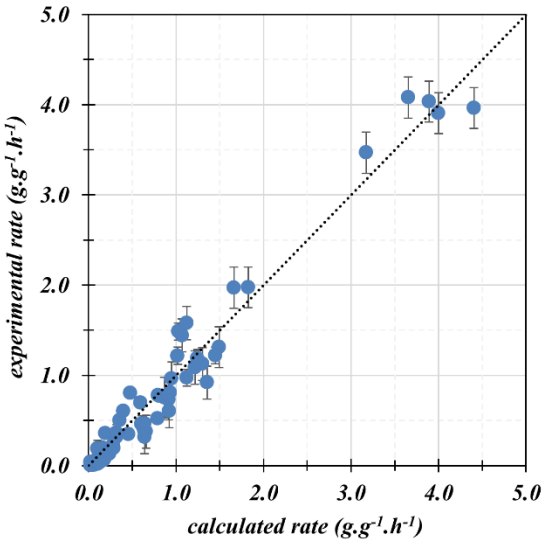

Figure S6: Parity plot showing calculated and experimental reaction rates at 100°C and WHSV of 48.4 g ethylene.g cat.$^{-1}$.h^{-1} for ethylene partial pressure ranging between 5 and 28 atm.

5. THEORETICAL BACKGROUND

Equation S4 describes the sorption equilibrium constant as function of enthalpy of adsorption and temperature[68]:

$$K_{eq}(T) = K_0 e^{-\frac{\Delta H_{ads}}{RT}} \quad \text{(S4)}$$

In which K_{eq} (in atm^{-1}) is the equilibrium constant between adsorption and desorption for both reactants and products, K_0 (in atm^{-1}) is the pre-exponential factor and depends on the conditions at which sorption data was collected, ΔH_{ads} is the heat of adsorption (in $J.mol^{-1}$), T is the temperature (in K), and R is the ideal gas constant (8.314 $J.mol^{-1}.K^{-1}$).

6. SENSITIVITY ANALYSIS

Table S4: Sensibility table showing the contribution of each kinetic parameter on the reaction rate expressions shown in Table 3.2 (Chapter 3) for the *"cascade co-oligomerization"* model after a disturbance of 5% on the value of the kinetic parameter

Kinetic parameter[1]	$r_{C_2H_4}$	$r_{C_4H_8}$	$r_{C_6H_{12}}$	$r_{C_8H_{16}}$
k_4^+	-0.33	0.00	-0.96	0.00
k_6^+	-0.50	-1.60	0.00	0.00
$\boldsymbol{k_9^+}$	***-0.02***	***0.05***	***-0.04***	***0.00***
k_{11}^+	-0.18	0.65	0.00	-1.00
$\boldsymbol{k_{14}^+}$	***0.00***	***0.00***	***0.00***	***0.00***
$\boldsymbol{k_{16}^+}$	***0.00***	***0.00***	***0.00***	***0.00***
K_1	-0.61	-1.39	-0.75	0.22
K_2	-0.82	-1.60	-0.96	0.00
K_3	-0.33	0.00	-0.96	0.00
$\boldsymbol{K_5}$	***0.00***	***0.00***	***0.00***	***0.00***
K_7	-0.20	0.70	-0.04	-1.00
K_8	-0.20	0.70	-0.04	-1.00
K_{10}	-0.18	0.65	0.00	-1.00
K_{12}	0.44	0.44	0.44	0.44
$\boldsymbol{K_{13}}$	***0.00***	***0.00***	***0.00***	***0.00***
$\boldsymbol{K_{15}}$	***0.00***	***0.00***	***0.00***	***0.00***

[1] Parameters in bold can be neglected based on the criterion assumed for the sensitivity analysis.

7. "ETHYLENE COORDINATION-INSERTION" MODEL

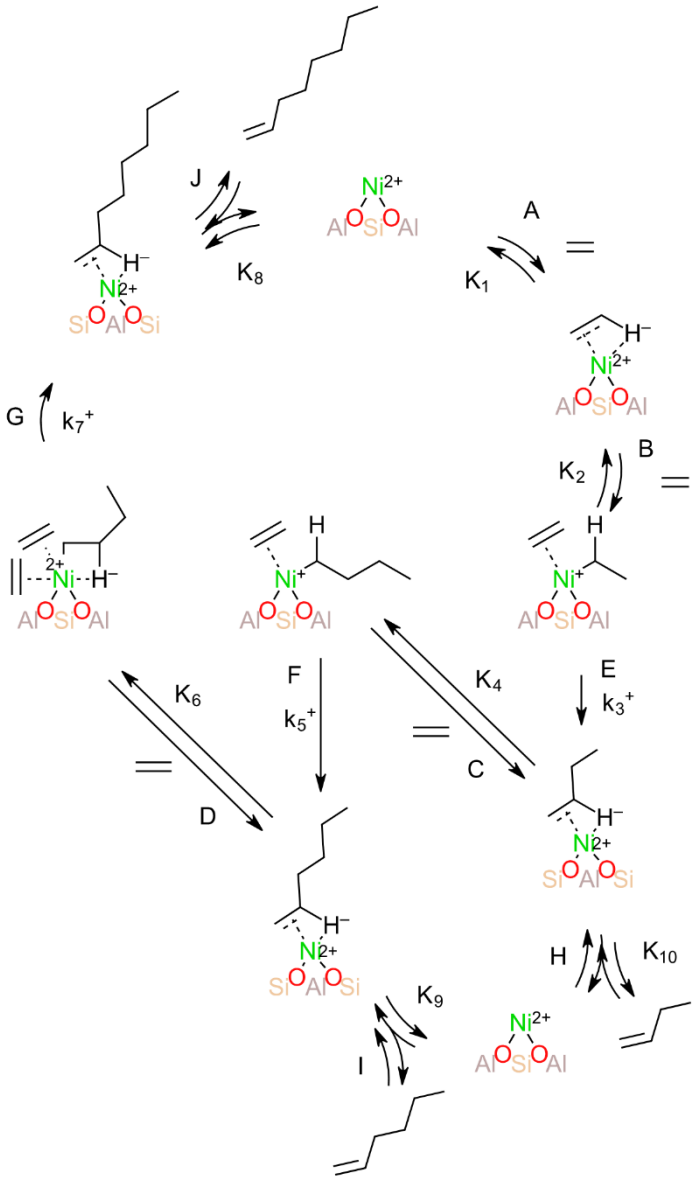

Figure S7: Reaction pathway based on simple ethylene coordination-insertion steps.

Table S5: Kinetic expressions developed using the LHHW kinetics based on the reaction network shown in Figure S7.

reaction step	Chemical Equations	Kinetic expressions
A	$C_2H_4 + Ni^{2+} \leftrightarrow [Ni^{2+} - H^-] - C_2H_3$	$\theta_{[Ni^{2+}-H^-]-C_2H_3} = K_1 P_{C_2H_4} \theta_{Ni^{2+}}$
B	$[Ni^{2+} - H^-] - C_2H_3 + C_2H_4 \leftrightarrow C_2H_3 - Ni^+ - C_2H_5$	$\theta_{C_2H_3-Ni^+-C_2H_5} = K_2 P_{C_2H_4} \theta_{[Ni^{2+}-H^-]-C_2H_3} = K_1 K_2 P_{C_2H_4}^2 \theta_{Ni^{2+}}$
C	$[Ni^{2+} - H^-] - C_4H_7 + C_2H_4 \leftrightarrow C_2H_3 - Ni^+ - C_4H_9$	$\theta_{C_2H_3-Ni^+-C_4H_9} = K_4 P_{C_2H_4} \theta_{[Ni^{2+}-H^-]-C_4H_7} = K_4 K_{10} P_{C_2H_4} P_{C_4H_8} \theta_{Ni^{2+}}$
D	$[Ni^{2+} - H^-] - C_6H_{11} + C_2H_4 \leftrightarrow C_2H_3 - Ni^+ - C_6H_{13}$	$\theta_{C_2H_3-Ni^+-C_6H_{13}} = K_6 P_{C_2H_4} \theta_{[Ni^{2+}-H^-]-C_6H_{11}} = K_6 K_9 P_{C_2H_4} P_{C_6H_{12}} \theta_{Ni^{2+}}$
E	$C_2H_3 - Ni^+ - C_2H_5 \rightarrow [Ni^{2+} - H^-] - C_4H_7$	$r^E_{[Ni^{2+}-H^-]-C_4H_7} = k_3^+ \theta_{C_2H_3-Ni^+-C_2H_5} = k_3^+ K_1 K_2 P_{C_2H_4}^2 \theta_{Ni^{2+}}$
F	$C_2H_3 - Ni^+ - C_4H_9 \rightarrow [Ni^{2+} - H^-] - C_6H_{11}$	$r^F_{[Ni^{2+}-H^-]-C_6H_{11}} = k_5^+ \theta_{C_2H_3-Ni^+-C_4H_9} = k_5^+ K_4 K_{10} P_{C_2H_4} P_{C_4H_8} \theta_{Ni^{2+}}$
G	$C_2H_3 - Ni^+ - C_6H_{13} \rightarrow [Ni^{2+} - H^-] - C_8H_{15}$	$r^G_{[Ni^{2+}-H^-]-C_8H_{15}} = k_7^+ \theta_{C_2H_3-Ni^+-C_6H_{13}} = k_7^+ K_6 K_9 P_{C_2H_4} P_{C_6H_{12}} \theta_{Ni^{2+}}$
H	$[Ni^{2+} - H^-] - C_4H_7 \leftrightarrow C_4H_8 + Ni^{2+}$	$\theta_{[Ni^{2+}-H^-]-C_4H_7} = K_{10} P_{C_4H_8} \theta_{Ni^{2+}}$
I	$[Ni^{2+} - H^-] - C_6H_{11} \leftrightarrow C_6H_{12} + Ni^{2+}$	$\theta_{[Ni^{2+}-H^-]-C_6H_{11}} = K_9 P_{C_6H_{12}} \theta_{Ni^{2+}}$
J	$[Ni^{2+} - H^-] - C_8H_{15} \leftrightarrow C_8H_{16} + Ni^{2+}$	$\theta_{[Ni^{2+}-H^-]-C_8H_{15}} = K_8 P_{C_8H_{16}} \theta_{Ni^{2+}}$
balance of active sites	$\theta_* + \theta_{[Ni^{2+}-H^-]-C_2H_3} + \theta_{[Ni^{2+}-H^-]-C_4H_7} + \theta_{[Ni^{2+}-H^-]-C_6H_{11}} + \theta_{[Ni^{2+}-H^-]-C_8H_{15}} = 1$ $\theta_{Ni^{2+}} + K_1 P_{C_2H_4} \theta_{Ni^{2+}} + K_{10} P_{C_4H_8} \theta_{Ni^{2+}} + K_9 P_{C_6H_{12}} \theta_{Ni^{2+}} + K_8 P_{C_8H_{16}} \theta_{Ni^{2+}} = 1$	
Implicit rate expressions	$\sum r_{C_2H_4} = -r^E_{[Ni^{2+}-H^-]-C_4H_7} - r^F_{[Ni^{2+}-H^-]-C_6H_{11}} - r^G_{[Ni^{2+}-H^-]-C_8H_{15}}$ $\sum r_{C_4H_8} = r^E_{[Ni^{2+}-H^-]-C_4H_7}$ $\sum r_{C_6H_{12}} = r^F_{[Ni^{2+}-H^-]-C_6H_{11}}$ $\sum r_{C_8H_{16}} = r^G_{[Ni^{2+}-H^-]-C_8H_{15}}$	
Explicit rate expressions	$-r_{C_2H_4} = \frac{k_3^+ K_1 K_2 P_{C_2H_4}^2 + k_5^+ K_4 K_{10} P_{C_2H_4} P_{C_4H_8} + k_7^+ K_6 K_9 P_{C_2H_4} P_{C_6H_{12}}}{1 + K_1 P_{C_2H_4} + K_{10} P_{C_4H_8} + K_9 P_{C_6H_{12}} + K_8 P_{C_8H_{16}}}$ $r_{C_4H_8} = \frac{k_3^+ K_1 K_2 P_{C_2H_4}^2}{1 + K_1 P_{C_2H_4} + K_{10} P_{C_4H_8} + K_9 P_{C_6H_{12}} + K_8 P_{C_8H_{16}}}$ $r_{C_6H_{12}} = \frac{k_5^+ K_4 K_{10} P_{C_2H_4} P_{C_4H_8}}{1 + K_1 P_{C_2H_4} + K_{10} P_{C_4H_8} + K_9 P_{C_6H_{12}} + K_8 P_{C_8H_{16}}}$ $r_{C_8H_{16}} = \frac{k_7^+ K_6 K_9 P_{C_2H_4} P_{C_6H_{12}}}{1 + K_1 P_{C_2H_4} + K_{10} P_{C_4H_8} + K_9 P_{C_6H_{12}} + K_8 P_{C_8H_{16}}}$	

Table S6: Sensibility table showing the contribution of each kinetic parameter on the reaction rate expressions shown in Table S5 for the *"ethylene coordination-insertion"* model after a disturbance of 5% on the value of the kinetic parameter

Kinetic parameter[1]	$r_{C_2H_4}$	$r_{C_4H_8}$	$r_{C_6H_{12}}$	$r_{C_8H_{16}}$
k_3^+	-0.40	-1.00	0.00	0.00
k_5^+	-0.38	0.00	-1.00	0.00
k_7^+	0.25	0.00	0.00	-1.00
K_1	-0.02	-0.63	0.39	0.39
K_2	-0.40	-1.00	0.00	0.00
K_4	-0.38	0.00	-1.00	0.00
K_6	-0.25	0.00	0.00	-1.00
K_8	0.22	0.22	0.22	0.22
K_9	0.25	0.00	0.00	-1.00
K_{10}	-0.16	0.22	-0.79	0.22

[1] Parameters in bold can be neglected based on the criterion assumed for the sensitivity analysis.

8. REACTION ORDER ASSESSMENT

8.1 "Cascade co-oligomerization"

$$\theta^* = \frac{1}{1+K_1P_{C_2H_4}+K_7P_{C_4H_8}+K_{12}P_{C_8H_{16}}} \quad \text{(S5)}$$

$$\ln(\theta^*) = \ln(1) - \ln\left(1 + K_1P_{C_2H_4} + K_7P_{C_4H_8} + K_{12}P_{C_8H_{16}}\right) \quad \text{(S6)}$$

$$\frac{\partial \ln(\theta^*)}{\partial P_{C_2H_4}} = -\frac{\partial \ln\left(1+K_1P_{C_2H_4}+K_7P_{C_4H_8}+K_{12}P_{C_8H_{16}}\right)}{\partial P_{C_2H_4}} \quad \text{(S7)}$$

$$P_{C_2H_4}\frac{\partial \ln(\theta^*)}{\partial P_{C_2H_4}} = -\frac{P_{C_2H_4}K_1}{1+K_1P_{C_2H_4}+K_7P_{C_4H_8}+K_{12}P_{C_8H_{16}}} \quad \text{(S8)}$$

8.2 "Solely ethylene coordination-insertion steps"

$$\theta^* = \frac{1}{1+K_1P_{C_2H_4}+K_{10}P_{C_4H_8}+K_9P_{C_6H_{12}}+K_8P_{C_8H_{16}}} \quad \text{(S9)}$$

$$\ln(\theta^*) = \ln(1) - \ln\left(1 + K_1P_{C_2H_4} + K_{10}P_{C_4H_8} + K_9P_{C_6H_{12}} + K_8P_{C_8H_{16}}\right) \quad \text{(S10)}$$

$$\frac{\partial \ln(\theta^*)}{\partial P_{C_2H_4}} = -\frac{\partial \ln\left(1+K_1P_{C_2H_4}+K_{10}P_{C_4H_8}+K_9P_{C_6H_{12}}+K_8P_{C_8H_{16}}\right)}{\partial P_{C_2H_4}} \quad \text{(S11)}$$

$$P_{C_2H_4}\frac{\partial \ln(\theta^*)}{\partial P_{C_2H_4}} = -\frac{P_{C_2H_4}K_1}{1+K_1P_{C_2H_4}+K_{10}P_{C_4H_8}+K_9P_{C_6H_{12}}+K_8P_{C_8H_{16}}} \quad \text{(S12)}$$

Table S7: Calculated sum of the squared difference between experimental and calculated reaction orders. Cells in bold represents the total sum of the squared difference for each model

	"cascade co-oligomerization"	*±Δz**	*"solely ethylene coordination-insertion steps"*	*±Δz**
butene	2.9	0.1	0.0	0.1
hexene	4.4	0.1	53.3	1.3
octene	0.9	0.0	41.6	1.1
total	***8.3***		***94.9***	

** ±Δz = standard error calculated with a confidence level of 95%.*

VITA

Gabriel Viana Sueth Seufitelli is born in Rio de Janeiro, Rio de Janeiro, Brazil in 1991. He completed high school at the Pedro II High School in Rio de Janeiro in 2008 and went to the Federal Rural University of Rio de Janeiro, where he studied Mathematics for one year before entering the Chemical Engineering Program. He received his bachelor's degree in Chemical Engineering in June 2016 and started his master's study in the same year at the University of Washington. In March 2018, he received his Master of Science in Environmental and Forest Sciences in Dr. Fernando Resende's lab and started his Ph.D. studies in the same year with Dr. Fernando Resende. In September 2019, Dr. Rick Gustafson became his advisor. In the last 2 years of his Ph.D. study, he taught 3 courses in the Bioresource Science and Engineering program at the University of Washington. In June 2021, he received his Ph.D. degree in Environmental and Forest Sciences under Dr. Rick Gustafson's supervision.